

Dissertation

[kumulativ]

zur Erlangung des akademischen Grades eines

Dr. rer. nat.

an der Friedrich-Schiller Universität

Plasmonische Metamaterial-Strukturen als Quellen gesteigerter Sensitivität in FT-IR- und VCD-Messsystemen

vorgelegt dem Rat der Chemisch-Geowissenschaftlichen Fakultät der
Friedrich-Schiller-Universität Jena

von

Richard Theodor Knipper

Forstweg 3
07745 Jena

Jena, 13. April 2018

Gutachter:

1.
2.
3.

Tag der öffentlichen Verteidigung:

Eidesstattliche Erklärung

Ich erkläre hiermit eidesstattlich, dass ich die vorliegende Arbeit selbständig angefertigt habe. Die aus fremden Quellen übernommenen Gedanken sind als solche kenntlich gemacht. Die Arbeit wurde bisher keiner anderen Prüfungsbehörde vorgelegt und auch nicht veröffentlicht. Ich bin mir bewusst, dass eine unwahre Erklärung rechtliche Folgen haben kann.

Datum

Unterschrift

Danksagung

Zuvorderst möchte ich Prof. Dr. Jürgen Popp für dieses interessante Thema und die Aufnahme in seine Arbeitsgruppe danken, sowie für die vielen Ratschläge und Diskussionen der letzten Jahre, welche diese Arbeit in seiner Form ermöglicht haben. Nicht zuletzt die vielen hilfreichen Anregungen zu wissenschaftlichem Denken, dem Präsentieren von Ergebnissen und der Arbeit als Wissenschaftler haben mir auf meinem Weg sehr geholfen. Dieser Dank gebührt weiterhin Dr. Dana Cialla-May und Dr. Karina Weber, durch deren Betreuung - wissenschaftlich wie organisatorisch - diese Arbeit in besonderer Weise beeinflusst wurde, und welche mir bei Planung von Experimenten wie auch der Interpretation der Daten stets hilfreich zur Seite standen. Ebenfalls danke ich Prof. Dr. Heidemarie Schmidt für die vielen Tipps und Hinweise während der Abschlussphase meiner Arbeit. Neben der Möglichkeit neue und spannende Aufgaben als Technologe in ihrer Abteilung anzugehen ermöglichte sie mir den wissenschaftlichen Freiraum um meine Dissertation abzuschließen.

Besonders möchte ich weiterhin PD. Dr. Thomas G. Mayerhöfer danken. Als steter Ansprechpartner und Ideengeber hat er in besonderer Weise diese Arbeit mit beeinflusst, und ohne seinen Rat und seine Hilfe wäre diese Arbeit nicht denkbar gewesen. Neben der Interpretation der Ergebnisse und dem gemeinsamen Entwickeln von Ideen waren es seine vielen Simulationen, die dieses Thema vielversprechend machten. Das gleiche Lob gebührt Dr. Uwe Hübner, welcher durch das Bereitstellen der technologischen Infrastruktur wie auch aktiver Mitarbeit an den verwendeten Substraten eine Basis für die schnelle und effektive technologische Weiterentwicklung der Substrate geschaffen hat. Auch Prof. Dr. Vladimir Kopecky von der Karls-Universität Prag danke ich an dieser Stelle für die ausdauernde und engagierte Hilfe. Durch die Möglichkeit in seiner Arbeitsgruppe und durch ihn selbst VCD-Spektren aufzunehmen, und seine andauernde Bereitschaft zu wissenschaftlicher Diskussion hat er weite Teile dieser Arbeit überhaupt erst ermöglicht. Auch die unermüdliche Zuarbeit beim Erstellen der Manuskripte sei an dieser Stellen allen dreien sehr gedankt.

Auch meiner Arbeitsgruppe – Andreea Radu, Sophie Patze, Sezin Yüksel, Vera Dugandzic, Xiao-Shan Zheng, Melina Yarbakht, Olga Zukovskaja, Barbara Seise,

Maria Küllmer und Martin Jahn – möchte ich hier gebührend danken. Das großartige Klima unter den Kollegen der JBCI hat mit vielen guten Gesprächen, Diskussionen und gemeinsamen Unternehmungen seinen Beitrag zu dieser Arbeit geleistet.

Weiterhin wäre diese Arbeit ohne die vielen kleinen und großen Hilfen meiner Kollegen und Freunde nicht möglich gewesen. Mario Ziegler, Andreas Ihring, Sebastian Goerke, Dirk Franke, Stefan Wötzel, Elmar Herbst, Anja Schumann und Paul Voigt sind nur einige wenige, die ich hier herausstelle, aber noch vielen anderen gebührt mein Dank, auch wenn ich hier nicht jeden einzelnen aufzählen kann. Ebenfalls danke ich Frank Hänschke, der mir durch viele Zugeständnisse ermöglicht hat, diese Arbeit neben dem Beruf abzuschließen.

Auch meiner Familie – meinen Eltern und Brüdern – danke ich für die bedingungslose Unterstützung und die Möglichkeit, die Promotion auch mal zu vergessen. Auch die vielen anderen Menschen, welche mich privat während meiner Dissertation begleitet haben, möchte ich hier nicht vergessen.

Vielen Dank dafür!

Zusammenfassung + Abstract

Zusammenfassung

In den Lebenswissenschaften und in der Pharmazie besteht ein kontinuierlicher Bedarf an neuen, immer leistungsfähigeren spektroskopischen Techniken. Neben der Entwicklung vollkommen neuer Techniken spielt die Weiterentwicklung bestehender Ansätze eine wichtige Rolle. Besonders die FT-IR-Spektroskopie als eine der am besten etablierten Techniken überhaupt schien ihre maximale Leistungsfähigkeit bereits vor über einer Dekade erreicht zu haben. Mit der fortschreitenden Entwicklung der Plasmonik und deren Einsatzfelder konnte jedoch u.a. die Sensitivität spektroskopischer Verfahren signifikant erhöht werden. Die Plasmonik und die dadurch zu erreichende oberflächenverstärkende Spektroskopie bereichert seit Jahren die Raman-Spektroskopie (SERS) und seit Kurzem auch die FT-IR-Spektroskopie (SEIRA). Besonders durch die Anwendbarkeit in bestehenden Messsystemen wird dieser Ansatz attraktiv gegenüber einer völligen Neuentwicklung der experimentellen Ausstattung. Eine große bestehende Basis an Geräten und geschultem Personal erleichtert hier die Umsetzung neuer Konzepte auf Basis etablierter Messaufbauten.

Für diese Umsetzbarkeit werden allerdings hohe Anforderungen an die oberflächenverstärkenden Substrate selbst gestellt. Da die Plasmonenbanden ein signifikanter Teil der Signalspektren sind, muss ihre Wechselwirkung mit den Analytbanden genau verstanden werden, um die Daten fehlerfrei zu interpretieren. Diese Wechselwirkung aufgrund der Änderung der dielektrischen Funktion ist unvermeidlich und bedarf eines tiefen Verständnis des zugrundeliegenden Wirkmechanismus der plasmonischen

Verstärkung. Insbesondere im Bereich der VCD-Spektroskopie ist dies, wie durch diese Arbeit gezeigt werden konnte, jedoch nicht immer vollständig gegeben. Um Fragen zum Endomorphismus von pharmazeutischen Substanzen und für die Lebenswissenschaften relevanten Moleküle zu adressieren, ist ein verstärktes Messsignal aus einer Wechselwirkung mit einer Plasmonenresonanz allerdings eines der wichtigsten Hilfsmittel. Maßgeschneiderte, auf die Anwendbarkeit optimierte Substrate gehören hier bisher zu den Ausnahmen der oberflächenverstärkenden Substrate. In dieser Arbeit wurden solche großflächigen Metamaterial-*Arrays* erstmals mit einem primären Fokus auf die Lebenswissenschaften konzipiert und realisiert. Hierbei bestätigte sich die Annahme, dass Metamaterial-*Arrays* bestehende Systeme stark aufwerten können. So konnte mittels einer großflächigen SHA-MPA-Struktur eine signifikante Verstärkung von Analytbanden im MIR-Spektralbereich gezeigt werden und gleichzeitig ein robustes Konzept zur Vermeidung von Messartefakten etabliert werden. Dazu wurden in den *Arrays* selektiv durch das anregende Licht Plasmonenresonanzen stimuliert, so dass der reine Beitrag der plasmonischen Verstärkung zum Messsignal durch eine Differenzbildung ermittelt werden kann. Besonders im Zusammenhang mit dem kontinuierlichen wissenschaftlichen Diskurs hinsichtlich der Verstärkungsfaktoren ist dieser Kontrollmechanismus ein wichtiges Mittel zur Evaluierung der Leistungsfähigkeit. Am Musteranalyt ODT konnte dieses im Experiment demonstriert werden, und erste Versuche mit DNA zeigten das breite Anwendungsspektrum der verwendeten Methodik auf.

Die Konzepte des SHA-MPA auch für chirale Messungen nutzbar zu machen war ein weiterer Schritt dieser Arbeit. Da bei diesem Verfahren normalerweise Messsignale im Bereich 10^{-4} - 10^{-5} erreichbar sind, ist hier eine Signalverstärkung direkt mit einer Reduzierung des instrumentellen Aufwand und der Messzeit verbunden. Weiterhin zeigten die Metamaterial-*Arrays* ein sehr gutes SNR bei Probenvolumen von $1.5 \mu\text{l}$. Da enantiomereine Stoffe, besonders in der Pharmazie, sehr schwer zu synthetisieren sind ist die geringe benötigte Analytmenge ein weiterer Vorteil gegenüber den Standardtechnologien. Um das SHA-*Array* in kommerziellen Messsystemen einsetzen zu können, wurde der Aufbau des *Array* grundlegend verändert und der Teil des

perfekten Absorbers entfernt. Dies ist für Transmissionsmessungen unausweichlich, da ein MPA zwingend optisch dicht ist. Transmissionsmessungen werden in der VCD-Spektroskopie allerdings nahezu exklusiv eingesetzt werden. Somit wurde erstmalig ein in Transmission arbeitendes chirales Metamaterial-*Array* realisiert, bei dem in nahezu resonanter Anregung die Lage der untersuchten Analytbanden und der Plasmonenresonanz im gleichen Spektralbereich lagen. Da es sich zudem um ein 2D-Metamaterial-*Array* handelt, welches erst durch die wiederholte Anordnung der Einheitszelle chiral wird, stellte es eines der Extremfälle der momentan in der wissenschaftlichen Forschung verwendeten möglichen Ansätze dar, ein VCD Signal durch oberflächenverstärkende Spektroskopie zu steigern. Hierbei wurde insbesondere eine unerwartet starke optische Aktivität des Metamaterial selbst beobachtet, welche zu den stärksten je gemessenen eines 2D-*Arrays* im MIR gehört. Des Weiteren zeigten die *Arrays* eine einfache Handhabung und die mehrfache Verwendbarkeit, welche von anwendungsorientierten Ansätzen gefordert wird. Somit lassen sich vollständige Messreihen auf dem selben *Array* durchführen, was die Bedeutung der Plasmonenbande insgesamt mindert, da ihre Präsenz bei allen Messungen gleichbleibend ist. Durch Entfernen des MPA-Teil wurden außerdem Schlitze durch die gesamte Tiefe des Substrat geöffnet, so dass Kapilarkräfte das zu untersuchende Analyt direkt in den Bereich höchster plasmonischer Verstärkung transportieren. Dieses Verhalten ist sehr vorteilhaft für die Anwendung der Methodik in Routineprozessen.

Zur Beantwortung der Frage, ob chirale Verstärkung in einem 2D-chiralen Metamaterial möglich ist, wurden die Metamaterial-*Arrays* mittels α -Pinene zu einem Sensor modifiziert. Es zeigte sich hier eine dem jeweiligen α -Pinene-Enantiomer entsprechende plasmonische Verschiebung unerwarteter Stärke. Die Verstärkung der Analytbanden selbst konnte ebenfalls mit Einschränkungen beobachtet werden. Die aus der Theorie unerwartete Ausbildung eines effektiven Mediums aus *Array* und Analyt überlagert diesen Effekt, und stellt in sich selbst ein völlig neuartiges Verhalten des Systems dar, welches neue Fragen der theoretischen Beschreibung dieses Systems eröffnet. Auf dieser Basis ließ sich aufzeigen, dass die etablierten Theorien zu chiralen Metamaterialien nicht in der Lage sind, korrekte Vorhersagen zum plasmonischen

Verhalten zu treffen. Somit lieferte diese Arbeit neben einem Sensorkonzept, welches sowohl FT-IR als auch VCD-Spektrometer stark in ihrer Funktion erweitert auch einen Beitrag zur Entwicklung der Theorie oberflächenverstärkender chiraler Metamaterialien und bereichert die zumeist theoretischen Betrachtungen um unerwartete und signifikante experimentelle Ergebnisse.

Abstract

Naturally, both pharmaceuticals and life sciences are in constant need of technologies of increasing efficiency. To achieve this, new methodologies are developed while established ones are refined. Especially FT-IR spectroscopy, which, already a decade ago, had been thought to have reached its climax, has gained new attention as plasmonics moved from research departments to application. Plasmonics and surface-enhanced spectroscopy had a high impact on Raman spectroscopy (SERS) and, lately, FT-IR spectroscopy (SEIRA). In particular the possibility to use these techniques in existing measuring systems made them more attractive than developing something new from scratch, even more so as the availability of equipment and skilled personnel facilitate the implementation of new concepts based on established measuring designs.

This, however, makes high demands on the surface-enhanced substrates themselves. To be able to interpret the measured data correctly, their interactions with analyte bands need to be understood in detail, as the plasmon bands can be found in the signal spectra themselves. However, as has been shown in this work, this expectation could not be met fully, especially when it came to VCD spectroscopy. To approach questions on the endomorphism of pharmaceutical substances and molecules that are of interest for the life sciences, an enhanced measuring signal stemming from the interaction with a plasmon resonance is of high importance. Substrates that are optimized for their applicability are an exception when it comes to surface-enhanced substrates. In the course of this work, such large-area metamaterial arrays have been designed with a primary focus on the life sciences. Here, the assumption could be confirmed that metamaterial arrays are a promising possibility to refine existing systems. With the help of a large-area SHA-MPA structure, we could show a significant enhancement of the analyte bands in the MIR range and, at the same time, devise a robust concept to avoid artefacts created by the measurement process. Additionally, by selectively stimulating the orientation of the polarisation axis of the incident light within the arrays, we stimulated plasmon resonances – thus making it possible to determine the contribution of the plasmon enhancement to the overall signal only, calculated by

subtracting the nonresonant excitation from the resonant one. Especially in view of the continuing scientific discourse about enhancement factors, this control mechanism provides an important instrument to evaluate efficiency. Using the example analyte ODT as well as DNA (first experiments), we could demonstrate the broad spectrum of applications for the method used.

Another aim of this work was to harness SHA-MPA for chiral measurements as well. Usually, this method achieves measuring signals of up to 10^{-4} - 10^{-5} - resulting in long measurement times, and thus any increase of signal strength can be translated to a decrease in instrumental effort or measuring time. Furthermore, the metamaterial arrays showed a very good SNR at sample sizes of $1.5 \mu\text{l}$. As enantiomere-pure materials are hard to synthesize, especially for pharmaceutical applications, the possibility to work with very small amounts of analyte is another advantage over standard technologies. To be able to use the SHA-array in commercial measuring systems, the design of the array was changed essentially – removing the perfect absorber from the setup. This is unavoidable for measurements of transmission as an MPA is, by design, optically sealed. Measurements of transmission are exclusively used in VCD spectroscopy. Thus we, to the best of our knowledge, for the first time, realised a chiral metamaterial array which works in transmission, where – while the resonant incitation remains the same – analyte bands and plasmon resonance are within the same spectral range. As it further comprises a 2D-metamaterial array which turns into a chiral one only by the repeated use of the single cell, this is one of the extremal cases of the current possibilities in research to increase the VCD signal by surface-enhanced spectroscopy. Here, we could observe an unexpectedly high optical activity of the metamaterial itself – being one of the highest ever measured for a 2D-array in MIR conditions. In addition, it is inexpensive to employ the arrays as they are insensitive to mechanical failure and can be used several times – features which are often asked for in designs focused on application. This makes it possible to do several runs of measurements on the same array; thus reducing the impact of the plasmon band as those remain the same for all individual measurements. By removing the MPA part, the slits are also opened throughout the whole substrate.

Due to this, capillary forces directly transport analyte to the area where plasmon enhancement is at its highest. This behaviour is advantageous for the application of the method in routine processes.

To answer the question if chiral enhancement is possible in a 2D chiral metamaterial, we modified the metamaterial-arrays with the help of α -pinene to achieve a sensor. We could observe an unexpectedly high plasmonic shift. Further, we observed an enhancement of the analyte bands within certain limits. Contrary to theory, the unexpected formation of an effective medium superimposes this effect - in itself a completely new behaviour of the system which opens up new questions for its theoretical description. Based on this, we could show that established theories on chiral metamaterials are not sufficient to make correct assumptions about plasmon behaviour. Apart from a sensor concept which furthers both FT-IR as well as VCD spectroscopy, this work thus adds to the development of a theory for surface-enhanced chiral metamaterials and adds to the mostly theoretical considerations with unexpected and significant experimental results.

Inhaltsverzeichnis

Zusammenfassung + Abstract	vii
1 Einleitung	3
2 Grundlagen der plasmonischen Signalverstärkung	9
2.1 Nanostrukturierte SEIRA-Substrate für die Spektroskopie	9
2.1.1 Plasmonische Grundlagen	10
2.1.2 Absorbanz, EIT/EIA und EOT	15
2.1.3 Perfekte Absorption	18
2.1.4 Chiralität	19
2.1.5 Nanostruktur plasmonischer Substrate	20
3 Aktuelle Entwicklungen in der SEIRA- und VCD-Spektroskopie	25
3.1 Oberflächenverstärkende Substrate	26
3.1.1 Perfekte Absorber	28
3.1.2 Entwicklung der chiralen Plasmonik	30
4 Vorliegender Forschungsansatz	33
4.1 Konstruktive Ansätze der Signalsteigerung	34
4.2 SHA-MPA als spektroskopisches Werkzeug	39
4.3 Chirale Metamaterialien als potentielle Quellen chiraler Verstärkung	42
4.4 Vorteile und Nachteile plasmonischer Ansätze in der Spektroskopie .	46
5 Abschließende Betrachtung	51
5.1 Fazit	51
5.2 Ausblick	54
6 Publikationen und Konferenzbeiträge	57
6.1 Publikationen	57
6.1.1 Ultra Sensing by Combining Extraordinary Optical Transmission with Perfect Absorption [P1]	57

Inhaltsverzeichnis

6.1.2	Plasmonic nanostructures for surface enhanced spectroscopic methods [P2]	67
6.1.3	Observation of Giant Infrared Circular Dichroism in Plasmonic 2D-Metamaterial Arrays [P3]	106
6.1.4	Slit-enhanced chiral- and broadband infrared ultra-sensing [P4]	112
6.2	weitere Publikationen	123
6.2.1	THz Absorption in Fabric and Its Impact on Body Scanning for Security Application [P5]	123
6.2.2	A low power 10 V programmable array based on Nb x Si _{1-x} Josephson junctions for metrology applications	130
6.2.3	A dry-cooled AC quantum voltmeter	130
6.3	weitere Veröffentlichungen	130
6.3.1	Hochsensitive infrarotspektroskopische Analytik mittels plasmonischer Feldverstärkung	130
6.4	<i>non-peer-review</i> - Publikationen, Tagungsbände	130
6.4.1	Wafer- and membrane-based plasmonic sensor surfaces for ultra-sensitive molecular spectroscopy	130
6.4.2	Plasmonische Strukturen für die Bioanalytik	131
6.5	Autorenbeiträge	131
6.5.1	Erklärung zu den Eigenanteilen des Promovenden	134
6.6	Konferenzbeiträge (Poster)	138
6.6.1	weitere Poster und Publikationen	138
6.7	Lebenslauf	139

Abbildungsverzeichnis

2.1	Anregungsmöglichkeiten eines Oberflächenplasmon-Polariton (rot) and der Phasengrenze Gold-Dielektrikum. a) Otto-Geometrie mit Prisma per Luftspalt, b) Kretschmann-Geometrie mit Prisma ohne Luftspalt und dünner Metallschicht c) Anregung durch Oberflächenstruktur (Gitter) zur Impulserhaltung d) Anregung über eine Nanoantennen passender Größe.	11
2.2	Dispersionsrelation eines Oberflächenplasmon im Vergleich zur Lichtlinie eines Photon. Beide Kurven schneiden sich nur für $k=0$. Durch ein Prisma oder Gitter wird ein Betrag k_x aufaddiert, so dass das Photon (blaue Kurve) ein Oberflächenplasmon (rote Kurve) anregen kann. Das Oberflächenplasmon liegt rechts von der Lichtlinie, hat also eine kleinere Wellenlänge als elektromagnetische Strahlung in Luft. . . .	12
2.3	Absorption einer Molekülbande die an eine Plasmonenresonanz unterschiedlicher Lage koppelt (1600, 1700, 1730 and 1750 cm^{-1}). Je nach Oszillatorparametern der Simulation und Kopplungsstärke wird ein EIT-, EIA-Verhalten oder ein nahezu ungestörtes Verhalten (blaue Kurven) erreicht. Es wird ersichtlich, dass eine Resonanzanregung (Lage der Plasmonenresonanz gleich der der Molekülabsorption) nicht die höchste Signalverstärkung erreicht. Nach [?].	16
2.4	Beispielhafte Darstellung der Chiralität für ein 2D-händiges Objekt (Spirale, <i>Array</i> aus Nanoschlitzten). Diese sind jeweils ab der (n+1)-ten Dimension achiral. Ein 2D chirales Objekt ist also im dreidimensionalen Raum achiral. Dies entspricht den Operationen Rotation und Translation in 2D. Durch diese lässt sich das $+45^\circ$ Enantiomer a) nicht in das -45° Enantiomer b) überführen. Die Spiegelung (gestrichelte Linie) als Symmetrieoperation in 3D überführt jedoch das -45° Enantiomer in das $+45^\circ$ Enantiomer. Dieses findet direkte Anwendung in 6.1.3 und 6.1.4.	19

Abbildungsverzeichnis

3.1 Simulation der Feldüberhöhung des Plasmon innerhalb des Schlitzes bei einer Schlitzausdehnung von ± 25 nm für eine variierende Dicke des Polyethylens (PE) an den Schlitzwänden (0 nm entspricht kein PE bis 50 nm, was vollständig gefüllten Schlitzten entspricht), nach [?]] 27

4.1 Ausgangsstruktur des SHA-MPA. a) REM und b)SIM-Fluoreszenzaufnahme des gleichen *Arrays* zum Beweis der selektiven Anreicherung des Analyten (SAMSA) in den Schlitzten. Die in a) sichtbaren Schlitz zeigen als einziges ein in b) messbares Fluoreszenzsignal. Die Stege sind aufgrund des Auflösungsvermögens nicht sichtbar, lassen sich jedoch im Fourierraum erkennen. (Maßstab: $3 \mu\text{m}$) c) Skizze der für die Simulation genutzten Einheitszelle, welche in a,b) und d) gestrichelt eingezeichnet ist (b=910 nm; a=1100 nm; d=45 nm; c=1005 nm) c) REM-LEI-Nahaufnahme der Schlitzstruktur,(Maßstab: 100 nm) nach 6.1.1. 36

4.2 Ausgangsstruktur des chiralen SHA. a) REM-SEI Aufnahme der Vorderseite eines SHA-*Array* mit -45° Schlitzorientierung b)REM-LEI des gleichen *Arrays* auf der Rückseite der Struktur zeigt die durchgehenden Schlitz. Ein rückseitig angeregtes -45° *Array* entspricht einem $+45^\circ$ *Array* aufgrund der 3D Rotation. c) Skizze der für die Simulation genutzten Einheitszelle (a = 1800 nm, b = 1000 nm, c1 = 1700 nm, c2 = 1000 nm und der Schlitzbreite d1,d2 = 50 nm) d)Orientierung der linearen Anregungspolarisation zum *Array*. Dabei entspricht 0° einer resonanten Anregung des Hauptschlitzes. 38

4.3 a) Einzelschlitz-*Array* mit 40 nm breiten Schlitzten inkubiert mit ODT, resonant angeregt (0° orientiertes linear polarisiertes Licht; rot) und nichtresonant angeregt(90° linear polarisiertes licht; grün). b)Gleiche Anregungsbedingungen für ein Einzelschlitz-*Array* mit 50 nm breiten Schlitzten inkubiert mit ODT . c) Spektrum für ein Einzelschlitz-*Array* mit 50 nm breiten Schlitzten inkubiert mit DNS/PBS Mischung (rot: 0° orientiertes lin. pol. ;grün : 90° orientiertes lin. pol.). Das blaue Spektrum zeigt die Referenzmessung in Transmission der reinen DNA. Aus [6.1.4] 40

4.4	Messung eines ODT gefüllten x - <i>Arrays</i> mit linear polarisiertem Licht unterschiedlicher Einfallsausrichtung. Erkennbar ist die Verstärkung der CH_2 und CH_3 Banden des ODT. [unten links] Ausschnittartige Darstellung der CH_2 (s) 1466 cm^{-1} Deformationsschwingung, welche mit der verstärkten Anregung des Plasmon korreliert (von 90° zu 0° , resultierend in 4.1% geringerer Reflektion. [unten rechts] CH_2 und CH_3 symmetrische und asymmetrische Streckerschwingung. Die genauen Anregungsbedingungen werden in Appendix, Abbildung 1 dargestellt. Aus [6.1.4]	41
4.5	Messungen an zwei x - <i>Arrays</i> mit $+45^\circ$ bzw. -45° orientiertem zweiten Schlitz, sowie einem achiralen <i>Array</i> mit 90° Orientierung als Negativkontrolle. Es zeigt sich die sehr gute Spiegelsymmetrie der beiden Enantiomere ($+45^\circ$ Schlitzausrichtung) und das bis dato höchste gemessene CD Signal von 0.83 für ein 2D Metamaterial. [unterer Teil] Vergrößerung der Mittelachse zeigt ein minimales CD Signal des achiralen <i>Arrays</i> , bei dem es sich um ein Artefakt handelt. $\frac{1}{4}$ der PEM bei 2800 cm^{-1} ; Probenrotation mit 0.1 Hz. Aus [6.1.3].	44
4.6	Vergleich von normaler (durchgehende Linie) und invertierter (gestrichelte Linie) Orientierung (also Wechsel der Händigkeit durch Inversion) gemessen mit L-, R- und einem Racemat von α -Pinene eines $+45^\circ$ <i>Arrays</i> . Neben einer starken plasmonischen Verschiebung von 993 cm^{-1} zeigt sich der Spektralbereich von $2800 - 3000\text{ cm}^{-1}$ ohne scharfe Bandenstruktur. Entgegen der Erwartung zeigen beide Enantiomere eine unterschiedlich stark ausgeprägte Verschiebung der Plasmonenbande. Diese ist hier unabhängig von der Händigkeit des <i>Arrays</i> . Das stützt die Theorie eines effektiven Mediums. Aus [6.1.4]	45
.1	[Appendix 1] Relative Orientierung des linear polarisierten Anregungslicht zur Ausrichtung des Schlitzarray. Wie ersichtlich regt sowohl $+30^\circ$ als auch -30° orientiertes Licht die primäre Resonanz bei 2050 cm^{-1} an, jedoch ist die Anregung der sekundären Resonanz bei 3200 cm^{-1} ungleich, da die Polarisations Ebene für -30° fast parallel zum sekundären Schlitz orientiert ist. Aus [6.1.4, supplement]	143

Abkürzungen

Abbildungsverzeichnis

Abkürzung	Deutsche Entsprechung	Englische Entsprechung
EBL	Elektronenstrahl-lithographie	Electron-beam lithography
EIT	elektromagnetisch induzierte Transparenz	Electromagnetically induced transparency
EIA	elektromagnetisch induzierte Absorption	Electromagnetically induced absorption
EOT	Außergewöhnliche optische Transmission	Extraordinary optical transmission
SERS	Oberflächenverstärkte Raman-Spektroskopie	Surface enhanced Raman spectroscopy
LSPR	lokalisierte Oberflächenplasmonenresonanz	Localized surface plasmon resonance
MPA	Metamaterial(basierter) perfekter Absorber	Metamaterial(-based) perfect absorber
REM	Rasterelektronenmikroskopie	Scanning electron microscopy
OA	Optische Aktivität	Optical activity
ORD	Optische Rotationsdispersion	Optical rotation dispersion
ROA	Raman optische Aktivität	Raman optical activity
SEIRA(S)	Oberflächenverstärkte Infrarot-Absorptions-(Spektroskopie)	Surface enhanced infrared absorption (spectroscopy)
SHA	Subwellenlängen Lochanordnung	Subwavelength hole array
SNR	Signal-Rauschverhältnis	Signal-to-noise ratio
SPP	Oberflächenplasmon-Polariton	Surface plasmon polariton
VCD	Schwingungs-Zirkular-Dichroismus	Vibrational circular dichroism

1 Einleitung

Als eine der grundlegenden Techniken der Spektroskopie hat sich die Fouriertransform-Infrarotspektroskopie (FT-IR) seit den 1980er Jahren bis heute zu einem bedeutenden Werkzeug und Standard in der Forschungslandschaft und der Industrie entwickelt. Besonders das robuste und gut erschlossene theoretische Grundgerüst leistet hierbei einen zentralen Beitrag zur Popularität dieser Standardmethode, auch da die Phase der intensiven Weiterentwicklung der Theorie einige Zeit zurückliegt. Die daraus resultierende, flächendeckende Versorgung von Hochschulen und Laboren mit leistungsfähigen und ausgereiften Geräten ist daher ein Schlüsselaspekt der hohen Bedeutung der FT-IR-Spektroskopie. Der direkte Zugang zu chemischen Bindungsinformationen über die entsprechenden Schwingungsfrequenzen¹ und die schnelle Analysemöglichkeit ohne direkten Kontakt zur Probe sichern die weiterhin bestehende Anwendbarkeit in der Grundlagenforschung bis hin zu Routineanwendungen, wie bspw. Qualitätskontrollen in der chemischen Industrie und Lebensmittelanalyse. Insgesamt bildet FT-IR damit eine komplementäre Technik für die Hochdruck-Flüssigkeitschromatographie (HPLC) und die Magnetresonanzspektroskopie (NMR) in chemischen Routinekontrollen sowie der Raman-Spektroskopie und der davon abgeleiteten SERS-Spektroskopie. Die Geräteentwicklung und die Theorie der Methode FT-IR kann als im weitesten Sinne abgeschlossen betrachtet werden, wobei weiterhin eine stetige Verbesserung der FT-IR-Methodik stattfindet. Lediglich in der Schwingungszirkulardichroischen (VCD) Spektroskopie zur Aufklärung der Struktur der Isomere – einem Seitenzweig der FT-IR – ist die Entwicklung verhältnismäßig wenig fortgeschritten. Die Markteinführung des VCD-Verfahrens erfolgte erst im Jahre 1993. Kosten und Aufwand der Methode beschränken die Anwendung jedoch seitdem fast ausschließlich auf die pharmazeutische Industrie sowie die Kontrolle chemischer Synthesen.

Gegenüber anderen Technologien wie SERS ist die Signalintensität der SEIRA-Spektroskopie deutlich geringer, weshalb sie vielfach zwischen SERS und Raman

¹Es muss angemerkt werden, dass diese Zuordnung allerdings nicht immer trivial ist

1 Einleitung

Spektroskopie eingeordnet wird. Diese ist durch eine Abhängigkeit der vierten Ordnung von der elektrischen Feldstärke ($\propto \vec{E}^4$) für SERS und durch eine Abhängigkeit zweiter Ordnung ($\propto \vec{E}^2$) für SEIRA abzuschätzen, und ist zurückzuführen auf eine plasmonische Wechselwirkung zwischen Analyt und Oberfläche. Dies geschieht durch das Ausnutzen von Elektronenschwingungseffekten, den sogenannten Oberflächenplasmonen (SPP, surface plasmon polariton), welche eine lokale Überhöhung des elektrischen Feldes ermöglichen. Bestrebungen, plasmonische Verstärkung zu nutzen, werden seit dem Entstehen der SERS-Technik auch im Bereich von SEIRAS unternommen. Die resultierende oberflächenverstärkende IR-Absorptions-Spektroskopie (SEIRAS) nutzt besagte strukturierte Oberflächen mit dem Ziel der Erhöhung der Signalintensität durch Verstärkung der Absorption von Schwingungsbanden. Die nur verhältnismäßig geringen Verstärkungsfaktoren von typischerweise unter 10^3 ließen diese Technik jedoch bisher wenig leistungsfähig erscheinen. Diese Annahme ist jedoch nur dann haltbar, wenn lediglich die reine Verstärkung betrachtet und der Quotient aus Verstärkung und grundlegendem Effekt (Stokes-Streuung für SERS und Absorption für SEIRA), d.h. die gesamte Photonenausbeute über eine analytisch relevante Fläche, außer Acht gelassen wird. Bei der VCD-Spektroskopie resultiert die lange Messzeit im Stundenbereich aus der Kombination der Photonenausbeute mit der Schwäche des Effekts selbst, da die Differenz zweier IR-Messungen gebildet wird. Die FT-IR-Spektroskopie selbst benötigt eine breitbandige Anregung über den gesamten zu messenden Bereich (mit Ausnahme fortgeschrittener Ansätze wie dem Nutzen von Quantenkaskadenlasern), wohingegen die Anregung bei der Raman-Spektroskopie über eine Wellenlänge im nahen ultravioletten Spektralbereich bis hin zum nahen Infrarot erfolgt, wobei die Anregung im sichtbaren Spektrum dominiert. Betrachtet man die dabei genutzte Stokes-Streuung, so wird typischerweise etwa eines von einer Million Photonen-Stokes gestreut und damit für die Detektion nutzbar. Durch Oberflächeneffekte erreichen Techniken wie SERS und SEIRA hier eine höhere Signalverstärkung durch die Verstärkung des elektrischen Feldes, was bei beiden Ansätzen zu einer gesteigerten Photonenausbeute führt.

Ziel dieser Promotionsarbeit ist die Realisierung des oberflächenverstärkenden Ansatzes für die FT-IR- und VCD-Spektroskopie, besonders in den Lebenswissenschaften. Hierbei profitiert das Feld von Fortschritten in der Simulationstechnik und in der Herstellungstechnologie. So wird erstmalig eine zielgerichtete Entwicklung von mikrostrukturierten SEIRA-Substraten ermöglicht. In der vorliegenden Arbeit wird deutlich, dass die Verstärkung der Molekülabsorption unter Verwendung von mikrostrukturierten Antennenarrays die Verstärkung von – bisher überlegenen – Inselfilmen auch unter Betrachtung der Gesamtfläche des Sensors übertrifft, aller-

dings der Effekt der Plasmonenbande die praktische Nutzbarkeit dieser Methode voraussichtlich einschränkt.

Diese im Spektrum selbst präsente Plasmonenbande als zugrunde liegender Effekt der SEIRA-Spektroskopie beschreibt die Anregung von Elektronenschwingungen durch Wechselwirkung mit Photonen. Bedingt durch das Gesetz der Impulserhaltung geschieht dies nur, wenn die Oberfläche des anzuregenden Materials Bedingungen erfüllt. Inselfilme, welche lange Zeit die Forschung dominierten, bieten nur minimale Anpassungsmöglichkeiten der Geometrie und daraus resultierend der gezielten Anregbarkeit, da sie ein reiner physikalischer Schichtwachstums- und Oberflächeneffekt sind. Die Struktur der Oberfläche zu steuern ist jedoch zwingend nötig für die Optimierung des Resonanzverhaltens von plasmonischen Sensoren. Eine Möglichkeit, um Resonanzbedingungen zu garantieren, ist es, anstelle des Aufwachsens von besagten Inselfilmen mit einer Nanostrukturierung der Oberfläche zu arbeiten, wie sie auch bei vielen Substraten für die SERS Spektroskopie genutzt wird. Sowohl SERS als auch SEIRAS sind über diesen Mechanismus verwandt und teilen größtenteils ihre Entwicklungshistorie sowie grundlegende Vor- und Nachteile gegenüber nicht oberflächenmedierten Effekten.

Ein großer Vorteil von SEIRA ist die bereits genannte Kompatibilität mit bestehenden Messsystemen. Sie ist eines der wenigen Konzepte, welche die bestehende Spektroskopie aufwertet, ohne bestehende Geräte obsolet werden zu lassen. Eine Anwendung beispielsweise in der Pharmatechnologie wird im Gegensatz zu disruptiven Technologien durch bestehende Messaufbauten erleichtert. Neben der als grundlegend anzusehenden Signalverstärkung bieten plasmonisch aktive SEIRA-Substrate weitere vorteilhafte Aspekte. Durch Oberflächen- und Materialabhängigkeit des Effekts lässt sich dieser der gewünschten resonanten Wellenlänge anpassen. Somit lassen sich Breitband- und Hoch-Tiefpass-Eigenschaften mit der Signalverstärkung einstellen. Dieses ermöglicht eine selektive Verstärkung bestimmter spektraler Absorptionsbanden. Dies könnte es in Zukunft ermöglichen, auf optische Vorfilter in Sensoren zu verzichten oder den „Fingerabdruck-Bereich“ einer bestimmten chemischen Bindung selektiv zu verstärken. Naheliegend ist zum Beispiel die $CH_2 - CH_3$ -Streckschwingung, welche sowohl in der Überwachung von Verbrennungsprozessen als auch unterschiedlichsten Anwendungen in den Lebenswissenschaften große Relevanz besitzt. Durch eine geschickte Wahl der Nanoantennen-Geometrie lässt sich das Metamaterial selektiv gegenüber der Polarisationsrichtung des einfallenden Licht gestalten. Durch die Ausrichtung der Polarisation des Anregungslichtes realisiert man so „schaltbare“ Verstärkungen, welche z.B. für Auswerteverfahren wie die sogenannte *lock-in*-Verstärkung genutzt werden könnten, bei denen die Anregung mit

1 Einleitung

einer bekannten Frequenz moduliert ist, um das SNR der Messung zu verbessern.

Ein Nachteil des SEIRA-Ansatzes ist der erhöhte Aufwand beispielsweise gegenüber kolloidbasierten Ansätzen der Plasmonik. Jedoch lassen sich durch die Mikrostrukturierung noch weitere Eigenschaften mit dem Material verbinden. Diese erhöhen teils stark die Anwendbarkeit als Sensor. So sind eine selektive Bindungsfähigkeit oder Kapillarkräfte durch Mikroschlitzte und Oberflächenmodifikationen realisierbar. Es entstehen bei durchgängig geschlitzten Membranen Kapillarkräfte, welche sich für die Probenmodifikation nutzen lassen. Da die Plasmonik in weiten Teilen durch metallische Oberflächen abgebildet wird, lassen sich besonders selektive Bindungen zu Edelmetallen wie Thiol- und Aminobindungen experimentell nutzen. Dadurch wird das SEIRA-Sensorkonzept äußerst vielseitig und leistungsfähig. Für Transmissionsmessungen im Infraroten sind Metallschichten jedoch selbst bei sehr geringen Schichtdicken ungeeignet und Siliciumwafer sind ebenfalls nur bedingt transparent genug hierfür. So ist es für diese Messungen unabdingbar, einen von geschlossenen Schichtsystemen abweichenden Designansatz zu finden. Plasmonisch aktive Metallstrukturen müssen dazu entweder auf einem transparenten Trägermaterial wie KBr oder auf dünnen, zumeist aus Siliciumnitrid bestehenden Membranen aufgebracht werden. Durch den weiterführend genutzten membranbasierten Ansatz lässt sich als Funktion weiterhin eine außerordentliche optische Transmission (Transmission durch Aperturen kleiner der Wellenlänge) im Sensor erreichen. Neben diesen Eigenschaften lassen sich die mikrostrukturierten Oberflächen auch mit einer „Händigkeit“ versehen, wodurch Substrate mit einer sehr hohen optischen Aktivität (OA) und möglicher chiraler Verstärkung erzeugt werden können. Wenn es gelingt, diese chirale Plasmonik zur selektiven Verstärkung von Molekülen bestimmter Händigkeit (Enantiomere) einzusetzen, würde dieses neben normalen FT-IR-Geräten auch VCD-Geräte stark aufwerten. Hier sind sowohl Ansätze der direkten Verstärkung der Absorptionsbanden des Analyten denkbar, wie auch eine indirekte Messung über die Resonanzverschiebung der Plasmonenbande. Diese Ansätze versprechen einen reduzierten Messaufwand und geringere Messzeiten, was eine breitere Anwendung von VCD-Messungen erlauben könnte.

In der vorliegenden Promotionsarbeit wird dargestellt, wie erstmalig großflächige Arrays von $10^3 \times 10^3$ Nanoantennen als perfekter Absorber und chirales Metamaterial für VCD- und FT-IR-Anwendung gefertigt wurden. Im Gegensatz zu den bisher präsenten kleinflächigen SEIRA-Sensoren kann somit bei einem geringen Analytvolumen dennoch auf hochkomplexe Messsysteme mit stark vergrößernden Optiken verzichtet werden. Die Entwicklung hin zu oberflächenverstärkenden Substraten ist somit auch im VCD- und IR-Bereich vielversprechend und potentiell in der Lage,

eine substantielle Aufwertung dieser spektroskopischen Standardtechnologien zu bewirken.

Im Fokus dieser Arbeit steht somit die Entwicklung und der Test eben dieser Substrate in neuen Anwendungsfeldern der FT-IR- und VCD-Spektroskopie. Ziel dieser Arbeit ist es weiterhin, den Ansatz der konstruktiven Signalsteigerung in IR- und VCD-Messsystemen durch den Einsatz plasmonischer Substrate zu überprüfen, und abschließend die Frage zu adressieren, ob eine oberflächenverstärkte VCD-Messung unter diesen Rahmenbedingungen möglich ist. Darüber hinaus wird diese Arbeit überprüfen, inwieweit eine spätere Anwendbarkeit dieser Ansätze in den Lebenswissenschaften möglich ist. Besonders die Präsenz der Plasmonenbanden in den Spektren wirft in diesem Zusammenhang Fragen der Anwendbarkeit auf, welche im Rahmen dieser Arbeit adressiert werden sollen. Im Versuch konnte gezeigt werden, dass eine substantielle Steigerung der Signalintensität ebenso wie schaltbare plasmonische Verstärkungen und ein sehr ausgeprägtes chirales Verhalten zu erreichen war. Es zeigte sich, dass der plasmonische Effekt zu Überlagerungen in den Signalspektren, insbesondere bei VCD-Messungen, führte und damit die Interpretation der Daten erschwerte. Dennoch gelang es erstmalig, eine Struktur zu erzeugen, bei der die Anregungsfrequenz des Plasmon-Polariton und die des Analyten im selben Frequenzbereich liegen. Dies ist ein Indiz dafür, dass „echtes“ oberflächenverstärktes VCD möglich ist.

Die hier in Kapitel 1 eingeführte Thematik und besonders die Herausforderungen bei der Realisierung des Ansatzes der plasmonisch verstärkten Spektroskopie in SEIRA und VCD werden im Folgenden detailliert betrachtet. In Kapitel 2 – Grundlagen der plasmonischen Signalverstärkung – wird ein Einblick in die wissenschaftlichen Grundlagen der FT-IR- und SEIRA-Technologie sowie der Plasmonik und der optischen Aktivität gegeben. Weiterhin werden die zugrunde liegenden Fertigungstechnologien beleuchtet und deren Funktion in den gezeigten Substraten vorgestellt. Kapitel 3 – Aktuelle Entwicklungen in der SEIRA- und VCD-Spektroskopie – gibt einen Überblick über die aktuelle Forschungslandschaft im Bereich der SEIRA- und VCD-Spektroskopie. Besonderes Augenmerk liegt dabei auf dem aktuellen Forschungsdisput bezüglich oberflächenmediierter verstärkter CD-Spektren. Es wird auf die verschiedenen Richtungen innerhalb der Forschungsgemeinschaft eingegangen und die vorliegende Arbeit kontextuell darin verortet. Über die FT-IR Spektroskopie hinaus soll der oberflächenverstärkende Ansatz grundlegend diskutiert und der Weg zum chiralen Substrat und der Anwendung im VCD beleuchtet werden. Darauf aufbauend werden in Kapitel 4 – Vorliegender Forschungsansatz – die eigenen Forschungsansätze (im Licht der zugrundeliegenden Fragestellung) dargestellt und kritisch diskutiert.

1 Einleitung

Hieran schließt sich eine Auswertung der Ergebnisse im Rahmen der Ausgangsfragestellung an. In Kapitel 5 wird neben der abschließenden Einordnung der Ergebnisse ein kurzer Ausblick auf die durch diese Forschungsarbeit eröffneten neuen Fragen gegeben und der Einfluss auf den Stand der Theorie diskutiert.

2 Grundlagen der plasmonischen Signalverstärkung

2.1 Nanostrukturierte SEIRA-Substrate für die Spektroskopie

Neben den physikalischen Grundlagen zur Anregung eines Oberflächen-Plasmon-Polariton (im Weiteren als Plasmon bezeichnet; in Abgrenzung zu *bulk*- oder Volumenplasmonen) ist für das Design von SEIRA-Substraten die Kenntnis der Materialeigenschaften sowie ein sicherer Umgang mit den Werkzeugen der Mikrostrukturtechnologie zwingend nötig. Nur in Kombination sind so angepasste und präzise eingestellte Resonanzfrequenzen der Substrate zu generieren und Feldüberhöhungen zur Signalverstärkung zu erreichen. Basis aller hier gezeigten Überlegungen sind grundlegende Erkenntnisse aus der Plasmonik, welche wiederum aus den Maxwell'schen Gleichungen abgeleitet werden. Neben diesen sind die mit dem Plasmon verbundenen Effekte der extraordinären optischen Transmission, des elektromagnetisch induzierten Transparenz sowie der elektromagnetisch induzierten Absorption (EOT, EIT und EIA) von Bedeutung sowie ein Grundverständnis der optischen Aktivität und Chiralität. Zur Demonstration des Konzepts der subwellenlängen Lochanordnung in Verbindung mit einem metamaterialbasierten perfekten Absorber (SHA-MPA) wurde im Hinblick auf die Lebenswissenschaften der Messaufbau auf die spezifischen Fragestellungen angepasst. So wurde unter anderem die Messung in Transmission ermöglicht, um über Reflektions-/Transmissionmessungen experimentell die Probenabsorption bestimmen zu können. Dieses erfolgte auch im Hinblick auf die VCD-Spektroskopie chiraler Moleküle, bei der keine Reflektionskonfigurationen als verfügbarer Messaufbau existieren und somit Messungen in Transmission unabdingbar sind. Als Beispiel wurde die breitbandige Anpassbarkeit der zuvor gezeigten oberflächenmodifizierten Substrate gewählt und anhand von Modelanalyten wie Octadecanethiol und Lösungsmitteln sowie Proteinen demonstriert. Ziel war es, eine Chipplattform zur Verbesserung

2 Grundlagen der plasmonischen Signalverstärkung

der analytischen Möglichkeiten bestehender FT-IR Messplätze zu entwickeln, und mögliche chirale Eigenschaften dieses Sensorkonzepts zu beschreiben.

2.1.1 Plasmonische Grundlagen

Die Verstärkungsmechanismen SEIRA [?] und SERS [?] sind mit dem Konzept der Plasmonik untrennbar verbunden. Betrachtet man den SEIRA-Effekt, so stellt man fest, dass dieser komplementär zum SERS-Effekt ist und seine Konzeptionsgeschichte sich sehr lange parallel zu letzterem vollzog. Beide Effekte lassen sich auf die Plasmonik als zugrundeliegendes Phänomen zurückführen. Beobachtet man den Einfall einer elektromagnetischen Welle einer Frequenz λ auf eine glatte Metalloberfläche, so wird diese für den Fall einer perfekt glatten Oberfläche abhängig von der Wellenlänge größtenteils reflektiert. Dies geschieht in der klassischen Interpretation durch eine Anregung des freien Elektronengases (Fermigas) an der Oberfläche des Metalls, welches der Welle entgegen wirkt. In diesem Fall dringt die Welle somit nicht über die Tiefe des evaneszenten Feldes in das Metall ein¹. Lediglich ein kleiner Teil der Energie wird in Form von Wärme absorbiert. Quantenmechanisch betrachtet² verletzt die Einkoppelung der Welle in das Metall den Satz der Impulserhaltung. Vereinfacht man nun reale Metalle zu perfekten elektrischen Leitern (PEC), reduziert sich die Eindringtiefe [?] des evaneszenten Feldes ebenso wie die Absorption durch das Metall auf null [?]. Ein PEC ist somit ein „perfekter Spiegel“. Ist das Ziel jedoch die Kopplung von einfallender Welle und Metall (genauer der Oszillationen der freien Elektronen), um zum Beispiel eine Plasmonenschwingung anzuregen, muss das Problem der Impulserhaltung gelöst werden. Betrachtet man den \vec{k} -Vektor der einfallenden Welle, muss dieser für die Anregung eines Oberflächenplasmon um einen Betrag Δk_x in Richtung der Oberfläche erhöht werden, was bei perfekt glatten Oberflächen nicht möglich ist. Hintergrund ist, dass Photon und Plasmon den gleichen Impuls und die gleiche Wellenlänge (=Energie) benötigen, um die Kopplung zu erlauben. Der Impuls des Photon (k_c) im Freiraum ist jedoch niedriger als der des Plasmons gleicher Wellenlänge. Im Allgemeinen ist diese Erhöhung bei rauen Oberflächen jedoch möglich, da diese raue Oberfläche wie ein Gitter [?] mit einer Vielzahl an Gitterperioden wirkt. Somit ist die Anrauhung oder Mikrostrukturierung

¹Der zugrunde liegende Effekt wird auch Skin Effekt [?] genannt. Dieser beschreibt die Ausbildung eines der einfallenden Welle entgegen gerichteten Feldes im Metall. Je besser die Leitfähigkeit eines Materials ist, desto effektiver kann sich dieses Feld ausbilden, was wiederum die Eindringtiefe reduziert.

²Auch nach klassischer Theorie ist die Anregung nicht möglich – die einfallende Welle ist eine Transversalwelle und das Plasmon lässt sich als Longitudinalwelle beschreiben.

2.1 Nanostrukturierte SEIRA-Substrate für die Spektroskopie

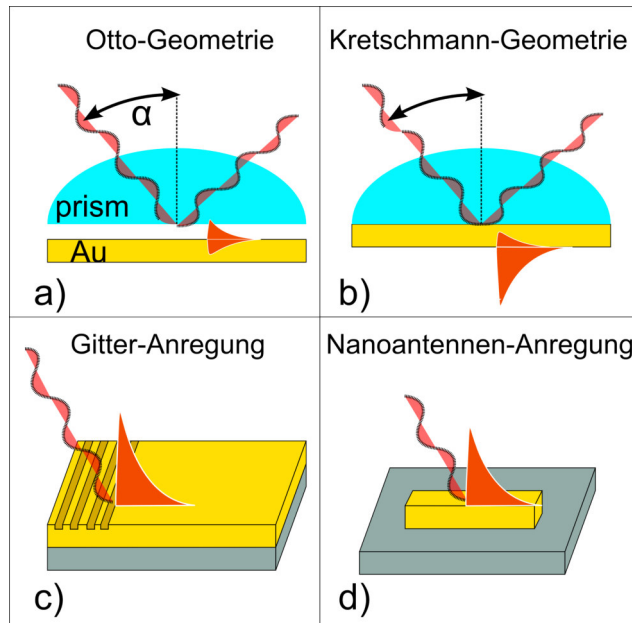


Abbildung 2.1: Anregungsmöglichkeiten eines Oberflächenplasmon-Polariton (rot) an der Phasengrenze Gold-Dielektrikum. a) Otto-Geometrie mit Prisma per Luftspalt, b) Kretschmann-Geometrie mit Prisma ohne Luftspalt und dünner Metallschicht c) Anregung durch Oberflächenstruktur (Gitter) zur Impulserhaltung d) Anregung über eine Nanoantennen passender Größe.

ein möglicher Weg, eine EM-Welle an ein oberflächengebundenes Plasmon zu koppeln bzw. dieses anzuregen, da

$$k_{SPP} = k_{x,Photon} \pm n * k_{Gitter} \quad (2.1)$$

mit der n-ten Ordnung des Gitters ist. Das angeregte Plasmon ist also eine Quasiteilchendarstellung einer kollektiven Elektronenschwingung, korrekterweise als Plasmon-Polariton bezeichnet, da die Beschreibung sowohl einen Teil der Schwingung im Metall (Plasmon) als auch im dielektrischen Medium wie Luft oder einem Isolator (Polariton) beinhaltet. Dies ist sofort daraus ersichtlich, dass die Schwingung unter Energieverlust (mit Ausdehnung in beide Teilräume und je nach Zusammenstellung von Metall und Dielektrikum unterschiedlich stark ausgeprägt) entlang der Grenzfläche propagiert [?]. Mit Erreichen von PEC-Bedingungen geht die Eindringtiefe im Metall gegen null. Somit ist einer der grundlegenden Mechanismen der plasmonischen Anregung die Absorption, welche jedoch die Weglänge des entlang der Oberfläche propagierenden Plasmon limitiert. Hieraus ergibt sich, dass die Ausbreitung des Plasmon endlich ist, da es im Falle eines verlustfreien Mediums nicht angeregt werden kann, sonst aber bei der Propagation entlang der Phasengrenze Energie dissipiert wird. Diese (Ober-

2 Grundlagen der plasmonischen Signalverstärkung

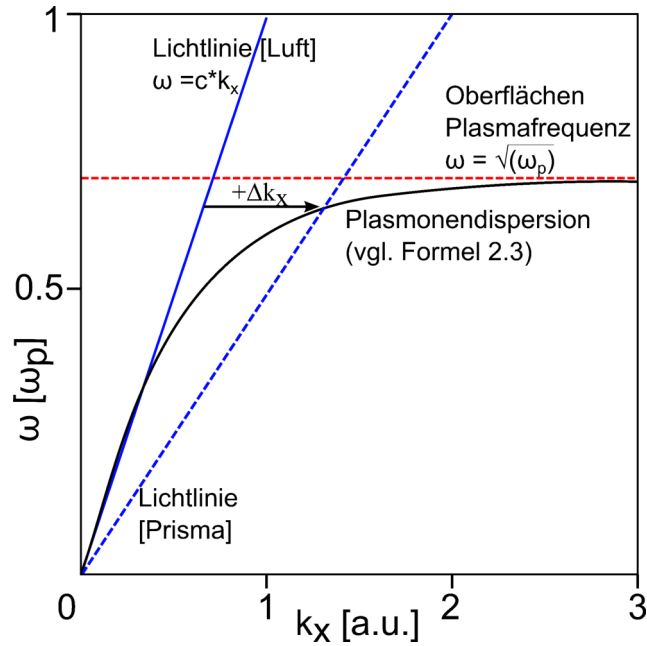


Abbildung 2.2: Dispersionsrelation eines Oberflächenplasmon im Vergleich zur Lichtlinie eines Photon. Beide Kurven schneiden sich nur für $k=0$. Durch ein Prisma oder Gitter wird ein Betrag k_x aufaddiert, so dass das Photon (blaue Kurve) ein Oberflächenplasmon (rote Kurve) anregen kann. Das Oberflächenplasmon liegt rechts von der Lichtlinie, hat also eine kleinere Wellenlänge als elektromagnetische Strahlung in Luft.

flächen-)Plasmonen unterscheiden sich wesentlich von den sog. Volumenplasmonen (*bulk plasmon*). Im Gegensatz zu diesen im Medium angeregten statischen Plasmonen, welche die Schwingung des Fermigas um die Atomrümpfe beschreiben, sind die Oberflächenplasmonen an eine Grenzfläche gebunden und propagieren entlang dieser Grenzfläche (*PSPP ; propagating surface plasmon polariton*). Sie haben allgemein eine geringere Energie als die Volumenplasmonen. Für die Betrachtung eines kleinen Metallpartikels nennt man Oberflächenplasmonen auch lokalisierte Plasmonen, da sie in diesem Fall nicht entlang der Oberfläche propagieren können sondern eine lokalisierte Schwingung des elektrischen Feldes um den Partikelschwerpunkt beschreiben. Die kolloidbasierte Plasmonik, deren Teilchen zu diesem Zweck kleiner als die Wellenlänge des anregenden Lichts sein müssen, um passenden Eigenschaften für die Impulserhaltung zu besitzen, ist ein Beispiel dafür. Die Eindringtiefe der Plasmonen in das Metall lässt sich (zumindest für kleine Frequenzen) über die Stromverdrängung (Skin-Effekt) beschreiben als:

$$z_{Metal} = \sqrt{\frac{\lambda}{2\pi} \frac{|\epsilon'_{Metal}| + \epsilon_{Diel.}}{\epsilon_{Metal}^2}}; \quad (2.2)$$

2.1 Nanostrukturierte SEIRA-Substrate für die Spektroskopie

mit den Dielektrizitätskonstanten von Metall und Dielektrikum. Generell ist die Eindringtiefe in das Metall geringer als in das Dielektrikum, was direkt aus den dielektrischen Funktionen resultiert. Für den Fall realer Metalle ist diese Größe ungleich null. Des Weiteren ist die Ausbreitung in diesem Fall wie bereits dargelegt limitiert, was sich durch die Plasmonendispersionsrelation beschreiben lässt. Diese lässt sich wiederum herleiten aus den Maxwell'schen Gleichungen zusammen mit den „Material equations“ nach [?]:

$$\vec{k} = \frac{\omega}{c_0} \frac{\epsilon_\omega \epsilon_{diel.}}{\epsilon_\omega + \epsilon_{diel.}}; \quad (2.3)$$

Die komplexwertige dielektrische Funktion [?] ist somit eines der wichtigsten Merkmale von plasmonischen Materialien. Im infraroten Wellenlängenbereich (780 nm bis 1 mm) ist die Materialauswahl für Anwendungen der Plasmonik aus diesem Grund stark eingeschränkt. Nur Metalle (und als Ausnahme Graphen [?]) sowie stark dotierte Halbleiter enthalten ausreichend freie Elektronen für eine hohe Plasmafrequenz, welche die Anregung von Plasmonen erlaubt – im Falle der Halbleiter jedoch nur im NIR- und VIS-Bereich. Unterhalb der Plasmafrequenz haben diese Stoffe einen negativen Realteil der Permittivität(ϵ). Für das Anregen eines Plasmons wird eine Materialkombination aus zwei Stoffen mit jeweils positivem Wert der dielektrischen Funktion (Dielektrika) und negativen Wert des Realteils der Permittivität benötigt, was lediglich durch Münzmetalle erfüllt ist. Der Realteil gibt hierbei an, wie die Ladungsverschiebung gegenüber der auslösenden EM-Welle nachläuft, verschoben um einen Phasenwinkel. Die Plasmafrequenz beschreibt weiterhin die Kreisfrequenz (Oszillationsfrequenz) des Fermigas, welches durch ein einfallendes elektrisches Feld gegenüber den Atomrümpfen ausgelenkt wird, und durch Coulombkräfte getrieben in die Ruhelage zurückschwingt.

$$\omega_p = \sqrt{\frac{n_e e^2}{\epsilon_0 m_e}} \quad (2.4)$$

Ist nun die einfallende Welle zu hochfrequent, das heißt höher als die Plasmafrequenz, wird das Metall transparent und es findet keine Wechselwirkung statt. Dieser Fall ist für die Anregung von Plasmonen nicht geeignet. Ist hingegen die Frequenz zu niedrig, steigt der Verlust an Energie durch die Umwandlung in Wärmeenergie. Dieses findet besonders im Bereich der Mikrowellenheizung Anwendung [?].

Für den einfachsten Fall eines sphärischen Partikels kleiner der Wellenlänge des

2 Grundlagen der plasmonischen Signalverstärkung

einfallenden Lichts bedeutet dieses konkret

$$E_{Kugel}^{\vec{}} = \frac{3 * \epsilon_{Medium}}{\epsilon_{Kugel} + 2 * \epsilon_{Medium}} * \vec{E}_0 \quad (2.5)$$

Das Feld im Inneren der Kugel wird also, bedingt durch die Annahme der Elektrostatik, dass der Kugeldurchmesser klein gegenüber der Wellenlänge ist, durch die dielektrischen Funktionen von Kugel und Umgebungsmaterial sowie durch die einfallende Welle bestimmt. Geht nun der Nenner gegen Null, wird die Wechselwirkung maximal. Hierbei handelt es sich um den sogenannten on-resonance-Fall, bei dem maximale Verstärkung bei Resonanz von Teilchengröße und einfallender Wellenlänge besteht. Für größere Wellenlängen ist dies nur durch eine Mikrostrukturierung zu erreichen, was kolloide Ansätze für den Spektralbereich $\leq 1 \mu\text{m}$ weniger vorteilhaft werden lässt. Diese Annäherung ist jedoch nur für Teilchen deutlich kleiner der einfallenden Wellenlänge gültig, und verliert beim Übergang zu planaren Substraten seine Gültigkeit. Bei Verwendung von mikrostrukturierten Substraten können die mikrostrukturierten Nanoantennen direkt vom einfallenden Licht angeregt werden.

Im Kontext der Spektroskopie mit oberflächenverstärkenden Substraten findet weiterhin die Kramers-Kronig-Beziehung Anwendung [? ?]. Diese verbindet den Real(ϵ_1)- und Imaginärteil (ϵ_2) sowohl für die komplexwertige dielektrische Funktion als auch für die Funktion des komplexen Brechungsindex, und spielt besonders bei der Vorhersage des Verhaltens von realen Material-Analyt-Kombinationen eine Rolle, da hier oft nur der Realteil der dielektrischen Funktion verfügbar ist. Es gilt hier

$$(n + ik)^2 = (\epsilon_1 + i\epsilon_2)\mu_1 \quad (2.6)$$

mit $\mu_1 = 1$ für nichtmagnetische Stoffe, dem Brechungsindex n und dem Absorptionsindex k .

Soll SEIRA im fernen Infrarot, also im THz-Bereich, betrieben werden, bleibt ein Großteil dieser Annahmen bestehen. Allerdings tritt die Annahme der PEC-Eigenschaften stärker hervor, sodass die bisher rein theoretische Betrachtungen der gegen Null gehenden Eindringtiefe im Metall hier direkte Relevanz erhalten. So wirken bereits wenige Nanometer Gold im THz Bereich als Spiegel mit vollständiger Reflexion.

2.1.2 Absorbanz, EIT/EIA und EOT

Bei der Betrachtung der IR-Spektroskopie fällt die starke Verbreitung der Definitiv-
 onsgroße Absorbanz (A) auf. Für eine korrekte Anwendung der Absorbanz ist die
 Unterscheidung zwischen Reflektionsabsorbanz und Transmissionsabsorbanz zentral,
 wird aber dennoch selten beachtet. Bei der Reflektionsabsorbanz [?]

$$-\log \frac{R}{R_0} = A \quad (2.7)$$

wird die unbelegte Probe mit der analytbelegten Probe verglichen. Bei der Transmis-
 sionsabsorbanz wird hingegen durch [?]

$$-\log T = A \quad (2.8)$$

eine Beziehung von Transmission und Absorbanz hergestellt. Sowohl (2.7) als auch
 (2.8) verstoßen aber als allgemeine Aussagen gegen die Maxwell'schen Gleichungen.
 Hier gilt zu beachten, dass nicht die Absorbanz (sowohl als Reflexionsabsorbanz als
 auch als Transmissionsabsorbanz) bei der IR-Spektroskopie als direkte Messgröße
 zugänglich ist, sondern nur Transmission und Reflexion. Nur wenn bestimmte Rah-
 menbedingungen eingehalten ³ werden, lassen sich beide Absorbanzen miteinander
 vergleichen. Dies gilt jedoch auch dann nicht ohne Beschränkungen. So dürfen Schich-
 ten nicht zu dünn gegenüber der Wellenlänge sein, da dieses zu Interferenzeffekten
 führt. Auch muss eine Probe mit einer Analytlösung immer mit der des reinen
 Lösungsmittels verglichen werden. Die Absorbanz muss über den Quotienten der
 beiden Transmittanzen definiert werden. Die Definition der Absorbanz nach Lambert-
 Beer ist nur unter diesen Einschränkungen überhaupt gültig. Es ist somit ratsam,
 die Größe der Absorbanz gegenüber den direkten Werten der Reflexionsmessung
 bzw. Absorptionsmessung zu vernachlässigen, zumal durch diese nicht gerechtfertigte
 Annahme [?] der Gültigkeit des (Bouguer-)Lambert-Beerschen Gesetzes in der Be-
 rechnung der Absorbanz Fehler in der Größenordnung einer Zehnerpotenz entstehen
 können.

Ein weiterer Effekt, der elementar für das Verständnis der plasmonischen Effekte in
 der IR-Spektroskopie ist, ist die sogenannte elektromagnetisch induzierte Transparenz
 (EIT, *electromagnetically induced transparency*) oder Absorption (EIA, *electromagne-
 tically induced absorption*). Die Zweite ist eng mit dem Begriff der Fano-Resonanz
 (präziser der Fano-ähnlichen Wechselwirkung) verbunden und beschreibt die Umkehr

³Eine genauere Ausführung findet sich in Ref. [?].

2 Grundlagen der plasmonischen Signalverstärkung

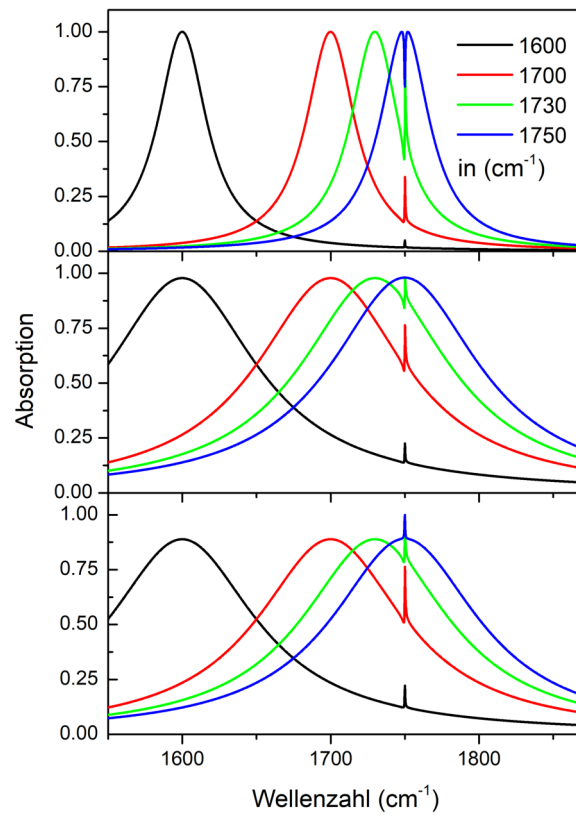


Abbildung 2.3: Absorption einer Molekülbande die an eine Plasmonenresonanz unterschiedlicher Lage koppelt (1600, 1700, 1730 and 1750 cm⁻¹). Je nach Oszillatorparametern der Simulation und Kopplungsstärke wird ein EIT-, EIA-Verhalten oder ein nahezu ungestörtes Verhalten (blaue Kurven) erreicht. Es wird ersichtlich, dass eine Resonanzanregung (Lage der Plasmonenresonanz gleich der der Molekülabsorption) nicht die höchste Signalverstärkung erreicht. Nach [?].

2.1 Nanostrukturierte SEIRA-Substrate für die Spektroskopie

einer Absorptionsbande zu einer Transmissionsbande, wenn diese an eine stärkere und vor allem breitere (plasmonische) Schwingung gekoppelt ist. Im Falle der plasmonisch verstärkten Spektroskopie ist zumeist die plasmonische Resonanz die stärkere Schwingung gegenüber der Molekülschwingung, welche angeregt wird. Somit ist eine Inversion der Bandenform in der Nähe der Resonanz möglich; die Absorptionsbande wird „transparent“. Mithilfe der elektromagnetisch-induzierten Absorption (EIA) wird die weitere Verstärkung einer Molekülschwingung beschrieben, der Kerneffekt der plasmonisch verstärkten Spektroskopie. Grundlegend für beide Effekte ist das Verhältnis von Strahlungsverlusten und intrinsischer Dämpfung des betrachteten Systems

$$\frac{\gamma_{Strahlung}}{\gamma_{intrinsisch}}, \quad (2.9)$$

die ein über-/unterdämpftes Schwingungssystem beschreiben. Da ein angebundenes Molekül den intrinsischen Dämpfungspart beeinflusst, ist die Betrachtung der Dämpfung, d.h. des Verhältnisses von Strahlungsverlusten zu intrinsischen Verlusten, eine der wichtigsten Größen für die Optimierung der plasmonischen Verstärkung. Besonders offensichtlich wird dieses für den Fall eines annähernd kritischen Systems ($\gamma_{Strahlung} \Rightarrow \gamma_{intrinsisch}$) welches durch den Beitrag der Molekülschwingung kritisch wird. In diesem Fall sinkt die Verstärkung der Molekülbande entgegen einer leicht verstimmtten Plasmonenbande wie in Abb. 2.3 gezeigt.

Bei der außergewöhnlichen optischen Transmission (EOT, engl. extraordinary optical transmission) als weiterem plasmonischen Effekt lässt sich beobachten, dass durch eine Öffnung (Radius r) kleiner der einfallenden Wellenlänge (λ) in einem Metallfilm mehr Licht propagiert, als nach klassischer Theorie von Bethe [?] möglich ist:

$$T \approx \frac{64}{27\pi^2} \left(\frac{r}{\lambda}\right)^2 \quad (2.10)$$

Ebbesen et al. [?] zeigen, dass in einem zweidimensionalen Array aus Öffnungen in einem Metallfilm mehr Licht transmittiert wird als aus der Summe der Fläche der Löcher zu erwarten war. Da die Minima und Maxima dieser Transmission mit der Lage der Plasmonenpeaks korrelieren, besteht in der Literatur Konsens über Plasmonenresonanzen als Grundlage dieses Effekts [? ?]. Plasmonenresonanzen als Ursache erklären ebenfalls die Abhängigkeit der EOT von den Materialeigenschaften des Arrays. Ausgiebig diskutiert werden diese Abhängigkeiten z.B in Ref. [?].

2 Grundlagen der plasmonischen Signalverstärkung

2.1.3 Perfekte Absorption

Sogenannte perfekte Absorber beschreiben eine Klasse von Metamaterialien, die aus einem Schichtsystem ⁴ bestehen, welches absorptionsverstärkende Eigenschaften hat. Genauer gibt es in diesen Systemen mindestens bei einer Wellenlänge Bedingungen, welche zu totaler Absorption des einfallenden Lichts führen. Zumeist wird hierbei eine der Schichten aus einem optisch dichten Material bei der Zielwellenlänge realisiert, im Infraroten zumeist Gold mit einer Dicke von mindestens 80-100 nm. Dann gilt $R+T+A=1$ mit $T=0$. Über dieser Schicht befindet sich eine dielektrische Füllung und eine nanostrukturierte Deckschicht, welche ebenfalls meistens aus Gold besteht sofern Anwendungen im Infraroten angedacht sind. Die Wellenlänge, bei der totale Absorption zu erwarten ist, ist ausschließlich von der Form und der dielektrischen Funktion der Deckschicht und der Dicke der dielektrischen Schicht abhängig. Findet nun ein impendanzangepasstes Design Anwendung, so gilt $R=0$, und es ist möglich, eine schmalbandige Resonanz mit einem hohen Q-Faktor ⁵ zu erzeugen, was wiederum eine signifikante Feldüberhöhung im Nahfeldbereich ermöglicht.

⁴ Im eigentlichen Sinne muss lediglich gelten $A=1-R-T=0$, jedoch ist die Bezeichnung mit dem zumeist verwendeten Schichtsystem oft synonym. A ist hierbei die Absorptanz, also das Verhältnis von einstrahlender zu absorbiertes elektromagnetischer Leistung

⁵Der Gütefaktor ist ein Maß für die Energieverluste in einem schwingungsfähigen System, allgemein definiert als $Q = 2 * \pi \frac{W}{V}$ mit W als Schwingungsperiode und V als Verlustleistung in dieser Zeit. Für eine Plasmonenschwingung beschreibt er deren Halbwertsbreite, FWHM.

2.1.4 Chiralität

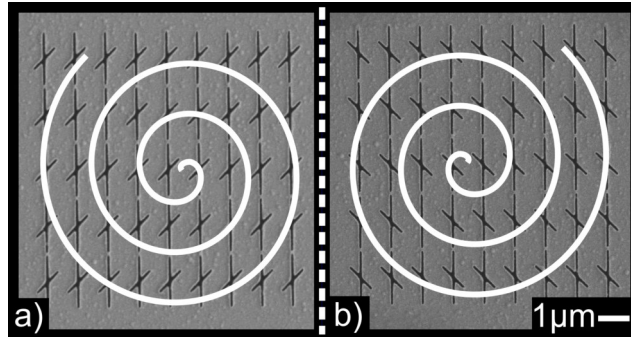


Abbildung 2.4: Beispielhafte Darstellung der Chiralität für ein 2D-händiges Objekt (Spirale, Array aus Nanoschlitzten). Diese sind jeweils ab der $(n+1)$ -ten Dimension achiral. Ein 2D chirales Objekt ist also im dreidimensionalen Raum achiral. Dies entspricht den Operationen Rotation und Translation in 2D. Durch diese lässt sich das $+45^\circ$ Enantiomer a) nicht in das -45° Enantiomer b) überführen. Die Spiegelung (gestrichelte Linie) als Symmetrieoperation in 3D überführt jedoch das -45° Enantiomer in das $+45^\circ$ Enantiomer. Dieses findet direkte Anwendung in 6.1.3 und 6.1.4.

Chiralität [?] oder Händigkeit (in der Kristallographie auch Enantiomorphie) beschreibt ein n -dimensionales Objekt in deren Eigenschaftsänderung durch Symmetrioperationen. Es gilt hierbei allgemein, dass ein n -dimensionales chirales Objekt in $n+1$ Dimensionen grundsätzlich achiral ist. So ist die linke Hand eines Menschen als 2D-Objekt durch Rotation nicht in die andere Hand überführbar, im 3D-Raum ist dieses durch Spiegelung jedoch möglich. Viele komplexe Moleküle zeigen diese Eigenschaft und existieren in verschiedenen Enantiomeren. Es ist besonders hervorzuheben, dass in den Lebenswissenschaften die meisten lebensnotwendigen Aminosäuren sowie viele medizinisch relevante Stoffe [?] chiral sind. Aus der Chiralität erwächst direkt die optische Rotationsdispersion [?] (ORD, *optical rotation dispersion*). Die ORD ist mit dem Zirkulardichroismus (CD, *circular dichroism*) über die Kramers-Kronig-Relation verbunden und beschreibt den sich ausbildenden Gangunterschied zweier orthogonal aufeinander stehender Polarisations Ebenen beim Durchqueren eines optisch aktiven Mediums, welches unterschiedliche, komplexwertige Brechungsindizes für diese Ebenen hat. Da lineares Licht als Kombination von links- und rechtshändig polarisiertem Licht angesehen werden kann, wirken diese Ebenen unterschiedlich auf die einfallende Welle. CD selbst beschreibt dann den Unterschied des Absorptionsvermögens beim Durchscheinen des Mediums mit links- oder rechtshändig polarisiertem Licht. Bei den im IR stattfindenden VCD-Messungen wird die Differenz dieser CD Spektren gebildet. VCD beschreibt somit die unterschiedliche Auswirkung der Moleküleigenschaften auf links- bzw. rechtszirkular polarisiertes Licht. Zu diesem Zweck ist die Definition der Orientierung der Probe notwendig. In der Praxis wird zumeist die Quellensicht

2 Grundlagen der plasmonischen Signalverstärkung

verwendet, rechts und links werden aus Blickrichtung von der Quelle ausgehend auf die Probe definiert. Die alternative Definition, die sogenannte Empfängersicht, definiert diese Größen entlang der Sichtachse ausgehend vom Detektor. Somit lassen sich beide Bezugssysteme durch Inversion ineinander überführen.

2.1.5 Nanostruktur plasmonischer Substrate

Für die in der Plasmonik relevante Oberflächenstrukturierung gibt es verschiedene Ansätze. Im Bereich kolloidbasierter Plasmonik werden diese Kolloide nahezu ausschließlich chemisch synthetisiert. Ausnahme ist die Laserablation basierend hochenergetischer Laserstrahlung, einem physikalischen Effekt. Chemische Reaktionen erlauben unbegrenzte Skalierbarkeit bei geringem experimentellem Aufwand. Nachteil ist jedoch die starke Einschränkung der Materialsysteme/Kombinationen und der erreichbaren Partikelformen. Weiter ist die Kontamination der Kolloide mit residualen Chemikalien ein limitierender Faktor, der zu stark präsenten Messartefakten führen kann. Darüber hinaus kann eine Reaktion nie vollständig Partikel derselben Größe und Beschaffenheit generieren oder modifizieren, sondern ist immer einer Streuung unterworfen. Kolloide sind daher vor allem für einfache Geometrien und „schwache“ Anforderungen an Formhaltigkeit und Reproduzierbarkeit geeignet. Sie profitieren von einem großen Probenvolumen, so dass eine Mittlung über viele Teilchen sehr einfach möglich ist. Ausgenommen sind Synthesen auf Basis von DNA-Gerüsten, welche eine gesteuerte „chemische“ Reaktion ermöglichen. Sie sind jedoch aufgrund ihrer Komplexität und der damit verbundene Kosten nicht als grundlegende Technik anzusehen.

Aufgrund der Nachteile chemischer Synthesen ist die Nanostrukturierung insbesondere im Bereich der Forschung für die Herstellung der plasmonischen Strukturen von besonderer Bedeutung. Die Mikrostrukturierung ist durch aktuelle technologische Entwicklungen in der Lage, fast absolute Kontrolle über Geometrie zu gewährleisten. Durch die Anforderung an die im weiteren thematisierten Substrate ist die Nanostrukturierung die momentan einzig nutzbare Technologie der Forschung, welche diese Anforderungen erfüllt. Die hohen Kosten der EBL ließen sich bei der Überführung in die Massenproduktion reduzieren (z.B. mittels Immersionslithographie) und stellen somit keinen limitierenden Faktor dar. Die in dieser Forschungsarbeit verwendeten Substrate sind allesamt nanostrukturiert und basieren auf denselben grundlegenden Technologien, von denen im Folgenden die Elektronenstrahlolithographie und die Verwendung von SiN-Membranen gesondert dargestellt werden sollen.

EBL – Elektronenstrahlolithographie

Bei dieser Methode wird ein Elektronenstrahl [?] über einen positiv-*resist* oder negativ-*resist* geführt, was entweder Bindungen brechen (Photopositiv, z.B. PMMA and ZEP520 [?]) oder entstehen lässt (Photonegativ, SU8 [?] oder MAN6000.23) und so die Löslichkeit gegenüber Lösungsmitteln durch das Entstehen/Brechen von kovalenten Bindungen beeinflusst. Optische Lithographie ist aufgrund des Abbe-Limits auf eine Auflösung größer als 500 nm beschränkt und daher nicht anwendbar für die Belichtung der meisten plasmonischen Strukturen. Ansätze wie Immersionslithographie [?] sind für die Forschung wenig relevant, zumal beide Ansätze lithographische Masken benötigen und somit weniger flexibel als die maskenlose Elektronenstrahlolithographie sind. Die Belichtung mittels Elektronenstrahl hingegen geschieht orts aufgelöst und durch einen Elektronenstrahl, welcher die Probe abstrahlt. Durch die sehr kleine Wellenlänge eines Elektronenstrahls, welche typischerweise wenige Pikometer beträgt, ist es möglich, sehr präzise Strukturen bei gleichzeitig fast perfekter Geometrie-Kontrolle bis unter 10 nm [?] zu erzeugen. Einzig die Strahlaufweitung und der *proximity*-Effekt [?] beschränken die Auflösung. Die langsame Schreibzeit einer EBL, welche maßgeblich die entstehenden Kosten beeinflusst, lässt sich bei den hier verwendeten Strukturen mittels sog. Charakterprojektion [? ?] stark reduzieren, ein Faktor 100 ist erreichbar.

Siliciumnitrid als Membranmaterial

Da bei der Messung in Transmission besondere Anforderungen an Transparenz, Stabilität und dielektrische Eigenschaften des Substratmaterial gestellt werden, ist hier oft das Herstellen von Strukturen auf Membranen nötig. Siliciumnitrid (SiN) ist aufgrund seiner außerordentlichen Stabilität und der guten Einstellbarkeit der Zug- oder Druckspannung einer SiN-Schicht aktuell die beste Wahl für die Herstellung von freitragenden Membranen, welche dadurch die nötige Transparenz bekommen und ein Aspektverhältnis erlauben, das vollständig geschlitzte Membrane erlaubt⁶. Die SiN-Schichten werden mittels plasmaunterstützter Abscheidung aus der Gasphase (PE-CVD) oder Niederdruck-Gasphasenabscheidung [?] (LP-CVD) hergestellt und sind zumeist auf leichte Zugspannung von etwa 50 MPa eingestellt. Des Weiteren eignet sich Siliciumnitrid besonders aufgrund fehlender Absorptionsbanden, mit Ausnahme der Phononenbande, für Anwendungen im IR-Bereich [?].

⁶Das vollständige Durchätzen der Schlitze ist nur bis zu einem bestimmten Verhältnis von Schlitzbreite zu Schlitztiefe möglich, üblicherweise 1:10. Dünne, aber stabile, Membrane erlauben eine kleinere Dicke des Schichtpaket ohne mechanische Problem zu verursachen.

Numerische Simulationsmethoden

FDTD - Finite difference time domain

FDTD [?] ist ein mathematisches Verfahren zur Integration von zeitabhängigen Differentialgleichungen (*time domain*). Es ist somit als sogenannter Löser für die Maxwell'schen Gleichungen einsetzbar. Die Lösung erfolgt über sogenannte Yee-Zellen [?]⁷, an deren Ortskoordinaten jeweils \vec{E} und \vec{H} für einen bestimmten Zeitpunkt t errechnet werden. Diese Lösungen dienen dann zur Berechnung des jeweiligen \vec{E} -Felds und \vec{H} -Felds zu einem späteren Zeitpunkt $t+\Delta t$. Die örtliche Änderung ergibt sich für das \vec{E} -Feld durch $\text{rot}\vec{H}$ der angrenzenden Punkte der Zelle und analog für \vec{H} . Für die Lösung muss weiterhin jedem Punkt des resultierenden Gitters eine Permittivität, Permeabilität und Leitfähigkeit zugewiesen werden, welche in die Maxwell'schen Gleichungen eingehen. Als zeitabhängige Technik bietet FDTD den Vorteil, dass eine breitbandige Anregung [?] berechnet werden kann. Das vereinfacht die Suche nach Resonanzen. Der Rechenaufwand lässt sich weiterhin mit der Feinheit des Gitters steuern. Gerade an Grenzflächen oder sog. *hot-spots* [?] lässt sich diese Feinheit selektiv erhöhen, was zu einer verbesserten Genauigkeit in diesen Bereichen führt, ohne den Rechenaufwand für die Simulation extrem zu steigern. Ein Vertreter dieser Technik ist Lumerical FDTD[®], welches für die hier gezeigten Anwendungen genutzt wurde.

FEM - Finite Elemente Methode

Bei der FEM [?] wird das Simulationsvolumen in kleinere – finite – Elemente unterteilt und für diese gelöst. Dies geschieht für jedes Volumenelement einzeln. Die Differentialgleichungen werden unter Beachtung der jeweiligen Randwertbedingungen gelöst. Randbedingungen sind beispielsweise durch Dirichlet oder Neumann beschrieben, also entweder ein vorgegebener Funktionswert (Dirichlet) oder dessen Ableitung (Neumann). Weiterhin sind periodische Randbedingungen möglich, sodass ein effektiv ununterbrochenes Gebiet simuliert werden kann. Anschließend wird aus diesem – gelösten Teilgebiet – wieder das gesamte Simulationsvolumen rekonstruiert. Mit diesen bekannten Lösungen kann dann das Ausgangsproblem gelöst werden. Ein typischer Vertreter dieser Technik ist Comsol Multiphysics[®].

Sowohl FEM als auch FDTD streben bei korrekter Lösung denselben Wert an. So kann für eine hohe Diskretisierung (d.h. ein feines Gitter bzw. kleine Teilmengen) beobachtet werden, dass beide Lösungen konvergieren. Daher eignet sich die jeweils

⁷Die Ausdrücke Yee-Zelle und Yee-Gitter werden oftmals synonym verwendet.

2.1 Nanostrukturierte SEIRA-Substrate für die Spektroskopie

andere Methode zur Validierung der gefundenen Ergebnisse, was den simultanen Einsatz beider Techniken vorteilhaft erscheinen lässt.

3 Aktuelle Entwicklungen in der SEIRA- und VCD-Spektroskopie

Die Entwicklung der SEIRA-Spektroskopie wird in den letzten zwei Jahrzehnten hauptsächlich auf die Steigerung des Verstärkungsfaktors bezogen. Meilensteine wie Einzelmolekülempfindlichkeit und Verstärkungsfaktoren größer 10^9 sind jedoch der SERS-Spektroskopie vorbehalten. Auch durch die Tatsache das bei der SEIRA-Spektroskopie zumeist nichtresonant angeregt wird reduziert die erreichbaren Verstärkungsfaktoren. Um die zur Anfangszeit SEIRAs vorherrschenden Inselfilme abzulösen wurde in den letzten 15 Jahren verstärkt an Mikrostrukturierungsmethoden gearbeitet. Diese bieten die in Kapitel 2 genannten Vorteile wie Formhaltigkeit und Reproduzierbarkeit, sowie perfekte Geometriekontrolle. Dieses ist insbesondere in Verbindung mit leistungsfähigen Simulationsprogrammen ein Hauptgrund der immer besseren SEIRA-Konzepte. Beim Übergang von rein akademischen Betrachtungen zu einer anwendungsbasierten Konzeption von SEIRA-Substraten werden jedoch Probleme mit der Wichtigkeit des Verstärkungsfaktors ersichtlich. Als Maß für die real messbare Signalverstärkung ist der Verstärkungsfaktor hier ungeeignet, da die wenigen Bereiche hoher Feldintensität (auf welche sich der Verstärkungsfaktor bezieht) nur durch große inaktive Bereiche ermöglicht wird. Ein Beispiel hierfür sind sog. *bow-tie*-Antennen mit einem aktiven Bereich weniger Nanometer bei einer Größe der Einheitszellen von typischerweise 3-15 μm . Erst seit kurzem wird aktiv an Substraten geforscht, welche bezogen auf die Gesamtfläche des *array* eine hohe Verstärkung erreichen. Ein vielversprechender Ansatz sind hierbei Nanolöcher, da diese eine höhere Packungsdichte bei stärker lokalisierten Felder ermöglichen (gegenüber Nanoantennen). Im Gegensatz zu den ursprünglichen Inselfilmen sind diese Ansätze technologisch komplexe Mehrschichtsysteme. Durch die Kombination von dielektrischen und metallischen Schichten wurde völlig neuen Eigenschaften dieser Nanolöcher erzeugt. Hierbei liegt ein Fokus der Entwicklung auf perfekten Absorbern, welche in der Vergangenheit besonders aufgrund der hohen flächenbezogenen Signalverstärkung verstärkt wissenschaftliches Interesse geweckt haben. Weiter ist ein relativ neuer Zweig der SEIRA-Spektroskopie, die oberflächenverstärkende VCD-Spektroskopie

3 Aktuelle Entwicklungen in der SEIRA- und VCD-Spektroskopie

zu erwähnen. Diese erzeugt durch chirale und achirale Strukturen eine verbesserte Detektion der chiralen Eigenschaften eines Analyten.

3.1 Oberflächenverstärkende Substrate

Seit der Formulierung des Babinet-Prinzips¹ und der Erkenntnis, dass weite Teile der Antennentheorie [?] und der resultierenden Ansätze über einen großen Frequenzbereich transferierbar sind, ist eine Vielzahl verschiedener Nanoantennen realisiert worden. So sind neben einfachen Linearantennen (Dipolantennen) auch Phasennarrays [?] und Yagi-Uda-Antennen [?] von der Radiotechnik über etwa 7-8 Größenordnungen verkleinert in der Plasmonik wiederzuentdecken. Besonders die Linearantennen, welche durch das Babinet-Prinzip Aufschlüsse über das Verhalten der weniger verbreiteten schlitzbasierten Substrate geben, haben eine vergleichsweise lange Entwicklungsgeschichte:

Linearantennen, oder auch Nanostäbe (engl. *nanorods*) oder Nanodrähte (engl. *nanowires*) sind zumeist Stäbe aus Münzmetallen in Länge etwa der halben Wellenlänge der angestrebten Resonanzwellenlänge (unter Vernachlässigung des Substratmaterials), bzw. $\frac{\lambda}{2 \cdot n_{\text{mittel}}}$ mit dem Mittelwert der umgebenden dielektrischen Funktionen. Eine Ausnahme bildet hier Aluminium, das selbstpassivierend ist. Da es zudem günstiger als Gold ist, verfügt es über eine größere Massentauglichkeit, besonders mit Blick auf Lab-on-a-chip-Anwendungen und Einwegensensoren. Da es sich bei Nanostäben um Dipolantennen handelt, kann hier besonders leicht die Kopplung zweier Antennen und somit von Plasmonenmoden untersucht werden. Dies wurde von Neubrecht et al. [?] bereits in der Frühphase mikrostrukturierter SEIRS-Substraten gezeigt. In der theoretischen Betrachtung findet meist nur eine Einzelantenne oder ein Dimer Beachtung. Aufgrund dessen wurden diese Strukturen auch als erstes in der Analytik verwendet [?]. Interessanterweise erfolgte hierbei diese Demonstration bereits mit Octadecanethol (ODT) als Analyten. ODT bildet hierbei Monolagen² aus. Neubrecht et al. arbeiteten jedoch mit einer Einzelantenne, weshalb hier eine Synchrotronquelle nötig war, um ein brauchbares SNR zu erhalten.

Im Gegensatz zur Ausrichtung dieser Arbeit lag der Fokus von Neubrecht et al. nicht auf der Anwendung der Substrate zur Verstärkung einer Analytaborption. Der

¹Beim Prinzip von Babinet wird eine plasmonisch aktive Struktur mit ihrer inversen Struktur korreliert. Hierbei verhalten sich die Plasmonenresonanzen in Reflektion und Transmission ebenfalls invers. Ein Nanoloch kann so z.B. auf eine Linearantenne zurückgeführt werden.

²Das ODT bindet sich aufgrund einer Thiolgruppe an die Goldoberfläche, das restliche ungebundene Octadecanethiol bildet mit der Zeit Disulfatgruppen und kann abgespült werden.

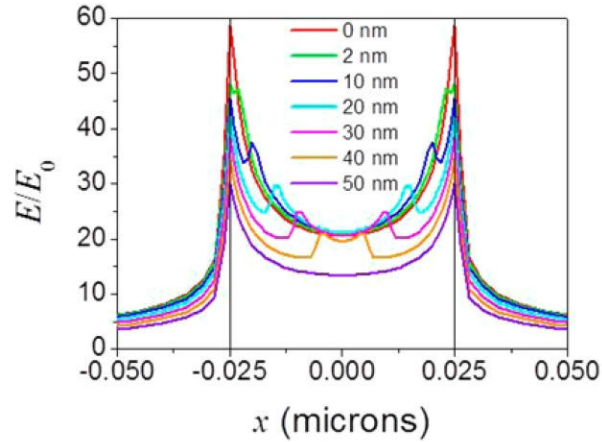


Abbildung 3.1: Simulation der Feldüberhöhung des Plasmon innerhalb des Schlitzes bei einer Schlitzausdehnung von ± 25 nm für eine variierende Dicke des Polyethylens (PE) an den Schlitzwänden (0 nm entspricht kein PE bis 50 nm, was vollständig gefüllten Schlitzzen entspricht), nach [?]

Übergang zu *Arrays* von Nanoantennen erscheint für die tatsächliche Anwendung allerdings unabdingbar, da im Gegensatz zu SERS kein \vec{E}^4 Teil zur Verstärkung beiträgt, der in der Lage wäre, ein schwaches Flächensignal zu kompensieren. Arbeiten von Adato et al. [?] zeigen bereits früh, dass diese *Arrays* geordnet sein müssen, um ihre maximale Leistungsfähigkeit zu erzielen. Eine geordnete Anordnung von *Arrays* ist mit kolloidbasierte Ansätzen allerdings nicht realisierbar was wiederum problematisch ist, da aus der gegenseitigen Beeinflussung der Plasmonenbanden ein maximaler Flächenfüllfaktor für *Arrays* aus Nanoantennen ergibt. Wie bereits in der Arbeit von Weber et al. [?] gezeigt wird, beeinflussen sich zwei nebeneinander aufgebraute Nanoantennen, sobald diese näher als eine kritische Distanz $\frac{\lambda_{Resonanz}}{4 * n_{Substrat}}$ angenähert werden. Dies verursacht eine starke Rotverschiebung der Plasmonenresonanz. Somit ist ein maximaler Füllfaktor von etwa 5.5% bei idealisierten Bedingungen anzunehmen und ungeordnete Anordnungen zeigen eine geringere Verstärkung des Signals oder eine stärkere Rotverschiebung. Dieser Füllfaktor ist auch der Grund dafür, dass der Ansatz von linearen Nanoantennen zunächst grundsätzlich gegenüber Inselfilmen unterlegen scheint [?]. Aufgrund der bereits diskutierten Abhängigkeit von \vec{E}^2 statt \vec{E}^4 sind die durch Linearantennen gebildeten hot-spots nicht in der Lage, den geringen Füllfaktor zu kompensieren. Weiterhin zeigt die Verwendung von *Arrays* für die Anwendung einen weiteren Nachteil. Durch die Benutzung von FT-IR Mikroskopen (z.B. Hyperion 2000 von Bruker) ist die Anregung der Nanoantennen nicht mehr durch einen lotrechten Einfall anzunähern. Mit einem Öffnungswinkel von etwa 18° haben Schwarzschildobjektive eine NA von 0.4. Das Verhalten von Nanoantennen unter diesen Bedingungen wird beispielsweise in den Arbeiten von

3 Aktuelle Entwicklungen in der SEIRA- und VCD-Spektroskopie

Maaß und Tauber [?] betrachtet.

Die Nachteile der Linearantennen hatten in letzter Zeit verstärkt Arbeiten an Schlitzanordnungen (also der inversen Form einer Linearantenne) zur Folge. Mit ersten Publikationen zu Lochanordnungen in den Jahren 2003-2004 [?] in Ni-Substraten ist dieser Zweig der SEIRA-Forschung vergleichsweise jung. Ein gesteigertes Interesse an Schlitzgeometrien gibt es seit etwa 2015, beginnend mit Arbeiten von Huck et al. [?]. Wie erwartet ließ sich mithilfe des Babinet-Prinzips und den Maxwell'schen Gleichungen die korrekte Schlitzlänge berechnen. Die bei etwa $3,3 \mu\text{m}$ resonanten Schlitze hatten eine Länge von etwa $1 \mu\text{m}$. Bereits hier wird einer der Hauptvorteile der Schlitzgeometrie ersichtlich. Während bei der Nanoantenne das Feld mit dem Abstand zur Oberfläche abklingt, bildet sich in den Schlitzen ein vom Abstand zur Wand linear ansteigendes E-Feld (Nahfeld) aus (siehe Abbildung 3.1). Somit kann ein größeres Analytvolumen (maximal das gesamte Schlitzvolumen) zur Signalintensität beitragen. Die in [?] gezeigte Signalverstärkung wurde dementsprechend mit dem 3-fachen der analogen Nanoantennen angegeben. Wichtig ist hier anzumerken, dass die Schlitzbreite mit 100 nm nicht dem Optimum entspricht, die Signalintensität also noch Steigerungspotential hat. Ebenfalls 2015 wurde von [?] der Ansatz des Designtransfers am Beispiel einer Dolmenstruktur gezeigt. Hier lässt sich bereits der Einfluss der Fano-ähnlichen Resonanz erkennen, die zu stark veränderten IR-Spektren führt. Für eine Routineanwendung dieser Substrate ist dies als hinderlich anzusehen, da diese dadurch immer eine Hintergrundkorrektur benötigen. Trotzdem zeigte sich erneut die Überlegenheit von Schlitzanordnungen mit etwa 9% Signalintensität für eine 13 nm dicke PMMA-Schicht in Reflexion.

3.1.1 Perfekte Absorber

Liu et al. [?] waren die ersten, die das Konzept des perfekten Absorber-Schichtsystems in der Plasmonik, bestehend aus Al_2O_3 und Gold beschrieben und für die Anwendung vorschlugen. Die Resonanzfrequenz lag hierbei bei etwa $6 \mu\text{m}$. Dieser Absorber wurde jedoch nicht auf seine SEIRA-Eigenschaften hin untersucht. Dies wurde wiederum 2012 von Chen et al. [?] anhand einer Kreuzstruktur demonstriert, welche zwei getrennte Resonanzen aufgrund unterschiedlicher Länge der Kreuzarme erzeugte. Es wurde eine Absorption für beide Resonanzen von etwa 98% erreicht, bei einem Abstand der Resonanzen von 1000 cm^{-1} . Besonders zeigte sich im Vergleich mit einer freistehenden Nanoantenne ohne perfekte Absorber Schicht-Struktur ein zwei- bis sechsfach höherer Verstärkungsfaktor, der zudem homogener als bei einer ebenfalls realisierten nicht-PA Struktur ausfiel. PMMA als Analyt (eine typische Wahl im IR

3.1 Oberflächenverstärkende Substrate

aufgrund der guten Handhabbarkeit und Schichtdickenkontrolle) zeigte für die C-H und C=O Region (Abstand etwa 1000 cm^{-1}) des Spektrums ein Reflektionssignal von 15% für C=O und 2% für C-H.

Der Ansatz von linearen Nanoantennen als strukturierte Metallschicht wurde 2016 von Cetin et al. [?] demonstriert. Hier wurden 2 Nanoantennen verschiedener Länge genutzt, was sich in zwei Plasmonenresonanzen zeigte, die wiederum erneut für PMMA optimiert wurden (C-H und C=O). Die Signalverstärkung durch den PA-Aufbau wurde hier mit dem Faktor 2 angegeben. Li et al. [?] verwendeten ebenfalls eine Struktur aus Nanoantennen als Metallschicht im PA-Aufbau. Hierbei wurden Kreuze aus Gold auf Al_2O_3 genutzt, mit einer Resonanzfrequenz von etwa $6.5 \mu\text{m}$ und $2.5 \mu\text{m}$. Dies lässt auf ein Resonanz höherer Ordnung schließen. Als Beispiel für einen potentiell in den Lebenswissenschaften nutzbaren perfekten Absorber schlugen im Jahr 2015 Chen et al. [?] hexagonal geordnete Aluminiumscheiben auf Al_2O_3 vor. Hier wurde weiterhin der Zwischenraum (freies Al_2O_3) funktionalisiert (10-CDPA), womit die Analyse von Proteinen möglich erscheint.

Bei der Betrachtung als spektroskopisches Werkzeug werden die Eigenschaften des PA-Aufbaus zumeist nicht auf perfekte Absorption hin optimiert. Als Mittel der Signalverstärkung ist die maximale Feldverstärkung der vollständigen Absorption des einfallenden Lichts vorzuziehen. Dieses wurde demonstriert anhand von Goldscheiben auf Tantaloxid [?] mittels Dodecanethiol (DDT), welches große spektrale Ähnlichkeit mit ODT hat. Hier wurde fast ohne Artefakte durch Fano-Wechselwirkungen ein Analytensignal verstärkt, ohne dass die Struktur eine perfekte Absorption aufwies. Brown et al. [?] optimierten ihre Struktur ebenfalls nicht auf perfekte Absorption hin und erzeugten stattdessen eine Interferenzverstärkung [?], welche das Signal um den Faktor 5 verstärkt. Ein aktueller Trend für PA-Designs ist somit weniger die vollständige Absorption als vielmehr die maximal erreichbare Signalverstärkung. Dieses erscheint sinnvoll, da die Absorption selbst keinen direkten Einfluss auf die Signalstärke hat. Diese Abwandlung des PA-Ansatz wurde ebenfalls in dieser Forschungsarbeit gezeigt, ohne dass hundertprozentige Absorption erreicht oder angestrebt wird, sondern vielmehr die Signalverstärkung maximiert wurde.

Statt dieses Ansatzes lässt sich auch mit einer möglichst minimalen dielektrischen Schicht im PA-Aufbau eine Signalverstärkung erreichen [?]. Chen et al. versahen Nanoantennen mit einer „PA-Schicht“, einer etwa 5nm dicken Al_2O_3 Schicht sowie einem Edelmetall (Silber). Dieser Ansatz verlässt jedoch den Bereich klassischer PA-Ansätze. Durch Erzeugung einer Kavität ähnelt dieser Aufbau einem Fabry-Perot-Interferometer. Der PA-Ansatz bleibt somit, gerade aufgrund seiner guten

3 Aktuelle Entwicklungen in der SEIRA- und VCD-Spektroskopie

Vereinbarkeit mit Nanoantennen, vielversprechend für die plasmonische Verstärkung. Alle Ansätze ist jedoch als Schwachpunkt die fehlende Transmission gemein, was besonders bei instrumentellen Limitierungen auf reine Transmissionsmessungen, wie in der VCD-Spektroskopie der Fall, problematische Auswirkungen hat. Die Entwicklung hin zu oberflächenverstärkender VCD-Spektroskopie wird im weiteren Verlauf dargestellt.

3.1.2 Entwicklung der chiralen Plasmonik

In Bezug auf die plasmonisch verstärkte Spektroskopie hat sich seit der ersten Beschreibung durch Hartstein et al. [?] die Sichtweise von einer rein theoretischen Beschreibung zu einer anwendungsorientierten [?] Perspektive verschoben. In den letzten Jahren weckte die Plasmonik auch im Infraroten den Anspruch, die Verstärkung über die bereits vorher mögliche Monolagenempfindlichkeit hinaus zu erhöhen, zumal diese schon mittels konventioneller Techniken erreichbar war. Methoden wie ATR (engl. attenuated total reflection) [?] oder IRRAS (engl. infrared reflection-absorption spectroscopy) [?] ermöglichen es, Monolagen von Analyten zu detektieren, auch wenn der Absorptionsquerschnitt im Vergleich zu Fluoreszenz [?] typischerweise mehr als 3 Größenordnungen geringer ist. Eine weitere Signalerhöhung ist bei diesen konventionellen Techniken nicht zu erwarten.

Mit Blick auf SERS lässt sich allerdings feststellen, dass die plasmonische Verstärkung trotz des kleinen Wirkquerschnitts der Raman-Streuung Signalverstärkungen bis hin zu Einzelmolekülempfindlichkeit [?] ermöglicht. Es scheint also wahrscheinlich, dass der Einphotonenprozess der Absorption, obwohl schwächer als der Zweiphotonenprozess SERS, von der plasmonischen Feldverstärkung profitiert. Dabei nähert sich der Verstärkungsfaktor mittlerweile dem von mittelmäßigen SERS-Substraten an [?]. Diese sogenannten hot-spots sind jedoch stark lokalisiert und nicht flächendeckend, so dass selbst für Arrays von Nanoantennen [?] nur eine schwache Flächenverstärkung generiert wird. Frühe Versuche mit z.B. Synchrotronquellen lassen diesen Ansatz aufgrund der experimentellen Anforderungen weiterhin wenig anwendbar in der Spektroskopie erscheinen. Dies gilt besonders für Gebiete wie die Lebenswissenschaften und solche, wo der Analyt nicht in großen Mengen zur Verfügung steht. Weiterentwickelte Designs wie die in dieser Arbeit gezeigten Schlitzarrays adressieren jedoch genau dieses Problem. Der Ansatz geschlitzter Membrane, welche EOT [?] und passivierte Oberflächen zum Zweck selektiver Bindung kombinieren, ist eine dieser Möglichkeiten. Die grundlegende Idee, plasmonisch aktive Löcher kleiner der Wellenlänge des anregenden Lichts einzusetzen, wurden erstmals 2003 beschrieben[?]

], die erstmalige Umsetzung von Schlitzen, wie sie ein Teil dieser Arbeit ist, stammt aus dem Jahre 2014 [?]. Huck et al. [?] beschrieben 2015 die Vor- und Nachteile von Schlitzen und Nanoantennen und verglichen beide Ansätze. Es zeigte sich, dass Schlitze vorteilhaft sind, da sie im Vergleich mit entsprechenden Nanoantennen³ im Freiraum einen schwächeren E-Feld Abfall innerhalb des Schlitzes zeigen. Cheng, Yang and Gao publizierten in 2015 weiterhin eine dolmenartige Schlitzstruktur [?]. Analog einer einfachen Schlitzgeometrie zeigten Cetin et al.[?] eine H-Struktur aus zwei parallelen und einem vertikalen Schlitz. Dieses stark anisotrope plasmonische System, mit einer Polarisationsrichtung entlang des horizontalen Schlitzes und zwei Resonanzen für vertikal polarisiertes Licht erlaubt das unabhängige Anregen der Resonanzen zum Zweck der breitbandigen Verstärkung. Dies darzulegen ist ein weiteres Anliegen dieser Arbeit. In der Arbeit von Cetin et. al wurde darüber hinaus ebenfalls erstmals eine freitragende SiN Membran eingesetzt, welche Reflexions- und Transmissionsmessungen erlaubt. Während der Aufbau ähnlich der eigenen Arbeit in [P3] ist, wurden beide unabhängig entwickelt und beinhalten die SiN Membran als technologisches Kernstück. In [P3] beinhaltet der Schlitzaufbau zwei um 45 Grad zueinander gedrehte Schlitze. Bei unterschiedlicher Schlitzlänge ist ebenfalls die Anregung zweier Plasmonenresonanzen möglich, diese stehen jedoch nicht orthogonal aufeinander, was die Struktur bereits erwarten lässt. Diese Struktur, als Array angeordnet, ist jedoch weiterhin chiral, da bei regelmäßiger Anordnung im *Array* keine Spiegelsymmetrie besteht. Damit ist diese Anordnung optisch aktiv und zeigt ein starkes circular-dichroisches Signal. Somit erscheint sie als vielversprechender Kandidat für die chirale Verstärkung von optisch aktiven Substanzen. Diese Ansicht wird jedoch nur von einem Teil der Wissenschaftsgemeinschaft geteilt. Aus der Literatur lässt sich die Entwicklung zweier unterschiedlicher Strömungen ablesen. Während die eine Strömung in Richtung chiraler Strukturen (genauer einer händischen Struktur, die eine eigene optische Aktivität, CD, zeigt) forscht, geht die andere davon aus, dass ein chirales Metamaterial weder nötig noch hinreichend ist, um chirale Verstärkungen zu erzeugen. Ergebnisse veröffentlicht in [? ? ? ? ? ? ?] stützen die These der Notwendigkeit eines intrinsischen CD-Signals. Die Gegenströmung ist in der Literatur fast gleich stark vertreten [? ? ? ? ?]. Zusammenfassend wurde das theoretische Konstrukt von Schäferling et al. [?] im Jahre 2012 publiziert und fordert ein nicht-orthogonales \vec{E} und \vec{H} Feld im hot-spot der plasmonischen Resonanz als nötig und hinreichend für chirale Verstärkung. Es wird weiterhin postuliert, dass zweidimensionale Strukturen generell keine chirale Verstärkung zeigen können [?] und sich potentiell negativ auf das CD-Signal auswirken. Aktuell erfährt

³Die entsprechende Umkehrform nach Babinet-Prinzip im Falle der Schlitze sind Nanoantennen.

3 Aktuelle Entwicklungen in der SEIRA- und VCD-Spektroskopie

die chirale Plasmonik und der verwandte Mechanismus der oberflächenverstärkten Raman-optischen Aktivität [? ?] (SEROA, engl. *surface enhanced Raman optical activity*) eine stetig steigende Aufmerksamkeit. Neben der Anwendung in der Spektroskopie ist auch eine Anwendung in der Mikroskopie [? ?] und Optik [?] oder als optische Pinzetten absehbar. Wie kürzlich von Spector et al. [?] gezeigt, lassen sich mittels schlitzbasierten Systemen chirale Felder ebenfalls extrem stark lokalisiert erzeugen. Auch diese Technik profitiert vom EOT-Effekt (vgl. 2.1.2). Plasmonen lassen sich bis unter 10 nm lokalisieren [? ?], wobei Schlitzanordnungen besonders effektiv sind. Dies wurde erst kürzlich von Benz et al. gezeigt [?]. Der Beweis der starken Lokalisierbarkeit wurde mittels Photoelektronenmikroskopie erbracht [? ?] und gestattet die direkte Messung der Felder über einen Zwei-Photonen-Prozess. Wie Lineau et al. [?] berichten, könnte ebenfalls „die Möglichkeit, plasmonische Felder mit ungewöhnlichen Polarisationszuständen zu erzeugen [...] die Detektion von chiralen optischen Übergängen erlauben, die bisher verborgen blieben“.

4 Vorliegender Forschungsansatz

Wie in den vergangenen Abschnitten gezeigt, hat sich die Plasmonik in den letzten zwei Jahrzehnten zu einem erfolgversprechenden Werkzeug für die Spektroskopie entwickelt. Betrachtet man den Mehrwert, welcher der SERS-Ansatz für die Raman-Spektroskopie mit sich brachte, so erscheint der Wunsch nach einer äquivalenten Entwicklung für die IR-Spektroskopie nachvollziehbar. Der Wunsch einer substanziellen Verbesserung der FT-IR-Technik ist auch deswegen relevant, weil FT-IR-Spektrometer über einen sehr weiten Wellenlängenbereich bis hin zu etwa 1,5 THz wirksam sind. Das macht selbst Wellenlängenbereiche, die sonst Techniken wie THz *time-domain-spectroscopy* (THz TDS) vorbehalten sind, erreichbar, wie in eigenen Arbeiten [6.2.1] demonstriert werden konnte. Bei der Übertragung der Konzepte von der SERS- auf die SEIRA-Spektroskopie zeigen sich allerdings auch erste Herausforderungen, welche spezifisch für die SEIRA-Spektroskopie sind. Das erlangte Wissen im Bereich der theoretischen Grundlagen und Herstellungstechnologie der SEIRA wurde anschließend in einer Übersichtsarbeit dargelegt [6.1.2]. Die Beschränkung auf Mikrostrukturverfahren als Herstellungsstrategie resultiert daraus, dass kolloide Ansätze, auf die in der SERS-Spektroskopie häufig zurückgegriffen wird, aufgrund der im vorhergehende Kapitel dargelegten Gründe in der SEIRA-Spektroskopie wenig zielführend sind. Da das Problem des Füllfaktors (und des daraus resultierenden flächennormalisierten Verstärkungsfaktors) von plasmonisch aktiven Strukturen bedingt durch die Größe dieser Strukturen bei der SEIRA-Spektroskopie deutlicher wird als bei SERS, musste nach einem Weg gesucht werden, dieses zu umgehen. Beispielsweise kann mit dem Übergang von Kolloiden oder Inselfilmen hin zu Nanoantennen und letztendlich zu SHAs das Problem des flächennormalisierten Verstärkungsfaktors gelöst werden, da dieses die gegenseitige Beeinflussung der plasmonisch aktiven Bereiche reduziert, indem das Feld innerhalb der Schlitze lokalisiert ist. Zu diesem Zweck wurde ein reinraumbasiertes Sensor-konzept entwickelt, welches die großflächige Verstärkung von IR-Signalen ermöglicht [6.1.1]. Dies löst bereits eines der großen Probleme der SEIRA-Anwendung, die zu geringe absolute Signalverstärkung, und erfüllt somit bereits eines der Hauptziele der Arbeit. Die großflächigen *Arrays* sind in einem kommerziellen Setup (beispielhaft Hyperion2000 von Bruker mit 18x Schwarzschild

4 Vorliegender Forschungsansatz

Objektiv) einsetzbar, da die große aktive Fläche geringe oder keine vergrößernden Optiken des Messsystems voraussetzt. Dem Ziel maximaler Signalsteigerung folgend wurde eine Anordnung gewählt, die dennoch möglichst das gesamte Messfeld eines kommerziell verfügbaren IR-Mikroskops (etwa 0.6x0.6cm) oder VCD Spektrometers (etwa 2x2 cm) ausfüllt, wobei ein Kompromiss zwischen Herstellungsaufwand und Größe gefunden wurde. Darauf basierend wurde ein Sensor entwickelt, welcher die mögliche Signalverstärkung durch oberflächenverstärkten VCD-Spektroskopie beleuchtet [6.1.3]. Hierbei musste die Grundkonzeption des Sensors überarbeitet werden (Entfernen des MPA-Teils). Durch Einbringen eines zweiten plasmonisch-aktiven Schlitzes entstand ein breitbandig verstärkender Sensor, der über ein ausgeprägtes chirales Verhalten verfügt. Dieser sollte weiterhin in der Lage sein, die optische Aktivität von Analyten zu verstärken, was jedoch im Rahmen der hier vorgestellten Arbeit nicht abschließend geklärt werden konnte. Auf die Hindernisse, die einer vollständigen Klärung im Wege standen, wird im Abschnitt 4.4 genauer eingegangen. Es zeigte sich, dass die Präsenz der Plasmonenbande selbst in den Spektren den Nachweis der sehr kleinen Änderungen des chiralen Dichroismus substanziell erschwert und dieser nur durch die Kramers-Kronig Relation aus der Änderung der Brechzahl abgeleitet werden kann. Nichtsdestotrotz ließen sich mithilfe dieses Ansatzes erste Hinweise darauf finden, dass chirale Verstärkungen mit einem 2D-chiralen Sensor möglich sind. Dies greift eine der zentralen Fragen des aktuellen wissenschaftlichen Diskurses auf, weshalb die entwickelte Methodik das Potential besitzt, die zukünftige Entwicklung entsprechender Sensoren und die zugrunde liegende Theorie nachhaltig zu beeinflussen. Insbesondere die beobachtete beachtliche Stärke des CD und VCD Signals des chiralen plasmonischen Metamaterials lässt sich bis dato nicht theoretisch vorhersagen, sodass eine Weiterentwicklung der zugrundeliegenden Theorie nötig erscheinen. Hierbei wurden starke Hinweise auf die Ausbildung eines effektiven Mediums aus Metamaterial und chiralem Analyten gefunden, welche zu einer chiralen Doppelbrechung führen, einem Effekt der bisher nicht beschrieben ist und neue Fragen zur Theorie der chiralen plasmonischen Wechselwirkung von Metamaterial und Analyt aufwirft.

4.1 Konstruktive Ansätze der Signalsteigerung

Ausgehend von der Zielsetzung, ein leicht auf veränderte Messbedingungen anpassbares, verstärkendes SEIRA-Array zu entwickeln, wurde mittels Elektronenstrahlolithographie ein einfach zu handhabendes SEIRA-Array erforscht. Die Elektronenstrahlolithographie ist als sehr leistungsstarkes Werkzeug zwingend nötig, ist jedoch nicht

4.1 Konstruktive Ansätze der Signalsteigerung

beliebig skalierbar. Hier wurde der Ansatz der Charakterprojektion gewählt, wie in [6.4.1] beschrieben, um einen Kompromiss aus Schreibzeit und Größe des *Array* zu finden. Eine Gesamtgröße von 1x1 mm wurde als Messbereich des SHA-MPA-Sensors festgelegt, so dass knapp 639.000 plasmonisch aktive Schlitze gleichzeitig zur Signalgeneration beitragen (Das Messfeld selbst ist mit etwa 0.6x0.6 mm kleiner gewählt um etwaige Randeffekte zu vermeiden). Dies hat den Vorteil, dass sich – zwangsläufig auftretende – Streuungen in den Fertigungsparametern nur marginal auf das Gesamtsignal auswirken und die Beiträge der einzelnen Antennen bei Messung des gesamten *arrays* zwangsläufig gemittelt werden. Da die Schlitzstruktur (der SHA-Part des Designs) für die SEIRA-Spektroskopie eine möglichst große Signalverstärkung aufweisen sollte, wurde sie in der ersten Arbeit [6.1.1] um einen totalen Absorber-Schichtstapel (MPA) erweitert. Dieser ist komplementär zur SHA-Struktur und dient ausschließlich der weiteren Signalverstärkung. Zur Realisierung des perfekten Absorbers wurde eine Gold/Al₂O₃/Gold Schichtstruktur aus elektronenstrahlverdampftem Gold und auf Atomlagenabscheidung (ALD) basierendem Al₂O₃ hergestellt. Die ALD diente mit ihrer (sub-)atomlagengenauen Abscheidung der genauen Kontrolle der Schichtdicke der dielektrischen Zwischenschicht und damit der Lage der plasmonischen Resonanz bei 3,3 μ m. Mit derselben Technik wurde das Schichtpaket abschließend mittels einer SiO₂-Schicht passiviert, um eine unkontrollierte Bindung des Musteranalyten außerhalb der Schlitze zu verhindern. Die anschließende Strukturierung erfolgte über eine Elektronenstrahlolithographie auf Basis der Charakterprojektion (zur Reduzierung der Schreibzeit und der damit verbundenen Kosten) und einem Elektronenstrahlack (AR6200.09). Dieses Wissen um die sogenannte Top-Down-Herstellung von plasmonisch aktiven Strukturen (auch im SERS-Bereich) konnte bei der Erstellung einer Übersichtsarbeit zum Thema oberflächenverstärkender Substrate eingesetzt werden [6.1.2]. Die erzeugten Strukturen wiesen die bei EBL-Prozessen erwartete, sehr hohe, Homogenität auf. Bedingt durch den in [6.1.1] genutzten Fertigungsablauf an den Rändern der Struktur auftretende Redeposite, prägten jedoch ein eigenes C-H Signal auf, da diese sowohl durch den *resist* als auch durch das Analyt hervorgerufen werden. Diese Redeposite, eine Mischung aus Metall und *resist*, bilden sich bei der physikalischen Strukturierung in Anwesenheit von Lackmasken und lassen sich durch Reinigungsschritte mithilfe von Sauerstoffplasma nicht entfernen. Zum Zweck der Reinigung wurde eine abgewandelte Form der Ionenstrahlpolitur verwendet, bei der unter einem spitzen Winkel mittels reaktivem Ionenstrahl geätzt wurde. Dabei geht die Ätzrate (außer – aus geometrischen Gründen – an den Kanten) gegen null, sodass nur die orthogonal auf der Oberfläche stehenden Redepositkanten geätzt wurden. Falsch-positive CH₂- und CH₃-Banden im Spektrum wurden somit erfolgreich verhindert[4.1]. Zur weiteren Qualitätssicherung wurde dieser Schritt in alle weiteren

4 Vorliegender Forschungsansatz

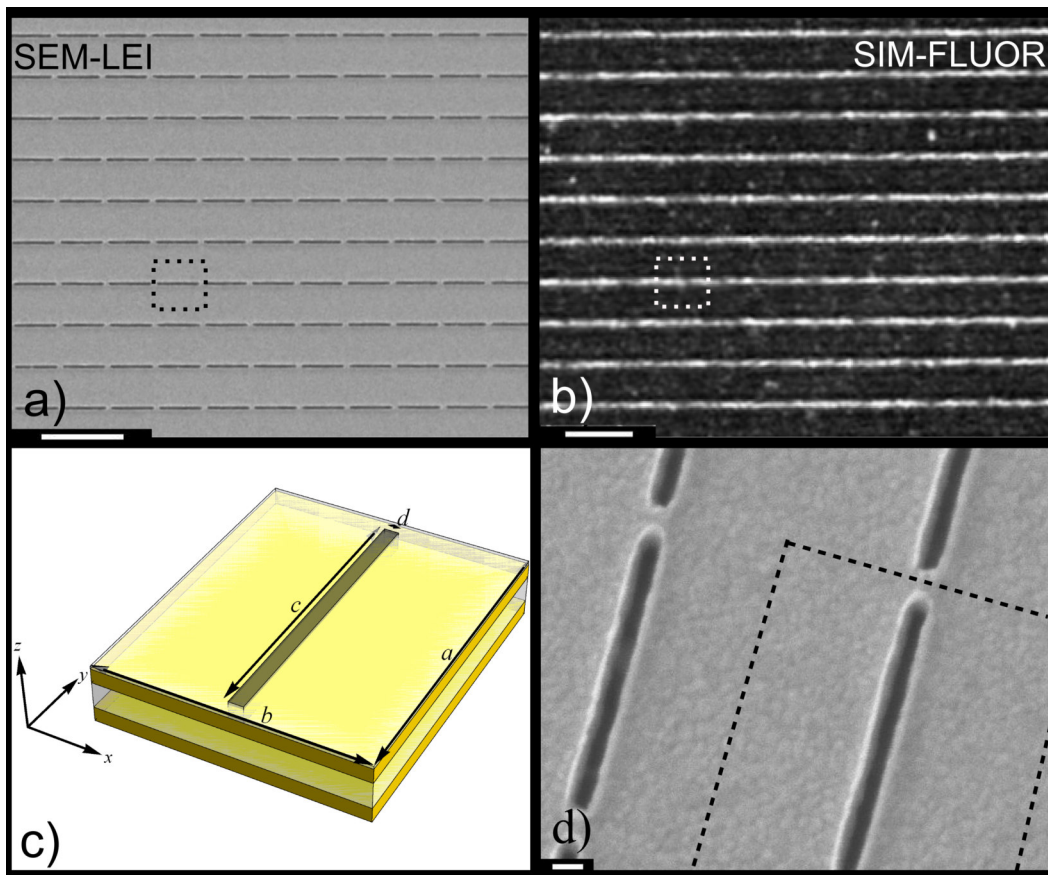


Abbildung 4.1: Ausgangsstruktur des SHA-MPA. a) REM und b)SIM-Fluoreszenzaufnahme des gleichen *Arrays* zum Beweis der selektiven Anreicherung des Analyten (SAMSA) in den Schlitzten. Die in a) sichtbaren Schlitzte zeigen als einziges ein in b) messbares Fluoreszenzsignal. Die Stege sind aufgrund des Auflösungsvermögens nicht sichtbar, lassen sich jedoch im Fourierraum erkennen. (Maßstab: $3\ \mu\text{m}$) c) Skizze der für die Simulation genutzten Einheitszelle, welche in a,b) und d) gestrichelt eingezeichnet ist ($b=910\ \text{nm}$; $a=1100\ \text{nm}$; $d=45\ \text{nm}$; $c=1005\ \text{nm}$) c) REM-LEI-Nahaufnahme der Schlitzstruktur,(Maßstab: $100\ \text{nm}$) nach 6.1.1.

4.1 Konstruktive Ansätze der Signalsteigerung

Entwürfe übernommen, bis die Technologie in [6.1.3 ; 6.1.4] auf die Verwendung einer Hartmaske (strukturierte Metallschicht) als Ätzmaske umgestellt wurde. Da diese ohne *resist* aufgebaut ist, besteht hierbei keine weitere Gefahr von Redepositen.

Da, bedingt durch den veränderten Messaufbau, in [6.1.3] Transmissionsmessungen nötig wurden, wurde auch die technologische Basis an die veränderten Messbedingungen angepasst. Weil ein PA-Aufbau zwingend optisch dicht ist, musste dieser im neuen Design für Transmissionsmessungen verworfen werden. Es erfolgte der Übergang zu einer tragenden Membranschicht auf SiN-Basis. Die resultierende reine SHA-Struktur besteht aus Gold auf einer Membranschicht, wobei Titan als Haftvermittler dient ohne die plasmonischen Eigenschaften der Struktur zu verändern¹. Die Passivierung erfolgte analog zu [6.1.1] mittels ALD-basierter Abscheidung von SiO₂. Als Besonderheit verfügt der in dieser Publikation beschriebene Sensor über vollständig geschlitzte Membranen (vgl. Abb. 4.2). Dies ermöglicht neben der EOT auch Kapillareffekte auf dem Sensor. Auf der Nitridseite aufgebracht flüssiges Analyt wird durch die Kapillarkräfte in die Schlitze transportiert. Somit findet in geeigneten Lösungsmitteln eine automatische Adsorption des Analyten an den sonst schwer erreichbaren Schlitzwänden statt. Statt wie in der vorhergehenden Technologie [6.1.1] gehen die Schlitze nun durch die gesamte Gold- und SiN-Dicke, welche aufgrund der Materialbeschaffenheit in zwei Schritten geätzt wurden. Nach dem Strukturieren des Au/SiO₂-Stapels wird die Silicium[100]-Rückseite des Sensors tiefen-geätzt, um die Membran selbst freizustellen; im Anschluss wird diese Membran trocken durch-geätzt. Zur Stabilisierung der Membran, welche sonst zu mehr als 98% durchtrennt worden wäre, wurde jeder zehnte Schlitz ausgelassen, was ein Traggerüst entstehen lässt (vVgl. Abbildung 1 in [6.1.3]). Die so realisierten Sensoren sind mechanisch sehr stabil und bei sorgfältiger Behandlung auch wiederverwendbar. Dieser Aspekt spielt besonders bei Vergleichsmessungen eine wichtige Rolle, da so zwischen einzelnen Messungen die Chipbasis nicht verändert werden muss. Die Stützstruktur macht den Sensor robuster gegenüber der Kristallisation von Analyten und sorgt dafür, dass er sowohl nass als auch trocken zur mehrfachen Nutzung gereinigt werden kann. Um die Wiederverwendbarkeit der hergestellten Sensor-Arrays zu überprüfen, wurde ein Chip bis zu vier mal eingesetzt. So wurde in [6.1.3 und 6.1.4] mehrfach Analyt abgelöst und bis zu vier mal neu inkubiert, was insbesondere für Vergleichsmessungen essentiell ist, da diese somit auf der selben Chipbasis durchgeführt werden können. Weiterhin verfügen die Chips durch die tiefen-geätzte Rückseite und die optisch dichte Goldschicht über eine Blende, welche nur Licht im Bereich der strukturierten Bereiche passieren lässt. Dieses ist besonders wichtig, wenn, wie im Falle von VCD-

¹Die Eigenschaften der Titanschicht werden durch den *proximity*-Effekt dominiert

4 Vorliegender Forschungsansatz

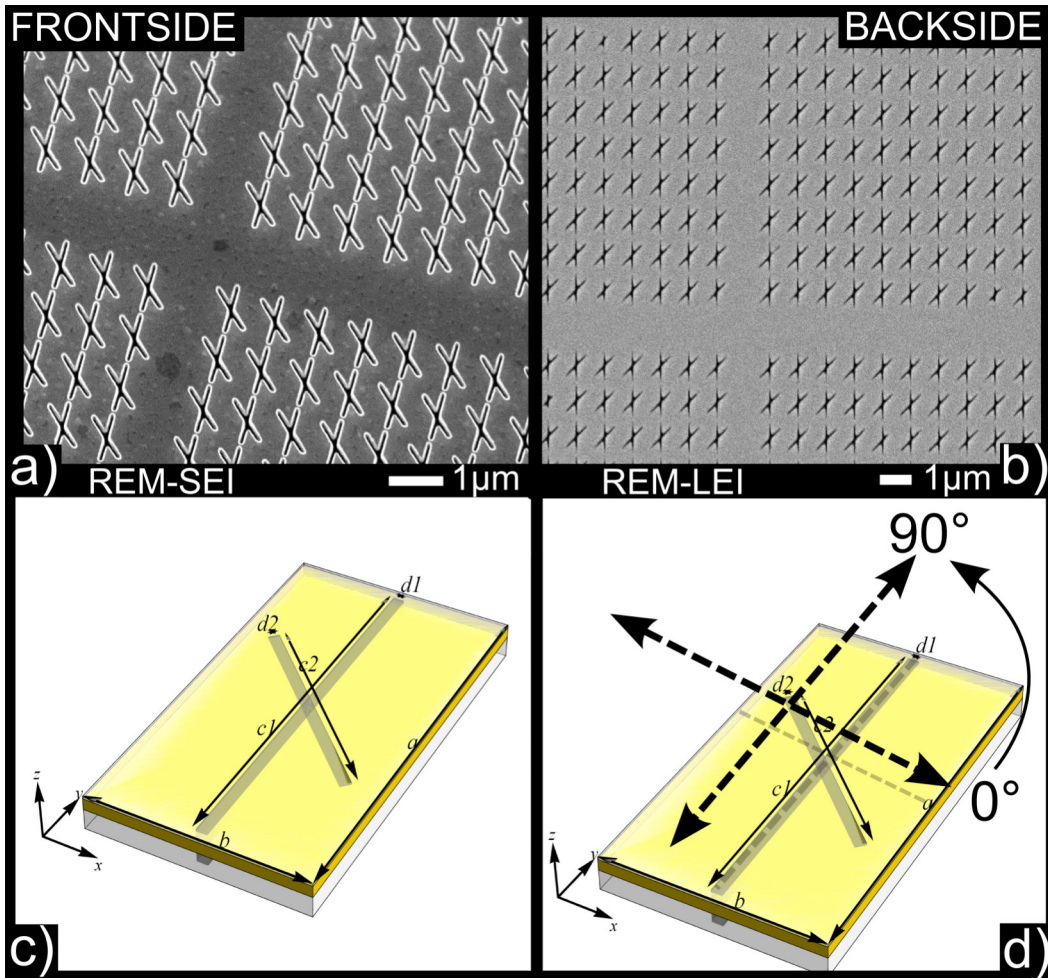


Abbildung 4.2: Ausgangsstruktur des chiralen SHA. a) REM-SEI Aufnahme der Vorderseite eines SHA-Array mit -45° Schlitzorientierung b) REM-LEI des gleichen Arrays auf der Rückseite der Struktur zeigt die durchgehenden Schlitze. Ein rückseitig angeregtes -45° Array entspricht einem $+45^\circ$ Array aufgrund der 3D Rotation. c) Skizze der für die Simulation genutzten Einheitszelle ($a = 1800$ nm, $b = 1000$ nm, $c1 = 1700$ nm, $c2 = 1000$ nm und der Schlitzbreite $d1, d2 = 50$ nm) d) Orientierung der linearen Anregungspolarisation zum Array. Dabei entspricht 0° einer resonanten Anregung des Hauptschlitzes.

4.2 SHA-MPA als spektroskopisches Werkzeug

Messungen, keine fokussierende Optik zur Verfügung steht. Sämtliches Licht, das den Sensor passiert, muss den optisch aktiven Bereich passiert haben und aufgrund des Funktionsprinzip der SHA durch einen der Schlitze transmittiert worden sein. Dies gewährleistet die maximale Interaktion von Licht und Analyt, da das gesamte Schlitzvolumen der *hot-spot* des Sensors ist. Durch oben beschriebenen Ansätze werden die Sensoren in kommerziellen Systemen anwendbar, weshalb eines der Ziele dieser Arbeit als erfüllt angesehen werden kann.

4.2 SHA-MPA als spektroskopisches Werkzeug

Der in [6.1.1] beschriebene SHA-MPA-Sensor ist in Reflexion einsetzbar und demonstrierte eine bis dahin unerreichte Signalverstärkung für SEIRA-Substrate auf mikrostrukturierter Basis. Wichtigste Designvorgabe war hierbei eine hohe flächennormierte Verstärkung, da diese eine höhere Relevanz für reale Anwendungen hat, bei denen nicht ein rein rechnerischer Verstärkungsfaktor, sondern die real erreichbare Gesamtsignalverstärkung wichtig ist. Die auf wenige Nanometer konzentrierte Verstärkung ist, bedingt durch den Verstärkungsmechanismus, wesentlich weniger zielführend als zum Beispiel in der SERS-Spektroskopie. Eine Signalsteigerung von unter 1% Absolutsignal auf etwa 30% Absolutsignal konnte demonstriert werden. Um dieses zu demonstrieren, wurden neben leeren Schlitzen auch mit verschiedenem Analyt befüllte Schlitze vermessen. Der Modelanalyt ODT zeigt hierbei eine dem Polyethylen vergleichbare Bandenstruktur im Bereich der C-H Banden und bildet weiterhin mit Gold selbstorganisierte Monolagen aus. Dieses ist insofern wichtig, als dass Polyethylen theoretisch gut beschrieben ist und entsprechende Literaturwerte der dielektrischen Funktion verfügbar sind, was wiederum genaue Vorhersagen mittels Simulationen ermöglicht. Die resultierenden Spektren (vgl. Abbildung 7 in [6.1.2]) zeigen das entsprechend der Simulationen zu erwartende Verhalten (vgl. Abbildung 5 in [6.1.2]). Es ist jedoch anzumerken, dass hierbei ein Anhaltspunkt gefunden wurde, dass (vermutlich bedingt durch van-der-Waals-Kräfte) keine wirkliche Monolage vorliegt. Dies ist für eine spektroskopische Routineanwendung jedoch nicht hinderlich, da Monolagen eher im Bereich der Messung von Verstärkungsfaktoren zu finden sind, und in realen Anwendungsfeldern nur eine untergeordnete Rolle spielen. Für bestimmte Anwendungsfelder könnte dieses Verhalten vorteilhaft sein, hier sind jedoch weitere wissenschaftliche Untersuchungen notwendig. Kontrollmessungen mittels SEM bestätigten, dass die Schlitze teilweise mit Analyt gefüllt waren, was in der Beurteilung der Leistungsfähigkeit berücksichtigt wurde. Trotz dieser Korrektur zeigte sich der Sensor anderen ähnlichen SEIRA-MPA-Ansätzen überlegen [? ? ? ? ?

4 Vorliegender Forschungsansatz

]. Verglichen mit Nanoantennen auf Sockeln, welche etwa 3% relatives Signal zeigen, sind es bei Schlitzanordnungen etwa 30% für den hier gezeigten SHA-MPA.

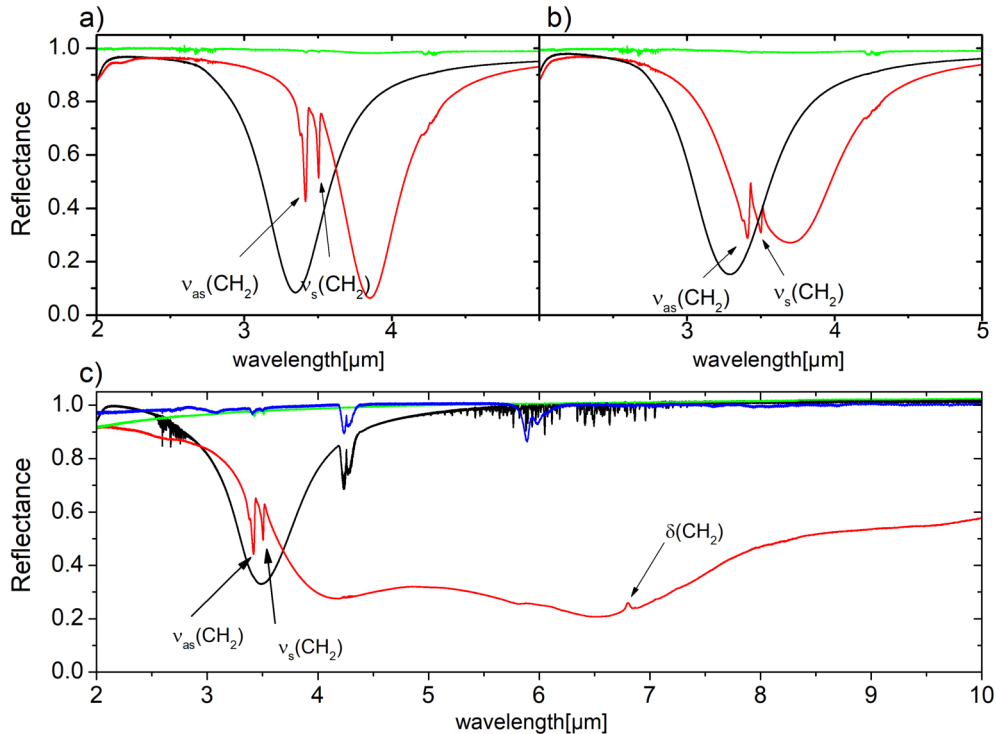


Abbildung 4.3: a) Einzelschlitz-Array mit 40 nm breiten Schlitz-Array inkubiert mit ODT, resonant angeregt (0° orientiertes linear polarisiertes Licht; rot) und nichtresonant angeregt (90° linear polarisiertes Licht; grün). b) Gleiche Anregungsbedingungen für ein Einzelschlitz-Array mit 50 nm breiten Schlitz-Array inkubiert mit ODT. c) Spektrum für ein Einzelschlitz-Array mit 50 nm breiten Schlitz-Array inkubiert mit DNS/PBS Mischung (rot: 0° orientiertes lin. pol.; grün: 90° orientiertes lin. pol.). Das blaue Spektrum zeigt die Referenzmessung in Transmission der reinen DNA. Aus [6.1.4]

Neben diesem Modelanalyten konnte weiterhin anhand von DNA(SS150)/PBS eine Musteranwendung demonstriert werden. Hierbei zeigte sich neben dem Analytsignal eine extreme Verbreiterung der Plasmonenbande, bedingt durch Kristallisation des PBS (KH_2PO_4 , NaCl , und KCl) und der damit einhergehenden starken Änderung der effektiven dielektrischen Funktion im Schlitzbereich. Trotzdem konnten auch in diesem Fall C-H₂ und C-H₃ Banden nachgewiesen werden (vgl. Abb. 4.3). Als Beweis der selektiven Bindung wurde zudem mittels Fluoreszenzspektroskopie der Farbstoff SAMSA-Fluorescein in den Schlitz-Arrays nachgewiesen. Dieser verfügt über eine Thiolgruppe und bildet dem ODT gleiche Bindungen zur Goldoberfläche aus. Insofern ist er für den Beweis der selektiven Anbindung des Analyten mittels Thiolgruppen bestens geeignet. Wie in Abbildung 1 [6.1.1] ersichtlich, erfolgte die Bindung wie

4.2 SHA-MPA als spektroskopisches Werkzeug

vorhergesagt nur im Schlitzbereich. Nachweisbar wird somit Analyt im Schlitzbereich angereichert, falls dieser Bindungen zur Goldoberfläche eingehen kann. Dieses ist gerade für die Analyse geringer Probenmengen und in den Lebenswissenschaften hilfreich², da vielfach N-H Bindungen auftreten, welche ebenfalls über den Stickstoff an das Gold binden können. Aufgrund der breitband-verstärkenden Eigenschaften

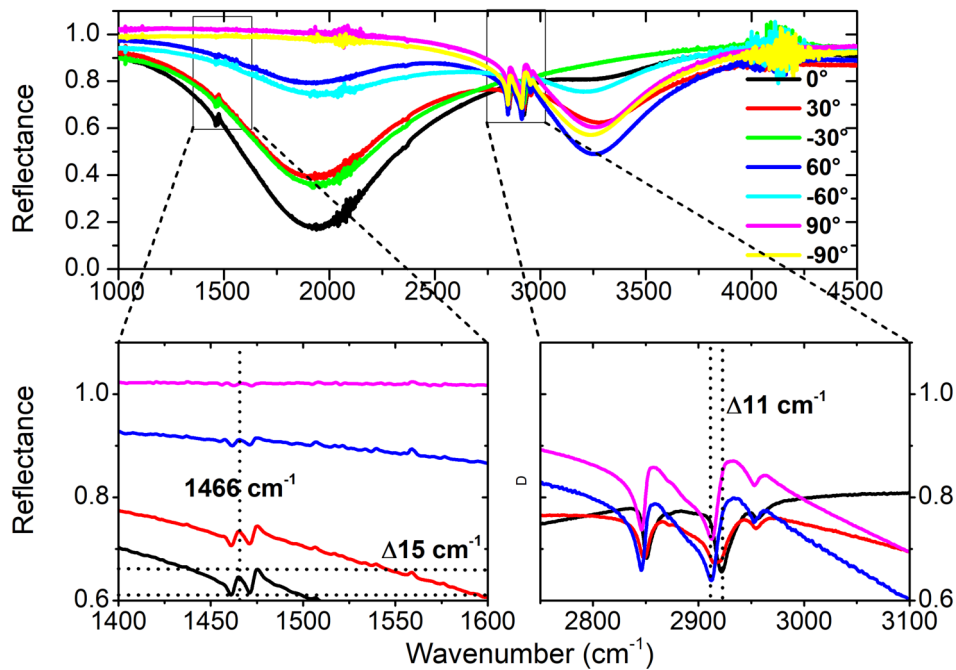


Abbildung 4.4: Messung eines ODT gefüllten *x-Arrays* mit linear polarisiertem Licht unterschiedlicher Einfallsausrichtung. Erkennbar ist die Verstärkung der CH₂ und CH₃ Banden des ODT. [unten links] Ausschnittartige Darstellung der CH₂ (s) 1466 cm⁻¹ Deformations-schwingung, welche mit der verstärkten Anregung des Plasmon korreliert (von 90° zu 0°, resultierend in 4.1% geringerer Reflektion. [unten rechts] 2 und CH₃ symmetrische und asymmetrische Streck-schwingung. Die genauen Anre-gungsbedingungen werden in Appendix, Abbildung 1 dargestellt. Aus [6.1.4]

des Doppelschlitzes, eignet sich auch dieser als spektroskopisches Werkzeug in FT-IR Anwendungen. Wie in Abbildung 4.4 gezeigt, ist es hierbei möglich, eine plasmonische Verstärkung über den gesamten MIR-Bereich (meist 1000-4000 cm⁻¹ zu erreichen. Da dies je nach Polarisationsrichtung erfolgt, handelt es sich um einen schaltbaren SEIRA-Verstärker, ein Ansatz, der zukünftig in Kombination mit Verfahren wie dem Lock-In Verstärkerprinzip³ eingesetzt werden könnte, da durch eine Rotation

²Wobei hier eine Thiol- oder Amidgruppe vorausgesetzt wird

³Hierbei handelt es sich um einen extrem schmalbandigen Bandpassfilter, der über eine periodische Modulation des Messsignals realisiert wird. Somit wird das SNR des Messsignals stark erhöht, eine

4 Vorliegender Forschungsansatz

der Polarisationsachse mit bekannter Frequenz auch die verstärkten Analytbanden moduliert werden. Interessanter ist jedoch die Anwendung in Bereichen der VCD-Spektroskopie, die durch die chirale Natur der *Arrays* zugänglich wird, da in diesem Feld ein aktiver wissenschaftlicher Diskurs über die theoretische Grundlagen geführt wird, welche durch diesen Ansatz um experimentelle Daten erweitert wurden.

4.3 Chirale Metamaterialien als potentielle Quellen chiraler Verstärkung

Für die Untersuchung des chiralen Metamaterialsensors wurde dieser in einer Haltevorrichtung fixiert und in einer Rotationseinrichtung des VCD-Spektrometers vermessen. Dabei wurde der Sensor von der Rückseite angeregt (die Goldseite wurde zum Detektor orientiert). Diese Orientierung diente der beschädigungsfreien Messung der Sensoren, da diese im Vorfeld nicht auf die Rotationseinheit angepasst wurde. Da die Rotation ein wichtiger Bestandteil der Artefaktunterdrückung des VCD-Spektrometers ist, wurde diese Strategie für alle weiteren Messungen gewählt. Beide Ausrichtungen des Sensors zur Quelle wurden verglichen, sodass der Ansatz der Anregung des Sensors durch die Nitridseite verifiziert werden konnte. In Simulationen erfolgte die Anregung über die Goldseite, was hier bei Rotation nicht möglich war, ohne den Sensor zu beschädigen. Für die Interpretation der Ergebnisse ist es wichtig zu bedenken, dass ein PEM ein schmalbandiges optisches Bauelement ist. Im Vorfeld der Messung musste ein Zielbereich für die Messung gewählt werden und der Arbeitsbereich des PEM angepasst werden. Dabei wurde 2800 cm^{-1} als Arbeitspunkt gewählt, mit einer Bandbreite von etwa $\pm 500\text{ cm}^{-1}$. Wichtig ist, dass der Arbeitsbereich des PEM graduell abfällt, wie es sich in Abbildung 2.5 widerspiegelt. Die so vermessenen Sensoren zeigten das erwartete VCD-Signal bei 3300 cm^{-1} . Ein Umdrehen des Sensors (Anregung durch die Vorder-/Rückseite) führte zu der erwarteten Spiegelsymmetrie des VCD-Signals [6.1.3]. Die Stärke des VCD-Effekts, welche mehr als 3 Größenordnungen über den im IR vorhandenen Signalstärken liegt, muss von einem möglichen Effekt der linearen Depolarisation abgegrenzt werden. Dieser könnte sich in den VCD-Spektren manifestieren. Zur Abgrenzung wurden weitere Sensoren mit veränderter Orientierung hergestellt, und der Effekt der linearen Depolarisation simuliert. Es konnten hierbei keine Anhaltspunkte für einen Ursprung des VCD-Signals in der linearen Depolarisation gefunden werden.

Verbesserung um 70 dB ist dabei erreichbar

4.3 Chirale Metamaterialien als potentielle Quellen chiraler Verstärkung

Zur Verifizierung wurde in einem zweiten Messversuch jeweils ein Sensor mit $+45^\circ$ und -45° Orientierung vermessen. Auch hier wurden die Proben mit 0.2-1 Herz rotiert, um Polarisationsartefakte zu unterdrücken. Beide Sensoren wurden dabei invertiert, sodass die Differenzspektren als weitestgehend frei von Artefakten angenommen werden können. Es zeigte sich, dass die Signalbande bei $\approx 2655 \text{ cm}^{-1}$ auf einen linearen Dispersionseffekt zurückzuführen ist. Simulationen mit PE zeigen jedoch, dass es sich hierbei um eine IR-Absorption handelt, die sich aufgrund der Polarisationsrichtung und jeweiligen Ausrichtung der Schlitze im Spektrum zeigt. Dies basiert auf der unterschiedlich starken Anregung bei unterschiedlichen Ausrichtungen des Sensors. Weiterhin konnte beobachtet werden, dass die IR-Spektren der $\pm 45^\circ$ Sensoren identisch für linear polarisiertes Licht sind. Neben einem schwachen Hintergrundspektrum konnte zudem eine Abweichung des VCD-Signals bei 2655 cm^{-1} bzw. 2663 cm^{-1} festgestellt werden. Die Abweichung zwischen den Bandenpositionen ist wahrscheinlich auf Streuung in den Fertigungsparametern zurückzuführen, welche diese lineare Depolarisationsbande beeinflussen. Aufgrund der Empfindlichkeit des Systems können selbst kleinste Abweichung durch ihre Stärke im resultierenden VCD-Spektrum auftauchen. Anhand der ebenfalls in [6.1.3,6.1.4] gezeigten CO_2 Band im VCD-Spektrum wurde induzierte Chiralität vermutet. Dies konnte jedoch nicht bestätigt werden. Vielmehr sind die aufgrund der Polarisationsrichtung angeregten Eigenmoden der Struktur unterschiedlich, was zu unterschiedlich starker Anregung führt. Eine linkszirkular polarisierte Anregung kann so beispielhaft die chiralen Eigenmoden der $+45^\circ$ -Struktur stärker anregen als die der -45° -Struktur.

Bei der Charakterisierung in einem ChiralIR 2X Spektrometer zeigte sich ein außerordentlich hohes CD-Signal (vgl. Abb. 4.5) von bis zu 0.83 für die leeren Sensoren. Dieses ist stärker als alle bis zu diesem Zeitpunkt vermessenen 2D-chiralen Metamaterialien. Ein auf SHA-Arrays basierender Sensor verspricht damit, ein geeigneter Kandidat für die Überprüfung von oberflächenverstärktem VCD zu sein. Diese Einschätzung wurde anschließend mit dem Modellanalyten α -Pinene verifiziert. Es zeigt sich, dass sich auch nach dem Inkubieren mit α -Pinene sowohl das $+45^\circ$ - als auch das -45° -Array weiter wie zwei Enantiomere verhalten – wobei es irrelevant war ob L- α -Pinene, R- α -Pinene oder ein Racemat von beidem verwendet wurde. Eine gravierende Verschiebung der Plasmonenbande von 990 cm^{-1} konnte für das Racemat auf einen -45° -Array beobachtet werden, wie in Abb. 4.6 gezeigt. Die L- und R- Formen liegen jeweils auf den Seiten des Racemat, in einem Abstand von 125 cm^{-1} . Allerdings ist das Racemat nicht zentriert zwischen den L- und R-Formen des Pinene. Dieses wurde als ein Effekt der Circulardoppelbrechung interpretiert, da die Verschiebung des Plasmon eine Funktion des Brechungsindex ist. Diese Beobachtung wurde ebenfalls

4 Vorliegender Forschungsansatz

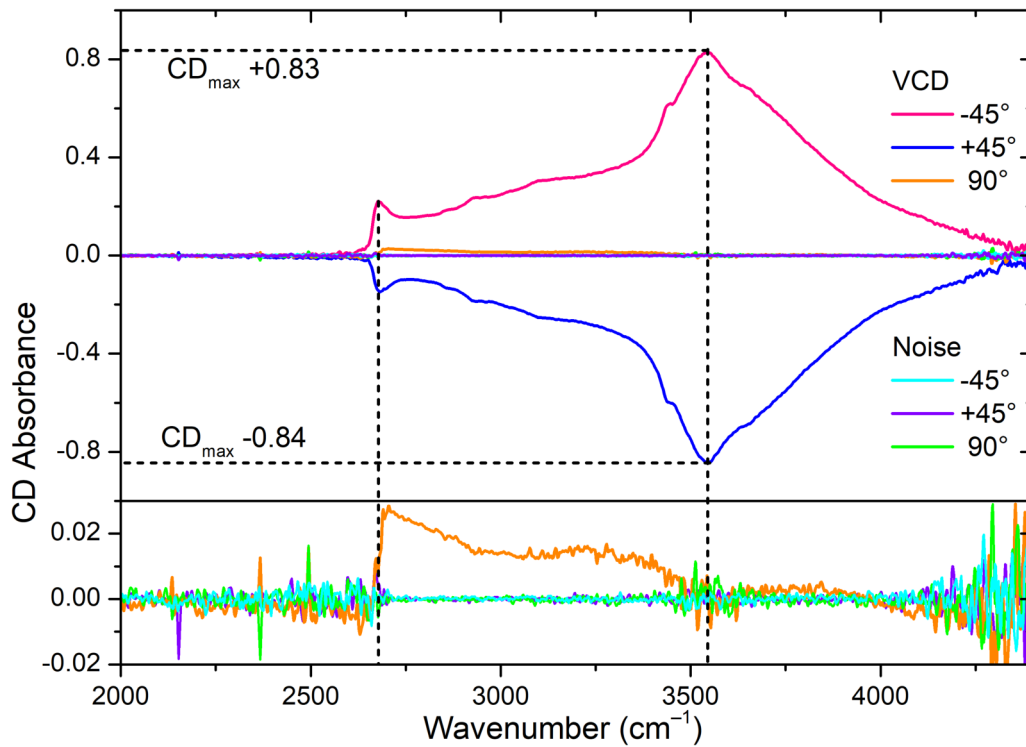


Abbildung 4.5: Messungen an zwei *x*-Arrays mit + bzw. -45°orientiertem zweiten Schlitz, sowie einem achiralen Array mit 90° Orientierung als Negativkontrolle. Es zeigt sich die sehr gute Spiegelsymmetrie der beiden Enantiomere(+/-45°Schlitzausrichtung) und das bis dato höchste gemessene CD Signal von 0.83 für ein 2D Metamaterial. [unterer Teil] Vergrößerung der Mittelachse zeigt ein minimales CD Signal des achiralen Arrays, bei dem es sich um ein Artefakt handelt. $\frac{\lambda}{4}$ der PEM bei 2800 cm⁻¹; Probenrotation mit 0.1 Hz. Aus [6.1.3].

4.3 Chirale Metamaterialien als potentielle Quellen chiraler Verstärkung

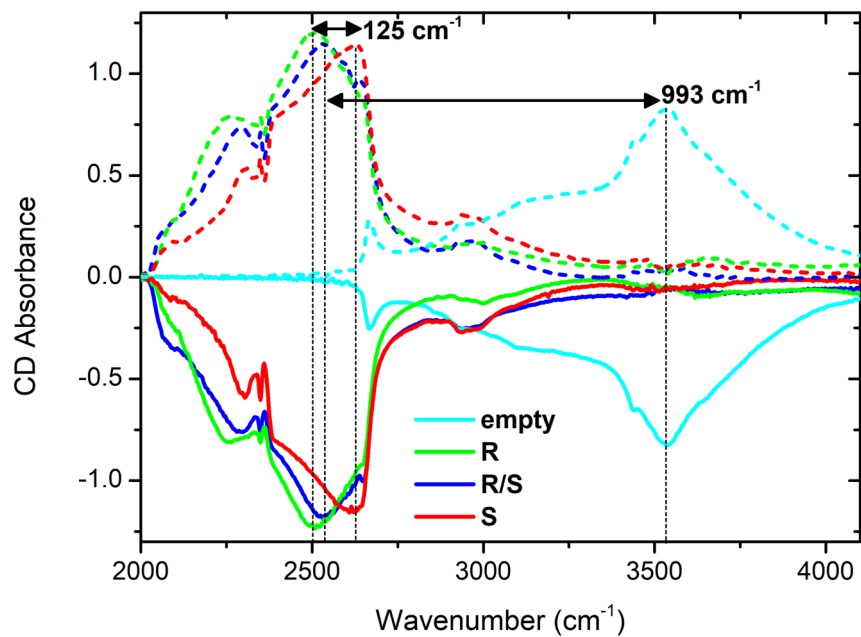


Abbildung 4.6: Vergleich von normaler (durchgehende Linie) and invertierter (gestrichelte Linie) Orientierung (also Wechsel der Händigkeit durch Inversion) gemessen mit L-, R- und einem Racemat von α -Pinene eines $+45^\circ$ Arrays. Neben einer starken plasmonischen Verschiebung von 993 cm^{-1} zeigt sich der Spektralbereich von $2800 - 3000\text{ cm}^{-1}$ ohne scharfe Bandenstruktur. Entgegen der Erwartung zeigen beide Enantiomere eine unterschiedlich stark ausgeprägte Verschiebung der Plasmonenbande. Diese ist hier unabhängig von der Händigkeit des Arrays. Das stützt die Theorie eines effektiven Mediums. Aus [6.1.4]

4 Vorliegender Forschungsansatz

auf einem $+45^\circ$ *Array* wiederholt (vgl. Abb. 7 in 6.1.4), wobei dieses unabhängig von der Händigkeit des benutzten *Array* auftritt. Mit 990 und 1020 cm^{-1} sind die plasmonischen Verschiebungen sehr ähnlich und haben eine fast identische Lage der Plamonenresonanzen. Dieses Verhalten ist unerwartet, da vorherige Publikationen eine Abhängigkeit von der Händigkeit des *Array* beschreiben (Hendry, 2010), und lässt auf die Ausbildung eines effektiven Mediums aus *Array* und chiralem Analyten schließen. Um die Quelle der unerwartet starken Circular Doppelbrechung zu verstehen, gilt es zu bedenken, dass Doppelbrechung und Dichroismus nicht unabhängig voneinander auftreten, wonach auch ein Circular dichroismus beobachtbar sein muss. Dieser lässt sich im Bandenbereich von 2800 und 3100 cm^{-1} erkennen, wo offensichtlich eine molekulare Absorption existiert, die ein der Plasmonenverschiebung gleiches Verhalten zeigt. Bei α -Pinene sind sowohl die IR-Absorptionsbanden als auch die daraus resultierenden VCD Banden in diesem kleinen Spektralbereich konzentriert. Da auch für das Racemat ein Signal in den Spektren erkennbar ist, ist zu schlussfolgern, dass aufgrund der plasmonischen Verstärkung auch ein IR-Beitrag in den CD Spektren sichtbar wird. Wenn dieser IR-Beitrag von den L- und R- α -Pinene abgezogen wird, zeigt sich zumindest für das untersuchte $+45^\circ$ -*Array*, dass das so entstandene effektive Medium sich wie zwei Enantiomere verhält (vgl. Abb. 8 in 6.1.4). Für das -45° -*Array* war diese Abhängigkeit jedoch weniger prägnant. Trotzdem ließ sich auch hier einfach zwischen Racemat und L- sowie R- α -Pinene unterscheiden. Auch wenn der Mechanismus des effektiven chiralen Mediums nicht weiter betrachtet werden konnte, da dieser Aspekt in der vorhandenen theoretischen Beschreibung noch nicht berücksichtigt wurde, zeigte dieses doch die mögliche Leistungsfähigkeit des SHA-*Array* als chiraler Sensor. Die unerwartet prägnante plasmonische Verschiebung könnte zukünftig die komplexen PEM in aktuellen VCD-Spektrometern ersetzen, so dass eine Messung analog zu UV/Vis Spektrometern möglich ist.

4.4 Vorteile und Nachteile plasmonischer Ansätze in der Spektroskopie

Der Hauptvorteil der plasmonischen Ansätze ist die damit erreichbare enorme Sensitivitätssteigerung, da insbesondere auf konventionellem Wege (IRRAS etc.) kaum weitere Sensitivitätssteigerungen erreichbar sind. Somit stellen plasmonische Metamaterialien unter anderem einen Lösungsansatz für IR-spektroskopische Forschungsfragen der Lebenswissenschaften und der Pharmazie dar, welcher im Wesentlichen alternativlos ist. Diese plasmonisch aktiven Metamaterialien, sowohl als perfekter Ab-

4.4 Vorteile und Nachteile plasmonischer Ansätze in der Spektroskopie

sorber als auch in Transmission als *SHA-Array* ermöglichen eine starke Analyt-Licht Wechselwirkung. Erreichbare Feldverstärkungen um das 60-fache (wie im Fall des *SHA-Arrays*), bedeuten bei Annahme der Verstärkung proportional zum Quadrat des E-Feldes ein um das 3600-fache gesteigertes Signal. Durch das stark reduzierte relevante Analytvolumen, welches lediglich dem Schlitzvolumen entspricht, wird weiterhin ein sehr vorteilhaftes Analyt-Signalverhältnis erreicht. Die reale Analytmenge ist deutlich geringer, da nicht die gesamte Analytmenge im Schlitz angelagert wird. Analyt auf der Oberfläche trägt jedoch aufgrund der Ausrichtung der Feldvektoren nicht zum Messsignal bei.

Nachteilig ist bei der plasmonischen Signalverstärkung im Wesentlichen die Deformation der Signalbanden. Im Gegensatz zur SERS-Spektroskopie zum Beispiel ist hier die Plasmonenresonanz ein Teil des Analytspektrums. Durch eine geschickte Wahl der Bandenposition lässt sich dieser Beitrag zumeist in einen Bereich niedriger Bedeutung verlegen, es bleibt jedoch Teil des Messergebnisses. Dies ist umso problematischer, da sich die Plasmonenresonanz mit zunehmender Analytbelegung aufgrund der Anregungsbedingungen verändert, also sich seine Bandenform ändert, indem sich deren Position in einen anderen Wellenbereich verschiebt. Besonders deutlich wird dies in Abb. 3, in der dargestellt ist, wie eine Füllung der Schlitze aus Salzen zu einer drastischen Deformation der Plasmonenbande führt. Diese Verstimmung und Verschiebung erschwert die rechnerische Kompensation der Plasmonenbande, da sich das Verhalten bei Belegung mit Analyt nur sehr schwer vorhersagen lässt. Weiterhin führt die Plasmonenresonanz zu einer Deformation der Analytbanden selbst. Ein wichtiges Beispiel dafür ist insbesondere der Fall der Fano-ähnlichen Wechselwirkung, da er sowohl zur Signalsteigerung als auch zu einer schlechteren Interpretierbarkeit der Ergebnisse führt. Je nach Stärke der Wechselwirkung kann eine Analytbande absorbieren oder transparent werden (EOT, EOA) und sich verschieben. Dieses muss im Vorfeld der Messung bekannt sein, damit es nicht zur Fehlinterpretation aufgrund der Bandenposition kommt. Mithilfe der zugrundeliegenden Theorie von Ugo Fano lässt sich dieses Verhalten zumeist vorhersagen, jedoch ist hierfür die Stärke der molekularen Absorption und des Plasmons nötig, welches jedoch wie dargestellt durch die Analytbelegung verstimmt wird. Somit lassen sich Spektren unter Umständen nicht von der Plasmonenbande selbst bereinigen, was besonders eine automatische Auswertung erschwert.

Evaluiert man die gezeigten Ansätze plasmonischer Verstärkung mit Blick auf kommerzielle Analysegeräte, ergeben sich mehrere potentielle Leistungsparameter. Wie oben gezeigt, wurden Strukturen in ausreichender Größe hergestellt, um Signalstärken bis zu 30% relativ zu erreichen. Durch die selektive Anregung bietet der *SHA-MPA*

4 Vorliegender Forschungsansatz

Sensor gleichzeitig die Möglichkeit einer Negativkontrolle: Bei einer Anregung mit linear polarisiertem Licht orthogonal zur Anregungsrichtung wird kein Plasmon angeregt und somit keine SEIRA-Verstärkung erzeugt. So lässt sich der direkte Analytbeitrag zum Signal durch einfache Differenzbildung entfernen. Aufgrund der Stärke des erzeugten Effekts spielt die Auflösungsgrenze sowie das SNR der verwendeten Geräte kaum eine nennenswerte Rolle. Somit lassen sich bereits mit 64 gemittelten Spektren rauscharme Ergebnisse generieren [6.1.1, 6.1.4]. Ebenso zeigte sich die Anwendbarkeit in einem kommerziellen VCD-Spektrometer, dem ChiralIR-2X (BioTools, USA). In diesem Anwendungsbeispiel diente der Sensor gleichzeitig als Blende, welche Streulicht reduziert und somit Artefakte verhindert, da die Messung in Transmission erfolgte und der Sensor bis auf die aktive Fläche optisch dicht ist. In diesem Fall zeigte bereits der leere Sensor eines der höchsten bis dahin beschriebenen CD-Signale von 0.83. Somit sind diese Sensorkonzepte vielversprechend und wie gefordert in kommerziellen Messgeräten einsetzbar. Die Herausforderungen, diese Sensorkonzepte in die Anwendung zu überführen, sind im Konzept selbst zu suchen.

Als größte Herausforderung aller gezeigten plasmonischen Ansätze ist die Präsenz der Plasmonenbanden selbst in den Spektren anzusehen. Die Lage der Resonanz ist einerseits entscheidend für die Signalverstärkung, andererseits ist es jedoch problematisch, eine Untergrundkorrektur durchzuführen. Wie in [6.1.1, 6.1.3 und 6.1.4] gezeigt, verschiebt sich die Plasmonenbande durch eine Veränderung der dielektrischen Funktion der Umgebung zu kleineren Wellenzahlen (für reale Medien verglichen zu Luft, da $\epsilon > 1$). Diese Rotverschiebung ist damit stark abhängig von der Analytbelegung des *Arrays*. Für den Fall nichtvollständiger Inkubation der Schlitze ergibt sich eine Streuung der Plasmonenverschiebung verschiedener Proben. Diese beeinträchtigt die Vergleichbarkeit und macht eine Ausgleichsrechnung der Untergründe nahezu unmöglich. Dies ist der Fall, da mit der Lage der plasmonischen Bande relativ zur Analytbande auch deren Verstärkung beeinflusst wird. Für die meisten praktischen Belange ist diese Abweichung zu vernachlässigen, sie spielt jedoch bei der VCD-Spektroskopie aufgrund der extrem niedrigen Signalstärken eine Rolle. Wann immer möglich, sollte daher eine Kontrollmessung auf demselben Substrat durchgeführt werden. Dieses wurde im Falle der SHA-MPA durch um 90°gedrehte Wiederholungsmessungen erreicht. Für die breitbandverstärkenden SHA-*Arrays*, welche für keine Polarisationsrichtung nichtverstärkend sind, ergab sich diese Möglichkeit hingegen nicht. Somit ist es hier wichtig, z.B. durch Inversion der Probe eine Korrekturmessung vorzunehmen. Durch Inversion wird so ein +45°orientiertes *Array* in ein -45°orientiertes überführt. Wenn nun der Einfluss der Anregungsseite zu vernachlässigen oder bekannt ist, kann ein Vergleich stattfinden, welcher frei von

4.4 Vorteile und Nachteile plasmonischer Ansätze in der Spektroskopie

entsprechenden Artefakten ist.

Zusätzlich stellen die Wechselwirkungen von Analytbande und der Plasmonenbande ein Problem für die praktische Anwendung dar. Die erwähnte Fano-Wechselwirkung führt zu einer Verstärkung oder Abschwächung der Signalbande sowie zu einer veränderten Bandenposition. Dieses macht insbesondere die automatische Auslese von Spektren nahezu unmöglich.

5 Abschließende Betrachtung

5.1 Fazit

Bestrebungen, die Empfindlichkeit in der Spektroskopie zu steigern, haben seit der Nutzung der plasmonischen Verstärkung große Fortschritte gemacht. Die stetig steigenden Anforderungen an eine sensitive Analytik bedingen neue innovative Methoden, wobei oberflächenverstärkende Technologien hier ein enormes Potential zeigen. Neben neuen analytischen Ansätzen und Techniken wie der *tip-enhanced* Raman-Spektroskopie (TERS) oder stärkeren Emittlern und sensitiven Empfängern wird zunehmend die Modifikation der unmittelbaren Analytumgebung betrachtet. Effekte wie der *lightning-rod*-Effekt und die chemische Verstärkung bei SERS zeigen das Potential dieser Ansätze, jedoch auch deren Limitationen. Da es sich nicht um „kontaktlose“ Ansätze handelt, spielt die Interaktion von Probe und Sensor hierbei eine entscheidende Rolle. Um das Potential der Methode für erfolgreiche Anwendungen in der Bioanalytik zu erproben, ist es notwendig, das Problem der starken Beeinflussung der Spektren durch die Plasmonenresonanzen zu lösen. Dieses ist eine andauernde Aufgabe bei der Verfolgung des Ziels, experimentelle Ansätze erfolgreich in die Anwendung zu überführen und diese letztendlich zu einer etablierten spektroskopischen Methode zu machen.

Ausgehend von dem Ziel, eine Quelle robuster und leistungsfähiger Verstärkung unabhängig von den untersuchten Analyten zu finden, galt der Fokus dieser Arbeit der Untersuchung eines oberflächenverstärkenden SEIRA-Arrays mit chiralen und achiralen Eigenschaften. Ein wichtiger Punkt, der hierbei adressiert wurde, war neben der signifikanten Steigerung der Sensitivität der Methode, die Loslösung von spezialisierten Messsystemen. Die Anwendbarkeit der SEIRA-Arrays auf nahezu jedem FT-IR und VCD-Spektrometer war eine der Kernforderungen. Zu diesem Zweck wurde auch ein Standard-FT-IR-Spektrometer und ein verbreitetes VCD-Spektrometer verwendet. Diese Geräte wurden ohne Modifikationen genutzt, um die Anwendbarkeit auch außerhalb eines Forschungslabors zu beweisen. Als Modellanalyten wurde

5 Abschließende Betrachtung

solche gewählt, die sowohl experimentell als auch in ihren zugrundeliegenden Spektroskopischen Eigenschaften wohldefiniert sind, wie beispielhaft das Octadecanethiol. Ausschlaggebend für die Ausrichtung dieser Arbeit war es, dass FT-IR-Spektrometer auf dem Markt weit verbreitet sind. Darüber hinaus wird die FT-IR-Spektroskopie als Standardwerkzeug spektroskopischer Aufklärung eingesetzt. Dies bedeutet eine hohe Verfügbarkeit technisch ausgereifter Geräte sowie eine sehr breite Wissens- und Anwenderbasis. Eine weitere Aufwertung dieser Technik durch SEIRA-Substrate stellt demzufolge einen vielversprechenden Ansatz mit dem Potential schneller Akzeptanz auch außerhalb Forschungswelt dar. Trotz ihres Alters sind nach wie vor ein Großteil der Informationen in der Materialanalytik und bei Standardfragen in der chemischen Industrie mit Hilfe dieser spektroskopischen Methode zugänglich. Der SEIRA-Ansatz hat hier das Potential, den größten Mangel der teils ungenügenden Sensitivität reiner FT-IR-Messungen zumindest teilweise zu kompensieren.

Die Wahl eines Lösungsansatzes fiel in dieser Arbeit auf ein SHA-MPA-Design. Dieses verspricht eine maximale Signalerhöhung durch den MPA-Teil bei gleichzeitig stark reduziertem Analytbedarf aufgrund der gezeigten selektiven Anbindung von Analyt durch eine Oberflächenpassivierung. Damit sich weiterhin Abweichungen bzw. Fertigungsinhomogenitäten weniger stark auf die Leistungsfähigkeit des Sensors auswirken, fiel die Wahl auf ein großflächiges *Array* von Metamaterialstrukturen, was zu einer Mittelung über viele Nanoantennen führt. Dies wiederum reduziert die Anforderungen an die Nachbereitung der Daten. Gleichzeitig reduziert sich auch die Anforderungen an die Optik des verwendeten Messsystems und ermöglicht Messungen im kollimierten Strahl bei Geräten ohne einen Mikroskopkanal, d.h. auch mit Geräten der Basisausstattung.

Durch die zusätzliche intrinsische Polarisationsabhängigkeit bieten diese *Arrays* die Möglichkeit einer Negativkontrolle auf dem gleichen Array durch die veränderte Plasmonenresonanz. So kann zwischen plasmonisch verstärktem Signalbeitrag und reinem Analytbeitrag unterschieden werden. Der Analytbeitrag ist unabhängig von der Polarisationsrichtung vorhanden, der plasmonisch verstärkte Beitrag nur in Resonanzbedingungen. So lässt sich ein Spektrum um den jeweiligen Beitrag bereinigen. Ein Nachteil dieses Ansatzes ist die ausschließliche Anwendbarkeit in Reflexionsanordnung. Dies erschwert unter Umständen die Interpretation der Daten und verkompliziert die Messanordnung. Als „Standardfall“ ist eine Transmissionsmessung deutlich erstrebenswerter. Aufbauend auf dem erfolgreich gezeigten leistungsfähigen SHA-MPA-Ansatz, wurde der Messansatz für Transmissionsmessungen optimiert. Durch ein Entfernen des MPA-Teils der Anordnung werden Transmissionmessungen ermöglicht, da die optisch dichte „Bodenplatte“ zwingend ein Bestandteil des

MPA-Aufbaus ist. Im gleichen Zuge wurde ein weiterer Schlitz in das Design integriert, um eine breitbandige Verstärkung zu erhalten, da die Verstärkung nur in der Nähe der plasmonischen Resonanzen stark ausgeprägt ist. Durch eine geschickte Anordnung der zwei Schlitze lässt sich weiterhin ein chirales Metamaterial erzeugen, was diesen Ansatz vorteilhafter erscheinen lässt. Das so entstandene chirale Metamaterial wurde aufgrund seiner zwei plasmonischen Resonanzen zuerst für den Einsatz als breitbandverstärkendes SEIRA-Metamaterial untersucht. Hierbei zeigte sich die gewünschte breitbandige Verstärkung im gesamten MIR-Bereich. Die chiralen Eigenschaften wurden anschließend genutzt, um eine der zentralen Fragen im Bereich chiraler Plasmonik zu adressieren: Ob es möglich ist, mittels chiraler plasmonischer Substrate das VCD-Spektrum eines Analyts zu verstärken. Zu diesem Zweck wurden beide Enantiomere des plasmonischen Metamaterials gefertigt ($+45^\circ$ und -45°) sowie ein achirales *Array* als Kontrollsubstrat (vergleichbar einem Racemat) mit einer Schlitzorientierung von 90° .

Insgesamt stellte sich heraus, dass die Substrate ohne Modifikationen in einem kommerziellen VCD-Spektrometer einsetzbar sind und weiterhin das bis dato höchste CD-Signal zeigten, das für ein 2D-Metamaterial berichtet wurde. Es ist somit einer der Extremfälle der im wissenschaftlichen Diskurs vorgeschlagenen Substrate, bei denen es um die Klärung der plasmonischen Verstärkung von VCD-Spektren geht. Bei unseren Untersuchungen zeigten sich die Herausforderungen der plasmonischen Verstärkung im Infrarot in Form einer Beeinflussung der Spektren durch die Plasmonenbande selbst. Dies ist durch die Ausbildung eines effektiven Medium zu erklären, welches die Bandenstruktur des Modellanalyten beeinflusst. Die Untersuchungen zeigen jedoch, dass es gelungen ist, ein SHA-*Array* mit einer kombinierten breitbandigen plasmonischen- und einer VCD-Verstärkung herzustellen und zu vermessen. Bei der Breitbandverstärkung bestätigte das *Array* das vorhergesagte Verhalten und es ließ sich eine schaltbare und ausgeprägte Breitbandverstärkung zeigen. Durch die intrinsische Chiralität des *Array* ist dieses weiterhin vielversprechend für oberflächenverstärkende VCD Messungen. Besonders im Bereich der Lebenswissenschaften mit fast ausschließlich chiralen Makromolekülen und Proteinen ist der membranbasierte Ansatz aufgrund der kleinen Probenvolumen vielversprechend. Zusammen mit den intrinsischen Kapillarkräften erlaubt dieses ein einfaches Probenhandling sowie möglicherweise eine Größenseparation von Makromolekülen aufgrund der kleinen Schlitzbreiten. Die chirale Antwort selber übertraf mit einem CD von 0.83 für das leere *Array* und mit einem CD Signal von ~ 1.2 für ein analytbelegtes *Array* deutlich die aus der Theorie entsprungene Erwartungen, und sich nach momentanem Kenntnisstand die größten gemessenen Werte eines 2D-*Arrays* im infraroten Spektralbereich.

5 Abschließende Betrachtung

Diese chirale Antwort und die gezeigte signifikante plasmonische Verschiebung lassen sich nach bestem Wissen nicht mit dem aktuellen Stand der Theorie beschreiben und geben möglicherweise Einblicke in eine völlig neue Wechselwirkung von chiralem Analyt und chiralem Metamaterial. Darüber hinaus ist die deutliche Verschiebung auch ein starkes Indiz, welches belegt, dass die angestrebte Oberflächenverstärkung eines chiralen Analyten in VCD-Messungen möglich ist. Somit erlauben unsere Ergebnisse den Schluss, dass oberflächenverstärkte VCD-Messungen tatsächlich möglich sind, gleichzeitig jedoch durch das Problem der Wechselwirkung mit dem Plasmon selbst stark in der Anwendbarkeit reduziert sind. Trotzdem eröffnen die Messungen einen ersten Blick auf oberflächenverstärktes VCD und bieten eine neue Perspektive auf bisher in der Theorie unbeschriebene Wechselwirkungen zwischen chiralen Metamaterialien und chiralen Analyten.

5.2 Ausblick

Neben fundamentalen neuartigen Erkenntnissen über Technologie und Theorie der plasmonischen Verstärkung bietet die vorgestellte Methode der SEIRA-Technologie neue Wege für die Analytik. Eine Möglichkeit der weiteren Optimierung ist in der Anpassung der Substrate zu sehen, um zukünftig den Einfluss der Plasmonenbande von dem des Signals zu isolieren bzw. die Plasmonenbande in einen spektroskopisch uninteressanten Bereich zu verschieben. Alternativ ließe sich durch ein Fertigen extrem schmaler Schlitze auf eine der Plasmonenbanden verzichten, da in diesem Fall die Verstärkung einer der Resonanzen immer breitbandiger wird. Dieses ist jedoch technologisch extrem anspruchsvoll und folgt nicht dem Gedanken einer leicht verfügbaren Aufwertung bestehender FT-IR und VCD-Spektrometer durch plasmonische Metamaterialien. Ein weiterer noch offener Untersuchungsgegenstand ist die Möglichkeit der Lock-In-Verstärkung. Da die plasmonischen Resonanzen optisch schaltbar sind, ließe sich über einen Zehner eine Modulierung auf das FT-IR-Signal aufbringen. Diese könnte anschließend gemäß dem Lock-In-Prinzip verstärkt werden, wobei weiterhin zwischen verstärktem und unverstärktem Signal unterschieden werden könnte. Als ferne Anwendung ist die Möglichkeit der Anregung von chiralen dunklen Moden zu nennen. Grundlegend ist jedoch die Erweiterung der theoretischen Basis der plasmonischen Verstärkung. Die in dieser Arbeit beschriebenen Wechselwirkungen bedingen neuartige Erklärungsansätze und Theorien. Dies hätte zur Folge, dass die chirale Plasmonik besser vorhersagbar wird. Somit wäre es zukünftig möglich, Fragestellungen wie die Ursache der gigantischen chiralen Antwort der Arrays abschließend zu beantworten. Dieses würde den Weg für noch

5.2 Ausblick

leistungsfähigere chirale Substrate liefern, welche maßgeschneidert auf Fragen der z.B. Lebenswissenschaften sind. Dieses kann analog zu der bereits in den letzten 10 Jahre beobachteten Entwicklung hin zu maßgeschneiderten und sehr leistungsfähigen breitbandverstärkenden SEIRA Arrays erfolgen, wie sie ebenfalls in dieser Arbeit gezeigt wurden.

6 Publikationen und Konferenzbeiträge

6.1 Publikationen

6.1.1 Ultra Sensing by Combining Extraordinary Optical Transmission with Perfect Absorption [P1]

Mayerhöfer, Thomas G.; **Knipper, Richard**; Hübner, Uwe; Cialla-May, Dana; Weber, Karina; Meyer, Hans-Georg; Popp, Jürgen *Ultra Sensing by Combining Extraordinary Optical Transmission with Perfect Absorption*, ACS Photonics (2015), 2 (11), pp 1567–1575, DOI: 10.1021/acsphotonics.5b00321

Reprinted with permission from ACS Photonics. Copyright (2015) American Chemical Society.

Ultra Sensing by Combining Extraordinary Optical Transmission with Perfect Absorption

Thomas G. Mayerhöfer,^{*,†} Richard Knipper,^{†,‡} Uwe Hübner,[†] Dana Cialla-May,^{†,‡} Karina Weber,^{†,‡} Hans-Georg Meyer,[†] and Jürgen Popp^{†,‡}

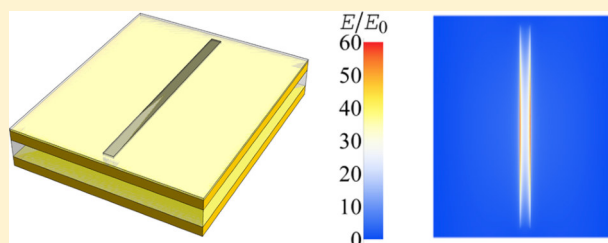
[†]Leibniz Institute of Photonic Technology (IPHT), Albert-Einstein-Str. 9, D-07745 Jena, Germany

[‡]Institute of Physical Chemistry and Abbe Center of Photonics, Friedrich Schiller University, Helmholtzweg 4, Jena, D-07743, Germany

Supporting Information

ABSTRACT: Extraordinary optical transmission and perfect absorption are two plasmonic-based optical phenomena that are both accompanied by high local field enhancements that can be exploited for biological and chemical sensing. Here we merge both phenomena in a slit array metamaterial perfect absorber consisting of a dielectric layer sandwiched between two metallic layers of which the upper layer is perforated with a periodic array of slits. Period and dimensions of the slits and thickness of the dielectric layer are tuned in a way that virtually all light of a certain wavelength incident on the surface passes through the slits and is subsequently absorbed. As a consequence, light–matter interaction is greatly enhanced in the slits. Thus, already small concentrations of analytes down to a monolayer attached to the sidewalls of the slits can be detected by refractive index sensing and identified by their spectral fingerprints with a standard mid-infrared lab spectrometer.

KEYWORDS: plasmonics, metamaterials, sensing, surface enhanced infrared spectroscopy, extraordinary optical transmission, perfect absorption



A metamaterial perfect absorber (MPA) is a subwavelength structured device in which all incident radiation is absorbed at a particular wavelength.¹ As a consequence, at this wavelength transmission and reflection are zero. In practice, zero transmission is made possible by a highly reflecting layer of a coinage metal, for example gold, with a sufficient thickness so that virtually no radiation can pass through. Absorption is usually caused by the excitation of a surface plasmon polariton (SPP). Since light cannot couple to a smooth metallic surface, it is the task of a proper surface structure to enable the excitation of an SPP at the desired wavelength. Usually this surface structure consists of metallic particles on a thin dielectric film to separate the particles from the basic metal layer. These metallic particles can have a variety of forms like, in the simplest cases, cylinders² or rectangular parallelepipeds,^{3–7} crosses,^{8,9} and more complicated forms like trapezoids and so on.^{10–12} The design of such metamaterial perfect absorbers was partially driven by the effort to avoid interactions between the individual particles and unit cells. In a few cases, however, the opposite design strategy was selected, that is, using a subwavelength hole array (SHA) instead of metallic particles as the surface structure.^{13,14} These structures are of particular interest also from a theoretical point of view, since perfect absorption at one wavelength would mean that all light shining on the MPA has to pass through the holes in order to be absorbed by the structure if the perforated metal layer is thick enough to block direct transmission. In refs 13 and 14,

however, a hole array layer is used that is optically thin at the resonance wavelength of the MPA, so that part of the light is transmitted directly through the metal layer. From an application oriented point of view, the SHA-MPA combination has very attractive features for both chemical and biological sensors. Compared to SHAs, the SHA-MPA combination can be expected to lead to much higher field enhancements within the holes, the “hot spots”. Further, compared to particle-based MPAs, with SHA-MPA it proves much easier to concentrate the analyte in these volumes of the highest field enhancements. If the resonance wavelengths of the SHA-MPA combination is tuned for the absorption at mid-infrared (MIR) frequencies, from the presence of the analyte not only will a band shift ensue due to the different dielectric environment of the gold surface,² but also chemical information will be provided by the enhancement of the spectral footprint of the analyte. This has already been shown for either SHAs with enhanced transmission¹⁵ or nanoantennas^{16–18} with plasmonic excitations in the MIR.

It was the goal of the present work to design and manufacture exactly this sort of SHA-MPA combination for the MIR spectral region. The structures we fabricated were then tested with the model analyte octadecanethiol and, additionally,

Received: June 10, 2015

Published: October 21, 2015

with DNA. We believe that the SHA-MPA combination proves to be a promising candidate to serve as an integral component of a future application for ultrasensitive biological and chemical detection and quantification.

The basic structure of one elementary cell of the SHA-MPA is depicted in Figure 1. A 50 nm gold film serves as the first

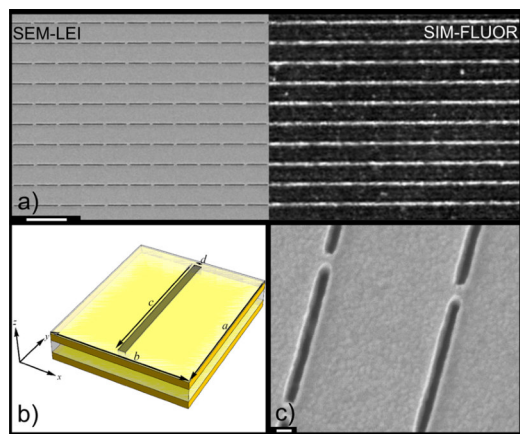


Figure 1. Structure of the subwavelength slit array metamaterial perfect absorber. (a) Combined SEM and SIM-FLUOR image (scale bar 2 μm). (b) Unit cell of the slit metamaterial perfect absorber. The layer stack of the fundamental structure consists of a 50 nm thick gold base layer followed by an Al_2O_3 layer and a second 50 nm thick gold layer (metal–insulator–metal layer stack). The top SiO_2 layer (thickness: 10 nm) serves to inhibit functionalization. The period in the y -direction of the unit cell is a , the one in the x -direction b . c is the slit length and d is the slit width, respectively. The depth of the slit is 60 nm so that the base level coincides with the surface of the Al_2O_3 layer. (c) Tilted SEM micrograph (scale bar 100 nm; pitch b , 910 nm; pitch a , 1100 nm; slit width d , 45 nm; slit length c , 1005 nm; $t_{\text{Al}_2\text{O}_3}$ = 90 nm; grating size, $1 \times 1 \text{ mm}^2$).

layer (the base). As gold films tend to grow in a columnar way with increasing thickness, causing poor thickness homogeneity, we decided to employ a base layer as thin as possible. Based on the optical constants of gold¹⁹ we calculated that a 50 nm gold film would exhibit a transmission of less than 1×10^{-3} for wavelengths larger than 2.26 μm , which is small enough for our goal to additionally enhance the electric field within the slits. On top of the 50 nm gold base layer, the dielectric layer was placed, for which we decided to use Al_2O_3 , and not SiO_2 . Not only is the onset of the Reststrahlenband of Al_2O_3 shifted to a higher wavelength than with SiO_2 ,²⁰ which in general allows for the building of an infrared active substrate down to about 10 μm (1000 cm^{-1}). Therefore, the resonance wavelength of the substrate will be tunable over most of the IR spectral range that is interesting for biological molecules. Furthermore, as will be shown later, the enhancement will be concentrated on the slit walls and not on the gold base layer. Employing Al_2O_3 as the dielectric, the slit will not penetrate the dielectric layer down to the base due to the very small Ar^+ -ion beam etching rate of Al_2O_3 . As a consequence, only the side walls of the slit will be able to be functionalized. On top of the dielectric, the thickness $t_{\text{Al}_2\text{O}_3}$ of which is in the range of 90 nm, a second 50 nm thick gold layer is placed. To prevent the surface layer from being functionalized, we applied a 10 nm thick layer of SiO_2 onto the second gold layer. This SiO_2 layer completes the layer stack. With a period a in the y -direction and b in the x -direction (see

Figure 1b), slits with a length c (along y) and width d (along x) are then etched out.

As a consequence of the design, the analyte can only be found in the region of the slits, which we could prove with help of high-resolution structured illumination fluorescence imaging (Figure 1a, right).

The original idea of this design was that for small widths d of the slits extraordinary high enhancement factors for the electric fields would follow. Indeed this proved to be the case, yet, as will be shown, only for very small slit widths $d < 20 \text{ nm}$ which are, at the moment, difficult to realize from the technological point of view. Nevertheless, even for $d = 50 \text{ nm}$ considerable enhancement factors result at the resonance wavenumbers, which can be explained by the fact that, with perfect absorption ($A = 1$), all the light has to pass through the slit. At the same time, the slit generates highly anisotropic optical properties. While the slit substrates show near perfect absorption in the infrared spectral range for x -polarized radiation, the substrates cannot be optically distinguished from an unstructured, thick gold layer for y -polarized radiation.

This is demonstrated by a numerical simulation employing the finite difference time domain (FDTD) method for a substrate with $t_{\text{Al}_2\text{O}_3} = 90 \text{ nm}$, $a = 1100 \text{ nm}$, $b = 910 \text{ nm}$, $c = 1000 \text{ nm}$, and $d = 50 \text{ nm}$ in Figure 2.

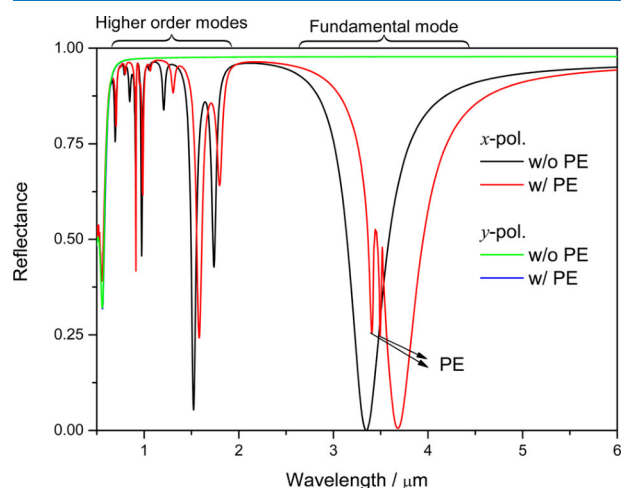


Figure 2. Simulated spectra of a subwavelength slit array metamaterial perfect absorber. Simulated reflectance spectra of a slit MPA with $a = 910 \text{ nm}$, $b = 1100 \text{ nm}$, $c = 1000 \text{ nm}$, $d = 50 \text{ nm}$, and $t_{\text{Al}_2\text{O}_3} = 90 \text{ nm}$ for normal incidence. The figure compares the x -polarized spectra of the slit MPA with an empty slit (black) and a slit filled with PE (red). The y -polarized spectrum (green/blue) does not vary with the slit content and is essentially that of an (unstructured) gold surface.

Since reflection spectroscopy requires recording a reference spectrum (in the IR spectral range often a gold mirror is used) for future application it might be possible to use a y -polarized spectrum of the substrate as this reference. (For the measurements shown below, however, a gold mirror served as reference.)

For the slit array perfect absorber we aim at a resonance around 3000 cm^{-1} in order to selectively enhance the C–H valence vibrations present in nearly all organic and biologic molecules which are located in this spectral range. According to our simulations the substrate with $t_{\text{Al}_2\text{O}_3} = 90 \text{ nm}$, $a = 1100 \text{ nm}$,

$b = 910$ nm, $c = 1000$ nm, and $d = 50$ nm has exactly such a resonance with less than 0.01% reflectance R , meaning that the absorption A is higher than 99.94% (since $A + R + T = 1$ and the transmittance of the base layer $T < 5 \times 10^{-4}$ at the resonance wavelength). In addition, the perfect absorber design leads to a very narrow absorption line with a full width at half-maximum (fwhm) of about $0.45 \mu\text{m}$. When the slit is loaded completely with PE, the simulation result changes in two ways (cf. Figure 2). First, we notice a shift of all resonances, including most of the higher order plasmon modes which populate the region below $2 \mu\text{m}$, to higher wavelengths, and second, we see a change of the band shape of the main resonance.

The resonance shift is a consequence of the changed dielectric properties of the medium in the slit.

The change in the band shape of the main resonance is due to the interaction of the SPP with the C–H vibrations of the PE. For PE, we expect two different C–H stretching vibrations, the asymmetric C–H stretching vibration $\nu_{\text{as}}(\text{CH}_2)$ at $3.427 \mu\text{m}$ (2918 cm^{-1}) and the symmetric C–H stretching vibration $\nu_{\text{s}}(\text{CH}_2)$ at $3.503 \mu\text{m}$ (2853 cm^{-1}). Inspecting the corresponding spectrum in Figure 2, we indeed find two additional bands, the minima of which are, however, slightly shifted to 3.406 and $3.494 \mu\text{m}$. The reason for this shift can be found in the Fano-type interaction between the comparably broad band absorption caused by the SPP and the narrow band resonances of the PE. When the wavelength of the plasmonic mode is shifted relative to the vibrational modes, the PE bands transform from electromagnetically induced absorption (EIA) to electromagnetically induced transparency (EIT). The latter occurs when the resonance frequencies of plasmon and vibration coincide. Since the medium in the slit and, with it, the index of refraction changes (the average index of refraction increases with the filling ratio), the SPP is shifted to a longer wavelength. As a consequence, the difference between the resonance frequencies of PE and SPP increases, resulting in a state in between EIA and EIT. This effect will be discussed in more detail later. In general, we can tune the resonance by varying the period in x -direction, the thickness of the Al_2O_3 -layer $t_{\text{Al}_2\text{O}_3}$ and the slit width. (N.B.: Altering the layer thickness of the structured gold layer would also have an influence, in particular, if decreased. However, since we want to make sure that direct transmission through this layer remains virtually zero, we did not vary the thickness of the gold layer.)

The dependence of the SPP wavelength on the slit parameters is demonstrated in Figure 3. Accordingly the reduction of the slit width from 70 to 10 nm leads to a shift of the resonance from about $3.25 \mu\text{m}$ up to $4.27 \mu\text{m}$. For slit widths lower than 30 nm, however, the reflectance increases from 1% to about 15% for 10 nm slit width. A lower change of the resonance wavelength can be achieved by varying the period in x -direction between 820 and 1000 nm. For $a = 820$ nm, the resonance wavelength is $3.18 \mu\text{m}$, which increases to $3.51 \mu\text{m}$ for $a = 1000$ nm. In contrast to the variation of the resonance wavelengths due to changing the slit width, the reflectance stays for the period range considered below 1%. Even less variation of the resonance wavenumber is achieved due to a variation of the thickness of the Al_2O_3 layer $t_{\text{Al}_2\text{O}_3}$. For $t_{\text{Al}_2\text{O}_3} = 60$ nm the resonance can be found at $3.47 \mu\text{m}$, which decreases with increasing $t_{\text{Al}_2\text{O}_3}$. Accordingly, we find for $t_{\text{Al}_2\text{O}_3} = 120$ nm, the resonance is at $3.32 \mu\text{m}$.

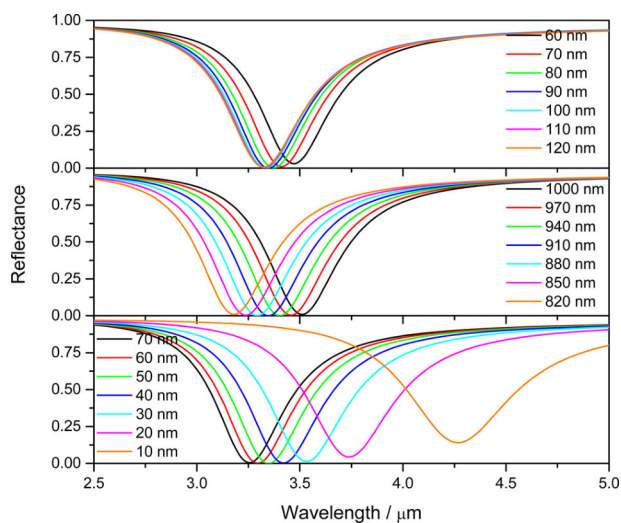


Figure 3. Dependence of the SPP wavelength on the slit parameters. Simulated reflectance spectra of the slit MPA for x -polarization. Shown are the influence of the variation of thickness of the Al_2O_3 -layer (upper panel) of the period a (middle panel) and the slit width d (lower panel). The nonvaried parameters correspond to those from Figure 2.

The enhancement of the electric field E relative to the initial field E_0 at the resonance wavelength is depicted in Figure 4.

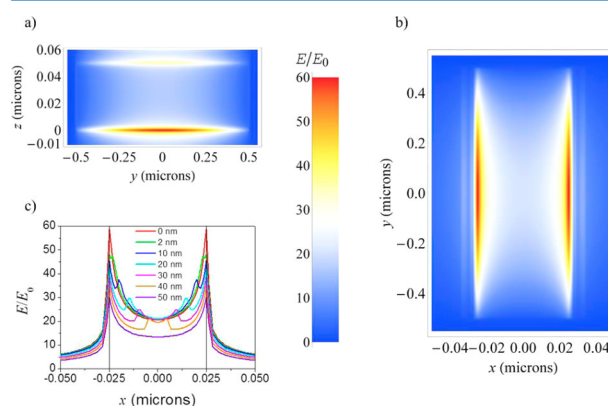


Figure 4. Electric field enhancement within the slit (same MPA as in Figure 2). (a) Electric field enhancement E/E_0 at a cross section within the slit 1 nm away from the slit wall ($x = 0.024 \mu\text{m}$). (b) Electric field enhancement E/E_0 at a cross section parallel to the surface of the substrate at the interface between Al_2O_3 and the second gold layer ($z = 0$ nm). (c) Electric field enhancement E/E_0 for $y = 0$ on the line where the enhancement is at the maximum, which is reached in the distance 0 – 1 nm away from the slit walls for different PE layer thicknesses. 10 nm, for example, means that both parts of the slit walls at the long sides that consist of gold (on the SiO_2 level the slits are unfilled) are covered with a 5 nm thick PE layer, leaving an empty slit with a width of 40 nm.

Accordingly, the enhancement is strongest one nm away from the slit walls within the slit along the long sides with a global maximum in the center of the long side. In the middle of the slit the amplification reaches a local minimum being lower for a completely filled slit than for an empty slit. Thus, even if the enhancement at first decreases with increasing z (see Figure 4a), it seems advisable to use the slit walls and functionalize them in order to bind and concentrate analytes in the

neighbored volumes. Of course, if the slit walls are covered with analyte (in our simulations PE), the dielectric properties change the distribution of the enhancement (see Figure 4c). The thickness indicated in Figure 4c gives the sum of the (equal) thicknesses of the “left” and “right” layer, for example, “thickness 10 nm” means that the thickness of the left and right layer amount to 5 nm each. Correspondingly, 50 nm thickness means that both thicknesses amount to 25 nm, which translates into the slit being completely filled with PE at the level of the gold layer (at the level of the top SiO₂ layer the slit is always assumed to be empty). In this case, the enhancement decreases continually until the center is reached, whereas in the cases where the medium part of the slit is not filled, the interface between PE and empty slit is characterized by a sudden increase of the enhancement. From the results presented in Figure 4, we conclude that the SEIRA (surface enhanced infrared absorption; to be more precise, this slit array supports SEIRR, as it operates in reflection mode) slit array MPA is less prone to fabrication errors than particle based substrates as the slits show their maximum enhancement generally at sides, whereas particles based structures show the maximum enhancement at corners and fine structures due to the lightning rod effect.^{21–28} It can be expected that such fine structures show a much stronger variance due to imperfect fabrication processes compared to edges of a slit. As a consequence, the deviations between different elementary cells can be expected to be much higher for particle based substrates than for slit-based substrates.

To determine how the spectral footprint changes with the thickness of the layers placed on the slit walls we performed different simulations the results of which are depicted in Figure 5. Even a thickness of 2 nm PE is easily detectable by a shift of the resonance band, whereas the spectral signature for this thickness is not easy to discern. Accordingly, the strengths of the slit MPA with this particular slit width $d = 50$ nm will be the detection of somewhat larger biomolecules, in particular, because of a reaction with capture molecules that are attached to the gold sidewalls.

Nonetheless, the sensitivity for the spectral fingerprint can be enlarged by decreasing the slit widths. As shown in Figure 5 (upper part), this shifts the main resonance to higher wavelengths but, nevertheless, increases the enhancement of the electric field strengths within the slit even for wavelengths comparably far away from the resonance range. This can be concluded from the comparison provided in the upper part of Figure 5, where the spectra of slits loaded with PE for slit widths from 70 nm down to 10 nm are shown. All spectra were calculated with a constant PE layer thickness of 5 nm at each long side, meaning that for the slit width 10 nm the slit is completely filled on the level of the gold sidewalls. Despite a strong redshift of the SPP resonance, which is, with $5.31 \mu\text{m}$, far away from the vibrational resonances of PE due to the C–H stretching vibrations, the latter are easily detectable in the spectrum.

The comparison between the spectrum of the substrate with loaded and unloaded slits within an extended wavelength range is given in Figure 6. In addition to the spectral signature of the PE C–H stretching vibrations and an extraordinarily strong shift of the SPP resonance, even the spectral signature of the weak deformation vibration $\delta(\text{CH}_2)$ at $6.779 \mu\text{m}$ (1475 cm^{-1} , $1460\text{--}1470 \text{ cm}^{-1}$ according to literature) can easily be detected. The corresponding spectral range is also of particular interest for biological sensing, as, in this range, the amide

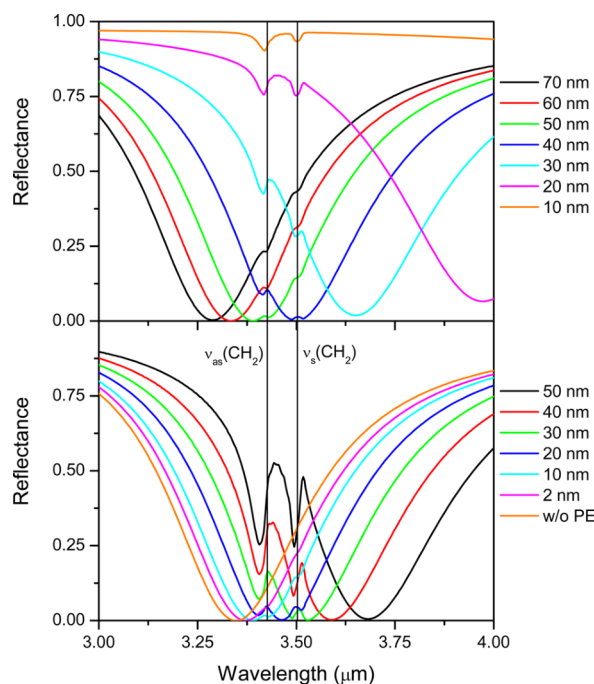


Figure 5. Simulated spectra of a subwavelength slit array metamaterial perfect absorber filled with analyte. Upper panel: influence of the slit width d on the normal incidence spectra when the PE layer thickness equals 10 nm. (For MPA with the smallest slit width this means that the slit is completely filled with PE on the level of the structured gold layer.) Lower panel: simulated reflectance spectra of a slit MPA with $a = 1100$ nm, $b = 910$ nm, $c = 1000$ nm, $d = 50$ nm, and $t_{\text{Al}_2\text{O}_3} = 90$ nm for normal incidence in the spectral region of the main resonance. The panel displays spectra for an empty slit (orange) and a slit completely filled with PE (black), as well as for different layer thicknesses (cf. Figure 4c).

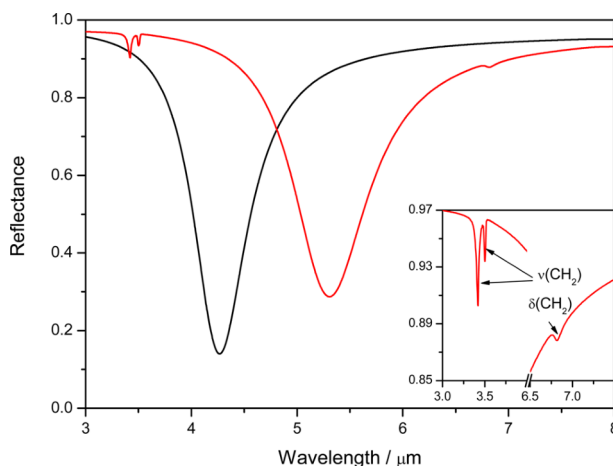


Figure 6. Simulated spectra of a subwavelength slit array metamaterial perfect absorber with 10 nm slit width. Simulated reflectance spectra of a slit MPA with $a = 1100$ nm, $b = 910$ nm, $c = 1000$ nm, $d = 10$ nm for normal incidence, and $t_{\text{Al}_2\text{O}_3} = 90$ nm. Here we compared the x -polarized spectra of the slit MPA with empty slit (black) and slit filled with PE (red). The inset gives an enlargement of the regions with PE absorptions.

vibrational peaks of proteins, which show much higher vibrational intensities than $\delta(\text{CH}_2)$, can be found.⁸ It is

remarkable that, for a slit width of 10 nm, the slit surface accounts only for about 1% of the whole area.

Nevertheless, the vast majority of the light passes through the slit at the wavelength of the resonance. (Note that we did not optimize the absorber for the slit width of 10 nm; virtually perfect absorption and an even better performance after optimization is likely.) The total volume of PE within the slit amounts to $1 \mu\text{m} \times 0.05 \mu\text{m} \times 0.01 \mu\text{m}$. To clarify, under the assumption that the PE covers the total surface of the substrate, this would correspond to a layer of about 0.5 nm thickness (only a few C atoms thick). Even if small slit widths below 25 nm are hard to obtain from a technological point of view at the moment (yet may be accessible, e.g., by the use of photochemical metal deposition^{17,18}), we are positive that this design will be valuable in the future once this limitation has been overcome. Since, despite its comparably narrow plasmon resonance, this slit perfect metamaterial absorber could be used not only for very sensitive refractive sensing, but also for enhancing most of the infrared spectral fingerprint of biomolecules with monolayer sensitivity, rendering it a highly desirable structure. In addition, the plasmon resonance is located in a spectral range between the stretching and bending vibrations of organic and biological molecules (between 3.5 and $5.5 \mu\text{m}$). Therefore, strongly enhanced but nearly undistorted spectra can be gained.

To prove the simulation results, we fabricated a number of slit MPAs with dimensions close to the one the simulated spectra of which were presented in Figure 2 ($a = 910 \text{ nm}$, $b = 1100 \text{ nm}$, $c = 1000 \text{ nm}$, $d = 50 \text{ nm}$, and $t_{\text{Al}_2\text{O}_3} = 90 \text{ nm}$). We recorded IR spectra of the slit MPAs as fabricated as well as loaded with analytes showing C–H bands comparable to that of PE. A standard analyte, octadecanethiol (ODT), was used as a stand-in for PE due to their similarity with respect to the infrared spectral signatures and the ability of ODT to form chemically bound monolayers on gold surfaces that resist washing. The corresponding spectra, which were taken from substrate surfaces with an area of 1 mm^2 are presented in Figure 7a,b. Accordingly, the spectra represent averages of the spectral behavior of about 10^6 elementary cells and slits, respectively (spectral variances on the substrates are comparably small, cf. Figure S4 in the Supporting Information). The spectra show signal intensities of the C–H stretching vibrations and shifts of the plasmon bands that clearly exceed those which can be caused by an ODT monolayer based on the results of the simulations (cf. spectrum of a 2 nm thick PE layer in Figure 5, lower panel). This outcome is somewhat surprising yet gratifying as we used standard protocols which include washing steps to remove any ODT that is not covalently bound to the gold surface via its Sulfide-group (cf. Supporting Information, infrared spectroscopy).

We can only speculate that within the slits the van-der-Waals interaction between the hydrocarbon backbones is strong enough to withstand removal by the solvent even when not bound to the metal so that more ODT than expected remained in the slit. Free ODT should, in contrast to bound ODT, show bands according to the H–S-stretching vibrations (usually located between 3.85 and $4.16 \mu\text{m}$). Unfortunately, these vibrations usually have comparably weak signal intensities, even when more thiol groups are present than in ODT. Therefore, it is not surprising that the corresponding bands cannot be seen in the spectra. We investigated the samples by SEM (Supporting Information, Figure S1), and the results support

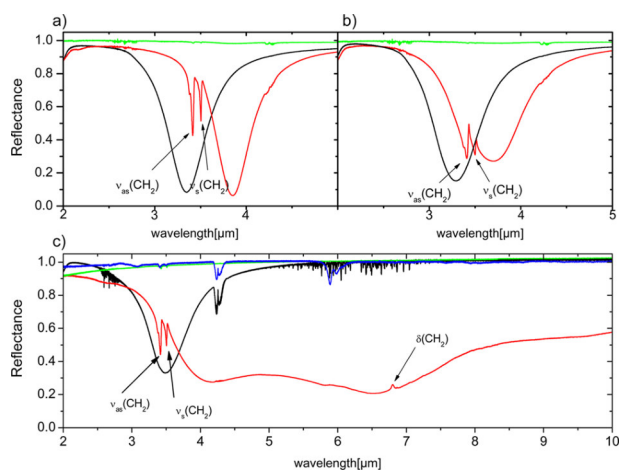


Figure 7. Experimental reflectance spectra of three slit MPAs at normal incidence ($a = 910 \text{ nm}$, $b = 1100 \text{ nm}$). (a) x -polarized spectra of a slit MPA ($c = 974 \text{ nm}$, $d = 40 \text{ nm}$, and $t_{\text{Al}_2\text{O}_3} = 90 \text{ nm}$) with empty slit (black) and after application of ODT, x -polarized (red) and y -polarized (green). (b) x -polarized spectra of a slit MPA ($c = 993 \text{ nm}$, $d = 50 \text{ nm}$, and $t_{\text{Al}_2\text{O}_3} = 90 \text{ nm}$) with empty slit (black) and after application of ODT, x -polarized (red) and y -polarized (green). (c) Spectrum of a slit MPA ($c = 930 \text{ nm}$, $d = 25 \text{ nm}$, and $t_{\text{Al}_2\text{O}_3} = 95 \text{ nm}$) before (black, y -polarized) and after application of a DNA/PBS mixture (red: y -polarized, green: x -polarized). Blue graph: Transmission spectrum of pure DNA.

the conclusion that the slits are partly filled by ODT. Even here the signal strengths are higher than expected on the basis of the simulation results (cf. Figure 5, lower part) since they exceed those for slits completely filled with PE. Yet, even if the analyte is not accumulated in the slits, the slit MPA outperforms competing plasmonic SEIRA substrate designs.^{17,29–32} The probably most basic design consists of an array of gold nanowires (“nanoantennas”) of about $1 \mu\text{m}$ lengths and being $0.1 \mu\text{m}$ diameter. In case of an end-to-end distance of the nanoantennas of 60 nm, the ODT signal in relative transmittance is about 1/3% of relative transmittance and increased to 1% if the end-to-end distance is decreased to 20 nm.¹⁷ Very recently, the signal strength was improved even further. This was reached by placing the nanoantennae on a pedestal which allows the analyte to access to the region of highest enhancement more easily and increases the signal strength from 1 to 3%,²⁴ which is still an order of magnitude lower than the signal generated in our SHA-MPA combination. Another very recent approach is given by fan-shaped gold nanoantennas on a dielectric/gold layer sequence that also exploits the perfect absorber principle for SEIRA. As a consequence of the design, very high enhancements are reached, but most probably due to a disadvantageous average enhancement (only a very small area/volume of the substrate shows the strong enhancements), only a signal increase of the relative reflectance of 0.2% could be reached.²² The signal strength is of the same order as the one also very recently reached by another perfect absorber based SEIRA substrate consisting of an array of nanoribbons.³² Compared to such particle-based nanoantennas, our slit based approach has the additional and strong advantage that slits are much less prone to fabrication errors. The reason for this lies in the fact that the maximum field enhancement is not reached at a corner of the structure, the form of which usually shows variances from individual particle to particle, but at an edge

(discussed above). This advantage is also exploited in ref 30, where nanogaps buried between two metals are used to generate SEIRA. Nevertheless, the signal in an albeit different analyte system (benzenethiol, peak at around 1475 cm^{-1}) does not exceed 0.2%. In general, we conclude that if design and accumulation are taken together, peak intensities for our SHA-MPA combination can be reached that exceed those of other SEIRA substrates by at least 1 order of magnitude.

As stated above, the slit is designed to also allow the detection of somewhat larger biomolecules. To prove this and since DNA contains a sugar–phosphate backbone, we decided to use it as a further model analyte to complete this study. As to be seen in Figure 7c, another at first unexpected enhancement of the C–H-bands (present due to the backbone-structure of DNA) occurs which goes hand in hand with an immensely broadened plasmon band. One explanation for this reproducible phenomenon would be that the crystallization of the salts in the PBS buffer (KH_2PO_4 , NaCl, and KCl) used to incubate and dry the DNA strongly increases the real part of the dielectric function of the effective medium inside the slit. If this is the reason for the broadening of the plasmon band, this effect would prove highly convenient as it would make it possible to tune the plasmon resonance wavelength and width to match the analyte bands by adding different salts with different dielectric properties to the incubation solution. The small slope in the nonresonant polarization direction can be explained by PBS crystals still being present on the surface of the substrate (despite the washing step), which scatter and thus subdue part of the signal. This scattering should also change the signal for the resonant polarization direction, but the effect is superimposed by the plasmonic resonance and therefore not observable. The extraordinarily broad plasmon band leads to the fact that the weak deformation vibration $\delta(\text{CH}_2)$ band around $6.8\ \mu\text{m}$ gets enhanced as well. The lack of N–H vibrations in the DNA/PBS spectrum of the MPA (which are present in the transmission spectrum of pure DNA, cf. Figure 7c) can be explained by the high content of thymine in the oligonucleotides used (and especially the part close to the gold surface), which has significantly less N–H than guanine, adenine, and cytosine.

Overall, we find that even with the slit widths d that can be achieved at the moment, our slit array metamaterial perfect absorber has the potential to outperform recent alternative approaches not only because of its mere performance, but also with respect to flexibility and potential. Through coating of less sensitive areas of the gold surface, the analyte is brought to selectively concentrate in the regions of highest enhancement. As a result, and in addition to refractive index sensing, our substrates provide a spectral fingerprint of analytes in the infrared spectral region strong enough to easily detect them via standard lab equipment. Most probably, the signals can be further enhanced and tuned by the addition of salts that crystallize in the slits. The crystallization strongly broadens the plasmon resonance so that the enhancement covers a large spectral region of the Mid-IR. Moreover, once smaller slit widths around 10 nm are technologically possible, the plasmon resonance can be shifted to the uninteresting spectral region between the stretching and deformation vibrations of the analytes. (N.B.: This also breaks the paradigm that the existence of a Fano-type interaction is a necessary prerequisite for surface-enhanced infrared spectroscopy!) As a consequence, the spectral fingerprints of the analytes would no longer be disturbed, while the stronger enhancement leads to the

coverage of the whole spectral region of interest. All in all, the slit array metamaterial perfect absorber has great potential as a future substitute for sensors based on the conventional excitation of surface plasmon resonances. To substitute conventional sensors is of particular interest in point-of-care analysis, due to the challenging needs for chemical sensitivity and less complex as well as more compact detection units.

METHODS

Numerical Modeling. The numerical modeling was carried out with the finite-difference time-domain (FDTD) method, as implemented in the software “FDTD solutions” from Lumerical. The FDTD method is a well-established technique to simulate the optical response of nanostructured materials.³³ It is based on the time-dependent Maxwell equations in partial differential form. To solve these, both space and time are discretized. The differentials are then estimated using central-difference approximations. The resulting equations are solved iteratively until a steady state behavior is reached. The convergence of the solutions to the exact solutions of the Maxwell equations depends on a suitable choice of the number of discretization steps and the simulation time. For our simulation, we validated convergence by letting selected simulations run with stronger discretization and longer simulation times. Selected simulations were cross-checked by modeling the structure again with the finite element method (FEM). Generally, we enforced stronger discretization within the slit and in the dielectric layer below the slit ($\Delta x = 1\text{ nm}$, $\Delta y = 5\text{ nm}$, $\Delta z = 2\text{ nm}$, where x is oriented parallel to the slit width, y to the length, and z to the depth). The residual structure was covered with an automatically generated grid by choosing Lumerical’s “high accuracy” inbuilt standard process. Due to the rectangular design of our SHA-MPA, we could also force the interfaces of the structures to coincide with the mesh. The total modeling volume was 810–1000 nm (period in x) by 1100 nm (period in y) by $11\ \mu\text{m}$ (z -direction; direction of the incoming light). To reduce calculation times, symmetry was exploited and periodic boundary conditions were applied at the x - and y -boundaries. The z -boundaries were surrounded by perfectly matched layers. For the gold layers, we used optical constants based on Johnson and Christy¹⁹ in parametrized form, as suggested by Etchegoin et al.,^{34,35} since these allowed for an overall better prediction of the experimental data than recent results for dielectric functions measured directly in the MIR^{36,37} (as a trade-off between full width at half minimum, position and value at minimum, cf. Supporting Information, Figure S2), SiO_2 and Al_2O_3 layers were modeled with built-in data from Palik.²⁰ Polyethylene (PE) was chosen as an organic analyte primarily since its optical constants in the infrared have been determined³⁸ and the bands in the spectral region of interest resemble those of one of the model analytes, namely, octadecanethiol¹⁷ and, to some extent, DNA.

Fabrication. To prepare the SHA-MPA gratings, we started with prefabricated Si chips (size $15 \times 15\text{ mm}^2$), which contain six numbered gold mirror plates with a size of $2 \times 2\text{ mm}^2$ and a gold thickness of 50 nm.³⁹

Several chips were individually coated with thin Al_2O_3 spacer films of different thicknesses $t_{\text{Al}_2\text{O}_3}$ (90, 95, and 100 nm), precisely fabricated by using atomic layer deposition (ALD) followed by the evaporation of a 50 nm thick gold layer. The gold layer was covered with a 10 nm thick SiO_2 top layer. The plasma-enhanced ALD process was performed with an OpAL-

reactor from Oxford Instruments (upgraded with an inductive-coupled plasma source). As precursors in the ALD processes, we used trimethylaluminum (TMAI) for aluminum oxide (Al_2O_3) and tris(dimethylamino)-silane (TDMAS) for silicon oxide (SiO_2). Al_2O_3 was deposited with thermal ALD, using water as second precursor. The deposition temperature was 120 °C. SiO_2 was deposited with remote oxygen plasma at a plasma pressure of 22.3 Pa. The growth rate of SiO_2 was estimated to $1.19 \pm 0.06 \text{ \AA/cycle}$, the rate of thermally deposited Al_2O_3 was $1.05 \pm 0.06 \text{ \AA/cycle}$.

The nanometer-scale slit patterns of the SHA-MPA gratings were made by shaped electron beam lithography and Ar^+ -ion beam etching. As electron beam resist the AR6200.09 from Allresist GmbH Berlin was used. The resist was spun to a thickness of 155 nm and was additionally covered with a 10 nm thick gold conduction layer made by thermal evaporation. The e-beam exposure of the six SHA-MPA gratings per chip (each with a size of $1 \times 1 \text{ mm}^2$) was performed using the shaped e-beam writer SB350 OS (50 keV, Vistec Electron Beam GmbH) at an electron dose of $400 \mu\text{C/cm}^2$. Employing this tool, the exposure time per grating was only 2.5 min.⁴⁰ The resist was developed for 60 s in AR600–546 (Allresist) and rinsed for 30 s in isopropanol (IPA). After the ion beam etching (60 s, 400 eV, 150 W, 0.5 mA/cm^2), the resist mask was removed and the surface cleaned by using an O_2 -plasma treatment (1 min, 50 W). Afterward, samples were polished with an angled ion-beam polishing to remove sidewall redeposition.

Depending on the layout size and the electron dose, SHA-MPA gratings with slit widths from 25 to 80 nm and slit lengths from 930 to 1000 nm were fabricated with a pitch of 910 nm in x -direction and 1100 nm in y -direction.

Infrared Spectroscopy. The IR reflection spectra were recorded with a Bruker Vertex 80v FT-spectrometer with an attached IR Microscope (HYPERION 2000) featuring a $15\times$ Cassegrain IR objective with 0.4 NA. The experiments were conducted with a resolution of 0.5 to 1 cm^{-1} . To polarize the incidence beam a KRS-5 polarizer was used with a spectral window from 7500 to 370 cm^{-1} . As detector, a LN-MCT detector from Bruker was employed (MCT-D316). Reflection measurements were referenced against Au mirrors. To minimize influence of ambient air, the spectrometer compartment was evacuated below 3 mbar and the microscope body and purge box were flushed with N_2 . Record mode was single-sided forward–backward sampling with Mertz and Blackman-Harris 3-term chosen for phase correction and apodization, respectively. As default, 64 spectra were averaged.

As samples were used octadecanethiol (Sigma-Aldrich, 98% purity) as well as SS150DNA oligonucleotides featuring a thiol group. In the case of octadecanethiol, the substrate was O_2 -plasma cleaned to remove any adhered organic contaminants to the surface before immersing the samples in $20 \mu\text{L}$ of 1:10 diluted saturated ODT + ethanol solution. After 40 min, the chips were cleaned with rinsing in running EtOH (4 s) before submersing in pure EtOH for 40 min. Drying was done by pressurized N_2 (5 s, until EtOH was completely evaporated).

For DNA measurements, DNA (100 μmolar concentration; TTTTTCAGCATGTGCTCCTTGATTCTATG with thiol group, from Eurofins) was diluted 1:10 in $5\times$ PBS buffer and the chip was covered with $20 \mu\text{L}$ of solution left to dry overnight (15 h), resulting in filled slits. Subsequently, the chips were rinsed for 20 s in deionized water to remove salt crystals formed by the PBS on the surface before drying in nitrogen gas and measurement.

Fluorescence Spectroscopy. For fluorescence imaging an ELYRA SIM (structured illumination microscope) was used with 488 nm laser excitation and a 520 nm filter for fluorescence light. The fluorophore (SAMSA fluoresceine A-685 from life-technologies) was sensitive at 495 nm and emission wavelength was 520 nm. The thiol group contained in this fluorophore was activated as by the manufacturer's instructions and drop-dried on the structure. Afterward, the chips were rinsed to remove nonbound fluorophore. Samples were then immersed in index-matching oil, covered with a cover slide and topped with more oil to prevent contamination. A $63\times$ objective with 1.4 NA was used to record the images shown in Figure 1. Data processing was automatically done by the Zen Software for the ELYRA microscope. Afterward, a Fourier-transformation was performed, giving an indication of the bridges between the slits in y -direction by showing a periodic signal. To avoid negative effects by of the oil used, other samples were also examined on a standard fluorescence microscope with $100\times$ objective (0.9 NA) made by Zeiss.

■ ASSOCIATED CONTENT

Supporting Information

The Supporting Information is available free of charge on the ACS Publications website at DOI: [10.1021/acsp Photonics.5b00321](https://doi.org/10.1021/acsp Photonics.5b00321).

Tuning of resonance wavelength, figure of merit, influence of the dielectric function of gold (PDF).

Movie S1. Simulated electric field changes of a slit MPA with $a = 910 \text{ nm}$, $b = 1100 \text{ nm}$, $c = 1000 \text{ nm}$, $d = 50 \text{ nm}$ and $t_{\text{Al}_2\text{O}_3} = 90 \text{ nm}$ (x -polarized, slit empty) in the spectral range of the main resonance (light pulse duration: 500 fs, center wavelength $3.35 \mu\text{m}$, overall length of the simulation: 1500 fs). a) View direction along $-z$, visible plane at $z = 0$ (interface between Al_2O_3 -layer and structured gold layer) (AVI). b) View direction along y -axis, visible plane at $y = 0$ (center of the slit) (AVI) c) View direction along x -axis, visible plane at $x = 0$ (center of the slit) (AVI)

Movie S2. Simulated electric field changes of a slit MPA with $a = 910 \text{ nm}$, $b = 1100 \text{ nm}$, $c = 1000 \text{ nm}$, $d = 50 \text{ nm}$ and $t_{\text{Al}_2\text{O}_3} = 90 \text{ nm}$ (y -polarized, slit empty) in the spectral range of the main resonance (light pulse duration: 500 fs, center wavelength $3.35 \mu\text{m}$, overall length of the simulation: 1500 fs). a) View direction along $-z$, visible plane at $z = 0$ (interface between Al_2O_3 -layer and structured gold layer) (AVI) b) View direction along y -axis, visible plane at $y = 0$ (center of the slit) (AVI) c) View direction along x -axis, visible plane at $x = 0$ (center of the slit) (AVI).

Movie S3. Simulated electric field changes of a slit MPA with $a = 910 \text{ nm}$, $b = 1100 \text{ nm}$, $c = 1000 \text{ nm}$, $d = 50 \text{ nm}$ and $t_{\text{Al}_2\text{O}_3} = 90 \text{ nm}$ (x -polarized, slit empty) in the spectral range of the main resonance (light pulse duration: 500 fs, center wavelength $6 \mu\text{m}$, overall length of the simulation: 1500 fs). a) View direction along $-z$, visible plane at $z = 0$ (interface between Al_2O_3 -layer and structured gold layer) (AVI) b) View direction along y -axis, visible plane at $y = 0$ (center of the slit) (AVI) c) View direction along x -axis, visible plane at $x = 0$ (center of the slit) (AVI).

■ AUTHOR INFORMATION

Corresponding Author

*E-mail: thomas.mayerhoefer@ipht-jena.de.

Notes

The authors declare no competing financial interest.

■ ACKNOWLEDGMENTS

Funding of the research projects “Jenaer Biochip Initiative 2.0” (03IPT513Y) within the framework “Unternehmen Region – InnoProfile Transfer” supported by the Federal Ministry of Education and Research, Germany (BMBF) and “PhoNa - Photonic Nanomaterials” (03IS2101A) supported by the German Federal Ministry of Education and by the Thuringian Ministry for Education, Science, and Culture is gratefully acknowledged. For the recording of the SIM-FLOUR image, we are deeply grateful to Martin Kielhorn and Rainer Heintzmann. For assistance in the preparation of the substrate, we are much obliged to the following colleagues: Hermann Roth (e-beam), Katrin Pippardt (resist and lithography), Birger Steinbach (evaporation), Katrin Kandra (ion beam etching), and Mario Ziegler (ALD).

■ REFERENCES

- (1) Watts, C. M.; Liu, X.; Padilla, W. J. Metamaterial electromagnetic wave absorbers. *Adv. Mater.* **2012**, *24*, 98–120.
- (2) Liu, N.; Mesch, M.; Weiss, T.; Hentschel, M.; Giessen, H. Infrared perfect absorber and its application as plasmonic sensor. *Nano Lett.* **2010**, *10*, 2342–8.
- (3) Song, Y.; Wang, C.; Lou, Y.; Cao, B.; Li, X. Near-perfect absorber with ultrawide bandwidth in infrared region using a periodically chirped structure. *Opt. Commun.* **2013**, *305*, 212–216.
- (4) Wu, C.; Shvets, G. Design of metamaterial surfaces with broadband absorbance. *Opt. Lett.* **2012**, *37*, 308–310.
- (5) Hendrickson, J.; Guo, J. P.; Zhang, B. Y.; Buchwald, W.; Soref, R. Wideband perfect light absorber at midwave infrared using multiplexed metal structures. *Opt. Lett.* **2012**, *37*, 371–373.
- (6) Bouchon, P.; Koechlin, C.; Pardo, F.; Haidar, R.; Pelouard, J. L. Wideband omnidirectional infrared absorber with a patchwork of plasmonic nanoantennas. *Opt. Lett.* **2012**, *37*, 1038–40.
- (7) Liu, Y.; Gu, S.; Luo, C.; Zhao, X. Ultra-thin broadband metamaterial absorber. *Appl. Phys. A: Mater. Sci. Process.* **2012**, *108*, 19–24.
- (8) Li, Y.; Su, L.; Shou, C.; Yu, C.; Deng, J.; Fang, Y. Surface-enhanced molecular spectroscopy (SEMS) based on perfect-absorber metamaterials in the mid-infrared. *Sci. Rep.* **2013**, *3*, 2865.
- (9) Grant, J.; Ma, Y.; Saha, S.; Khalid, A.; Cumming, D. R. Polarization insensitive, broadband terahertz metamaterial absorber. *Opt. Lett.* **2011**, *36*, 3476–8.
- (10) Aydin, K.; Ferry, V. E.; Briggs, R. M.; Atwater, H. A. Broadband polarization-independent resonant light absorption using ultrathin plasmonic super absorbers. *Nat. Commun.* **2011**, *2*, 517.
- (11) Feng, R.; Ding, W.; Liu, L.; Chen, L.; Qiu, J.; Chen, G. Dual-band infrared perfect absorber based on asymmetric T-shaped plasmonic array. *Opt. Express* **2014**, *22*, A335.
- (12) Xiong, X.; Xue, Z.-H.; Meng, C.; Jiang, S.-C.; Hu, Y.-H.; Peng, R.-W.; Wang, M. Polarization-dependent perfect absorbers/reflectors based on a three-dimensional metamaterial. *Phys. Rev. B: Condens. Matter Mater. Phys.* **2013**, *88*.10.1103/PhysRevB.88.115105
- (13) Hu, C.; Zhao, Z.; Chen, X.; Luo, X. Realizing near-perfect absorption at visible frequencies. *Opt. Express* **2009**, *17*, 11039–11044.
- (14) Fang, Z.; Zhen, Y.-R.; Fan, L.; Zhu, X.; Nordlander, P. Tunable wide-angle plasmonic perfect absorber at visible frequencies. *Phys. Rev. B: Condens. Matter Mater. Phys.* **2012**, *85*.10.1103/PhysRevB.85.245401
- (15) Limaj, O.; D’Apuzzo, F.; Di Gaspare, A.; Giliberti, V.; Domenici, F.; Sennato, S.; Bordi, F.; Lupi, S.; Ortolani, M. Mid-Infrared Surface Plasmon Polariton Sensors Resonant with the Vibrational Modes of Phospholipid Layers. *J. Phys. Chem. C* **2013**, *117*, 19119–19126.
- (16) Weber, D.; Albella, P.; Alonso-Gonzalez, P.; Neubrech, F.; Gui, H.; Nagao, T.; Hillenbrand, R.; Aizpurua, J.; Pucci, A. Longitudinal and transverse coupling in infrared gold nanoantenna arrays: long range versus short range interaction regimes. *Opt. Express* **2011**, *19*, 15047–15061.
- (17) Pucci, A.; Neubrech, F.; Weber, D.; Hong, S.; Toury, T.; de la Chapelle, M. L. Surface enhanced infrared spectroscopy using gold nanoantennas. *Phys. Status Solidi B* **2010**, *247*, 2071–2074.
- (18) Neubrech, F.; Weber, D.; Katzmann, J.; Huck, C.; Toma, A.; Di Fabrizio, E.; Pucci, A.; Hartling, T. Infrared optical properties of nanoantenna dimers with photochemically narrowed gaps in the 5 nm regime. *ACS Nano* **2012**, *6*, 7326–32.
- (19) Johnson, P. B.; Christy, R. W. Optical Constants of the Noble Metals. *Phys. Rev. B* **1972**, *6*, 4370–4379.
- (20) Palik, E. D. *Handbook of Optical Constants of Solids, Five-Vol. Set: Handbook of Thermo-Optic Coefficients of Optical Materials with Applications*; Elsevier Science: New York, 1997.
- (21) Adato, R.; Altug, H. In-situ ultra-sensitive infrared absorption spectroscopy of biomolecule interactions in real time with plasmonic nanoantennas. *Nat. Commun.* **2013**, *4*, 2154.
- (22) Aksu, S.; Cetin, A. E.; Adato, R.; Altug, H. Plasmonically Enhanced Vibrational Biospectroscopy Using Low-Cost Infrared Antenna Arrays by Nanostencil Lithography. *Adv. Opt. Mater.* **2013**, *1*, 798–803.
- (23) Bochterle, J.; Neubrech, F.; Nagao, T.; Pucci, A. Angstrom-Scale Distance Dependence of Antenna-Enhanced Vibrational Signals. *ACS Nano* **2012**, *6*, 10917–10923.
- (24) Brown, L. V.; Zhao, K.; King, N.; Sobhani, H.; Nordlander, P.; Halas, N. J. Surface-enhanced infrared absorption using individual cross antennas tailored to chemical moieties. *J. Am. Chem. Soc.* **2013**, *135*, 3688–95.
- (25) Huck, C.; Neubrech, F.; Vogt, J.; Toma, A.; Gerbert, D.; Katzmann, J.; Härtling, T.; Pucci, A. Surface-Enhanced Infrared Spectroscopy Using Nanometer-Sized Gaps. *ACS Nano* **2014**, *8*, 4908–4914.
- (26) Kusa, F.; Ashihara, S. Spectral response of localized surface plasmon in resonance with mid-infrared light. *J. Appl. Phys.* **2014**, *116*.15310310.1063/1.4898316
- (27) Liberman, V.; Adato, R.; Mertiri, A.; Yanik, A. A.; Chen, K.; Jeys, T. H.; Erramilli, S.; Altug, H. Angle- and polarization-dependent collective excitation of plasmonic nanoarrays for surface enhanced infrared spectroscopy. *Opt. Express* **2011**, *19*, 11202–11212.
- (28) Neubrech, F.; Beck, S.; Glaser, T.; Hentschel, M.; Giessen, H.; Pucci, A. Spatial Extent of Plasmonic Enhancement of Vibrational Signals in the Infrared. *ACS Nano* **2014**, *8*, 6250–6258.
- (29) Brown, L. V.; Yang, X.; Zhao, K.; Zheng, B. Y.; Nordlander, P.; Halas, N. J. Fan-Shaped Gold Nanoantennas above Reflective Substrates for Surface-Enhanced Infrared Absorption (SEIRA). *Nano Lett.* **2015**, *15*, 1272–80.
- (30) Chen, X.; Ciraci, C.; Smith, D. R.; Oh, S. H. Nanogap-enhanced infrared spectroscopy with template-stripped wafer-scale arrays of buried plasmonic cavities. *Nano Lett.* **2015**, *15*, 107–13.
- (31) Huck, C.; Toma, A.; Neubrech, F.; Chirumamilla, M.; Vogt, J.; De Angelis, F.; Pucci, A. Gold Nanoantennas on a Pedestal for Plasmonic Enhancement in the Infrared. *ACS Photonics* **2015**, *2*, 497–505.
- (32) Ishikawa, A.; Tanaka, T. Metamaterial Absorbers for Infrared Detection of Molecular Self-Assembled Monolayers. *Sci. Rep.* **2015**, *5*, 12570.
- (33) Bondeson, A.; Rylander, T.; Ingelström, P. *Computational Electromagnetics*; Springer: New York, 2005.
- (34) Etchegoin, P. G.; Le Ru, E. C.; Meyer, M. An analytic model for the optical properties of gold. *J. Chem. Phys.* **2006**, *125*, 164705.
- (35) Etchegoin, P. G.; Le Ru, E. C.; Meyer, M. Erratum: “An analytic model for the optical properties of gold. *J. Chem. Phys.* **2006**, *125*, 164705; *J. Chem. Phys.* **2007**, *127*, 189901.

(36) Olmon, R. L.; Slovick, B.; Johnson, T. W.; Shelton, D.; Oh, S. H.; Boreman, G. D.; Raschke, M. B., Optical dielectric function of gold. *Phys. Rev. B: Condens. Matter Mater. Phys.* **2012**, *86*, [10.1103/PhysRevB.86.235147](https://doi.org/10.1103/PhysRevB.86.235147)

(37) Trollmann, J.; Pucci, A. Infrared Dielectric Function of Gold Films in Relation to Their Morphology. *J. Phys. Chem. C* **2014**, *118*, 15011–15018.

(38) Zolotarev, V. M.; Volchek, B. Z.; Vlasova, E. N. Optical constants of industrial polymers in the IR region. *Opt. Spectrosc.* **2006**, *101*, 716–723.

(39) Huebner, U.; Pshenay-Severin, E.; Alaei, R.; Menzel, C.; Ziegler, M.; Rockstuhl, C.; Lederer, F.; Pertsch, T.; Meyer, H.-G.; Popp, J. Exploiting extreme coupling to realize a metamaterial perfect absorber. *Microelectron. Eng.* **2013**, *111*, 110–113.

(40) Huebner, U.; Falkner, M.; Zeitner, U. D.; Banasch, M.; Dietrich, K.; Kley, E.-B. Multi-stencil character projection e-beam lithography: a fast and flexible way for high quality optical metamaterials. 30th European Mask and Lithography Conference, Dresden, Germany, June 24, 2014, SPIE: Bellingham WA, 20149231; [10.1117/12.2065944](https://doi.org/10.1117/12.2065944)

6.1.2 Plasmonic nanostructures for surface enhanced spectroscopic methods [P2]

Jahn, Martin; Patze, Sophie; Hidi, Izabella Jolan; **Knipper, Richard**; Radu, Andreea; Mühlig, Anna; Yüksel, Sezin; Peksa, Vlastimil; Weber, Karina; Mayerhöfer, Thomas G.; Cialla-May, Dana; Popp, Jürgen *Plasmonic nanostructures for surface enhanced spectroscopic methods*, Analyst (2016), 141, pp 756 , DOI: 10.1039/C5AN02057C

Reproduced by permission of The Royal Society of Chemistry.

Cite this: *Analyst*, 2016, **141**, 756

Plasmonic nanostructures for surface enhanced spectroscopic methods

Martin Jahn,^{a,b} Sophie Patze,^{a,b} Izabella J. Hidi,^{a,b} Richard Knipper,^{a,b} Andreea I. Radu,^{a,b} Anna Mühlig,^{a,b} Sezin Yüksel,^{a,b} Vlastimil Peksa,^c Karina Weber,^{a,b} Thomas Mayerhöfer,^{a,b} Dana Cialla-May^{*a,b} and Jürgen Popp^{a,b}

A comprehensive review of theoretical approaches to simulate plasmonic-active metallic nano-arrangements is given. Further, various fabrication methods based on bottom-up, self-organization and top-down techniques are introduced. Here, analytical approaches are discussed to investigate the optical properties of isotropic and non-magnetic spherical or spheroidal particles. Furthermore, numerical methods are introduced to research complex shaped structures. A huge variety of fabrication methods are reviewed, e.g. bottom-up preparation strategies for plasmonic nanostructures to generate metal colloids and core-shell particles as well as complex-shaped structures, self-organization as well as template-based methods and finally, top-down processes, e.g. electron beam lithography and its variants as well as nanoimprinting. The review article is aimed at beginners in the field of surface enhanced spectroscopy (SES) techniques and readers who have a general interest in theoretical modelling of plasmonic substrates for SES applications as well as in the fabrication of the desired structures based on methods of the current state of the art.

Received 6th October 2015,
Accepted 23rd December 2015

DOI: 10.1039/c5an02057c

www.rsc.org/analyst

^aInstitute of Physical Chemistry and Abbe Center of Photonics, Friedrich Schiller University Jena, Helmholtzweg 4, 07743 Jena, Germany.

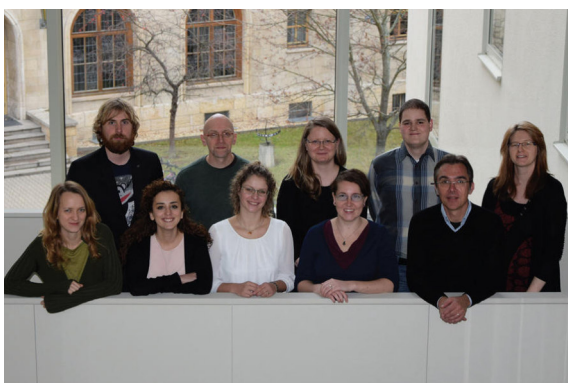
E-mail: dana.cialla-may@uni-jena.de

^bLeibniz Institute of Photonics Technology (IPHT), Albert-Einstein-Strasse 9, 07745 Jena, Germany

^cInstitute of Physics, Charles University in Prague, Ke Karlovu 5, 121 16 Prague 2, Czech Republic

1. Introduction

Metallic nanostructures are known to show interesting optical properties within the electromagnetic spectrum from UV to the MIR spectral region. As an example, they are utilized to enhance the optical signal in fluorescence, Raman and IR



From left to right: Andreea I. Radu, Richard Knipper, Sezin Yüksel, Thomas Mayerhöfer, Sophie Patze, Dana Cialla-May, Izabella Hidi, Martin Jahn, Jürgen Popp, Karina Weber

The research group Jena Biochip initiative (JBCI), embedded within the research group of Prof. Dr Jürgen Popp, is headed by Dr Karina Weber and Dr Dana Cialla-May. The objective of JBCI is

the research and establishment of novel chip-based detection methods for biomolecules and pathogens that are based on specific metal deposition reactions as well as the application of innovative plasmonic active metallic nanostructures in bioanalytics. As an example, surface enhanced spectroscopic methods such as SERS are in focus. The JBCI group works on the fabrication and characterization of powerful SERS substrates achieved by bottom-up and top-down methods. By combining SERS with microfluidics, SERS measurements in high throughput and under reproducible conditions are performed by JBCI addressing analytical questions in therapeutic drug monitoring, pathogen diagnostics and the detection of ecological harmful substances. Additionally, SERS is applied in food and environmentally relevant detection schemes by the group. Moreover, the research group deals with the simulation, fabrication and characterization of SEIRA substrates. Finally, the sample preparation is an important research topic of JBCI e.g. extraction and amplification. Thus, the entire analysis chain is covered by JBCI to address the needs of modern bioanalytics.

Analyst

spectroscopies. In the Late Antiquity period the optical properties of gold nanoparticles were employed for coloring glass and artworks, evidently without knowledge about the physical phenomenon arising from nanometer-scaled metallic particles. The Late Roman Lycurgus Cup, which appears red when illuminated from behind and, in contrast, green when illuminated from the front, is one of the most prominent representatives of the optical effect of gold nanoparticles in artworks.^{1,2}

In the 19th century, Michael Faraday described for the first time the preparation of gold nanoparticles as well as their intense red-violet color as a function of the particles.^{3,4} Today, it is commonly known that the underlying phenomenon is attributed to the excitation of localized surface plasmon resonances based on the collective oscillation of the electron cloud within the metal nanoparticle.⁵ An analytical solution of Maxwell's equations for the scattering of an electromagnetic wave by a metallic sphere was presented in 1908 by Gustav Mie.^{2,6} These findings provided the basis for the research on plasmonic effects of metallic nanoparticles as well as their applications in a variety of application fields *e.g.* chemical analysis and catalysis,^{7–9} detection of biomolecules,^{10–12} medicine (diagnosis, imaging and therapy),^{7,9,13,14} detection of pollution and heavy metal ions,¹⁵ small inorganic compounds,¹⁶ food analysis investigating food additives and contaminations¹⁷ and, as recently summarized, ultrafast optical processes.¹⁸

In section 2, the interaction of light with metallic nanostructures based on the excitation of surface plasmon polariton modes, field enhancement as well as various types of surface enhanced spectroscopic (SES) techniques will be introduced. The focus of this review article is the optical simulation and fabrication of nanostructures which are utilized in SES techniques. Therefore, in section 3, the simulation of the optical properties of metallic nanostructures is described in detail. Here, a variety of nanoparticle structures and arrangements of nanostructures are introduced. To prepare the exceptionally designed nanostructures as well as arrays, various bottom-up, top-down and self-organization methods are available. Thus, in sections 4, 5 and 6, we introduce these fabrication methods in the order of increasing complexity. As a consequence, the interested reader will get a comprehensive overview of the fabrication routines of plasmonic nanostructures to accomplish the desired optical concept.

2. Theoretical background

Due to the interaction of light with metallic nanoparticles, surface plasmon resonances are excited and, as a consequence, a strong electromagnetic field is induced on the metallic surface. This resonant excitation composed of the oscillation of electrons in metallic nanoparticles and their related local field enhancement is known as localized surface plasmon polariton (LSPP).⁵ Its physical concept is depicted in Fig. 1A. Here, the metal nanoparticle acts as a dipole antenna and emits light according to the characteristic of a Hertzian dipole. The spectral position of the plasmon resonance is defined by

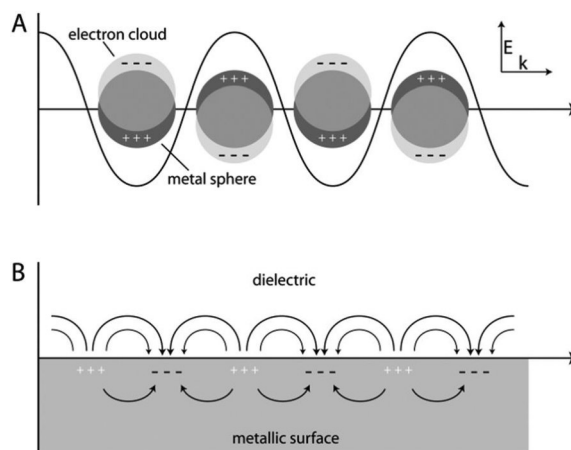


Fig. 1 Schematic illustration of (A) localized and (B) propagating surface plasmon polaritons. E depicts the electric field vector and k the wave vector.

the plasmon resonance condition ($\text{Re}(\epsilon_i) \approx -2\epsilon_a$; $\text{Im}(\epsilon_i) \ll 1$; $\text{Re}(\epsilon_i)$ – real part of the dielectric constant of the metal; $\text{Im}(\epsilon_a)$ – imaginary part of the dielectric constant of the surrounding medium).¹⁹ It is tunable by changing the surrounding medium as well as the size, shape and material of the nanoparticles.^{20,21} In the case of planar metal surfaces, propagating surface plasmon polariton (PSPP) modes are found at boundaries between the dielectric and metal conductors.⁵ This is illustrated in Fig. 1B. However, an excitation of the PSPP mode at a smooth metallic surface is only possible if the k vector of the incoming light is parallel to the surface.²² Thus, the so-called Kretschmann or Otto configurations, which are based on the concept of the attenuated total reflection, have to be applied. The strong dependency of the surface plasmon resonance on changes of the refractive index in the close vicinity of a planar metal surface is used in bioanalytics by SPR sensors.^{23,24} Micro- and nanostructuring of the metallic surface enable the excitation of PSPP modes by electromagnetic waves with the k vector with a non-parallel orientation to the surface.²² Here, the spectral position of the PSPP mode is defined by the incidence angle of light and the grating constant of the periodically structured surface (grating coupling). The patterning of metallic surfaces enables PSPP modes, which are accompanied by near-field enhancements of the electric field E .

By using these effects, various application fields in ultra-sensitive analytics open up. Accordingly, the electromagnetic field enhancement is applied for enhancing the Raman cross-section (surface enhanced Raman spectroscopy, SERS),^{25–27} fluorescence (surface enhanced fluorescence, SEF),^{28–31} as well as the IR absorption (surface enhanced infra-red absorption, SEIRA).^{32,33}

2.1 Surface-enhanced Raman spectroscopy (SERS)

The SERS effect was first discovered in the 70s of the last century when the Raman signal of the pyridine adsorbed on roughened silver electrodes was investigated.^{34–36} Due to the

high sensitivity and molecular specificity, the SERS technique became a powerful tool in chemical, biochemical and biological application fields.^{10,37,38} SERS is applied as a diagnostic and imaging tool in medicine, e.g. immuno assays employing SERS tags, for research on the interaction of metallic nanoparticles with cells,^{7,9,13,14,39} for the investigation of catalytic reactions at plasmonic active surfaces,⁷⁻⁹ to detect environmental pollution^{15,40} and to investigate food additives and contaminations.¹⁷ By combining SERS with microfluidic devices, high throughput measurements under reproducible conditions are available.⁴¹⁻⁴³ In order to describe the enhancing mechanism in SERS, two contributions are discussed: the electromagnetic as well as the chemical enhancement. The main contribution to the SERS signal is based on the electromagnetic mechanism, which is described in the following paragraphs.

Surface plasmon polaritons can be excited in nanostructured metallic surfaces or metallic nanoparticles if the wavelength of the incident light meets the plasmon resonance condition.¹⁹ As a result, a strong electromagnetic field with an evanescent character is induced on the metallic nanostructure. Since the plasmon resonance has to overlap with the excitation wavelength applied in the SERS experiment, silver, gold and copper are preferentially used in the visible and NIR spectral ranges, and aluminum, ruthenium, rhodium, palladium and platinum in the UV region.^{44,45} As a consequence, the Raman modes of a molecule which is located in close vicinity to the nanostructure are enhanced since the Raman intensity is proportional to the squared incident electromagnetic field intensity. Based on the characteristics of a Hertzian dipole, the Raman scattered light is emitted – summarized over all orientations of the molecule – in all spatial directions. It is collected and detected according to the aperture of the microscope objective. In addition, the Raman scattered light undergoes a further enhancement if the Raman mode also overlaps with the plasmon resonance. In the literature, this phenomenon is named emission enhancement or the second part of the electromagnetic mechanism and has been investigated theoretically^{46,47} as well as experimentally.⁴⁸⁻⁵⁰ As a consequence, Raman modes next to the plasmon resonance are the most intense.

The overall electromagnetic enhancement factor G shows a fourth-power dependency and is defined as follows:^{48,50-52}

$$G = M_{\text{Loc}}(\omega_{\text{L}})M_{\text{Loc}}(\omega_{\text{R}}) = \frac{|E_{\text{Loc}}(\omega_{\text{L}})|^2 |E_{\text{Loc}}(\omega_{\text{R}})|^2}{|E_0(\omega_{\text{L}})|^2 |E_0(\omega_{\text{R}})|^2} \quad (2.1.1)$$

$$\approx \frac{|E_{\text{Loc}}(\omega_{\text{L}})|^2 |E_{\text{Loc}}(\omega_{\text{R}})|^2}{|E_0|^4}$$

with M_{Loc} being the local field enhancement at the laser excitation frequency (ω_{L}) and the frequency of the Raman mode (ω_{R}). Moreover, E_{Loc} is defined as a locally enhanced electromagnetic field and E_0 is the electromagnetic field of the incident laser light. Based on theoretical considerations, the influences of shape, size, material and interparticle distances of nanoparticles on the SERS enhancement factor are investigated.⁵³ Here, the maximum electromagnetic enhancement factor under SERS conditions is theoretically estimated to be 10^{11} .

The chemical mechanism, which contributes to the overall SERS enhancement by a factor of 10^1 to 10^3 , is understood as the sum of various contributions: (1) signal enhancement based on chemical interactions between a molecule and a nanoparticle in the ground state, (2) SERS enhancement due to resonant excitation of charge transfer processes between a nanoparticle and a molecule and (3) resonance Raman enhancement based on the excitation of an electronic transfer within the molecule.⁵⁴

When comparing SERS and Raman spectra, spectroscopically forbidden Raman modes are observable under SERS conditions. In 1988, the variation in spectroscopic selection rules based on field gradients in optical tweezers had already been discussed; however, without giving an experimental proof.⁵⁵ As already mentioned, the electromagnetic field, which is induced on the surface of the metallic nanoparticle, shows an evanescent character and, thus, the molecules of interest in the close vicinity of the surface are strongly affected by the field gradient. This leads to a breakdown of the conventional selection rules applied for Raman spectroscopy.⁵⁶ Observations of spectroscopically forbidden Raman modes within the SERS spectrum under near-field conditions are established and referred to as the field gradient Raman effect.⁵⁷ Moreover, forbidden electronic transitions, induced by the field gradient effect, are observable in the form of resonance Raman bands in the SERS spectra of carbon nanotubes.⁵⁸

The changes in Raman intensities of various modes within the SERS spectrum are discussed based on surface selection rules.⁵⁹⁻⁶¹ A molecule is characterized by its Raman tensor and the orientation relative to the metallic surface. The enhancement of various Raman active modes is dependent on field components parallel and perpendicular relative to the surface. Due to the dominance of the Raman tensor diagonal component over the Cartesian coordinate parallel to the surface normal, only vibrations with a dynamic dipole perpendicular to the surface will be observed. Raman modes, which are oriented parallel to the metal surface, are – if at all – detected with very weak intensity.

Another important parameter with respect to the interaction of plasmon modes with molecular excitonic resonances is the so-called coupling rate. This depends on the oscillator strength of the molecular resonance and the mode volume of the confined fields. If the coupling rate approaches the dephasing rate of the two resonances the approximation of weak coupling, in which both resonances are treated independently, is no longer valid. This means, energy is coherently exchanged between the plasmon and the exciton and, hence, hybridized resonances are formed. This transition from the weak- to the strong-coupling regime can be observed experimentally in the form of the so-called Rabi splitting and Fano-like resonances in the scattering spectrum.⁵⁶

2.2 Surface-enhanced fluorescence (SEF)

The detection of fluorescence is one of the most common techniques for assays utilized in drug detection, high-throughput screening or cellular imaging. The sensitivity of fluorescence

Analyst

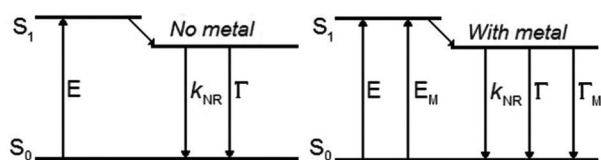


Fig. 2 Jablonski diagram for inclusion of metal–fluorophore interactions (modified from Hao *et al.*⁷³).

to the local environment due to chemical interactions can be used to monitor for example pH changes, viscosity or local polarity. In order to increase the intensity of fluorescence, the most fundamental property of a fluorophore, its radiative decay rate, has to be changed. This rate can be changed by modifying the photonic mode density around the fluorophore by positioning it in the proximity of a metal surface or particle. A 1000-fold fluorescence enhancement near a metal particle had been theoretically predicted already in 1981,⁶² which was later experimentally confirmed.^{63,64} In several studies, the application of SEF in (bio)analytics is introduced. As an example, dual-mode SERS-fluorescence nanoparticle arrangements are employed among others for the detection of markers on cells.⁶⁵ Further on, SEF is a promising detection tool in immunoassays⁶⁶ to detect the toxin microcystin-LR⁶⁷ or the tumor marker carcinoembryonic antigen.⁶⁸ SEF is additionally applied to detect mercury ions relevant in environmental science.⁶⁹ Finally, the potential of the SEF method is illustrated by an antenna-in-box device, which can be utilized for single-molecule experiments at physiologically relevant concentrations.⁷⁰

To understand the fluorescence enhancement in close proximity to metal surfaces, first the processes related to fluorescence will be briefly described. Fig. 2 shows the basic excitation and emission processes in molecules. A molecule is excited by absorbing a photon (E). Then the molecule swiftly relaxes to the excited state S_1 , from which it drops back to the ground state S_0 either by radiating a photon (Γ) or by any form of non-radiative process (k_{NR}). The average time a molecule stays in the excited state is described as its lifetime τ_0 .

$$\tau_0 = \frac{1}{\Gamma + k_{NR}} \quad (2.2.1)$$

The fluorescence quantum yield Q_0 is defined in general as the ratio between radiative decay and total decay, or, in other words, the ratio between the number of emitted and absorbed photons.

$$Q_0 = \frac{\Gamma}{\Gamma + k_{NR}} \quad (2.2.2)$$

Both the lifetime and quantum yield can be strongly affected by the surrounding environment. A very significant change occurs in the proximity of a metal surface. One effect is the enhancement of the local field (E_M) by the interaction with the surface plasmons. Another effect is the increase of the radiative decay rate by including the metal-induced radiative

rate Γ_M . This leads to the following modifications of eqn (2.2.1) and (2.2.2) for the lifetime τ_M and quantum yield Q_M :

$$\tau_M = \frac{1}{\Gamma + \Gamma_M + k_{NR}} \quad (2.2.3)$$

$$Q_M = \frac{\Gamma + \Gamma_M}{\Gamma + \Gamma_M + k_{NR}} \quad (2.2.4)$$

A more detailed theoretical description is given in the literature.³¹ With an increase of Γ_M the lifetime decreases and the quantum yield increases. Since the maximum number of photons per second emitted by a molecule is roughly proportional to the inverse of the lifetime, a shorter lifetime leads to a higher photon flux, especially with a higher illumination intensity. Additionally, the reduced lifetime of the excited state increases the fluorophore photostability. In order to achieve the maximum possible enhancement it is desirable to achieve an overlap between the fluorophore emission wavelength and the surface plasmon resonance of the metallic structure.

Moreover, the interspace between a fluorophore and the metal surface is very important. In the case of very small gaps (<2–3 nm), the fluorescence is quenched due to energy transfer to the metal surface. The optimal distance for fluorophores from a surface is still a subject of discussion, but it generally ranges between 5 nm (ref. 71) and 20 nm,⁷² with most of the research studies agreeing on a displacement of around 10 nm.^{28,30,73,74} However, the surface enhancement of fluorescence has already been reported for silver nanoparticle aggregates with an interparticle distance of only 1–2 nm.⁶⁴ In such narrow gap regions the local electromagnetic fields seem to be strong enough in order to enhance the fluorescence signal despite the quenching processes. The spacing between a metal surface and a fluorophore is usually achieved by a non-conductive layer with a defined thickness, *e.g.* composed of Al_2O_3 ,⁷³ SiO_2 ⁷² or DNA strands.²⁸ Another important effect, which influences the total fluorescence enhancement, is the possibility of non-radiative emission directly into the metal.⁶⁴ This additional decay pathway, in combination with the increased radiative decay rate, can lead to the breakdown of the general molecular electronic dynamics.⁵⁶ When the total enhanced decay rate equals the vibrational relaxation rate, or exceeds it, direct emission from the excited vibrational states in S_1 cannot be neglected anymore. The nature of this emission, again, can be radiative as well as non-radiative. In the latter case, an anomalous ratio between the intensities of SERS and SEF signals is observable. If the radiative decay is dominating, the shape of the fluorescence spectrum is changed and it becomes blue-shifted relative to the spectrum of a free space molecule. A comprehensive overview of this so-called fast-dynamics SEF can be found elsewhere.⁵⁶

Further on, metal surfaces are also utilized for studying the Förster Resonance Energy Transfer (FRET) between molecules. This is based on a dipole–dipole interaction between a donor and an acceptor molecule. This interaction is strongly dependent on the distance between the molecules, and it has been proven that the presence of metallic surfaces can increase the

strength of donor–acceptor interactions, and therefore increase the Förster distance, which is defined as the distance at which the FRET is 50% effective, by up to 75%.⁷⁵

2.3 Surface-enhanced infrared absorption (SEIRA)

SEIRA and SERS share the same mechanism of an electromagnetic enhancement model. Therefore, SEIRA also depends on analyte–surface structure interactions to couple incident light into plasmon resonances, as it is described for the SERS mechanism. The enhancement of absorption bands between 2850 cm⁻¹ and 2960 cm⁻¹ was demonstrated first by Hartstein *et al.*⁷⁶ in a metal-on-analyte-setup and also in an analyte-on-metal-configuration, called the metal under/overlay geometry, and later proved by Hatta *et al.*⁷⁷ Results and advances in the emerging field of SEIRA are comprehensively reviewed.^{78,79} Recently, several studies reported on SEIRA application fields, *e.g.* the detection of protein monolayers,⁸⁰ an investigation of the chemical interaction between recognition proteins with target antibodies⁸¹ as well as research on few nm thick organic layers.^{82–84} Moreover, biolabels based on SEIRA active fluorophore–antibody nanoconjugates are described as promising tools in fast, reliable and multiplexed screening.⁸⁵

A significant difference of SEIRA in contrast to SERS is the different frequency range, and thus the application of different metals as an enhancing medium. In SERS, silver, gold and copper for the visible and NIR spectral regions and aluminum, rhodium, ruthenium, palladium and platinum for the UV region are preferentially used as plasmonic materials. For the infrared range of SEIRA, the plasmon resonance condition ($|\text{Re}(e)| \gg \text{Im}(e)$), and with this the excitation of plasmon polariton modes, is fulfilled additionally for the metals indium, protactinium, nickel and lead. However, since copper, indium and aluminum tarnish fast and feature low enhancement, not much attention has been paid to these materials.

Relying on the same surface enhancement effect as SERS, the surface selection rules already known are applied as well. Namely, away from the plasmon frequency only dipole changes normal to the surface result in enhanced absorption bands. The short-ranged enhancement model was also proven for SEIRA,^{86–88} where Langmuir Blodgett spacer films support the distance relationship for the enhancement to be

$$|E_{\text{loc}}|^2 = \frac{4p^2}{d^6} \quad (2.3.1)$$

with $p = \alpha VE$ being the dipole moment [α = polarizability; V = volume of the metal island] and d = distance from the metal surface. Again, as for SERS, a chemical contribution is also present for SEIRA as molecules can be oriented by chemisorption with a particular axis perpendicular to the surface, leading to a stronger absorption of the dipole changes along this axis. Furthermore, charge-transfer processes boosting the absorption-cross-section are also present but are nearly negligible.

In 2012, Alonso-Gonzalez *et al.*⁸⁹ further improved and solidified the SEIRA theory by shedding light on the electromagnetic mechanism of scattering in surface enhanced

processes. Briefly, not only the f^2 dependent infrared absorption

$$f^2 = \frac{|E_{\text{loc}}|^2}{|E_{\text{in}}|^2} \quad (2.3.2)$$

has to be taken into account, but also the f^4 dependent structure-mediated scattering. The scattering effect by the metal antenna-like structures, whether metal-island or artificial, is considered to be small. But regarding the fourth power dependency, it may be an important contributor in SEIRA as well as in comparison to the case of SERS.

3. Simulation of plasmonic nanostructures

Knowing how electromagnetic waves interact with metallic nanoparticles and nanostructured metallic surfaces is crucial to exploit and optimize them for specific applications. A variety of theoretical approaches have been developed to get further insight into the physics of these plasmonic structures.^{90,91} For predicting the light scattering behavior of isotropic and non-magnetic spherical or spheroidal particles the analytical approach of the Mie theory can be used.⁹² In this theory, the fields in the Maxwell equations are expressed as spherical harmonics. It is also possible to extend this theory to predict the plasmonic properties of core–shell nanoparticles.^{93,94} By introducing the electrostatic approximation, also known as quasi-static or long-wavelength approximation, the problem of solving the Maxwell equations is reduced to the solution of Poisson's equation for an electrostatic field.^{95,96} In this simplified picture, the electromagnetic wave is treated as a uniform electric field whose field vector oscillates up and down with the frequency ω . Therefore, it is obvious that the approximation is only valid in cases where the important dimensions are sufficiently smaller than the wavelength. Even though the maximum dimension is limited to $\frac{\lambda}{20}$, the electrostatic approximation is often applied for larger particles because of their simplicity.⁹⁵

For the description of the optical properties of more complex shaped structures a variety of numerical methods like the discrete dipole approximation (DDA),⁹⁷ the dyadic Green's tensor method,⁹⁸ the boundary elements method (BEM),⁹⁹ the finite elements method (FEM)¹⁰⁰ and the finite difference time domain (FDTD) or frequency domain (FDFD) method¹⁰¹ with their numerous variants are applied. These methods are based on solving the Maxwell equations either in the frequency domain (DDA, BEM, FEM and FDFD) or in the time domain (FDTD). In the case of the DDA the particles are assumed to consist of small dipoles which reduces the problem to the investigation of electromagnetic interactions of coupled dipoles.⁹⁰ The Green's tensor method is based on the volume integral equation for scattering, whereby the Green's dyad gets introduced to compute the total electric field.^{98,102} To avoid

convergence difficulties and singularities at the mesh center it is also possible to transform the equation into its surface integral expression.¹⁰³ Furthermore, both methods, DDA and Green's tensor method, are extendable to cover thermal effects and calculate the temperature profiles of plasmonic structures.¹⁰⁴ In BEM the surface integral formulation of the Maxwell equations is used to solve the problem by discretization.⁹¹ The concept of discretization is also used in FEM and FDTD. For FEM the Helmholtz equations are discretized in space and are solved numerically. Thereby, the aim is to find solutions which fulfill the boundary conditions. In FDTD the discretization is used in space as well as in time. The differential equations are expressed in terms of difference quotients and get solved for every space element in each time step. A detailed explanation of these numerical techniques is beyond the scope of this work and can be found elsewhere.^{90,91} The FDTD method has the benefit of a comparably simple implementation and provides in contrast to FEM, spectral broad-band information on a single run.^{105,106} On the other hand, FDTD is based on a rectangular grid which causes inaccuracies while computing curved or highly dynamic surfaces. In FEM modelling triangular or tetrahedral meshes are used. Thus, this technique handles the modeling of round shaped structures more efficiently. Regarding the computational performance, FDTD is more limited by the speed and number of processors, whereas, FEM is more memory demanding.

An important phenomenon is the coupling of particle plasmons which happens when nanoparticles are in close vicinity to each other. Thereby an increase in field strength by several orders of magnitude can be observed. In addition to numerical methods, an alternative approach for the investigation of this coupling behavior was developed: the so-called plasmon hybridization method.^{107–109} In analogy to the hybridization of atomic orbitals in the molecular orbital theory the plasmon modes of coupled nanoparticles can be seen as "hybridized" plasmon modes resulting from the interaction of the plasmons of the involved nanoparticles. These interactions result in low energy "bonding" and high energy "anti-bonding" plasmon modes which correspond to the symmetric and antisymmetric coupling of the modes. Aside from a qualitative understanding, the plasmon hybridization method also delivers quantitative results in good agreement with the Mie theory and numerical approaches.^{107,108,110} For investigating the plasmonic response of more complex shaped nanoparticles this model is also applicable. Here, the particle is assumed as being decomposed into simple-shaped parts. The plasmon resonances from the particle can then be treated as the result of the hybridization of the plasmon modes from these artificial parts. In the case of a nanoshell, for example, the plasmon modes follow from the assumed interaction of the plasmons from a sphere and a spherical cavity (see Fig. 3).

3.1 Coupled nanoparticles

Adjusting the spectral position of plasmon resonances to the desired working wavelength is vital for designing and optimizing plasmonic substrates for spectroscopic applications. The

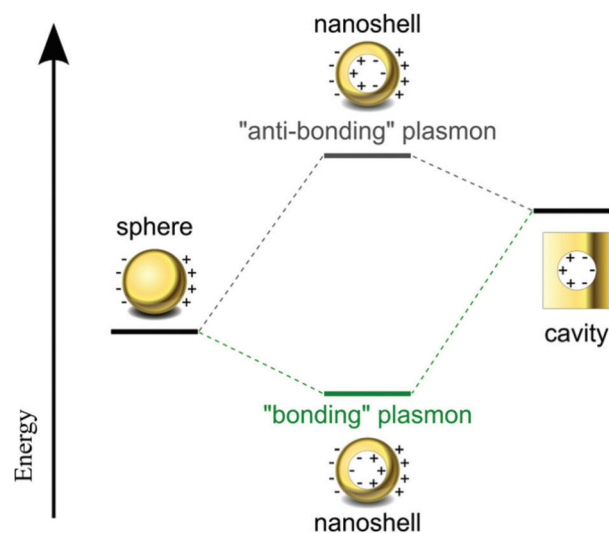


Fig. 3 Energy level diagram to depict the principle of the plasmon hybridization model at the example of a metal nanoshell. The resulting anti-symmetrically ("anti-bonding") and symmetrically (bonding) coupled plasmon modes of the nanoshell originate from the imagined interaction between the plasmons of a sphere and a cavity (modified from Prodan *et al.*¹⁰⁷).

optical response of metallic nanoparticles can be tuned by changing their size, shape, material as well as the surrounding medium.^{5,94,111–114} An additional approach is to couple them with nearby placed nanoparticles by means of their electromagnetic near-fields. This coupling of plasmon modes leads also to the formation of volumes between the particles with strongly enhanced electromagnetic fields, the so-called "hot-spots".^{115–119} Nowadays, there are several established fabrication techniques for the production of nanostructures with well-defined design parameters for tailoring the interaction between the plasmon resonances. A widely used group of approaches is self-organizing processes by which dimers or larger aggregates of identical as well as diverse particles can be realized.^{120–123} For the generation of nanostructures on plain substrates by bottom-up techniques the phenomenon of self-organization plays a prominent role.¹²⁴ On the other hand nanofabrication techniques like nanosphere lithography, electron beam lithography (EBL) or focused ion beam milling (FIB) can be applied for producing arbitrary structures with high reproducibility.^{25,125–127}

Independently of the fabrication technique, the gap size is a crucial parameter for the design of plasmonic structures as it has a remarkably influence on the coupling strength and thus on the resonance frequency. In order to calculate the extinction efficiency spectrum of nanoparticle dimers and trimers the DDA method can be employed.¹²⁸ Earlier, a universal scaling rule for the coupling of the plasmon modes of nanosphere pairs was found.¹²⁹ According to that, the spectral position of the plasmons only depends on the distance between the particles in length units normalized to the particle dimensions in spectral regions with a low variance of optical con-

Critical Review

stants. Within the study this scaling behavior is proven to be also valid for pairs of spheroids, cylinders and rods as well as for nanosphere trimers. The resonance frequency of the bonding plasmon mode shows an exponential decay (red-shift) with a decreasing interparticle distance, whereas the near-field enhancement is increasing. Thereby, the relative red-shift is dependent only on the ratio of the gap size and a characteristic size parameter of the structure. Parameters like the particle shape, material (considering low variances in optical constants) and the surrounding medium do not affect this scaling rule. Furthermore, the authors forecast that this scaling behavior is a general phenomenon which should be valid for the three-dimensional case as well. For tuning the resonances of nanoparticle arrangements to the desired wavelength this scaling rule can be very helpful.

However, for a given gap size the influence of the particle shape in the gap region cannot be neglected. Especially in the case of nanoparticle pairs with small gap sizes, their shape has a remarkable effect on the coupling behavior of plasmon modes. To get further insight, silver nanocube dimers with gap widths in the lower nanometer range of about 1–2 nm were investigated by means of spatial modulation spectroscopy.¹³¹ In this study, the resulting optical extinction spectra were compared with DDA and FEM calculations to clarify the origin of the observed spectral features. It is shown that the local surface plasmon resonance splits into two modes in dependence on the curvature of the cube corners. This proves that small changes in the particle shape, especially for the case of small gap sizes, have a strong influence on the plasmonic properties. Thus, the exact particle shape in the close proximity regime should be taken into account for designing and tailoring plasmonic substrates.

Aside from particles with a spherical or a cubical geometry often nanorods are used as building blocks for nanoparticle dimers. A lot of attention is also paid to triangular shaped structures the corners of which show strongly enhanced local fields due to the lightning rod effect. Based on calculations carried out using the DDA method it can be concluded that the extinction spectra of triangular nanoprisms are independent from the polarization of the incident light while the distribution of the local electric fields is remarkably dependent on it.¹³⁰ The strongest near-fields caused by the main plasmon resonance occur at the two corners of the edge which is parallel to the electric field vector. A study for investigating the local field distribution of quasi two-dimensional crystalline metallic nanoprisms came to the same result.¹³² By using interferometric tip-scattering scanning near-field optical microscopy (s-SNOM) to probe the evanescent fields and the DDA method to determine the origin of the measured plasmon resonances it was shown that in addition to dipole quadrupole and higher order modes are also excitable. Normally these modes get dampened as a result of the interaction in the bulk material, but not in this case due to the small thickness of the nanoprisms, which is in the range of the skin depth. Nevertheless, it has to be taken into account that the radiation into the far-field of higher order modes is of in general a rather low inten-

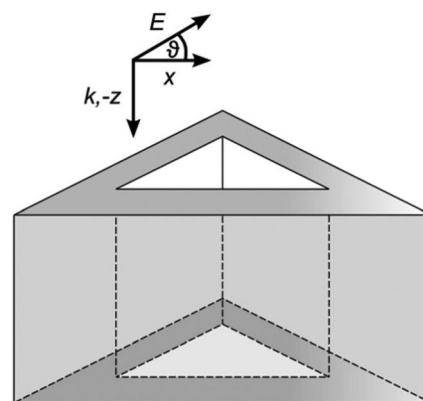


Fig. 4 Schematic illustration of a hollow triangular nanoprism and the polarization of the incident light. The simulation was performed for different angles θ in the range between 0 and 60 degrees (modified from Zhang *et al.*¹³⁰).

sity because of their weak coupling to dipolar modes. In addition, it was found that the highest local field enhancement in the case of multipole modes is, counter intuitively, not necessarily located at the tips of such structures. According to the authors, attention should be paid to these facts for tailoring the optical properties of nanoprisms for spectroscopic applications. In the more complex case of hollow triangular shaped structures (see Fig. 4) the local electric field distribution at the outer sides is the same as for solid prisms. The differences occur inside the structure, where additional hot spots arise.¹³⁰ The strongest local field is thereby located at the inner corner opposite to the edge the corners of which are the hot-spots in the case of solid triangles. Furthermore, the main plasmon peak of solid prisms splits up into two prominent features in the extinction spectrum of the hollow triangles. These bands are both red shifted with respect to the solid triangular structures. Besides adjusting their optical response by increasing the edge length, which leads to a further red shift, hollow triangles can be tuned by changing the size of the inner triangle. Hence, the adjustability as well as the number of effective hot spot areas per structure can be increased by using hollow nanotriangles instead of solid ones. However, the greater technical effort for realizing these structures should also be kept in mind.

As mentioned earlier, triangular particles are also often used as building blocks for dimers, which will thus be described as bowtie antennas. In a study based on the Green's tensor technique the optical properties of nanorod pairs and bowtie antennas were compared (see Fig. 5a and b).¹³³ Both structures show a strong field enhancement in the gap region. In all simulated cases nanorod pairs which are aligned along their long axes achieve a higher field enhancement. In the case of nanorod pairs the plasmon resonances also depend much more strongly on the gap width than for bowtie antennas. Besides this, the spectral position of the plasmon resonances can, independently from the type of the structure, be controlled by the length of the two coupled antennas. In con-

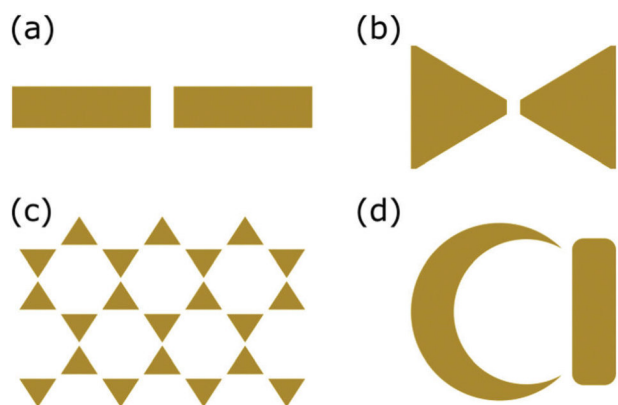


Fig. 5 Geometry of different simulated metal nanostructures: (a) nanorod pair, (b) bowtie antenna (modified from Fischer *et al.*¹³³), (c) Fischer pattern (modified from Galarreta *et al.*¹³⁴) and (d) nanocrescent coupled to a nanostrip antenna (modified from Kumar *et al.*¹³⁵).

clusion, nanorod pairs seem to be more convenient for applications in which the near-field enhancement plays a more crucial role than bowtie structures. Otherwise, the plasmon resonances of bowtie antennas are more sensitive to refractive index changes compared to those of coupled nanorods. This is the reason why the former are a more suitable choice as platforms for surface plasmon sensing. Another often used SERS substrate which also relies on coupled triangular shaped nanostructures is the so-called Fischer pattern (see Fig. 5c), which is fabricated by means of nanosphere lithography. In contrast to Bowtie antennas the triangles are arranged in this case in a hexagonal grid. By FDTD simulations a clear dependency of the electric field distribution on the wavelength and the polarization of the incident light was found.¹³⁴ Another crucial parameter which determines the plasmon resonance frequency is the edge length of the triangles. Furthermore, it is shown that the highest field enhancement occurs at the gaps between the corners of the triangular structures for parallel to the connection axes polarized light. However, the authors conclude from their results that Fischer patterns in view of near-field enhancement per unit area are not necessarily optimal structures. For increasing the number of hot-spots maybe the use of hollow triangles as building blocks could be a suitable solution.

Nanocrescents are promising structures for surface enhanced spectroscopy because of their strong field-enhancement at both sharp ends. The ability of tuning the optical properties of metallic nanocrescents by changing their geometry was shown in various studies.^{136–138} An alternative approach for altering the plasmon resonances and near-field enhancement of such structures is the coupling to another metallic nanoparticle (see Fig. 5d).¹³⁵ In this numerical study, based on a 2D FEM approach, a gold nanostrip antenna is brought into the close vicinity of gold nanocrescents. The coupling of the plasmon modes causes a red-shift of the nanocrescents' dipolar-resonance. The spectral position of this mode as well as its near-field enhancement depends on the length of the nanostrip as well as on its distance to the crescent. Hence,

there are new degrees of freedom for tailoring the resonance frequency of the nanocrescents' dipolar mode without changing the shape of the structure itself. Furthermore, the field enhancement in the hot-spot of the coupled structures has an anisotropic behavior and can therefore be tuned by the angle of the incident light.

Another suitable platform for SERS applications with strongly enhanced local fields is two-dimensional subwavelength nanohole arrays.¹³⁹ In a comparative study the transmittance and SERS intensity of shallow and deep nanohole arrays with different diameters and edge-to-edge distances were investigated.¹⁴⁰ Based on three-dimensional FDTD calculations and SERS measurements it was shown that deep nanohole structures deliver the highest signal intensities. An explanation for this behavior is given by the coupling strength between the cavity plasmon modes of the top gold layer and the modes of the gold disks at the bottom of the cavities. In the case of shallow nanocavities there is a strong coupling, which leads to a weakening of the local electromagnetic fields and reduces in this way the SERS intensity. In contrast to this, the weakly coupled plasmon modes in deep nanohole structures result in strongly enhanced local electromagnetic fields and cause strong SERS signals. For this reason, avoiding a strong coupling between the two gold layers seems to be beneficial in such cavity structures to achieve high signal intensities.

Due to their strong and reproducible signal networks of corrugated silver nanowires and also nanowires with attached nanoparticles have attracted attention in the last few years as SERS substrates. Simulations for five different model structures were carried out to get a deeper insight into the enhancement mechanisms of these structures.¹⁴¹ For the calculation of the electric field distribution a three-dimensional FDTD method was used. It is seen that corrugated nanowires provide higher field enhancements compared to smooth nanowires. Therefore, the density of the wires also plays a crucial role. With increasing density the number of gaps between the nanowires also increases but the gap size decreases. This results in more and brighter hot spots for a dense nanowire network in comparison with one of a lower density. The most homogeneous SERS signals were achieved with asymmetrically ordered nanowires. Such highly asymmetric substrates cause a depolarization of the incident light which leads to a higher uniformity of the gained signals. Furthermore, the attached nanoparticles enhance the local electric fields additionally by the interaction of their localized plasmon modes with the plasmon resonances of the nanowire.

The principle applicability of large aperiodic structures for surface enhanced spectroscopy derived from mathematical algorithms was investigated in a study based on the generalized Ohm's law approach.¹⁴² Different structures like Fibonacci and the Rudin-Shapiro pattern as well as the random walk method generated cluster-cluster aggregates are part of this study. In addition an algorithm for generating random deterministic structures is applied. The authors found evidence for an inversely proportional relation between the density of hot spots and the maximal obtainable field enhancement in such

deterministic structures. The design parameters for optimizing the average signal enhancement can be estimated on the basis of the degree of disorder in the pattern. Such deterministic aperiodic structures, which can in principle be produced by EBL, could be applicable for surface enhanced sensing techniques. In addition, these results could lead to a more detailed understanding of the optical properties of planar, poorly ordered nanoparticle assemblies.

The coupling of plasmon modes in close spaced arrangements of metallic nanoparticles results in the formation of new modes, which can be described *via* using the plasmon hybridization method.^{107,108} Because of symmetry reasons the excitation of anti-bonding modes by normally incident light is forbidden.¹⁴⁴ Furthermore, out-of-phase modes in symmetric nanoparticle dimers are “dark” as well because of their vanishing resulting dipole moment.¹⁴⁵ For this reason special illumination strategies or asymmetric plasmonic structures are needed to investigate these modes in experiment. One approach is the excitation and direct observation of anti-bonding modes *via* two-photon excited photoluminescence (TPPL).¹⁴⁶ In combination with FDTD calculations the near-field enhancement depending on the gap size between two rod-shaped nanoantennas and their aspect ratios was investigated. Aside from the increasing near-field enhancement with a decreasing gap-size smaller gaps lead to strong coupling which enables the selective excitation of the anti-bonding modes. These show a lower enhancement factor accompanied with a higher quality factor, which is defined as the ratio of the spectral peak position and its full width half maximum. On account of this, anti-bonding modes might be more interesting for near-field engineering and surface plasmon sensing than for surface enhanced spectroscopy.

This conclusion can be supported by a study based on a 3D FEM model for the calculation of the extinction spectra of asymmetric double split ring nanostructures (see Fig. 6).¹⁴³ Several electromagnetic resonances are found which originate from the coupling of the dipole with dipole modes as well as the dipole with multipole modes. Their spectral position is thereby clearly dependent on the degree of asymmetry. With respect to applications where the field enhancement is crucial it is shown that the dipole-dipole as well as the dipole-quadrupole bonding modes deliver a higher near-field enhance-

ment in the two gap regions than the anti-bonding modes. The spectral position of the bonding modes is thereby located in the near-infrared region.

As seen before, breaking the structures’ symmetry is another approach for the excitation of normally dark modes. By doing this, in-phase and out-of-phase modes should be visible simultaneously. Easily viable structures for investigating this effect are asymmetric dimers which can be realized by using particles which differ in size or material. Based on polarized scattering spectroscopy symmetric and asymmetric pairs of silver and gold nanospheres were investigated.¹⁴⁵ The measured spectra were corroborated with data gained by applying a coupled dipole-dipole model in the electrostatic approximation as well as the DDA method. For homodimers as well as size-asymmetric heterodimers the observed modes and their spectral position are explicable using the plasmon hybridization model while taking the asymmetry into account. In contrast to this, there is an unexpected red shift of the anti-bonding mode observed for asymmetric couples of silver and gold nanospheres. The origin of this effect is the coupling of interband absorption processes in the gold nanoparticles with the silver plasmon mode. Because of this, the plasmon hybridization model, in which normally the approximation of free electrons is used, needs to be expanded by considering interband transitions. Furthermore, due to the interaction of the partners in asymmetric heterodimers a couple of interesting effects like avoided crossing of plasmon modes, Fano resonances and an asymmetric scattering behavior can arise.¹⁴⁷ These effects have been studied extensively for dimers consisting of differently sized gold nanospheres and -shells (see Fig. 7) by FDTD calculations and the use of the plasmon hybridization method. In addition angle dependent dark-field spectroscopy at single heterodimers was carried out to prove and support the theoretical findings. Because of the fact that such a variety of effects appears in the case of an asymmetric couple of spheres it is pointed out that for more complex structures a virtually similar behavior is expected.

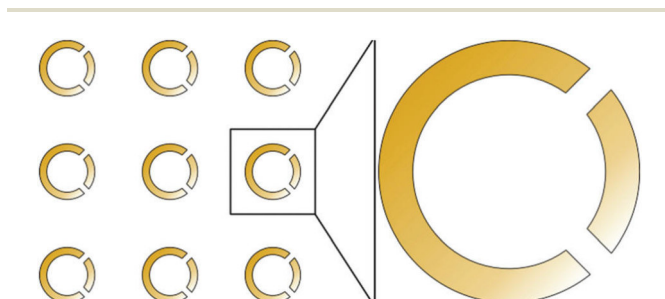


Fig. 6 Scheme of an array of asymmetric double split ring nanostructures (modified from Ding *et al.*¹⁴³).

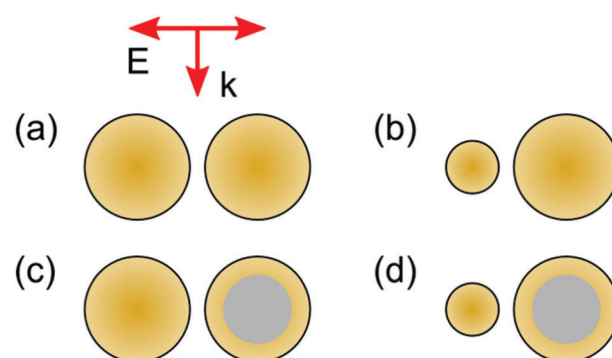


Fig. 7 Scheme of the simulated dimer structures: (a) gold nanosphere homo- and (b) heterodimers as well as (c) same and (d) different sized gold nanosphere/nanoshell heterodimers. The red arrows depict the polarization and direction of the incident light (modified from Brown *et al.*¹⁴⁷).

In an earlier FDTD study it has already been shown that symmetry breaking has a remarkable effect on the optical response of nanoparticle assemblies and Fano resonances can appear.¹⁴⁸ As an example, metallic rings with a disk of the same material placed in their center were chosen. For symmetric arrangements two modes are observable which are formed by the interaction of the resonances of the ring and the disk: a subradiant bonding and a superradiant antibonding mode. In contrast, Fano-resonances arise in non-symmetric structures due to the interaction between the quadrupolar mode of the ring and the dipolar disk resonance. Due to the high sensitivity of such structures to a change of the refractive index of the material between the disk and the ring they are well suited as platforms for surface plasmon resonance sensing.

The central issue in the research studies reviewed before is the effect of coupling between closely arranged nanoparticles on their optical properties. Another question of interest for designing plasmonic structures is the influence of the substrate material on nearby placed nanoparticles. In a combined experimental and theoretical study this subject was investigated for the case of dielectric substrates.¹⁴⁹ For spherical bulk and core-shell nanoparticles a splitting of the dipolar mode into two dipolar modes polarized parallel and perpendicular to the surface was found. For a qualitative understanding of this behavior the simplified picture of image charges can be used. According to this, the spectral splitting is dependent on the dielectric constants of the substrate material, the distance between the particle and the substrate and the polarization of the incoming electromagnetic wave. The spectral shift between the two differently polarized plasmon modes increases thereby linearly with an increasing dielectric constant. Additionally, the highest influence is observed for bulk material gold nanospheres. From this study follows that the influence of the substrate material on the plasmon modes of nanoparticles cannot be simply neglected and should be taken into account for simulations as well as for experimental studies.

Also related to this topic is the interaction between nanoparticles and a thin metallic film. Based on single-particle dark-field spectroscopy the scattering spectra of spherical gold nanoparticles on top of a thin gold film as well as partly inserted into a gold film were recorded.¹⁵⁰ To reveal the origin of the observed optical resonances the electric field distribution was calculated by using the FDTD method. In the case of particles on top of the gold film the prominent spectral features arise from highly confined gap modes with azimuthal angular momenta. In contrast to this, strong dipole moments perpendicular and parallel to the film are responsible for the discovered scattering maxima of partly embedded particles. In both cases the resulting scattering spectra depend strongly on the polarization of the incident light. Additionally, a strong polarization dependency of the radiation pattern for particles on top of the gold film is observed.

For calculating the resulting electric fields in the more complex case of the interaction between the plasmon modes of a plain metallic layer and a nearby placed single metallic

nanowire or grid the dyadic Green's tensor method was applied.¹⁵¹ In order to get the optical response the authors employed additionally a scattering matrix based formalism. The interaction between the wire and the film leads to a red shift of the localized surface plasmon of the wire. This mode depends mainly on the layer-wire distance whereas the layer thickness itself has only a weak influence on the observed shift. In the case of the grid a contrasting behavior was observed. Now the localized resonance of the wire can be tuned by changing the thickness of the metallic film. For the design of substrates, in which a dielectric spacer layer separates the structure from a plain metallic film,¹⁵² it should be important to consider these findings.

Another interesting question, regarding SEF, is the interaction of a spontaneous optical emitter like a fluorescent molecule with a metallic nanorod dimer. A model based on the Green's theorem surface integral equations was used for the description of the electromagnetic fields involved in this problem.¹⁵³ From it, the influence of the position and the orientation of the molecule on the radiative and non-radiative decay rates was investigated. For molecules in the center of the gap with a dipole moment parallel to the dimer axis the largest enhancement of the radiative decay rate was found which is attended by an increase of the quantum efficiency of the emitter. Furthermore, the molecule position and orientation of the dipole has also a strong influence on the near- and far-field pattern of the emitted light.

The resonance fluorescence of single molecules in the vicinity of a plasmonic nanostructure was investigated by applying Green's tensor technique.¹⁵⁴ Therewith, the near-field of these nanostructures, which consists of four nanostrip antennas, was determined. Based on this the fluorescence spectrum of a nearby placed dibenzanthanthrene molecule was calculated for different molecule positions. The resulting spectra show additional sidebands which can be explained by the splitting of the two-level system into a four-level system. Hereby, two competing effects play an essential role: the near-field enhancement and the modification of the decay rate. Both effects show a clearly visible dependency on the position of the molecule with respect to the four nanostripes. Positions with a high near-field enhancement combined with a low influence on the decay rate are optimal for recording resonance fluorescence spectra. Additionally, the spectral position of the plasmon modes should be tuned to match with the molecules resonances. By careful balancing of the aforementioned effects it is possible to realize conditions for observing phenomena like the Mollow triplet and photon antibunching of molecular fluorescence.

3.2 Core-shell nanoparticles

Core-shell nanoparticles open up more design options by combining advantages of different materials. Hence, particles are realizable which not only have the desired optical but also chemical properties for a certain application. Moreover, due to the fact that they consist of materials with different optical properties there are more parameters available for tailoring

their plasmonic behavior. A general guideline for optimizing the absorption and scattering properties of coated metal nanoparticles consisting of four basic steps was presented in the case of spherical core-shell nanospheres.¹⁵⁵ Because of their spherical geometry the method of choice for calculating the electromagnetic fields is the Mie theory. According to the proposed scheme the starting point is the definition of realistic boundaries for the optimization parameters. The next step involves preliminary calculations of the scattering energy to select the parameter range for the simulation on the basis of a certain threshold. Afterwards, the selection of the material takes place followed by optimization of the particle geometry. From this, it is possible to deduce from the calculations additionally the tolerances of the design parameters and with it the critical parameters for optimizing the particles. Moreover, this method of design is not limited to tuning the optical response of spherical particles. It can be as well adapted to other geometries by using for example FEM for the field computation.

Bimetallic multilayer nanoparticles with a dielectric or metallic core combine the stronger plasmon resonances of silver with the stability of gold nanoparticles.¹⁵⁶ Furthermore, an outer gold layer is also beneficial for biomedical applications. By numerical calculations based on the Mie theory it is found that the extinction efficiency of nanoparticles with a silver core or an inner shell and an outer shell of gold is higher than that for pure gold core-shell and multilayer nanoparticles. Besides the particle size, the crucial parameters for tuning the optical response of the nanoshells are the thicknesses of the dielectric layers and the outer shell. In accordance with the aforementioned study it was shown that a thin gold layer on silver nanoshells with a dielectric core (see Fig. 8) is beneficial with respect to the near-field enhancement which is stronger than that for pure silver shell nanoparticles.¹⁵⁷ It was found that the charges which are induced by the interaction of the conduction electrons with the incoming electromagnetic wave at the inner and outer surfaces of each layer have an opposite sign

for the silver and gold layers (compare Fig. 8). A variation of the layer thickness of either the silver or the gold layer results in two competing effects. In a thicker layer more conduction electrons exist which contribute to the induced charge and this leads to a stronger near-field enhancement. On the other hand, a thicker layer causes a more pronounced separation between the inner and outer surfaces of the layer which reduces the effect of one of the surfaces on the other layer. Due to this the near-field enhancement is reduced. Therefore, the interplay of both effects has to be taken into account for designing and optimizing double layered core-shell nanoparticles.

Aside from using bilayer particles to combine the benefits of different metals, nanoshells made of a bimetallic alloy have also attracted interest in the last few years. The optical response of bimetallic nanoshells can not only be tuned by varying the shell thickness but also by a change of the material composition.¹⁵⁸ In the hybridization model the plasmon modes of the nanoshells result from the coupling between the solid sphere and inner wall cavity modes. The hybridization strength depends thereby remarkably on the dielectric constants and the wall thickness. Because of this dependence an increasing gold content as well as a decrease in shell thickness leads to a red shift of the LSPR. The highest achievable field enhancement, which is also dependent on these two parameters, was found to be located for lower gold content particles in the near-infrared region. Because of the transparent window of biological tissues in this spectral region and their better biocompatibility in comparison to pure silver nanoshells such alloy core-shell nanoparticles are promising for biomedical applications.

The transition from spherical to spheroidal shaped nanoshells yields a higher tuning ability and local field enhancement.¹⁵⁹ In a study based on DDA it was pointed out that the origin of this behavior is the dependency of the LSPR hybridization strength on the aspect ratio of the nanoshell structure. The hybridization strength corresponds to the polarizability which is greater for the long axes of elongated structures than for a sphere. Hence, the higher the aspect ratio of a particle is, the stronger is the coupling between the LSPR of the inner and outer sides of the shell. This results in a higher sensitivity of the plasmon resonance spectral position to a change in shell thickness. In addition, because of the larger near-field enhancement they are also more suitable for surface enhanced spectroscopy compared to spherical particles.

Also in the case of nanoshells the influence of a broken symmetry on their plasmon resonances is of interest. Breaking the symmetry of spherical core-shell nanoparticles by displacing the dielectric core from the center (see Fig. 9) allows the hybridization of multipolar sphere and cavity modes.¹⁶⁰ This leads to a couple of excitable plasmon resonances which can be tuned by varying the offset of the core. The maximum field enhancement of these structures called nanoeggs is located nearby the thinnest part of the shell. With an increase of the core offset the plasmon resonances corresponding to the maximum field enhancement get red shifted until the core

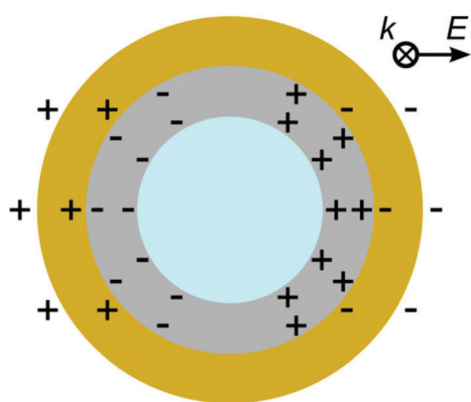


Fig. 8 Schematic illustration of the hybridization of the dipolar plasmon mode in silica-silver-gold nanoshell particles (modified from Wu *et al.*¹⁵⁷).

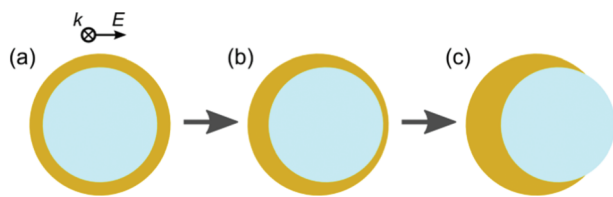


Fig. 9 Depiction of different structures realized by displacing the dielectric core of core-shell nanoparticles relative to their center: (a) symmetric core-shell (without offset), (b) nanoegg and (c) nanocup particles (modified from Knight *et al.*¹⁶⁰).

drives through the shell surface ending up with a nanocup structure. An increase in the core offset will further lead to a blue shift of the observed modes. By knowing this, the optical properties like field confinement and the relation between scattering and absorption can be tailored for the specific task by changing the particle size, core displacement as well as selecting a plasmon resonance which should be excited.

A further promising concept to increase the near-field enhancement is the use of core-shell nanoparticles designed for nanolasing applications.¹⁶¹ Such particles consist of a noble metal core surrounded by a dielectric coating which contains a gain material. As a gain material covalently bonded fluorophores whose emitting frequency matches with the lasing wavelength were used. By applying the Mie theory the lasing frequencies as well as the thresholds of such nanostructures were calculated. Silver is, due to its smaller ohmic losses in comparison to gold, the more suitable core material. Besides silica dielectrics also with a higher (lower) refractive index are usable as coating materials which result in a longer (shorter) lasing wavelength. The calculations of the electric fields in proximity to these nanoparticles suggest stronger enhanced fields for particles with a gain compared to ones without. The closer is the gain to the threshold for lasing the higher is the resulting enhancement.

In summary, a wide range of plasmonic nanostructures has been investigated by simulations for applications in surface enhanced spectroscopic techniques. Within this section, metallic nanostructures ranging from single and isolated particles up to complex shaped architectures were in the focus. For further application schemes, the here described particles are suitable to be applied for detection under wet conditions (for example metal colloids) as well as arranged on substrate materials for chip-based applications. The fabrication routines for the preparation of the here described and simulated nanostructures will be introduced within the following sections reviewing bottom-up, self-organized, template-based as well as top-down methods for substrates suitable for surface enhanced spectroscopic techniques.

3.3 Complex shaped nanoparticles

Most of the articles discussed in section 3.1 were focused on the coupling of unconnected nanoparticles caused by their electromagnetic near-field. Two important results of this coup-

ling are the strong modification of their plasmon modes due to hybridization and the formation of hot-spots. A promising approach to further increase the near-field volume between two parallel arranged nanorods is to connect them on one side with an additional bar which results in a planar U-shaped structure.¹⁶² By using the DDA method it was shown that in a couple of parallel arranged nanorods only transversal plasmon modes can be excited whereas in U-shaped nanostructures longitudinal dipole and multipole resonances are also excitable. The reason therefore is the direct coupling of the electrons in the two parallel rods of the U-shaped structure by the connecting bottom rod which is perpendicularly aligned. Additionally it was found that the frequency of the plasmon modes in such an arrangement is dependent exponentially on the radii of the rods and shows a linear dependency on the distance between the two parallel rods. Besides the high tunability of U-shaped nanostructures they provide more hot-spots in comparison to parallelly arranged nanorods. Hence, a pattern made of such structures seems to be well suited as the substrate for surface enhanced spectroscopic methods. The same is true for split-ring resonators which are very similar in shape. A smaller gap at their opening provides an additional hot-spot. Nanorods in which a small gap is cut also show strongly enhanced fields but this enhancement goes hand in hand with a decrease in the quality factor due to dipole radiation losses.¹⁶³ The local field distribution of straight nanorod antennas was compared to that of different strength bent ones ending up eventually in split-ring structures. According to the presented results it is possible to reduce the losses by scattering nearly completely by taking split-ring structures with a gap-width of 10 nm. This reduction of radiation losses is caused by a decrease in the electric-dipole moment. Hence, the quality factor is increased accompanied by a high field enhancement which makes these structures promising candidates as substrates for surface enhanced spectroscopy techniques.

Instead of preparing positive structures on a substrate it is also possible to use cavities in the metal layer of the same shape. According to the generalized Babinet theorem, the transmission and reflection spectra of the positive and negative structures show the same behavior but are interchanged under irradiance with complementarily linear polarized light (see Fig. 10).¹⁶⁴ Additionally, the electric field distribution of the positive structure is qualitatively similar to the magnetic field distribution of the inverted one. Hence, the plasmonic eigenmodes of both types of structures can be denoted in the same way. Furthermore, a complementary behavior of the effective material parameters was found. In spite of the lack of perfect conductivity and the finite film thickness of these structures,^{164,165} the qualitative validity of this theorem was shown for several shapes like nanorod antennas,¹⁶⁶ U-shaped structures¹⁶⁷ and split-ring resonators.¹⁶⁴ By means of dark field microscopy and FEM simulations the advantages of using inverse structures were also demonstrated for nanocrescents.¹⁶⁵ Crescent-shaped nanoholes combine the high tunability of their plasmon resonances by changing the geometric

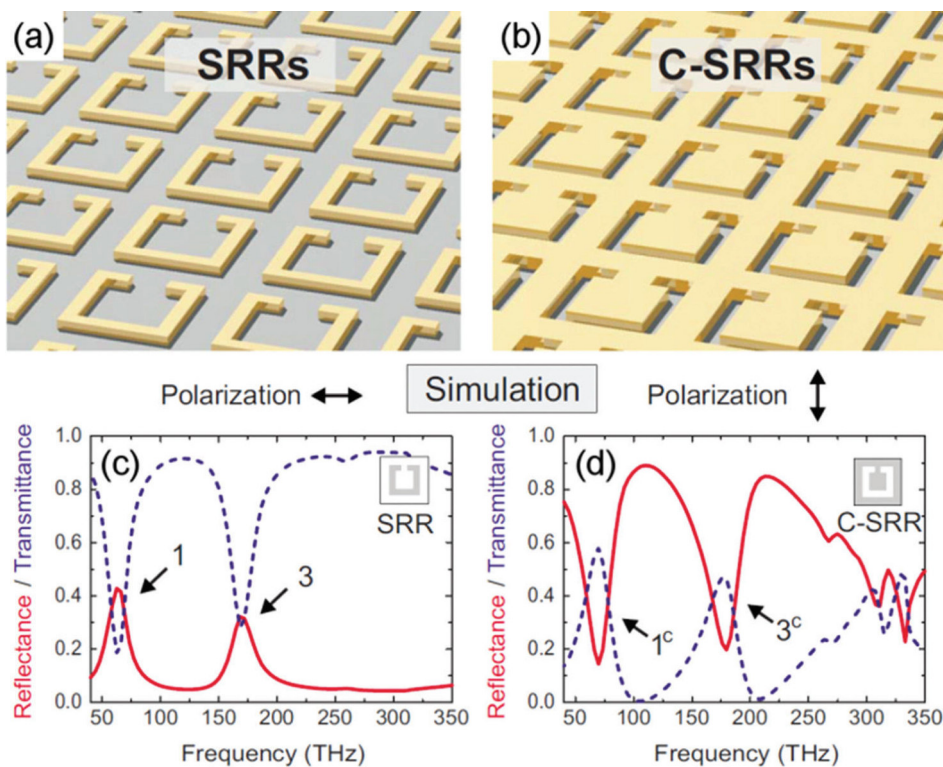


Fig. 10 Schematic illustration of (a) positive and (b) negative split-ring resonator structures. Transmittance (blue, dotted) and reflectance (red, solid) curves calculated for (c) positive and (d) negative structures illuminated with complementary linear polarized light. The numbers mark the first- and third-order eigenmodes of the split-ring resonators (adapted with permission from T. Zentgraf, T. P. Meyrath, A. Seidel, S. Kaiser, H. Giessen, C. Rockstuhl and F. Lederer, *Phys. Rev. B: Condens. Matter*, 2007, **76**, 033407,¹⁶⁴ copyrighted by the American Physical Society ©2007).

parameters with the possibility of fabricating sharper tips in comparison with positive crescents. This results in a higher local field enhancement for the nanohole type of crescent structure. In addition, analyte molecules can be caught more effectively inside the cavities.

As already shown, the plasmon hybridization model is a powerful approach for analyzing qualitatively and quantitatively the optical properties of coupled nanoparticles. Moreover, it was shown that this model is also applicable for investigating the optical properties of more complex shaped nanoparticles. An example of this is a study on metallic tori with different aspect ratios.¹⁶⁸ The aspect ratio is herein defined as the ratio of the tube to the torus radius. For incident light which is polarized parallel to the torus plane an intense low energy feature, assigned to a dipolar in plane plasmon mode, and a high energy feature, corresponding to several overlapping higher order excitations, were found in the absorption spectrum. The dipolar mode is strongly dependent on the aspect ratio and, hence, highly tunable. In the case of weak hybridization, which is fulfilled for aspect ratios smaller than 0.8, this mode can be described as a plasmon of an infinite cylinder. The spectral position of this mode is thereby dependent on the circumference of the torus. In contrast, for perpendicular polarized light two spectrally less separated features arise in the spectrum. These peaks can be interpreted as

bonding and antibonding combinations of two different infinite cylinder plasmons. Both resulting resonances show only a slight dependence on the aspect ratio. Because of the good agreement of these results compared to those obtained *via* using FDTD calculations the usability of the plasmon hybridization method for complex shapes like a toroidal geometry is proven. Furthermore, it should be as well possible to treat toroidal core-shell nanoparticles within this framework. Even the plasmon resonances of symmetry broken structures like nanobowls, open nanocages and open nanoeggshells can be well described by the plasmon hybridization model.¹⁶⁹ While using the FDTD method the height dependence of the dipolar and quadrupolar plasmon modes existing in such structures was investigated. These modes are the result of the interaction between the dipolar nanohole plasmon resonances, which appear at the opening of these structures, and the dipolar as well as quadrupolar plasmon modes of the non-symmetry broken closed shell structures. By cutting the full shell structure a red shift of the dipolar bonding mode is caused. Furthermore, a hyperbolic dependency of this mode on the height of the structure exists for all simulated shapes. From the viewpoint of using the envisaged structures as platforms for surface enhanced spectroscopy methods they show promising highly enhanced local fields close to the corners and edges.

Another technique for treating complex shaped structures is based on the Coulomb interaction of the surface charges at the walls of the particles.¹⁷⁰ In order to get the distribution of the surface charges the intensity of the local electric fields and their direction contours was calculated *via* the DDA method. From this, it was possible to investigate the surface plasmon resonances of metallic nanotubes. The optical properties of the nanotubes are tunable by changing their aspect ratio as well as their wall thickness. Hence, they combine the tunability of shell nanoparticles and nanorods with the additional benefit that analyte molecules can bind outside and inside the nanotube. This makes them promising candidates for surface plasmon sensing as well as surface enhanced spectroscopies. Furthermore, the herein presented approach is also extendable to the investigation of the plasmon coupling of other complex shaped metallic nanoparticles.

By considering metal nanorods as resonators for PSPPs it is possible to develop a model based on Fabry–Pérot interferences to calculate the local electric fields and the associated field enhancement.¹⁷¹ The partial reflection of PSPPs at the end of the antennas results in interferences which cause the local field enhancement. The amplitude and the phase of the reflected part of the propagating mode are estimated using a simple Fresnel reflection model as well as by full field FDFD simulations. By comparing the calculated electric fields with the field maps resulting from the FDFD model the usability of the Fabry–Pérot model was validated. The good accordance between both models shows that metallic structures with dimensions on the wavelength scale indeed behave as resonators for propagating plasmon modes. In principle this model should be adaptable for treating particles of different shapes as well. Hence, it is a helpful tool for tailoring and optimizing metallic nanostructures for plasmonic applications.

Designing plasmonic devices can also be performed on the basis of transformation optics which was shown for structures with broadband light-harvesting capabilities.¹⁷² By applying a conformal transformation an infinite plasmonic structure with a broadband absorption spectrum can be transferred into a finite structure which shows the same absorption behavior (see Fig. 11). In doing so, a non-realizable structure with the desired optical properties is convertible into a viable one. Starting from two semi-infinite structures, a metallic thin film and a sandwich structure consisting of two metallic slabs separated by a dielectric layer, the authors end up with two promising structures by using this technique: a crescent shaped cylinder and two attached cylinders. Besides their capability of broadband light-harvesting these structures deliver strong field enhancements. This opens another analytical path for designing nanostructures for surface enhanced spectroscopy methods.

In the last few years a lot of research effort was put in the exploration of fabrication techniques for plasmonic nanostructures. However, structures which are produced at the limits of technical feasibility often differ in shape from the idealized structures used for modeling the optical parameters. Therefore, an important question for designing plasmonic

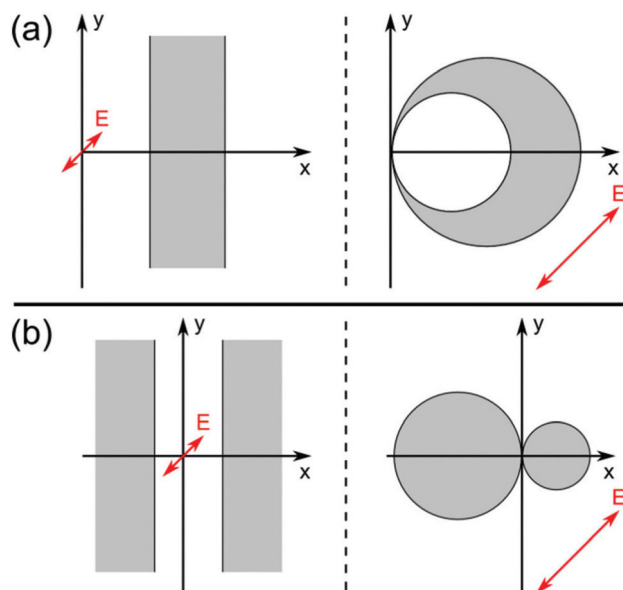


Fig. 11 Semi-infinite structures (left) and *via* conformal transformation resulting plasmonic nanostructures. Two examples are depicted: (a) a crescent shaped cylinder obtained from a thin metal layer and (b) a heterodimer of two touching cylinders resulting from two metallic slices separated by a dielectric layer (modified from Aubry *et al.*¹⁷²).

nanostructures based on simulation results is the effect of shape imperfections and also the surface roughness on their optical properties. For the ring-like plasmon resonances in gold nanoring–disk nanostructures a considerable deviation between the calculated and measured spectral positions was discovered.¹⁷³ To get a deeper insight into this phenomenon structures with rounded edges were simulated by applying BEM. This leads to a significant red shift of the ring-like plasmon wherefore the calculated extinction spectra matches very well with the measured one. The explanation for this effect is given by the variation of the mean wall thickness due to the rounding of the ring edges. Hence, there is a stronger inter-wall interaction which results in an observed spectral shift of about 25% for a change in the mean wall thickness of 10%. Additionally, the surface roughness seems to have also a slight influence on the position of the spectral features. In contrast to these findings, the disk-like plasmon shows a minor dependency on the sharpness of the disk edges. A reasonable explanation for this behavior is that the deformation of the structure is small in comparison to its size.

The question concerning the necessity of taking the irregular shape of non-ideal nanostructures into account was also considered in a study on the emission behavior of molecules nearby these structures.¹⁷⁴ To simulate the excitation and re-emission enhancement of molecules close to a pair of metallic nanostructures BEM was applied as well. For comparison, the calculations were carried out for an ideally as well as for a non-ideally shaped nanostructure pair. The parameters for the shape of an experimentally realized non-ideal pair of nanoantennas were therefore extracted from a scanning electron microscopy

(SEM) image. In the far-field no difference in comparison with the ideal structure is visible, whereas the near-field depends notably on irregularities of the structures. Hence, the irregular shape of fabricated nanostructures should be taken into account if the particle localization is crucial for the investigation.

4. Bottom-up preparation strategies of plasmonic nanostructures

Plasmonic nanostructures can be fabricated by a variety of methods. This section will highlight the progress in the field of bottom-up fabrication within the last few years. Reported metal nanostructures as plasmonic materials range from classical metal colloids, to core-shell nanoparticles and structures as well as complex-shaped nanoparticles prepared by seed mediated growth.

4.1 The classical approach – metal colloids

Metallic nanoparticles suspended in an aqueous environment are one of the most frequently applied SERS substrates in the last few years. Classically, the nanoparticles are prepared by simple and easy-to-follow wet chemical processes. The most commonly used method to produce silver nanoparticles is based on the reduction by citrate, a protocol published by Lee and Meisel.¹⁷⁵ Following this procedure, a solution of citrate buffer is added dropwise to a boiling solution of silver nitrate. A change in color to turbid grey-yellow indicates the successful generation of silver nanoparticles. For the application as a SERS substrate, the signal intensity can be increased dramatically by adding salts *e.g.* KCl, NaCl or MgSO₄ due to the formation of aggregates.¹⁷⁶ Hot spots are generated by means of nano-sized gaps between silver nanoparticles which are known as one of the most commonly applied substrates in SERS. As an example, single silver nanostructures produced by the Lee–Meisel protocol have been used for a fundamental investigation of the electromagnetic enhancement of the SERS mechanism.¹⁷⁷ Moreover, these nanostructures are applied in surface enhanced hyper Raman scattering (SEHRS).¹⁷⁸ They can be also used in combination with further bioanalytical techniques, *e.g.* microfluidic lab-on-a-chip devices.^{179–183} Liu *et al.* employed citrate-reduced AgNPs in a microdroplet PDMS detector for trace level crystal violet detection with a LoD of 3.6 nM.¹⁸⁴ A SEF-based immunoassay employing silver NPs produced by the Lee–Meisel protocol was presented by Zhang *et al.*¹⁸⁵ Within this investigation a glass slide with several polyelectrical layers was covered with BSA (bovine serum albumin) and antigens before binding silver-antibody nanoconjugates (SANC).

The citrate reduction was also adapted for the production of gold nanoparticles. To do so, trisodium citrate was injected into a boiling solution of HAuCl₄. Finally, a suspension of AuNPs results, wherein the particle size can be manipulated by changing the amount of added trisodium citrate.¹⁸⁶ These AuNPs have been used recently to detect melamine in milk

with a detection limit of 0.017 mg l⁻¹.¹⁸⁷ Kämmer *et al.* compared the UV-SERS enhancement potential of citrate reduced gold nanoparticles with the enhancement of palladium, platinum and silver colloids as well as Au–Ag and Ag–Au core-shell structures, using melamine as a test molecule.¹⁸⁸ Within this study, gold nanoparticles with a diameter of 120 nm activated with KBr were identified to be the best combination of nanoparticles and activation agents to detect melamine by UV-SERS at an excitation wavelength of 244 nm.

In conclusion, a rather high number of studies about citrate reduced metal nanoparticles can be found in the literature; however, only a limited number of them could be covered within this review. The combination of metal NPs with other techniques *e.g.* microfluidics is a very promising field, although the question of time stability and reproducibility remains.

Besides the Lee–Meisel protocol, the reduction of silver nitrate can be performed by using sodium borohydrate as a reduction agent.¹⁸⁹ As an example, borohydrate reduced silver nanoparticles have been employed as adenosine detectors based on the fluorescence enhancement of a label molecule.¹⁹⁰ Additionally, borohydrate reduced copper NPs are employed in SERS applications.¹⁹¹ A further approach for generating plasmonic nanostructures for SEF is the usage of silver nanoprisms. These metallic nanostructures were produced by irradiation of borohydrate reduced silver nanospheres, whereas nanoprisms with a high yield were obtained after 70 h.¹⁹² Munechika *et al.* characterized nanoprisms as a SEF substrate by illustrating the enhancement of the photoluminescence of quantum dots.¹⁹³

In 2003 Leopold and Lendl published a fast preparation protocol for SERS active silver colloids at room temperature by reducing silver nitrate with hydroxylamine hydrochloride.¹⁹⁴ Hydroxylamine reduced silver NPs are very promising because of a minimal spectral background when applied as SERS substrates combined with an easy preparation protocol.¹⁹⁵ To illustrate the potential as a SERS substrate, several analyte substances have been investigated, *e.g.* zidovudine, melamine,¹⁹⁶ paroxetine,¹⁹⁷ and amoxicillin.¹⁹⁸ Additionally SEF experiments for the detection of quinacridone were performed by using Leopold–Lendl colloids.¹⁹⁹ The protocol has been adapted to an immobile device for the detection of pathogens causing urinary tract infections.²⁰⁰ The bacteria sample was applied on a positively charged glass surface, followed by a two-step synthesis of the SERS-active substrate. A silver nitrate solution was added and allowed to adhere (1 h), and subsequently a hydroxylamine hydrochloride reducing agent was added (1 h reaction time). The generated silver islands were applied as SERS substrates to discriminate *Escherichia coli* and *Proteus mirabilis* bacteria. Additionally, the Leopold–Lendl silver colloid can also be prepared *in situ* on the bacteria cell wall for SERS-based detection of pathogens.²⁰¹

In addition to the well-established protocols for citrate, borohydrate and hydroxylamine reduced metallic nanoparticles, further bottom-up strategies are developed. As an example, ethylenediaminetetraacetic acid (EDTA) was employed as a

reducing agent,²⁰² detecting dye-labelled DNA.²⁰³ A one-step synthesis of star-like gold nanoparticles, using hydroquinone solution in water as a reducing agent, was presented by Morasso *et al.*²⁰⁴ For an electrochemical etching process a reduced graphene oxide (RGO)-covered Si wafer was immersed into a mixed solution of HF and AgNO₃.²⁰⁵ The AgNP-decorated RGO film on Si was utilized as a SERS substrate. As an alternative, RGO was heated to 60 °C under stirring and an aqueous AgNO₃ solution was added.²⁰⁶ After 48 h a RGO-AgNP product was obtained. The as-prepared RGO-AgNPs have been successfully combined with folic acid to yield a promising hybrid material with good biocompatibility and targeting ability, as well as applicability in Raman-based detection of live cancer cells. As a further strategy, the reduction of a silver ammonia complex with glucose to pure silver nanoparticles is reported, whereas the size of the particles is tuned by the amount of added ammonia.²⁰⁷ Photo-induced silver reduction in a flow cell was presented by Herman *et al.*²⁰⁸ Here, aqueous solutions of silver nitrate and NaOH/hydroxylamine hydrochloride were pumped into a flow cell and illuminated with a laser for 30 s. Thus, SERS-active silver substrates were produced inside the channel system. Further, by heating liquids in a microfluidic channel, gaseous bubbles and, at their interface, gold nanoparticle aggregates are generated.²⁰⁹ After drying, a highly SERS active ring is formed. Dimer and trimer gold nanoantennas were prepared on glass slides by aggregating commercially available colloidal suspensions of monodisperse, citrate stabilized gold nanoparticles.²¹⁰ The angular distribution of the experimentally measured SERS enhancement of these gold nanoantennas shows that most of the light is emitted at angles exceeding the critical angle of the air-glass interface. This finding was supported by theoretical considerations.

In conclusion, numerous strategies for bottom-up nanoparticle production protocols have been reported, whereas mostly silver and gold were used as plasmonic materials. In addition to the optimization of established protocols, new procedures have been designed. Thus, a wide range of applications, *e.g.* surface enhanced spectroscopy in life science, can give access to metallic colloidal nanoparticles.

4.2 Core-shell nanoparticles and structures

The usage of aqueous metallic colloidal suspensions has a number of advantages regarding the fast and simple production. However, the reproducibility of the results may be affected by spontaneous agglomeration of the nanoparticles,^{179,211} or surface passivation occurring during the transfer of the nanoparticles to different media.²¹² Therefore, attention was directed towards combining the plasmon resonance of a metal nanoparticle with the stability of another material by creating a core-shell structure. Depending on the preparation protocol, the obtained core-shell structure may consist of a dielectric shell which encapsulates a single nanoparticle of a desired dimension or an aggregation of a small number of nanoparticles.

Gold nanoparticles with a silica shell have a broad plasmon resonance band between 500 nm and 800 nm, depending on the number of cores and their arrangement in the silica shell.^{40,213–215} They are synthesized according to protocols consisting of mainly two steps. First, colloidal gold nanoparticles are prepared.^{186,216} Second, the colloidal Au particles are mixed with pH-activated sodium silicate.^{217,218} At this step, Raman reporter molecules could be optionally added to the mixture, creating SERS labels.^{37,217,219} The silica shell growth is performed with tetraethylorthosilicate (TEOS) and ammonia and continues until the desired shell thickness is obtained.²¹⁷ In order to separate the core-shell structures with different clustering degrees (*i.e.* monomers, dimers *etc.*) and to have narrow plasmon peaks, the nanoparticle suspension can be centrifuged in surfactant-free aqueous iodixanol with a linear density gradient.²²⁰ In the case of the particles produced by Tyler *et al.*,²²⁰ the highest SERS enhancement was observed for the trimer structure. Instead of Raman reporter molecules, fluorescence dyes can be integrated in the same type of gold-silica core-shell structure.^{221,222} As a result, enhanced fluorescence can be observed if the plasmon peak of the gold nanoparticle overlaps with the emission peak of the fluorescent dye.²²¹

Besides gold, other metals also such as silver or a combination of different gold and silver nanoparticles together with iron oxide can be used as the core material.^{223–229} In the case of silver, the plasmonic absorption range can be tuned from 400 nm (VIS) to 900 nm (NIR) depending on the dimensions and shapes of the nanoparticles.^{212,223,230} Moreover, according to Gole *et al.*²²³ silver-silica core-shell nanoparticles can be used for bio-medical applications, because of their diminished cytotoxicity. In order to enhance the medical applicability, iron oxide nanoparticles were synthesized with a silver-silica shell, creating nanoparticles with magnetic properties.²²³ As an example, nanoprobe for cancer cell separation are prepared by decorating magnetic nanobeads with SERS-active Au core-Ag shell nanorods.²³¹ These composites are coated with a silica layer, wherein CdTe quantum dots – the fluorescent agent – are immobilized. Thus, SERS-fluorescent joint spectral encoding (SFJSE) was realized. Furthermore, by employing single-DNA-tethered heterodimeric gold-silver core-shell nanodumbbells (GSND) the gap between two nanoparticles and the analyte can be tuned based on the applied DNA sequences (see Fig. 12).²¹⁴ The obtained particles are very specific and sensitive SERS substrates.

As a further strategy, silver nanoparticles are prepared by employing metal seeds.^{224,227} As an example, Au seeds with a size of 12 nm are synthesized by a modified Lee-Meisel protocol¹⁷⁵ and AgNO₃ is reduced on its surface employing ascorbic acid. In a next step, the obtained nanostructures are encapsulated in a silica shell. The resulting Au-seed Ag-growth nanoparticles with a silica shell had uniform dimensions. To realize bimetallic core-shell nanostructures, palladium hexagonal nanoplates were also applied as seeds.²²⁷ Depending on the AgNO₃/Pd ratio, the plasmon resonance could be tuned between 477 and 971 nm.

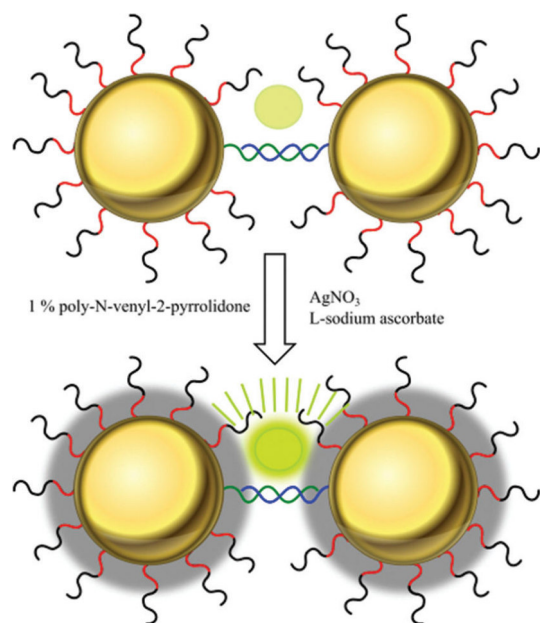


Fig. 12 Nanometer-scale silver-shell growth-based gap-engineering in the formation of the SERS-active GSND (modified from Lim *et al.*²¹⁴).

Various other combinations of bimetallic nanostructures have been developed for specific applications. For instance, Guo *et al.*²³² employed different ratios of gold ions for the core and platinum ions for the shell in order to achieve a plasmon resonance between 500 nm and 600 nm. Because of the low amount of different chemicals and the reaction at room temperature, the proposed fabrication is relatively easy. Also, dielectric materials *e.g.* NaYF₄:Yb,Er²³³ or BaTiO₃²³⁴ were used as core materials for AuNPs. Further, structures consisting of a liquid core containing fluorescent organic dyes and a gold shell were produced by miniemulsion techniques.²³⁵ Another example is realized by embedding small quantum dots in a gold shell. This is done by immobilizing gold ions into their surrounding layer and reducing these ions to metallic gold.²¹⁵ Moreover, the distance between quantum dots and their gold coat can be tuned by varying the thickness of the surrounding polyelectrolyte bilayer. These particles show a stable fluorescence intensity. Moreover, because of the reduced toxicity they can be used in biological systems.

Besides the core-shell structures, particle-in-a cavity or yolk-shell nanostructures also possess interesting optical properties. By tuning the core particle and the cavity's size, shape and material, the obtained nanostructures can be applied for the study of plasmon hybridization, optical trapping, the Fano-like resonance effect, SERS-based biosensing, and the magneto-optical effect.²²⁶ Preparation protocols have been developed for silica cavities with Au cores^{226,236} and further core-materials as Fe₂O₃.²²⁶ They were prepared using chemical bottom up methods and also top down techniques like ion milling. Gold particles in the ring structure can have their res-

onance in the NIR region and are considered as substrates for SERS-based molecule detection.

In addition to the most commonly used core-shell nanostructures with a silica exterior shell, various other materials have been used for encapsulation depending on the application field. Tian *et al.*^{218,237,238} developed protocols for preparing silver and gold nanoparticles with Al₂O₃,²¹⁸ MnO₃^{237,238} and Ag₂S²³⁸ shells. Wang *et al.*²²⁵ synthesized metal-carbon core-shell nanospheres and Zhang *et al.*²³⁹ prepared silver and gold cores with Cu₂O shells. Gold nanoparticles with a silver shell were applied in a SERS-based immunochromatographic assay (ICA) to detect phenylethanolamine as an illegal food additive.²⁴⁰ For combined SERS and SEF experiments, a fluorescence dye is implemented in a polymer layer between a gold core and a silver shell.²⁴¹ Mesoporous shells with a high potential for drug delivery were developed by Ran *et al.*²²⁸

Core-shell particles have been applied in shell-isolated nanoparticle-enhanced Raman spectroscopy (SHINERS).⁴⁰ Here, the signal enhancement is due to gold nanoparticles with an ultrathin silica or alumina shell. A monolayer of core-shell nanoparticles was spread over the surface to be probed. Thus, the chemical composition of any surface is detectable by SHINERS. Recently, SHINERS particles have been applied as noninvasive glucose sensors.²⁴² If the dielectric shell around a metal particle is thicker than the critical distance for minimum fluorescence quenching by the metal, these particles can be used for SEF and SERS experiments.²⁴³ Moreover, core-shell particles were immobilized on a substrate.^{211,244,245} The most commonly used immobilization technique implies at least two steps. In the first step, the substrate is cleaned and functionalized in order to be able to attach the nanoparticles. In the second step, the as-prepared substrate is immersed in a colloidal solution for different periods of time and then rinsed with water or alcohol.^{211,245} If needed, the obtained substrate can be further functionalized.

In conclusion, a wide range of preparation strategies for the synthesis of core-shell particles are available. Due to their increased stability combined with excellent enhancement properties, core-shell particles are promising tools in SES applications.

4.3 Complex-shaped nanostructures by means of seed mediated growth

The uniformity of the surface reactivity of the metallic nanoparticles plays a critical role when exploiting them in a particular application. One approach to achieve this is to synthesize nanostructures by the seed-mediated growth mechanism. Usually, small metallic particles used as seeds are added to a growth solution containing metal salts and a suitable reducing agent. The surface of the seeds has the role of catalyzing the reduction of the metal salts, a process that occurs more readily at the surface than in the bulk solution. Therefore, control over the final morphology is possible, resulting in particles with a high size monodispersity.^{126,246} Additionally, the aspect ratio and the shape of the resulting structures can be easily

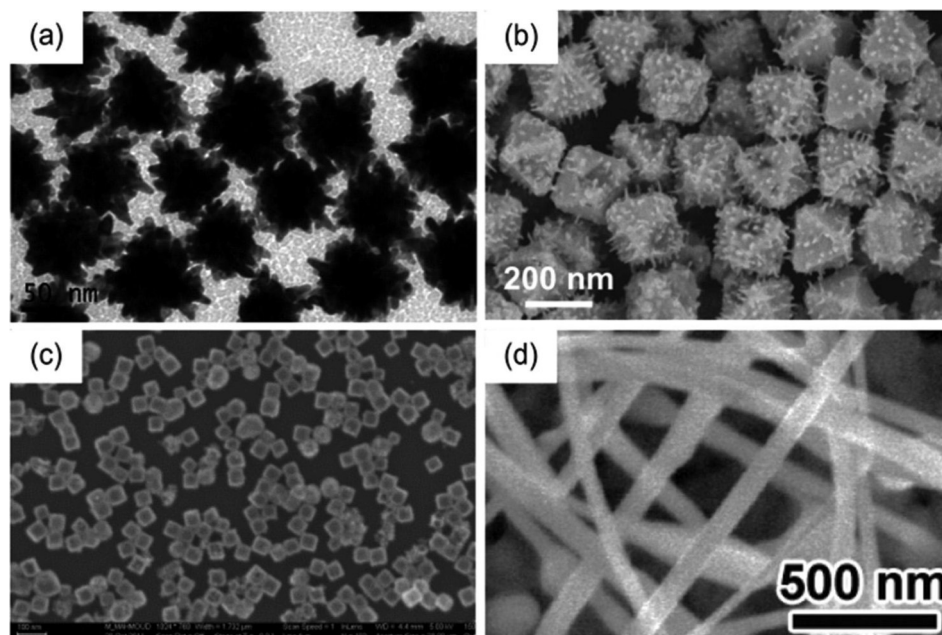


Fig. 13 SEM image of (a) gold nanostars (adapted with permission from S. Barbosa, A. Agrawal, L. Rodriguez-Lorenzo, I. Pastoriza-Santos, R. A. Alvarez-Puebla, A. Kornowski, H. Weller and L. M. Liz-Marzan, *Langmuir*, 2010, **26**, 14943–14950,²⁴⁷ copyright 2010 American Chemical Society). (b) Ag–Au spiky nanoparticles (adapted with permission from S. Pedireddy, A. Li, M. Bosman, I. Y. Phang, S. Li and X. Y. Ling, *J. Phys. Chem. C*, 2013, **117**, 16640–16649,²⁵⁵ copyright 2013 American Chemical Society). (c) SEM image of AuPt nanocages (adapted with permission from M. A. Mahmoud, *Langmuir*, 2013, **29**, 6253–6261,²⁴⁸ copyright 2013 American Chemical Society). (d) SEM image of Au nanowires (adapted with permission from Y.-C. Yang, T.-K. Huang, Y.-L. Chen, J.-Y. Mevellec, S. Lefrant, C.-Y. Lee and H.-T. Chiu, *J. Phys. Chem. C*, 2011, **115**, 1932–1939,²⁵⁴ copyright 2011 American Chemical Society).

manipulated. As a result, colloidal solutions of nanostars,²⁴⁷ nanocages,²⁴⁸ nanoplates^{249,250} and nanorods,^{251,252} can be obtained. Moreover, nanowires²⁵³ and nanothorns²⁵⁴ grown on substrates can also be synthesized either by electrochemical reactions or by chemical bath deposition. In Fig. 13, SEM images of selected complex-shaped nanostructures are illustrated.

Homogeneous as well as heterogeneous spiky nanostructures are mostly preferred when a high overall plasmonic excitation cross section is required. They gain their characteristics due to the hybridization of plasmons localized at the core and the tips of the nanoparticles. In order to obtain such kinds of structures, seeds with different shapes can be used.

Homogeneous structures, such as nanostars obtained by Barbosa *et al.*,²⁴⁷ are based on spherical Au nanoparticles and *N,N*-dimethylformamide (DMF) as the solvent for the growth solution. More specifically, seeds were prepared either by adding HAuCl₄ to a poly(vinylpyrrolidone) (PVP) solution in a DMF/H₂O mixture and reducing Au with NaBH₄, or by the standard citrate reduction method. As a subsequent step in the case of the second method, Au nanoparticles were transferred into ethanol through PVP modification. The as-prepared gold particles were used as seeds for another reduction process of chloroauric acid in DMF in the presence of PVP. The plasmon resonance in the visible region could be tuned by changing the ratio of Au³⁺/seed, temperature, size of the seeds and controlled pre-reduction from Au(III) to Au(I). There-

fore, when the optical enhancing properties of different nanostars were assessed for the detection of 1-naphthalenethiol, it was shown that structures with sharper tips yield higher intensities. A similar synthesis method was also employed to obtain colloidal suspensions of nanowires covered with sharp tips with a high SERS activity.²⁵⁶ In this case, ultrathin gold nanowires were used as seeds. They were prepared by reduction of chloroauric acid with oleylamine and with tri-isopropylsilane as the surfactant. *Via* thiol bridges, the analyte molecule-tainted nanowires were bound to a smooth gold film, giving an enhanced Raman signal. Gold nano-crosses prepared by a seed-growth reaction method and decorated with the dye Cy5 are applied as the SEF label in an immunosensor for the detection of microcystin-LR.⁶⁷

Furthermore, in order to obtain spiky heterogeneous nanostructures, Pedireddy *et al.*²⁵⁵ employed morphologically controlled Ag cores as seeds and high molecular weight PVP for the growth process. First, Ag octahedral nanoparticles were obtained by a polyol method²⁵⁷ while in the second step PVP (MW = 360 kg mol⁻¹) and HAuCl₄ were dropwise added to the seed solution. The anisotropic growth was attributed to a galvanic replacement mechanism,²⁵⁸ where the difference in standard reduction potentials for Ag and Au plays a major role.²⁵⁹ The length of the gold nanospikes could be varied from 10 to 130 nm by changing the amount of the gold precursor added and the injection rates. Field enhancements of up to 10⁴ were obtained in the case of 130 nm spikes. As another example for

an efficient SERS-active substrate, spiky nanourchin structures are prepared employing roughened and aminosilane-functionalized silica cores.²⁶⁰ Here, gold nanoseeds are immobilized on the surface of the silica cores and grow due to reduction processes into long wires.

The same galvanic replacement method can be also used to obtain gold nanoframes,²⁶¹ and gold–palladium and gold–platinum double-shell hollow nanoparticles²⁴⁸ starting from silver nanocubes. The seeds were prepared by reduction of silver nitrate by sodium sulfide in the presence of PVP in ethylene glycol. Chloroauric acid was added to the boiling seed solution and the gold frames were formed by galvanic replacement. The wall thickness of the frames could be tuned by varying the ratio of the added gold salt, whereas thinner walls brought a red shift in the plasmon resonance. In the case of double-shell hollow particles, the gold frames were further used as seeds. The palladium and platinum shells have been obtained by adding Na_2PdCl_4 or K_2PtCl_4 solution to the seeds. The experimental and theoretical calculations illustrated that the particles containing transition metals show SERS enhancement one factor less than the single shell ones.

One of the strategies to enhance the fluorescent emission of quantum dots (QD) is to conjugate them with silica coated gold nanorods (AuNR).²⁵¹ Due to surface plasmonic effects of the attached AuNR the excitation intensity and spontaneous emission of QDs is modified. In order to prepare the AuNRs, Li *et al.*²⁵¹ synthesized gold nanoparticle seeds by reducing chloroauric acid with sodium borohydrate in the presence of cetyltrimethylammonium bromide (CTAB). The as-prepared seeds were drop-wise added to the growth solution prepared by mixing aqueous silver nitrate, CTAB and chloroauric acid. The addition of tetraethylorthosilicate (TEOS) under alkaline conditions produced a silica coating on the AuNRs. Finally, QDs were mixed with the silica coated gold nanorods.

The seed mediated growth process can also be employed to obtain silver nanostructures.^{249,262–265} The easiest way is to prepare the seeds by a modified Lee–Meisel protocol, where silver nitrate was reduced not only by sodium citrate but also with sodium borohydrate. The growth solution was made by mixing CTAB, silver nitrate and ascorbic acid. Depending on the ratio of seed/growth media amount, silver nanoplates with varying diameters can be synthesized. The silver nanoplates were stabilized with a positively charged thiol layer. After functionalization with a carboxyl group containing mercapto-linker, the bioconjugation to a green fluorescence protein is possible and results in a 5.6 times brighter fluorescence based immunoassay than without metal activation.²⁴⁹

The previously presented synthesis methods resulted in colloidal suspensions of differently structured plasmonic nanoparticles. However, nanostructures immobilized on solid substrates have several advantages over the conventional ones. Concerning seed-mediated growth two approaches to prepare these types of structures are available: (1) to synthesize the metallic colloids and afterwards link those to a solid substrate and (2) to grow the nanostructures directly on the substrate. Gold nanorods obtained by seed-mediated growth were

immobilized on multiple substrates, such as electrospun polymer nanofibers,²⁶⁶ mesostructured silica films,²²² conductive indium tin oxide (ITO)-coated glass substrates,²⁶⁷ or gold film coated substrates. Additionally, as already mentioned, colloidal suspensions of nanowires covered with sharp tips can be immobilized *via* thiol bridges to a gold film. Furthermore, in order to obtain 3D SERS substrates 3D templates were decorated with plasmonic nanostructures. For this, a rough Au layer deposited by thermal evaporation on a large area silicon substrate served as the seed for the growth of ZnO nanowires (see Fig. 14).²⁵³ Subsequently, Au nanorods obtained by seed mediated growth were deposited on the poly(2-vinyl pyridine) (P2VP) modified ZnO nanowires. A SERS enhancement factor of 1.85×10^{14} was achieved for the analyte molecule 1,4-benzenedithiol.

In the second approach, gold seeds with a high monodispersity and homogeneous morphology can be easily formed on the surface of a bare ITO electrode by applying a short-term high overpotential.²⁶⁸ Then, due to the preferential deposition and reduction of AuCl_4^- anions on the existing Au seeds, the size of the gold nanoparticles will consequently become larger. By utilizing cyclic voltammetry, the gaps between adjacent nanoparticles can be controlled. The as-prepared substrates proved to have a high reproducibility, stability and an enhancement factor of $\sim 1.3 \times 10^6$ for the SERS signal. Furthermore, Yang *et al.*²⁵⁴ reduced and deposited AuCl_4^- on an ITO cathode coated sequentially with a layer of sputtered Ti and a layer of sputtered Au. The Au layer served as a seeding layer for Au nucleation. By controlling the growth parameters, a series of nanostructures was obtained, including nanoparticles, nanothorns and nanowires.

In conclusion, seed-mediated growth offers researchers a complete toolbox to obtain differently structured nanoparticles either in colloidal suspensions or on solid substrates. Additionally, these structures proved to offer high enhancements for both Raman scattering and fluorescence emission,

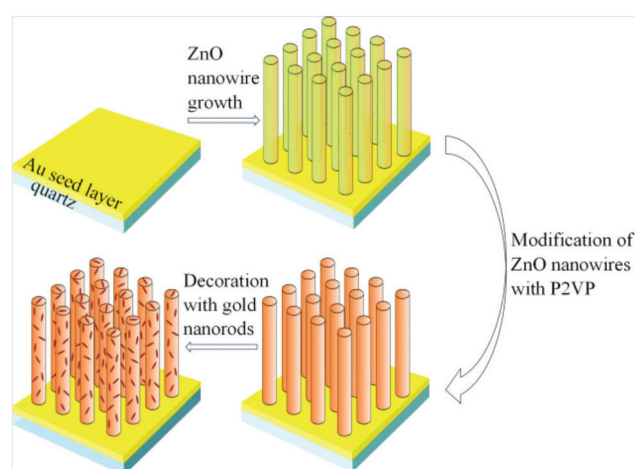


Fig. 14 3D SERS-active substrate based on the seed-mediated growth of ZnO nanowires (modified from Kattumenu *et al.*²⁵³).

having the additional advantage of being highly monodisperse.

5. Self-organization processes for the fabrication of assemblies and arrays

In the previous section, bottom-up fabrication strategies to produce metallic colloids, core-shell architectures and complex structures by seed mediated growth were reviewed. The following section focuses on the controlled assembly of bottom-up produced nanoparticles, the formation of clusters and the immobilization of nanoparticles on a substrate. Furthermore, self-organizing processes play an enormous role in template-based methods. For some preparation strategies, a clear classification of template-based or self-assembling processes is not possible since both approaches are applied for the production. Thus, we did the classification in the following section based on the structure-defining step.

5.1 Self-assembled nanoparticles, clusters and arrays

One of the easiest ways to create plasmonic substrates is the self-assembly of bottom-up nanoparticles from colloidal solutions. The methods are easy to handle, cost-efficient and the structures can be fabricated on non-planar substrates, or even on liquid/liquid interfaces.²⁶⁹ The nanoparticles can form different patterns with various degrees of complexity, from one-dimensional arrays to three-dimensional clusters. This self-assembly occurs as a result of reaching the minimal

energy state due to electrostatic interactions or (bio)chemical conjugations, or because of an applied external electric field.²⁷⁰

The electrostatic interaction that occurs between the nanoparticles themselves and also between the nanoparticles and the substrate is well known; however, it is difficult to tune or alter the properties of such structures.²⁷² Two principle strategies are available to create controllable nanosized gaps between nanoparticles: with small molecular weight substances like alkanethiols,²⁷³ or with high molecular weight substances like two compatible DNA strands,⁶⁴ proteins²⁷¹ or special macrocycles.²⁷⁴ A well-known and very strong bioconjugation is the streptavidin–biotin interaction.²⁷¹ By coating citrate-reduced gold nanoparticles with biotin the nanoparticles are conjugated at a distance of 8 nm with streptavidin as the linker molecule (see Fig. 15). The assembly of nanoparticles by biotin interactions only leads to a reduced gap size. With a defined distance of 5 nm between two gold nanoparticles, the analytical SERS enhancement factor is estimated to be 10^7 . Gold nanoparticles can also be assembled by utilizing cucurbit[*n*]uril, an organic macrocycle based on glycouril monomers.²⁷⁴ Here, the number of glycouril monomers defines the distance within the conjugate. Employing cucurbit[5]uril, distances of 0.9 nm between the gold nanoparticles with a plasmon resonance in the visible region could be created.

The assembly of nanoparticles in one dimension results in the arrangement of worm-like chains. These structures can be prepared by electrostatic interactions on a grooved surface (see Fig. 16),²⁷⁵ *via* covalent binding applying CTAB and thiol-terminated polystyrene,^{276,277} by side specific ligand exchange,

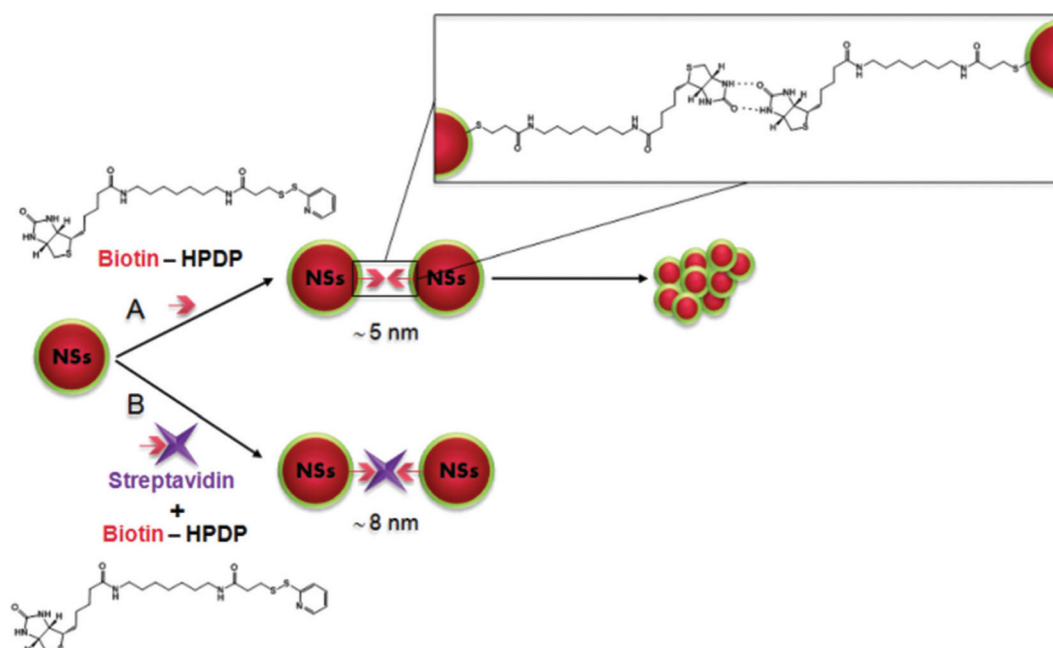


Fig. 15 Bioconjugation between functionalized nanoparticles using the biotin–streptavidin bonding (reprinted with permission from J. C. Fraire, L. A. Pérez, E. A. Coronado, *ACS Nano*, 2012, 6(4), 3441–3452,²⁷¹ copyright 2012 American Chemical Society).

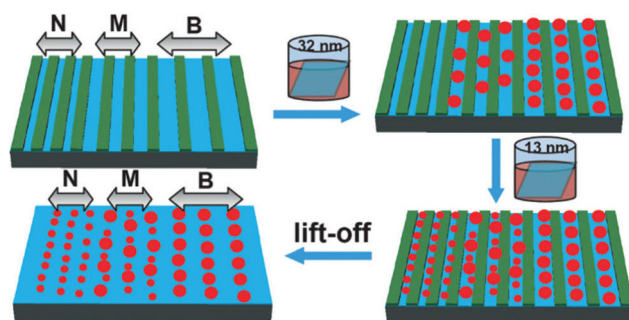


Fig. 16 Fabrication of multiplexed 1D nanoparticle arrays on a grooved surface (reprinted with permission from L. Jiang, Y. Sun, C. Nowak, A. Kibrom, C. Zou, J. Ma, H. Fuchs, S. Li, L. Chi and X. Chen, *ACS Nano*, 2011, 5(10), 8288–8294,²⁷⁵ copyright 2011 American Chemical Society).

by application of an external electromagnetic field²⁷⁸ or by AFM based techniques.²⁷⁹ These structures are applied for the development of theoretical models and basic research. However, the SERS-active substrate area is relatively small, decreasing the cost-efficiency of the fabrication process and, thus, making such substrates unattractive for life-science applications.

The fabrication of two-dimensional arrays is much easier in comparison with worm-like arrangements. The production of regular arrays based on self-assembly strategies is, in most cases, based on a combination of top-down and bottom-up techniques. The most common techniques used in the fabrication of such substrates include the dispersion of polystyrene beads on a surface, dispersion of metallic particles, deposition of metallic layers, functionalization of the surface, wet or plasma etching or e-beam lithography (EBL). By functionalizing the surface using various thiols, silanes or polymers, followed by the attachment of metallic nanoparticles from a solution, a very high signal enhancement can be obtained.²⁸⁰ This procedure can be repeated to form a multi-layered array, tuning its properties and sensitivity up to the detection of tens of molecules, or varying the distance between the layers by alterations of pH or salt concentration.²⁸¹ This approach allows for the fabrication of easily controllable SEF substrates.²⁸² Another common approach uses charged polystyrene nanospheres (nanotemplating), which tend to disperse on the glass surface, thus forming an even distribution pattern.²⁸³ A layer of metal is deposited onto the nanospheres,²⁸⁴ forming a temporarily stable substrate with both uniform enhancement areas and hot-spots.^{285,286} These substrates, known as film over nanospheres (FON), are compatible with mass production methods.

Furthermore, arrays can be created from nanoholes or nanovoids ordered in a regular pattern. Nanohole arrays can be prepared with conventional EBL or by using self-assembly of polystyrene nanospheres combined with wet etching processes for size reduction.^{287,288} These arrays are coated with evaporated silver,^{289,290} and gold²⁸⁷ or decorated by electroplating of Ni/Au.²⁸⁸ Finally, the polystyrene spheres are removed.

EBL nanohole arrays can be filled with nanoparticles by dipping the wafer in a colloidal solution and drying.¹²¹ In Fig. 17, such a fabrication procedure is introduced. The resulting arrays are very regular with tunable shapes of the holes, their periodicity and diameter. Gold arrays produced by the same routine are used for surface enhanced coherent anti-Stokes Raman spectroscopy (SECARS) experiments showing an enhancement of the coherent anti-Stokes Raman spectroscopy (CARS) spectrum by 10^9 .²⁸⁷ To prepare a regular pattern of nanovoids, gold nanoparticles are prepared on and in an inverse opal structure of TiO_2 .²⁹¹ Here, TiO_2 sol is infiltrated over self-assembled monodisperse polymer microspheres. After calcinations and removing the polymer beads, the gold nanoparticles are sputtered in the array. The DNA detection of the human immunodeficiency (HI) and the severe acute respiratory syndrome (SARS) virus are performed based on the enhanced fluorescence.

By patterning of silicon wafers with an array of lines utilizing EBL and reactive ion etching (RIE), silver nanoparticle suprastructures with a controllable size, morphology and position can be prepared.²⁹² Following this approach, a silver-amino acid complex is reduced *in situ* to pure silver particles, which self-assemble to form metal supraspheres. By applying this substrate in SERS, 4-aminothiophenol can be detected down to a concentration of 10^{-10} mol L^{-1} . Instead of positioning metal nanoparticles in a nanohole array, the inverse form of nanoantennas²⁹³ or nanopillars²⁹⁴ are prepared on a substrate. The pillars are prepared by self-assembly of the pretreated colloidal silver solution (citrate reduced) on a pure semitransparent silver mirror. A 1000-fold fluorescence enhancement was observed. Furthermore, the combination of bottom-up and top-down techniques is used for the production of different shapes of nanoantennas.^{293,295} First, pillars were prepared on a Si wafer by nanoimprint and RIE. The evaporation of gold leads to a self-assembly of small gold dots at the side of the pillar, showing a high SERS activity. This procedure is precise, simple, cost efficient and can create large areas of a regular pattern (in this case on a 4" wafer).

Ordered arrays of nanoparticles can also be prepared based on the production of nanocones of a silicon-germanium mixture.²⁹⁶ In this case, a silicon-germanium layer was placed and plasma was etched on a silicon wafer. As a result, a regular and homogeneous layer of nanocones was formed. The assembly of gold nanoparticles results in a SERS substrate with an enhancement factor of 2×10^8 , in this case used for the investigation of the analyte 1,2-bis-(4-pyridyl)ethylene.

Metallic nanoparticles can also be self-assembled in non-periodical arrangements. As an example, Lee *et al.*²⁹⁷ developed a "plasmonic paper", starting from a filter paper on which seed-mediated grown gold nanorods were adsorbed. By using this flexible plasmonic substrate, an enhancement factor of $\sim 5 \times 10^6$ for the SERS signal of a non-resonant analyte was found. Another flexible substrate was developed by using natural rubber and assembling gold nanoparticles.²⁹⁸ Here, a thin rubber film is dipped in a solution of gold(III) chloride solution. The reduction is triggered by the reducing agents

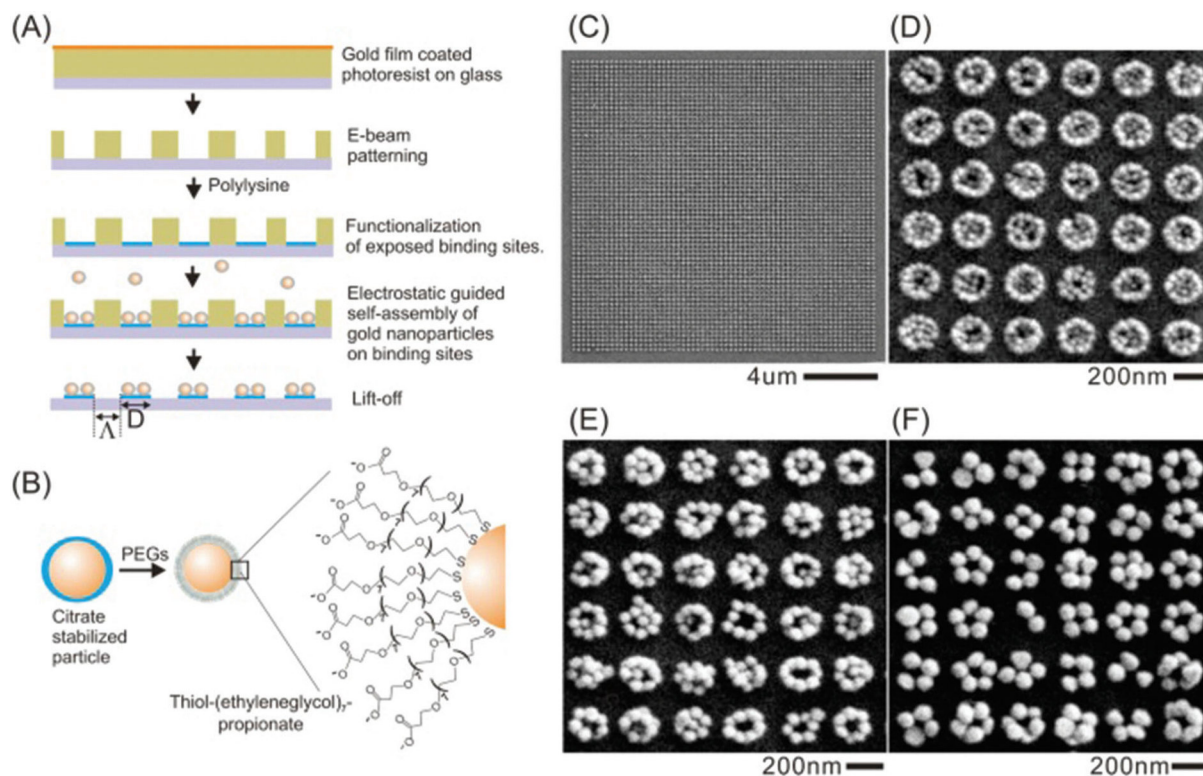


Fig. 17 Self-assembly of different gold particle patterns based on their size. (A) Fabrication scheme for the production of nanoparticle cluster arrays (NCA). (B) Functionalization of the nanoparticles with short PEG molecules. (C) SEM image of NCA and SEM images of NCAs with a gold nanoparticle diameter of (D) 40 nm, (E) 60 nm and (F) 80 nm (reprinted with permission from B. Yan, S. V. Boriskina and B. M. Reinhard, *J. Phys. Chem. C*, 2011, **115**(50), 24437–24453,¹²¹ copyright 2011 American Chemical Society.)

comprised in natural rubber. Moreover, spraying of silver nanocubes dispersed in chloroform and their assembling on quartz surfaces was reported.²⁹⁹ In the next step, a fluorescent conjugated polymer was assembled on this nanoparticle surface by using a Langmuir–Blodgett technique. Also, nanoparticles with a rosette-like structure are reproducibly created based on the self-assembly of enzymes on a surface.^{300–302} Here, silver nitrate is reduced by the enzymatic activity of the horseradish peroxidase. The self-assembling of plasmonic active particles in swellable polymers is done by preparing silver fibers and functionalizing them with gold nanorods embedded into reactive polyacrylic acid.³⁰³ The pre-prepared positively charged gold nanorods attach to the negatively charged silver nanowires in a simple wet chemical reaction. By varying the pH value, the distance between gold nanoparticles and the silver wire can be tuned due to the swelling of the reactive PAA layer, which also changes the plasmonic resonance wavelength. In order to increase the homogeneity of the physical properties of citrate-reduced gold nanorods, they can be functionalized by a layer-by-layer assembly of thin films. Here, positively charged rods are functionalized by positively charged thiol molecules.^{304,305} Other procedures can also be used for the functionalization of the structures in order to obtain certain application-related properties.^{306–308} For example, self-organization of gold nanoparticles in a solution

of *N*-methyl-*N*-hexadecylmorpholinium bromide (C16MMB) during crystallization leads to a plasmonic nanoparticle material which can be used for SERS experiments.³⁰⁹ Also, by heat treatment of an Ag⁺/polymer composite film on quartz glass, a large-area plasmonic active substrate can be prepared by a simple and cost-efficient protocol.³¹⁰

Three-dimensional substrates, whose complexity exceeds that of simple multi-layered arrays, can be fabricated directly in solvents. A more advanced building material for such clusters is amphiphilic micelle-like nanoparticles,^{269,311} which are composed of gold nanoparticles and amphiphilic block copolymers. Depending on nanoparticle sizes, solvent or copolymers length, they can be crafted into a variety of higher level structures. These structures are not fixed on any solid surface and can be used directly in solutions or *in vivo*. In Fig. 18, a scheme and SEM images of these amphiphilic micelle-like nanoparticles are depicted.

If particles without residual chemicals are needed, surfactant-free gold nanoparticles can be produced *via* laser ablation.³¹² Ultra-short laser pulses excite a submerged metal target causing it to eject nanoparticles into the surrounding medium, for example purified water. The advantage of this method is the absence of additional chemicals. Thus, no background contribution due to the stabilizer molecules is expected. The size of the nanoparticles is very homogeneous

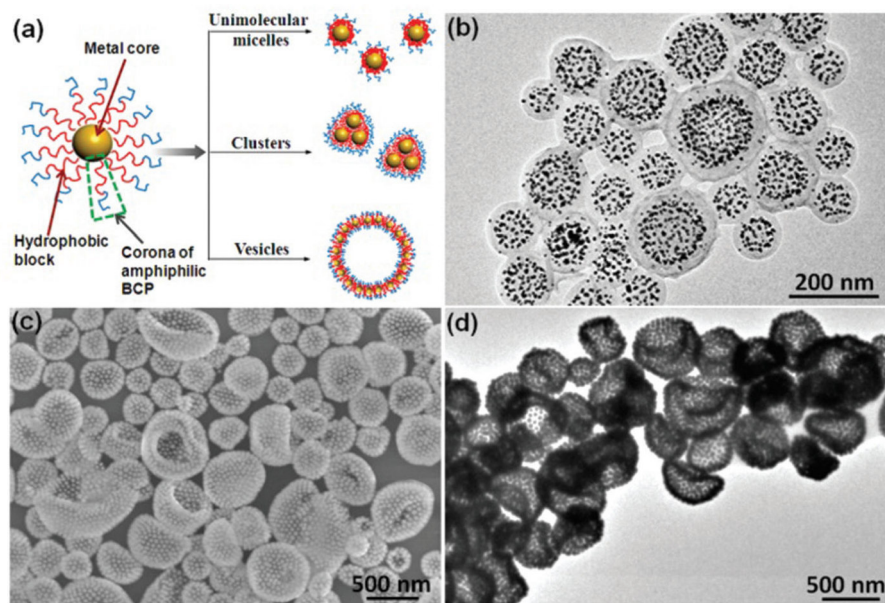


Fig. 18 Amphiphilic nanoparticles' structure (APMNS) and their vesicular assemblies. (a) Shows the production scheme for APMN, (b–d) show the TEM (b, d) or SEM (c) images for AMNPS with a polystyrene mass-weight of 34 000 and a gold-core diameter of 5 nm (b) or 40 nm (c, d) (reprinted with permission from J. He, X. Huang, Y.-C. Li, Y. Liu, T. Babu, M. A. Aronova, S. Wang, Z. Lu, X. Chen and Z. Nie, *J. Am. Chem. Soc.*, 2013, **135**(21), 7974–7984,³¹¹ copyright 2013 American Chemical Society).

and the size as well as the plasmonic active range can be tuned by the laser power and ablation time. With laser ablation processes also Au–Fe-alloys can be prepared which can be used as SERS substrates whereas the plasmonic range can be easily tuned by the amount of iron in the alloy.³¹³

In summary, the main advantage of self-assembly methods is their cost efficiency and the simplicity of preparation, allowing the fabrication of large plasmonic active areas. Although the resulting substrates may not be as uniform as top-down fabricated substrates, they provide high enhancement at a low cost, making them ideal for mass applications.

5.2 Template based methods

Another method to create complex plasmonic structures and arrays is based on the usage of template structures. Such template structures are prefabricated nanostructures with a specific orientation at the surfaces for preparing arrays of metal nanoparticles. These substrates allow the fabrication of large surface areas with a well-ordered, nanostructured architecture. Template based substrates are promising not only due to their plasmonic properties but also because of their smaller manufacturing effort and their high efficiency across a large area.

Another critical issue of plasmonic substrates is their storage lifetime which is affected by environmental conditions. Metals are the key element for surface enhanced spectroscopic techniques; however, if they lack stability, the SES performance is decreased, thus leading to a reduced shelf life. To overcome these issues, template based plasmonic structures are perfect candidates as SES substrates. They can be stored easily until needed and then coated with a metal for the respective chemi-

cal or biochemical application. Within the last few years, many research activities have been focused on template based plasmonic structures. In this section, we will summarize surface mask templates, biological templates, porous templates and sheet templates. For more comprehensive details about template based techniques, the reader is referred to the literature.³¹⁴

Most commonly, regular arrays of gold or silver nanostructures are prepared by employing polystyrene (PS), and other polymeric or silica spheres as templates which is known as nanosphere lithography (NSL).^{11,21,315–324} Here, monolayers of self-assembled nanospheres are arranged on a substrate by, for example, a spin coating process or self-assembly strategies. In the next step, the metal is deposited on the nanosphere layer. Finally, the nanospheres are removed and only nanostructures representing the holes in the lattice remain (see Fig. 19). In the last decade, the NSL procedure was widely used for the production of plasmonic arrays applied in bioanalytical detection schemes. Similar strategies based on the NSL concept are applied for assembling SiO₂ nanospheres and depositing carbon quantum dots into this geometry, building two-dimensional (2D) and three-dimensional (3D) honeycomb structures (see Fig. 20).³²⁵ First, a single layer of colloidal SiO₂ is assembled on a flat surface by using the Langmuir–Blodgett (LB) technique.³²⁶ In the next step, electrochemical deposition is applied to generate carbon quantum dots in the surface mask. In doing so, carbon quantum dots are deposited onto SiO₂ nanospheres under an applied voltage of 5 V, creating the structure of the honeycomb. Finally, the SiO₂ cores were removed by etching. Thus, these SiO₂ templates are often

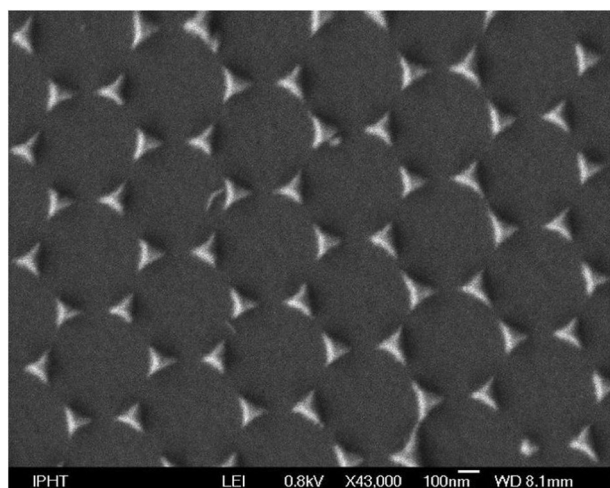


Fig. 19 SEM image of hexagonal arranged gold triangles prepared by nanosphere lithography (NSL).

called sacrificial templates creating new nanostructures which are made from other materials. In addition, 3D honeycomb structures are available by using a 3D colloidal SiO_2 nanosphere template. To apply these structures as SERS substrates, 40 nm of gold is deposited by sputtering. Moreover, to produce ZnO hollow nanosphere (HNS) arrays decorated with silver nanoparticles, PS nanosphere templating on silicon substrates

is employed.³²⁷ Here, a self-assembled PS nanosphere monolayer on a silicon substrate is used for generating ZnO HNS arrays. Within the production process, oxygen plasma is applied to control the size of the PS nanoparticles, followed by the deposition of a thin ZnO film onto the nanospheres. Finally, the top of the substrate is covered with silver. By this technique, the electrical field is concentrated in hot spots, which is good agreement with FDTD simulations. A further example for surface mask templates is vertically aligned 3D ZnO nanorods having plasmonic nanogaps sputtered with silver.³²⁸ Furthermore, atomic layer deposition (ALD) is used to apply TiO_2 onto semi-shell nanospheres in combination with gold. The most important property of these nanostructures is the self-cleaning function by UV photocatalytic degradation of the target molecules. Analogous to the previous fabrication routines, thin films of bowl shaped silver cavities are prepared by using PS sphere templates and electrochemical deposition.³²⁹ The plasmonic properties of these substrates are tunable by changing the silver thickness of the dips. As a SERS-based application of these silver cavities, a sandwich structure is introduced by applying the second layer of silver in order to identify the labeled proteins. The detection limit of TRIT and the Atto610 labeled protein is reported to be 50 and 5 pg mL^{-1} , respectively. Similar to bowl or honeycomb-like architectures are hollow-like nanostructures, which are of interest for fields like sensing and biomedical applications. Several strategies for generating hollow nanostructures

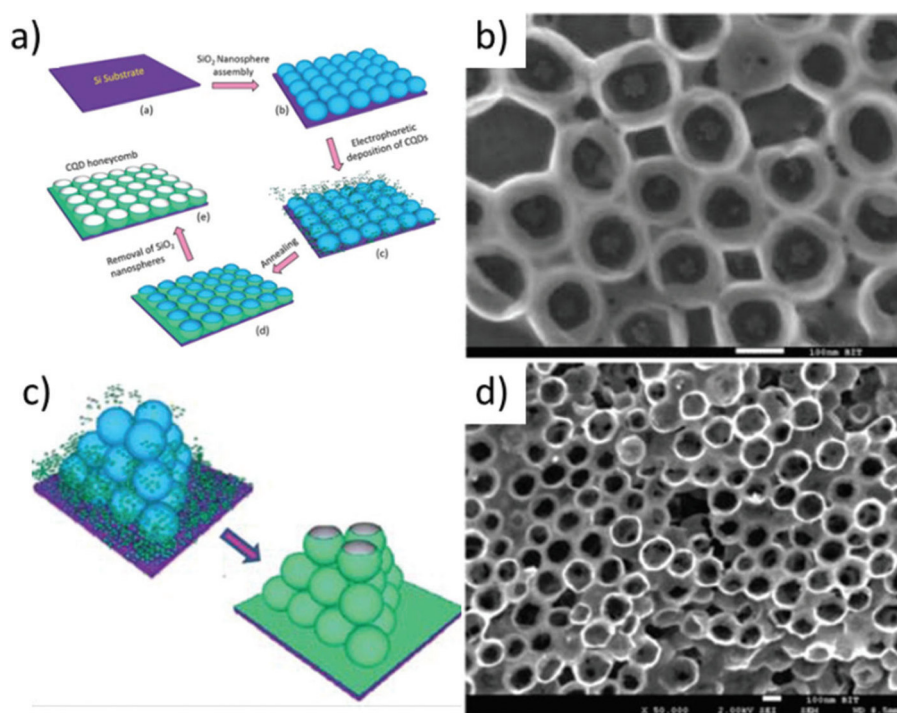


Fig. 20 Fabrication process for the formation of a 2D (a) and a 3D (c) honeycomb structure of carbon quantum dots and the related SEM images of the 2D (b) and 3D (d) structure (reproduced from Y. Fan, H. Cheng, C. Zhou, X. Xie, Y. Liu, L. Dai, J. Zhang and L. Qu, *Nanoscale*, 2012, 4, 1776–1781,³²⁵ with permission from The Royal Society of Chemistry).

working as sacrificial templates exist.³³⁰ Instead of producing hollow nanosphere structures, creating silver hollow micro cubes by using Cu₂O cubes as a chemical template is reported.³³¹ Thus, hollow micro cubes decorated with elementary silver are formed by chemical reactions between AgNO₃ and Cu₂O. With this highly porous shell structure, the detection sensitivity of SERS is as low as 10⁻¹⁴ M for rhodamine 6G.

Instead of using polymer or silica spheres as the template, porous Al₂O₃ produced by different anodizing techniques can be applied.^{332–334} These nanoporous templates are versatile platforms for sensing, storage and separation applications and are created by a two-step anodization of a thin aluminum film on the surface of silicon substrates (anodic aluminum oxide, AAO). The porous size and depths are controlled by the anodic oxidation. On this porous substrate template gold nanoparticles³³³ or silver or gold nanorods³³⁵ can be immobilized. Finally, the entire array can be coated with an evaporated thin gold layer.³³⁴ Furthermore, CdSe nanotubes are used as a template for structuring an aluminum oxide membrane, followed by an immobilization of gold nanoparticles.³³⁶ Thus, arrays of gold nanotubes with tunable sizes are created, providing a SERS enhancement of approximately 4 orders of magnitude. Alternatively, the periodic AAO structure can be loaded with self-assembled gold nanoparticles, creating high hydrophobic AAO channels.³³⁷ Instead of using porous AAO templates, other materials are available for creating nano- or micro-porous structures. For example, gold nanoparticles, embedded in dried poly(vinyl alcohol) gel, have a great stability and sensitivity detecting crystal violet down to 10⁻¹² M.³³⁸ Similarly, block copolymer nanostructures demonstrate a strategy for an imprinting mold with sub 100 nm diameter holes.³³⁹ This technique results in arrays of micro-porous cylinders with accommodating gold nanoparticles.

Applying sheet templates is advantageous in sensing, catalysis and biological applications which benefit from the material's good thermal and electrical conductivity, their catalytic activity, durability and porosity.³⁴⁰ Briefly, these functional materials are used for immobilization of metallic nanoparticles on the surface. In recent years the importance of graphene as a template substrate has increased, since this promising material shows excellent thermal and optical properties.³⁴¹ As an example, graphene is applied as a sacrificial template to produce monolithic macroporous gold films by a simple annealing process. The porosity of these metal substrates is controlled by the graphene/gold weight ratio. Moreover, thin multilayer polymer films are used as a template to attached gold nanoparticle arrays with calcination.³⁴² This template shows a good thermal and chemical stability and will allow applications in sensing, catalysis and optoelectronics.

Furthermore, template printing is described as an efficient and easy-to-perform technique.³⁴³ A PDMS template is evaporated with a thin gold layer. In an organic vapor the polymer swells and the gold cracks into small pieces. In the next step, the PDMS stamp is brought into contact with a self-assembled monolayer of thiols to peel the gold nanoparticles from the PDMS to the final substrate. Silicon wafers can also be

employed as a template material.³⁴⁴ Here, the silicon is structured with lithographic methods or a focused ion beam (FIB). Subsequently it is coated with a metal, which is then printed on a suitable substrate. These substrates show a plasmonic resonance in the green and red spectral regions and were used as SERS substrates with an enhancement factor of 1.4×10^7 . Furthermore, nanohole arrays³⁴⁵ and gold micro arrays produced by electron beam lithography³⁴⁶ are discussed as template structures. Since these templates are fabricated by top-down techniques, the reader is referred to the next section for more details.

In addition to the previously described surface-mask templates, nature provides flawless 3D structures with a high conformity as templates for SES substrates. Microorganisms like viruses and bacteria are applied as templates for assembling the nanoparticles.^{314,347} As an example, *Coscinodiscus asteromphalus* diatom frustules are used in combination with a wet chemical coating process, mimicking free standing gold nanostructures.³⁴⁸ This 3D hexagonal hole pattern allows for extraordinary optical transmission studies.

In conclusion, template based techniques have the advantage of better controlled geometries combined with an easy and large-scale fabrication of plasmonic substrates. However, because feature defects from the template can be converted to the final substrate, a high quality and robust template is crucial for the reproducibility of these substrates.

6. Top-down techniques for the preparation of highly reproducible plasmonic structures and arrays

In the previous sections, bottom-up and self-organization processes were discussed to produce plasmonic structures and arrays with different complexities. However, such techniques are limited to plasmonic architectures which resemble the specific geometry given by the respective chemical, biochemical or electrochemical reaction. A direct transfer of new and interesting optical characteristics obtained by numerical simulations of artificial patterns might be impossible because previously described fabrication strategies fail to reproduce the desired array. Within this section, the third main group of fabrication strategies for SES substrates, top-down routines, will be discussed. These strategies are the basis of the creation of artificially shaped plasmonic nanostructures with a high reproducibility and structural homogeneity.

In Fig. 21, a selection of possible nanostructures by means of top-down techniques is given. The SEM images illustrate the broad capabilities of electron beam lithography and related techniques. Within the following sections, the various top-down methods are illustrated in detail.

6.1 Template preparation by means of electron beam lithography

Electron beam lithography (EBL) is one of the most prominent techniques in creating periodic nanostructures for plasmonic

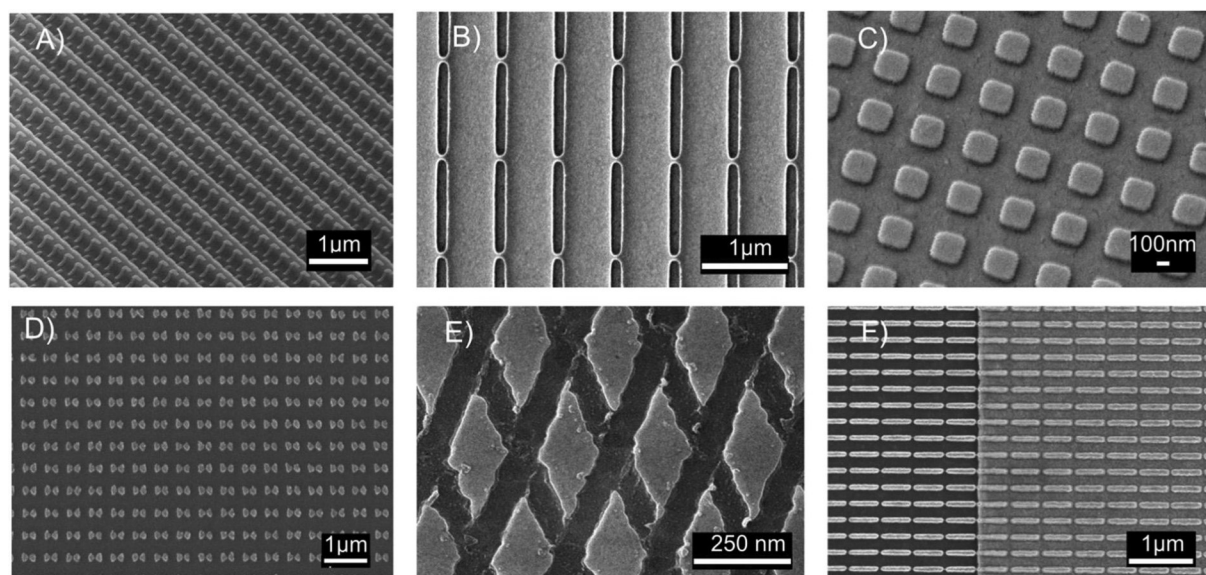


Fig. 21 SEM images of plasmonic arrays prepared by top down techniques illustrating the spectrum of achievable geometries: (A) chiral plasmonic structures prepared by a multilayer EBL process,³⁴⁹ (B) plasmonic gaps for enhanced sensing in the MIR region, combining the EBL and ICE-RIE processes, (C) SERS-active silver nano squares produced by EBL,³⁵⁰ (D) Bowtie antennas as the SERS substrate, (E) gold nanorhombs produced by EBL and RIE etching processes,^{50,351} (F) SEIRA structures produced by lift-off EBL.

applications.³⁵² Here, an electron beam is scanned over a positive resist, *e.g.* PMMA and ZEP520,³⁵³ or a negative resist *e.g.* Calixarenes and Su8,³⁵⁴ thus changing the solubility of the resist layer by a photochemical process. In the case of positive resist layers, the solubility of the illuminated area is increased due to degeneration of covalent bonds within the polymer. In negative resists, the illumination decreases the solubility, which is attributed to the forming of covalent bonds within the resist layer. After exposure, the intended structure is obtained by removing molecules with a higher solubility utilizing a suitable solvent like acetone.

Due to the diffraction limit, optical lithography is only feasible up to a lateral resolution of around 500 nm, although performance enhancing methods like immersion lithography become available.³⁵⁵ Since electrons have a much shorter wavelength, EBL structures below 10 nm are possible.³⁵⁶ Since the scanning operation is an integral part of the process, nearly perfect control of the electron dose and with this, precise control of the structural size is possible. However, the structural features are limited to 10 nm due to the beam broadening and the proximity effect.³⁵⁷ High costs for EBL are mostly attributed to the laborious devices used and/or slow speed of writing, but recent advances drastically reduce the processing time for periodic arrays of relatively simple shapes like squares and rods applying character projection.^{358,359}

A direct approach to generate periodically arranged plasmonic arrays is to apply an EBL structured template and cover or functionalize the layer directly. As an example, quasi 3D SERS substrates were generated by EBL on reflective substrates like silicon or ITO, or on homogeneous dielectric media as *e.g.* PDMS, and finally coated with gold.^{139,360} Based on the result-

ing SERS spectra of 4-mercaptopyridine, an enhancement factor of roughly 10^9 was estimated. Furthermore, these structures were used to detect microorganisms and to separate between Gram-positive and Gram-negative bacteria strains with SERS spectroscopy. Ring resonators could be produced by EBL forming concentric silver rings which have the same periodicity but a different width.³⁶¹ A SERS spectrum of R6G on this substrate had a much better signal-to-noise ratio with lower laser intensity (15 μ W) than a comparable SERS spectrum recorded on a silver film with a higher laser intensity (1.5 mW). Such split ring resonators are well described in theory and experiment.³⁶² Plasmon resonances of the EBL processed and silver-coated split ring resonators were detected in the visible and infrared spectral region, depending on the polarization of the *E*-field of the incident light. The enhancement factors for SERS measurement of 2-mercaptopyridine were calculated to be 10^3 . To detect myoglobin on a SERS substrate, nanograins on a gold-chromium substrate were prepared by means of electro-plating and EBL. Here, EBL-generated holes in a resist layer were subsequently filled *via* an electroplating process. After removal of the resist, individual Au-nanograins remained.³⁶³ By employing these substrates for SERS, reliable spectra of myoglobine were recorded. Finally, silver nano-squares prepared with EBL showed the dependency of the intensity of SERS signals on the thickness of the respective silver layer.³⁵⁰

These results demonstrate both the versatility and potential of EBL generated templates. Due to ongoing technical improvements, much of the limitations of EBL, *e.g.* poor speed and high costs, are resolved. Modern techniques such as character projection and high throughput setups significantly

decreased writing, in some cases, *e.g.* for regular patterns such as gratings, by several orders of magnitude. Finally, the masks created by EBL are essential for lift-off processes, which will be highlighted within the next paragraph.

6.2 Lift-off processes as part of lithographic methods

An alternative technique to prepare reproducible plasmonic arrays is based on employing templates for lift-off processes or as an etching mask. In a lift-off process, a structured resist layer (see above) is covered with a metal layer. Subsequently, the package is immersed in a solvent,³⁶⁴ which removes the resist and with that the metal on top of the resist. Only metallic nanostructures remain, which have been deposited through the openings of the resist layer onto the underlying substrate. The quality of the structures created crucially depends on the successful removal of unwanted patterns, requiring resist sidewalls accessible by the solvent. This excludes sophisticated deposition techniques such as atomic layer deposition, because its high surface conformity would cover all sidewalls, preventing the solvent to remove the resist.

The most common technique to produce nanoscale discs with small gap sizes between them is EBL-based lift-off.³⁶⁶ Two gold discs, one positioned over the other, are separated by a dielectric layer and finally covered with a fluorescent dye. The diameters of the discs and the thickness of the spacer between them vary and influence the plasmonic behavior. The variation of structural parameters can increase the fluorescence intensity up to 30 times. Moreover, pillar structures are available as plasmonic active substrates *via* lift-off processes in EBL. Two different types were defined: pillars with a metal cap standing on a dielectric (like SiO₂)³⁶⁷ and pillars with a metal cap standing on metallic films.^{368,369} Comparing the SERS enhancement factors, silicon pillars with a gold cap standing on a gold surface showed a, by two orders of magnitude, increased SERS enhancement over silicon pillars with a gold cap on a silicon surface.³⁶⁷ Depending on the diameter of one pillar and the gap between two pillars, the enhancement factor for benzenethiol could be calculated to be 1.2×10^8 .³⁶⁹ A quasi 3D gold nanostructure was fabricated based on applying an EBL-produced master-die, whereon a template was deposited. After removing the master it was coated with gold.³⁷⁰ Following a similar routine, the group prepared 2D nanohole arrays by coating the EBL structure aforementioned with gold and then lifting off the nanopillars with the help of a PDMS layer, resulting in gold nanoholes on silicon. Both structures were then tested as SERS substrates. The template stripping method can be further combined with other techniques. As an example, bottom up large scale fabricated hemispherical shell noble metal structures was applied as a template for the template stripping process.^{371,372} The template was formed by a porous Al₂O₃ film on aluminum *via* an anodization technique. A thin metal film was deposited onto the porous Al₂O₃ surface. The following steps were performed as in the classical template stripping process. With this method, the radii of the hemispherical cells were tuned and with this tuning the optical characteristics became possible. Template stripping is

not only restricted to nanoholes or void structures; also Bull's eye, pyramidal,³⁷³ groove, square-shaped bump, cylinder, hexagonal arrays^{374–376} and other structures could be produced by this method. These structures have much smoother surfaces in comparison to reactive-ion etched structures. Moreover, template-stripped structures could be maintained for Ag, Au or Cu metals, thus making integrated multilayer architectures possible.³⁷³ Finally, pyramidal structures could be utilized as tips for near-field spectroscopy techniques, *e.g.* tip-enhanced Raman spectroscopy (TERS). Such tips can be produced massively parallelly with a high yield, high reproducibility and high durability (see Fig. 22).³⁶⁵

To conclude, lift-off processes in lithographic methods guarantee for a high diversity of plasmonic substrates. However, the resistivity against etching and the achievable aspect ratio of the resist layer might limit the application of these approaches for the fabrication of nanostructure arrays.

6.3 Ion etching and ion beam etching in EBL-based processes

Template stripping methods as discussed in the previous section are limited with respect to the thickness of the metal layer and the deposition temperature. Ion etching (IE), as well as its directed form ion beam etching (IBE),³⁷⁷ are further options to process EBL templates. Moreover, IE as a purely physical process can be combined with a reactive gas like CF₄ or SF₆, resulting in reactive ion etching (RIE) or its directed form, reactive ion beam etching (RIBE). By depositing the functional layer and afterwards applying an EBL template (structured resist layer), the template acts as a protective layer where non-covered areas of the functional layer are removed.

As an example, gold nanorhombos were prepared by combining IBE with EBL. Here, a resist layer was deposited on a gold coated fused silica substrate.^{50,351} The resist layer was structured by EBL, followed by an argon ion beam etching to transfer the layout into the metal layer. A technique of ion implementation was created as a modification of IBE. Here, an aluminum layer was structured with a silver ion beam, resulting in a bimetallic Al–Ag-island film.³⁷⁸ The substrate showed a broad plasmonic range from UV to VIS for fluorescence enhancing experiments.

Whereas IBE and RIBE are directed but non-focused processes, in focused ion beam (FIB) milling, a focused beam is used to directly structure a functional or sacrificial metal layer, or even to modify resists comparable to EBL.^{379,380} FIB milling offers nearly perfect control over the size and shape of the structure, yet it is a rather time-consuming process. Thus, FIB milling can serve as a very good tool for scientific uses but is of little use for industrial production or high volume applications. Nevertheless, FIB milling has become an innovative tool in those cases where single antennas or small arrays suffice.^{381,382} Based on FIB milling and EBL, a noble metal nanoantenna centered in an area of photonic crystal cavities was prepared.³⁸³ Here, nanostructured tips, prepared by FIB, were coated with the metal applying chemical vapor deposition. In the next step, the plasmonic active tip was then

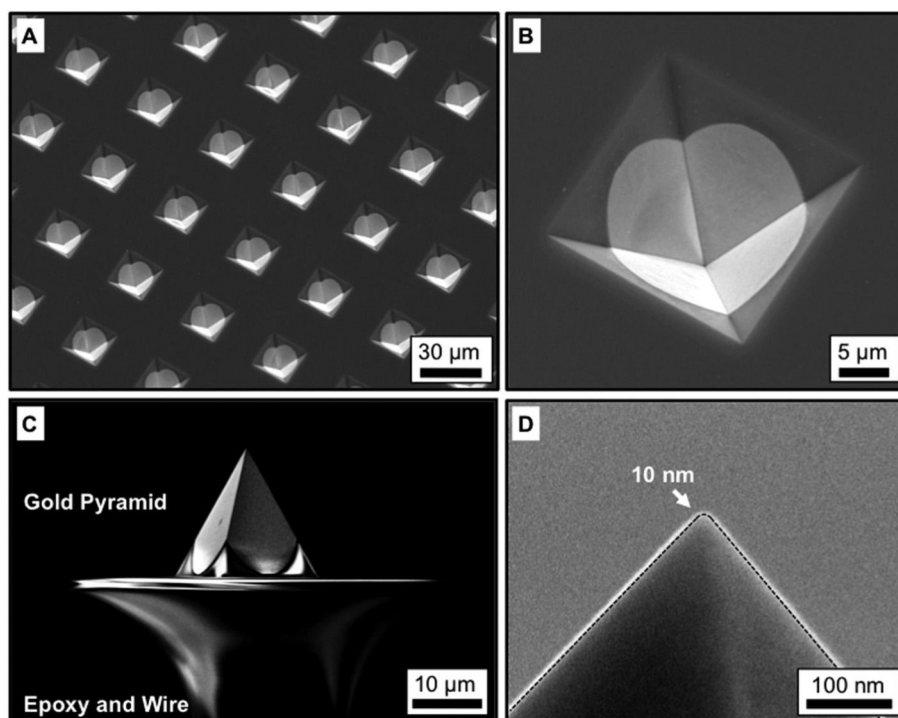


Fig. 22 SEM images of nanopyrramids fabricated with the help of a lift-off process. (A) Overview image in order to demonstrate the reproducibility of the applied technique. (B) Gold covered pyramid after performing the lift-off process. (C) Pyramid after template stripping and connection with a tungsten wire. (D) Close-up image of the pyramid apex. Its diameter is about 10 nm which makes it suitable for use as a TERS tip (adapted with permission from T. W. Johnson, Z. J. Lapin, R. Beams, N. C. Lindquist, S. G. Rodrigo, L. Novotny and S.-H. Oh, *ACS Nano*, 2012, 6, 9168–9174, copyright 2012 American Chemical Society³⁶⁵).

covered with silica. To characterize the enhancing properties, quantum dots of CdSe or a monolayer of organic compounds was arranged on the surface of the nanoantennas. The system could also be used in combination with atomic force microscopy (AFM) and allowed for reproducible signals of single molecules with a sub-wavelength resolution as well as in a far-field configuration. Further, ring resonators have been prepared with the FIB method.³⁸⁴ Gold rings with a decreasing diameter were arranged on a gold surface coated with chromium. By applying the fluorescent dye Alexa 647 on the surface of this structure, a fluorescence enhancement up to 120 was detected.

RIE processes can also produce impressive results if a high order of the surface structure is not aspired, *e.g.* for decorated silicon needles which have been demonstrated to show a strong signal enhancement. For example, a chrome layer for background reduction was introduced in combination with silver as a plasmonic metal.³⁸⁵ This process is only limited by the size of the device for RIE etching and produces substrates which are commercially available.

IE, RIE, IBE and RIBE as the most common etching techniques play a vital role for all micro- and nanostructure applications. By carefully modifying and adapting these processes to the demands of plasmonics, creative and effective solutions have been found for problems like scalability and performance. Nevertheless, more cost-efficient techniques are still

aspired. Amongst them nanoimprint lithography, which will be introduced in the next section, has the potential to become a standard procedure in nanoscale technology within the next decade.

6.4 Nanoimprint lithography (NIL) for high-throughput preparation

Nanoimprint lithography (NIL) combines a fast pattern transfer with a high scalability in size and throughput.^{386,387} Instead of repeated illuminations by EBL, one master is prepared by applying the techniques explained in the previous section. This negative master is further used to “stamp” a softened or uncured resist layer. Thus, the pattern transfer only takes some minutes structuring wafers up to 6” diameter. Moreover, even roll-to-roll methods can be applied.³⁸⁸ After acquiring a master die, this technique offers the easiest access to high volume substrates, scaling price and effort according to the amount of chips produced. As an example, SEM images of a master mold, the corresponding resist imprint and the obtained gold nanostructure are shown in Fig. 23.³⁸⁹

To fabricate aluminum nanovoid substrates for application as SERS substrates in the UV range, the NIL technique was combined with electron beam evaporation.³⁹⁰ Thus, biological molecules with an absorption in the UV region could be investigated under resonant conditions. Employing a soft nanoimprint lithography protocol, the fabrication of plasmonic

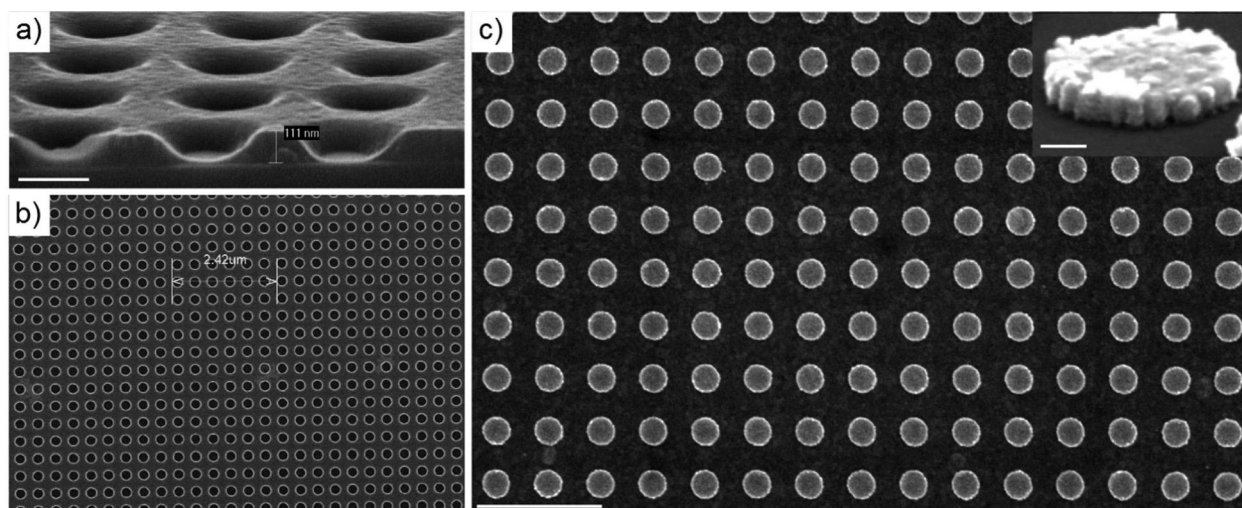


Fig. 23 SEM images of the nanoimprint process steps: (a) the master made by EBL on a silicon substrate, (b) the structure imprinted in a polymer (scale bar: 200 nm) and (c) the resulting gold structure after lifting the resist (scale bar: 1 μm). The inset in (c) represents an example of a nanodisk in detail (scale bar: 50 nm) (adopted from Cottat *et al.*³⁸⁹).

crystals was feasible.³⁹¹ Here, structured soft PDMS stamps were prepared to texture a polymer surface and coat it with a thin gold film. By doing so, a uniform hole array resulted in plasmonic resonances in the (near) infrared region. The SERS activity is characterized by applying benzenethiol as a model analyte. The enhancement factor was estimated to be 10^5 . A quasi-three-dimensional plasmonic crystal with a plasmonic response in the visible and NIR spectral regions showed comparable SERS enhancement properties for benzenethiol.³⁹² Here, the SERS enhancement depended on the diameter of the circular nanostructures and the periodicity of the array prepared by means of NIL. Employing NIL, a suspended nanohole array membrane was also prepared for applications in surface tension-driven flow-through SERS.³⁹³

Furthermore, filled hole arrays were created by NIL. To do so, a structure of petri-dish-shaped SiO_2 , with an inner core consisting of a silver disc, was fabricated as a SERS substrate.³⁹⁴ Because of the undercut resist layer (PMGI) and the oblique angle at which the SiO_2 was deposited, structures with sub-lithographic dimensions could be produced. Employing these structures as SERS substrates, rhodamine 6G was detected down to nanomolar concentrations. To fabricate ring structures (split rings *etc.*), a four-step procedure was developed.³⁹⁵ In the first step, an array of epoxy piles was formed by applying soft lithography. Secondly, thin metallic films were deposited on the piles, and, thirdly, the entire structure was embedded in an epoxy cube to prepare thin planes of 80 nm by employing an ultramicrotome (“nanoskiving”). In the final step, the epoxy material was etched. Depending on UV, VIS to IR based on the diameters of the rings and their periodicity. Moreover, metallic cavities (*e.g.* Ag nanoparticles) have been embedded in a dielectric medium (SiO_2) by using ion implantation based on a stencil made by soft lithography.²⁸² The

Raman signal of pyridine was strongly enhanced by employing this 3D approach, compared with the spectra of pyridine recorded on silver nanoparticles that were not implanted.

Finally, the NIL technique was combined with other methods to prepare complex plasmonic arrays. Gold substrates with a dielectric core of chitosan were prepared by molding the chitosan-hydrogel on glass substrates with nanoimprint lithography, followed by RIE and deposition of a thin gold film by seed mediated electroless plating.³⁹⁶

These advances demonstrate that NIL has become a suitable tool for plasmonics fabrication, promising cost-efficient, fast and large-scale solutions. It can be used both in combination with etching and template stripping, providing a well-tuned process with drastically reduced and high availability.

6.5 Template-stripping as a tool for the fabrication of ultra-smooth surfaces

Template-stripping nanofabrication is a technique supplying homogeneous, ultra-smooth surfaces with well-organized two-dimensional patterns over large areas. It is based on metals with low adhesion to the template surface. First, the metal is deposited onto the template surface (*e.g.* silicon template with Au or Ag). After that, an adhesion layer is added in order to attach a supporting glass wafer. In the final step, the glass-template sandwich is separated mechanically. Since the separation will occur between the layers with the weakest adhesion, the metal layer will stick to the glass wafer.³⁹⁷ For the fabrication of the template, techniques mentioned in the previous paragraphs can be applied.

As an example, the bottom-up large scale fabrication of hemispherical shell noble metal structures as a template for the stripping process was reported.^{372,398} By employing top down techniques it was possible to create nearly every 2D single structure element. Well-defined single particles like tri-

angles, donuts, equilateral-triangle plasmonic cavities, as well as bowtie antenna were prepared by a combination of the template stripping method and EBL structuring of a template. A metal (*e.g.* silver) layer was deposited on PMMA and glued to another substrate (*e.g.* silicon wafer) surface for transfer and cleaning which resulted in tunable plasmonic substrates for the VIS and IR spectral regions.

Template-stripping is an established technique, but far from a widespread application. This is due to challenges regarding the handling during the transfer process and the sensitivity for incomplete or faulty pattern transfers which hinder its incorporation into standard processes.

In conclusion, the advantages of applying top-down techniques to fabricate plasmonic arrays and structures are attributed to their very high homogeneity and reproducibility. However, these techniques are by far more expensive than bottom-up or self-organization processes. As production costs are high for most top-down techniques, the fabricated substrates should allow for reusability *e.g.* of the template structure. Due to the discussed issues in preparing such structures, however, they are mostly not applied for analytical tools with a high throughput. On the other hand, due to the more precise theoretical foundation, they are often chosen for fundamental research. Great efforts have been put into combining the high reliability of EBL with more cost-efficient and faster techniques to reduce costs and circumvent size limitations. Most prominently, NIL will gain importance for generating regular patterned substrates for analytical application scenarios, as it displays all advantages of EBL. Only, the flexibility in changing the nanostructure's shape and arrangement remains as an issue due to the application of a master die.

7. Conclusions

Within this comprehensive review on plasmonic nanostructures for surface enhanced spectroscopic methods, the interested reader has received an overview about the theoretical approaches to simulate plasmonic-active metallic nanoarrangements. In order to investigate the optical behavior of isotropic and non-magnetic spherical or spheroidal particles analytical techniques are applied. However, in the case of more complex shaped structures, numerical methods *e.g.* DDA, BEM, FEM, FTDT and FDFD come into operation. By means of these techniques, a high diversity of nanostructures and their arrays with varying complexities are accessible.

Further on, various fabrication methods based on bottom-up, self-organization and top-down methods are introduced. In order to fabricate the desired nanoparticles, a great variety of methods are available, *e.g.* bottom-up preparation strategies of plasmonic nanostructures to generate metal colloids, core-shell particles and complex-shaped structures employing seed-mediated growth. Moreover, to fabricate nanoparticle clusters and arrays, self-organization as well as template-based methods are applied. Finally, top-down processes, *e.g.* EBL and its variants as well as NIL, guarantee for an improved

homogeneity and reproducible character of the plasmonic devices applied in SES. Thus, the interested reader will identify the best-suited method to generate the desired plasmonic structure. By intelligent combination of bottom-up, self-organized or top-down techniques, innovative SES substrates with new optical behaviors might be achievable. However, the conspectus of the fabrication strategies within this review article cannot be complete, due to the enormous number of publications within this field.

In future work, the research on plasmonic substrates applied for SES techniques might focus on different directions depending on the read-out method. In the case of SERS, a huge number of plasmonic structures are described in the literature as well as their application towards (bio)analytics. Thus, the research might point to the direction of transferring innovative SERS substrates in relevant application fields *e.g.* clinical, food and environmental analytical schemes. Further on, SEF substrates show promising results in employing immunoassays as well as in combination with SERS as powerful labels in cell analysis. Thus, the generation of stable and reliable SEF substrates will be of great importance. Finally, the research on powerful SEIRA substrates might lead to tunable plasmonic arrays with optical properties that can be varied by simple structural changes to adjust different frequency ranges.

Acknowledgements

Funding of the research projects BioInter (13022-715) and FastTB (2013 FE 9058, 2013 VF 0019) by the Development Bank of Thuringia and the European Union (EFRE) as well as InfecToGnostics (13GW0096F) and JCBI 2.0 (03IPT513Y) by the Federal Ministry of Education and Research (BMBF), Germany is gratefully acknowledged. Moreover, we would like to thank the Czech Science Foundation P205/12/G118 for supporting the work of V. Peksa. Finally, funding of the PhD project of I. J. Hidi within the framework "Carl-Zeiss-Strukturmaßnahme" is gratefully acknowledged. Special thanks go to Torsten May for proof reading and many helpful discussions.

References

- 1 S. Becht, S. Ernst, R. Bappert and C. Feldmann, *Chem. Unserer Zeit*, 2010, **44**, 14–23.
- 2 S. A. Love, B. J. Marquis and C. L. Haynes, *Appl. Spectrosc.*, 2008, **62**, 346a–362a.
- 3 M. Faraday, *Philos. Trans. R. Soc. London*, 1857, **147**, 145–181.
- 4 P. P. Edwards and J. M. Thomas, *Angew. Chem., Int. Ed.*, 2007, **46**, 5480–5486.
- 5 K. A. Willets and R. P. Van Duyne, *Annu. Rev. Phys. Chem.*, 2007, **58**, 267–297.
- 6 G. Mie, *Ann. Phys.*, 1908, **330**, 377–445.
- 7 W. Xie and S. Schlücker, *Rep. Prog. Phys.*, 2014, **77**, 116502.

- 8 X.-J. Chen, G. Cabello, D.-Y. Wu and Z.-Q. Tian, *J. Photochem. Photobiol., C*, 2014, **21**, 54–80.
- 9 S. Schlücker, *Angew. Chem., Int. Ed.*, 2014, **53**, 4756–4795.
- 10 D. Cialla, S. Pollok, C. Steinbrücker, K. Weber and J. Popp, *Nanophotonics*, 2014, **3**, 383–411.
- 11 J. N. Anker, W. P. Hall, O. Lyandres, N. C. Shah, J. Zhao and R. P. Van Duyne, *Nat. Mater.*, 2008, **7**, 442–453.
- 12 W. Ma, H. Kuang, L. Xu, L. Ding, C. Xu, L. Wang and N. A. Kotov, *Nat. Commun.*, 2013, **4**.
- 13 S. McAughtrie, K. Faulds and D. Graham, *J. Photochem. Photobiol., C*, 2014, **21**, 40–53.
- 14 T. Vo-Dinh, Y. Liu, A. M. Fales, H. Ngo, H.-N. Wang, J. K. Register, H. Yuan, S. J. Norton and G. D. Griffin, *Wiley Interdiscip. Rev.: Nanomed. Nanobiotechnol.*, 2015, **7**, 17–33.
- 15 D.-W. Li, W.-L. Zhai, Y.-T. Li and Y.-T. Long, *Microchim. Acta*, 2014, **181**, 23–43.
- 16 R. A. Alvarez-Puebla and L. M. Liz-Marzán, *Angew. Chem., Int. Ed.*, 2012, **51**, 11214–11223.
- 17 J. Zheng and L. He, *Compr. Rev. Food Sci. Food Saf.*, 2014, **13**, 317–328.
- 18 E. L. Keller, N. C. Brandt, A. A. Cassabaum and R. R. Frontiera, *Analyst*, 2015, **140**, 4922–4931.
- 19 J. M. Chalmers and P. R. Griffiths, *Handbook of vibrational spectroscopy*, J. Wiley, 2002.
- 20 Y. N. Xia and N. J. Halas, *MRS Bull.*, 2005, **30**, 338–344.
- 21 A. J. Haes, C. L. Haynes, A. D. McFarland, G. C. Schatz, R. P. Van Duyne and S. Zou, *MRS Bull.*, 2005, **30**, 368–375.
- 22 S. A. Maier, *Plasmonics: Fundamentals and Applications: Fundamentals and Applications*, Springer, 2007.
- 23 S. A. Kim, K. M. Byun, J. Lee, J. H. Kim, D. G. A. Kim, H. Baac, M. L. Shuler and S. J. Kim, *Opt. Lett.*, 2008, **33**, 914–916.
- 24 C. Lausted, Z. Y. Hu, L. Hood and C. T. Campbell, *Comb. Chem. High Throughput Screening*, 2009, **12**, 741–751.
- 25 D. Cialla, A. März, R. Böhme, F. Theil, K. Weber, M. Schmitt and J. Popp, *Anal. Bioanal. Chem.*, 2012, **403**, 27–54.
- 26 S. Pahlow, A. März, B. Seise, K. Hartmann, I. Freitag, E. Kämmer, R. Böhme, V. Deckert, K. Weber, D. Cialla and J. Popp, *Eng. Life Sci.*, 2012, **12**, 131–143.
- 27 S. L. Kleinman, R. R. Frontiera, A.-I. Henry, J. A. Dieringer and R. P. Van Duyne, *Phys. Chem. Chem. Phys.*, 2013, **15**, 21–36.
- 28 J. R. Lakowicz, C. D. Geddes, I. Gryczynski, J. Malicka, Z. Gryczynski, K. Aslan, J. Lukomska, E. Matveeva, J. A. Zhang, R. Badugu and J. Huang, *J. Fluoresc.*, 2004, **14**, 425–441.
- 29 W. Knoll, F. Yu, T. Neumann, L. Niu and E. L. Schmid, in *Radiative Decay Engineering*, ed. C. D. Geddes and J. R. Lakowicz, Springer, US, 2005, pp. 305–332.
- 30 Y. Chen, K. Munechika and D. S. Ginger, *Nano Lett.*, 2007, **7**, 690–696.
- 31 E. Fort and S. Grésillon, *J. Phys. D: Appl. Phys.*, 2008, **41**, 013001.
- 32 K. Ataka and J. Heberle, *Anal. Bioanal. Chem.*, 2007, **388**, 47–54.
- 33 J. Kundu, F. Le, P. Nordlander and N. J. Halas, *Chem. Phys. Lett.*, 2008, **452**, 115–119.
- 34 M. Fleischmann, P. J. Hendra and A. J. McQuillan, *Chem. Phys. Lett.*, 1974, **26**, 163–166.
- 35 M. G. Albrecht and J. A. Creighton, *J. Am. Chem. Soc.*, 1977, **99**, 5215–5217.
- 36 W. Ahn and D. K. Roper, *ACS Nano*, 2010, **4**, 4181–4189.
- 37 Y. Wang and S. Schlucker, *Analyst*, 2013, **138**, 2224–2238.
- 38 W. Xie and S. Schlucker, *Phys. Chem. Chem. Phys.*, 2013, **15**, 5329–5344.
- 39 E. A. Vitol, Z. Orynbayeva, G. Friedman and Y. Gogotsi, *J. Raman Spectrosc.*, 2012, **43**, 817–827.
- 40 J. F. Li, Y. F. Huang, Y. Ding, Z. L. Yang, S. B. Li, X. S. Zhou, F. R. Fan, W. Zhang, Z. Y. Zhou, Y. Wu de, B. Ren, Z. L. Wang and Z. Q. Tian, *Nature*, 2010, **464**, 392–395.
- 41 A. Marz, T. Henkel, D. Cialla, M. Schmitt and J. Popp, *Lab Chip*, 2011, **11**, 3584–3592.
- 42 J. Sun, Y. Xianyu and X. Jiang, *Chem. Soc. Rev.*, 2014, **43**, 6239–6253.
- 43 W. Chao and Y. Chenxu, *Nanotechnology*, 2015, **26**, 092001.
- 44 Z.-Q. Tian, Z.-L. Yang, B. Ren, J.-F. Li, Y. Zhang, X.-F. Lin, J.-W. Hu and D.-Y. Wu, *Faraday Discuss.*, 2006, **132**, 159–170.
- 45 B. Ren, G.-K. Liu, X.-B. Lian, Z.-L. Yang and Z.-Q. Tian, *Anal. Bioanal. Chem.*, 2007, **388**, 29–45.
- 46 M. Kerker, D. S. Wang and H. Chew, *Appl. Opt.*, 1980, **19**, 4159–4174.
- 47 J. Gersten and A. Nitzan, *J. Chem. Phys.*, 1980, **73**, 3023–3037.
- 48 T. Itoh, K. Yoshida, V. Biju, Y. Kikkawa, M. Ishikawa and Y. Ozaki, *Phys. Rev. B: Condens. Matter*, 2007, **76**, 085405.
- 49 W. H. Zhang, H. Fischer, T. Schmid, R. Zenobi and O. J. F. Martin, *J. Phys. Chem. C*, 2009, **113**, 14672–14675.
- 50 D. Cialla, J. Petschulat, U. Hübner, H. Schneidewind, M. Zeisberger, R. Mattheis, T. Pertsch, M. Schmitt, R. Möller and J. Popp, *ChemPhysChem*, 2010, **11**, 1918–1924.
- 51 E. C. Le Ru and P. G. Etchegoin, *Chem. Phys. Lett.*, 2006, **423**, 63–66.
- 52 E. C. Le Ru, M. Meyer, E. Blackie and P. G. Etchegoin, *J. Raman Spectrosc.*, 2008, **39**, 1127–1134.
- 53 H. X. Xu, J. Aizpurua, M. Kall and P. Apell, *Phys. Rev. E: Stat. Phys., Plasmas, Fluids, Relat. Interdiscip. Top.*, 2000, **62**, 4318–4324.
- 54 L. Jensen, C. M. Aikens and G. C. Schatz, *Chem. Soc. Rev.*, 2008, **37**, 1061–1073.
- 55 P. Knoll, M. Marchl and W. Kiefer, *Indian J. Pure Appl. Phys.*, 1988, **26**, 268–277.
- 56 Y. S. Yamamoto, Y. Ozaki and T. Itoh, *J. Photochem. Photobiol., C*, 2014, **21**, 81–104.
- 57 E. J. Ayars, H. D. Hallen and C. L. Jahncke, *Phys. Rev. Lett.*, 2000, **85**, 4180–4183.
- 58 C. M. Aikens, L. R. Madison and G. C. Schatz, *Nat. Photonics*, 2013, **7**, 508–510.

- 59 A. Otto, I. Mrozek, H. Grabhorn and W. Akemann, *J. Phys.: Condens. Matter*, 1992, **4**, 1143–1212.
- 60 X. P. Gao, J. P. Davies and M. J. Weaver, *J. Phys. Chem.*, 1990, **94**, 6858–6864.
- 61 M. Moskovits and J. S. Suh, *J. Phys. Chem.*, 1984, **88**, 5526–5530.
- 62 J. Gersten and A. Nitzan, *J. Chem. Phys.*, 1981, **75**, 1139–1152.
- 63 A. Kinkhabwala, Z. F. Yu, S. H. Fan, Y. Avlasevich, K. Mullen and W. E. Moerner, *Nat. Photonics*, 2009, **3**, 654–657.
- 64 R. Gill and E. C. Le Ru, *Phys. Chem. Chem. Phys.*, 2011, **13**, 16366–16372.
- 65 P.-P. Fang, X. Lu, H. Liu and Y. Tong, *TrAC, Trends Anal. Chem.*, 2015, **66**, 103–117.
- 66 R. Zhang, Z. Wang, C. Song, J. Yang and Y. Cui, *J. Fluoresc.*, 2013, **23**, 551–559.
- 67 Y. Li, J. Sun, L. Wu, J. Ji, X. Sun and Y. Qian, *Biosens. Bioelectron.*, 2014, **62**, 255–260.
- 68 X. Yang, Y. Zhuo, S. Zhu, Y. Luo, Y. Feng and Y. Xu, *Biosens. Bioelectron.*, 2015, **64**, 345–351.
- 69 G. Zheng, J. Wang, L. Kong, H. Cheng and J. Liu, *Plasmonics*, 2012, **7**, 487–494.
- 70 D. Punj, M. Mivelle, S. B. Moparthi, T. S. van Zanten, H. Rigneault, N. F. van Hulst, M. F. Garcia-Parajo and J. Wenger, *Nat. Nano*, 2013, **8**, 512–516.
- 71 P. Anger, P. Bharadwaj and L. Novotny, *Phys. Rev. Lett.*, 2006, **96**.
- 72 N. I. Cade, T. Ritman-Meer, K. A. Kwakwa and D. Richards, *Nanotechnology*, 2009, **20**.
- 73 Q. Hao, T. Qiu and P. K. Chu, *Prog. Surf. Sci.*, 2012, **87**, 23–45.
- 74 X. F. Zhang, X. M. Kong, Z. P. Lv, S. W. Zhou and X. Z. Du, *J. Mater. Chem. B*, 2013, **1**, 2198–2204.
- 75 J. Zhang, Y. Fu and J. R. Lakowicz, *J. Phys. Chem. C*, 2007, **111**, 50–56.
- 76 A. Hartstein, J. R. Kirtley and J. C. Tsang, *Phys. Rev. Lett.*, 1980, **45**, 201–204.
- 77 A. Hatta, T. Ohshima and W. Suëtaka, *Appl. Phys. A*, 1982, **29**, 71–75.
- 78 W. Suëtaka, *Surface Infrared and Raman Spectroscopy: Methods and Applications*, Springer, 1995.
- 79 M. Osawa, *Bull. Chem. Soc. Jpn.*, 1997, **70**, 2861–2880.
- 80 K. B. Alici, *IEEE Trans. Nanotechnol.*, 2014, **13**, 216–221.
- 81 C. H. Wu, A. B. Khanikaev, R. Adato, N. Arju, A. A. Yanik, H. Altug and G. Shvets, *Nat. Mater.*, 2012, **11**, 69–75.
- 82 S. Bagheri, K. Weber, T. Gissibl, T. Weiss, F. Neubrech and H. Giessen, *ACS Photonics*, 2015, **2**, 779–786.
- 83 C. Huck, F. Neubrech, J. Vogt, A. Toma, D. Gerbert, J. Katzmann, T. Härtling and A. Pucci, *ACS Nano*, 2014, **8**, 4908–4914.
- 84 K. Chen, R. Adato and H. Altug, *ACS Nano*, 2012, **6**, 7998–8006.
- 85 A. Hornemann, D. Eichert, S. Flemig, G. Ulm and B. Beckhoff, *Phys. Chem. Chem. Phys.*, 2015, **17**, 9471–9479.
- 86 T. Kamata, A. Kato, J. Umemura and T. Takenaka, *Langmuir*, 1987, **3**, 1150–1154.
- 87 K. Itoh, K. Hayashi, Y. Hamanaka, M. Yamamoto, T. Araki and K. Iriyama, *Langmuir*, 1992, **8**, 140–147.
- 88 E. Johnson and R. Aroca, *J. Phys. Chem.*, 1995, **99**, 9325–9330.
- 89 P. Alonso-Gonzalez, P. Albella, M. Schnell, J. Chen, F. Huth, A. Garcia-Etxarri, F. Casanova, F. Golmar, L. Arzubiaga, L. E. Hueso, J. Aizpurua and R. Hillenbrand, *Nat. Commun.*, 2012, **3**, 684.
- 90 J. Parsons, C. P. Burrows, J. R. Sambles and W. L. Barnes, *J. Mod. Optic.*, 2010, **57**, 356–365.
- 91 F. D. Sala and S. D'Agostino, *Handbook of Molecular Plasmonics*, CRC Press, 2013.
- 92 C. F. Bohren and D. R. Huffman, *Absorption and scattering of light by small particles*, Wiley, 1983.
- 93 A. L. Aden and M. Kerker, *J. Appl. Phys.*, 1951, **22**, 1242–1246.
- 94 P. K. Jain, K. S. Lee, I. H. El-Sayed and M. A. El-Sayed, *J. Phys. Chem. B*, 2006, **110**, 7238–7248.
- 95 E. L. Ru and P. Etchegoin, *Principles of Surface-Enhanced Raman Spectroscopy: And Related Plasmonic Effects*, Elsevier Science, 2008.
- 96 S. Schlücker, *Surface Enhanced Raman Spectroscopy: Analytical, Biophysical and Life Science Applications*, Wiley, 2011.
- 97 M. A. Yurkin, D. de Kanter and A. G. Hoekstra, *J. Nanophotonics*, 2010, **4**, 041585.
- 98 O. J. F. Martin and N. B. Piller, *Phys. Rev. E: Stat. Phys., Plasmas, Fluids, Relat. Interdiscip. Top.*, 1998, **58**, 3909–3915.
- 99 V. Myroshnychenko, E. Carbó-Argibay, I. Pastoriza-Santos, J. Pérez-Juste, L. M. Liz-Marzán and F. J. García de Abajo, *Adv. Mater.*, 2008, **20**, 4288–4293.
- 100 J.-M. Jin, *The Finite Element Method in Electromagnetics*, Wiley, 2002.
- 101 A. F. Oskooi, D. Roundy, M. Ibanescu, P. Bermel, J. D. Joannopoulos and S. G. Johnson, *Comput. Phys. Commun.*, 2010, **181**, 687–702.
- 102 M. Paulus, P. Gay-Balmaz and O. J. F. Martin, *Phys. Rev. E: Stat. Phys., Plasmas, Fluids, Relat. Interdiscip. Top.*, 2000, **62**, 5797–5807.
- 103 Y. O. Agha, O. Demichel, C. Girard, A. Bouhelier and G. C. des Francs, *Prog. Electromagn. Res.*, 2014, **146**, 77–88.
- 104 G. Baffou, R. Quidant and C. Girard, *Phys. Rev. B: Condens. Matter*, 2010, **82**, 165424.
- 105 K. Diest, *Numerical Methods for Metamaterial Design*, Springer, 2013.
- 106 A. V. Lavrinenko, J. Lægsgaard, N. Gregersen, F. Schmidt and T. Søndergaard, *Numerical Methods in Photonics*, CRC Press, 2014.
- 107 E. Prodan, C. Radloff, N. J. Halas and P. Nordlander, *Science*, 2003, **302**, 419–422.
- 108 E. Prodan and P. Nordlander, *J. Chem. Phys.*, 2004, **120**, 5444–5454.
- 109 S. Lal, N. K. Grady, J. Kundu, C. S. Levin, J. B. Lassiter and N. J. Halas, *Chem. Soc. Rev.*, 2008, **37**, 898–898.

- 110 K. Bao, H. Sobhani and P. Nordlander, *Chin. Sci. Bull.*, 2010, **55**, 2629–2634.
- 111 K. L. Kelly, E. Coronado, L. L. Zhao and G. C. Schatz, *J. Phys. Chem. B*, 2003, **107**, 668–677.
- 112 K.-S. Lee and M. A. El-Sayed, *J. Phys. Chem. B*, 2006, **110**, 19220–19225.
- 113 C. Noguez, *J. Phys. Chem. C*, 2007, **111**, 3806–3819.
- 114 Y. Xia, Y. Xiong, B. Lim and S. E. Skrabalak, *Angew. Chem., Int. Ed.*, 2009, **48**, 60–103.
- 115 P. K. Aravind, A. Nitzan and H. Metiu, *Surf. Sci.*, 1981, **110**, 189–204.
- 116 N. Liver, A. Nitzan and J. I. Gersten, *Chem. Phys. Lett.*, 1984, **111**, 449–454.
- 117 J. M. McMahon, A.-I. Henry, K. L. Wustholz, M. J. Natan, R. G. Freeman, R. P. V. Duyne and G. C. Schatz, *Anal. Bioanal. Chem.*, 2009, **394**, 1819–1825.
- 118 N. J. Halas, S. Lal, W.-S. Chang, S. Link and P. Nordlander, *Chem. Rev.*, 2011, **111**, 3913–3961.
- 119 J. M. McMahon, S. Li, L. K. Ausman and G. C. Schatz, *J. Phys. Chem. C*, 2012, **116**, 1627–1637.
- 120 N. Ma, F. Tang, X. Y. Wang, F. He and L. D. Li, *Macromol. Rapid Commun.*, 2011, **32**, 587–592.
- 121 B. Yan, S. V. Boriskina and B. M. Reinhard, *J. Phys. Chem. C*, 2011, **115**, 24437–24453.
- 122 J. M. Romo-Herrera, R. A. Alvarez-Puebla and L. M. Liz-Marzán, *Nanoscale*, 2011, **3**, 1304–1315.
- 123 S. J. Barrow, A. M. Funston, X. Wei and P. Mulvaney, *Nano Today*, 2013, **8**, 138–167.
- 124 D. Mott, J. Lee, N. T. B. Thuy, Y. Aoki, P. Singh and S. Maenosono, *Jpn. J. Appl. Phys.*, 2011, **50**, 065004.
- 125 J. Henzie, J. Lee, M. H. Lee, W. Hasan and T. W. Odom, *Annu. Rev. Phys. Chem.*, 2009, **60**, 147–165.
- 126 M. Rycenga, C. M. Copley, J. Zeng, W. Li, C. H. Moran, Q. Zhang, D. Qin and Y. Xia, *Chem. Rev.*, 2011, **111**, 3669–3712.
- 127 M. Fan, G. F. S. Andrade and A. G. Brolo, *Anal. Chim. Acta*, 2011, **693**, 7–25.
- 128 P. K. Jain and M. A. El-Sayed, *J. Phys. Chem. C*, 2008, **112**, 4954–4960.
- 129 P. K. Jain, W. Y. Huang and M. A. El-Sayed, *Nano Lett.*, 2007, **7**, 2080–2088.
- 130 Z. Zhang, S. Zhang and Z. Xiong, *Plasmonics*, 2010, **5**, 411–416.
- 131 N. Grillet, D. Manchon, F. Bertorelle, C. Bonnet, M. Broyer, E. Cottancin, J. Lerme, M. Hillenkamp and M. Pellarin, *ACS Nano*, 2011, **5**, 9450–9462.
- 132 M. Rang, A. C. Jones, F. Zhou, Z.-Y. Li, B. J. Wiley, Y. Xia and M. B. Raschke, *Nano Lett.*, 2008, **8**, 3357–3363.
- 133 H. Fischer and O. J. F. Martin, *Opt. Express*, 2008, **16**, 9144–9154.
- 134 B. C. Galarreta, P. R. Norton and F. o. Lagugné-Labarthe, *J. Phys. Chem. C*, 2010, **114**, 19952–19957.
- 135 G. V. P. Kumar, *J. Opt. Soc. Am. B*, 2012, **29**, 594–599.
- 136 R. Bukasov and J. S. Shumaker-Parry, *Nano Lett.*, 2007, **7**, 1113–1118.
- 137 R. Bukasov, T. A. Ali, P. Nordlander and J. S. Shumaker-Parry, *ACS Nano*, 2010, **4**, 6639–6650.
- 138 J. Fischer, N. Vogel, R. Mohammadi, H. J. Butt, K. Landfester, C. K. Weiss and M. Kreiter, *Nanoscale*, 2011, **3**, 4788–4797.
- 139 J. Xu, L. Zhang, H. Gong, J. í. Homola and Q. Yu, *Small*, 2011, **7**, 371–376.
- 140 J. J. Xu, P. Guan, P. Kvasnicka, H. Gong, J. Homola and Q. M. Yu, *J. Phys. Chem. C*, 2011, **115**, 10996–11002.
- 141 C. F. Tian, C. H. Ding, S. Y. Liu, S. C. Yang, X. P. Song, B. J. Ding, Z. Y. Li and J. X. Fang, *ACS Nano*, 2011, **5**, 9442–9449.
- 142 R. Shugayev, *Opt. Express*, 2010, **18**, 24946–24960.
- 143 P. Ding, E. J. Liang, W. Q. Hu, G. W. Cai and Q. Z. Xue, *Photonics Nanostruct.*, 2011, **9**, 42–48.
- 144 A. M. Funston, C. Novo, T. J. Davis and P. Mulvaney, *Nano Lett.*, 2009, **9**, 1651–1658.
- 145 S. Sheikholeslami, Y.-w. Jun, P. K. Jain and A. P. Alivisatos, *Nano Lett.*, 2010, **10**, 2655–2660.
- 146 J. S. Huang, J. Kern, P. Geisler, P. Weinmann, M. Kamp, A. Forchel, P. Biagioni and B. Hecht, *Nano Lett.*, 2010, **10**, 2105–2110.
- 147 L. V. Brown, H. Sobhani, J. B. Lassiter, P. Nordlander and N. J. Halas, *ACS Nano*, 2010, **4**, 819–832.
- 148 F. Hao, Y. Sonnefraud, P. V. Dorpe, S. A. Maier, N. J. Halas and P. Nordlander, *Nano Lett.*, 2008, **8**, 3983–3988.
- 149 M. W. Knight, Y. Wu, J. B. Lassiter, P. Nordlander and N. J. Halas, *Nano Lett.*, 2009, **9**, 2188–2192.
- 150 D. Y. Lei, A. I. Fernandez-Dominguez, Y. Sonnefraud, K. Appavoo, R. F. Haglund, J. B. Pendry and S. A. Maier, *ACS Nano*, 2012, **6**, 1380–1386.
- 151 A. Christ, G. Lévêque, O. J. F. Martin, T. Zentgraf, J. Kuhl, C. Bauer, H. Giessen and S. G. Tikhodeev, *J. Microsc.*, 2008, **229**, 344–353.
- 152 C. M. Watts, X. Liu and W. J. Padilla, *Adv. Mater.*, 2012, **24**, OP98–OP120.
- 153 V. Giannini, J. A. Sanchez-Gil, O. L. Muskens and J. G. Rivas, *J. Opt. Soc. Am. B*, 2009, **26**, 1569–1577.
- 154 Y. Gu, L. Huang, O. J. F. Martin and Q. Gong, *Phys. Rev. B: Condens. Matter*, 2010, **81**, 193103.
- 155 T. Grosztes, D. Barchiesi, T. Toury and G. Grehan, *Opt. Lett.*, 2008, **33**, 2812–2814.
- 156 O. Peña-Rodríguez and U. Pal, *Nanoscale Res. Lett.*, 2011, **6**, 279–279.
- 157 D. J. Wu and X. J. Liu, *Appl. Phys. Lett.*, 2010, **96**, 151912.
- 158 D. Wu and X. Liu, *Appl. Phys. Lett.*, 2010, **97**, 061904.
- 159 N. Hooshmand, P. K. Jain and M. A. El-Sayed, *J. Phys. Chem. Lett.*, 2011, **2**, 374–378.
- 160 M. W. Knight and N. J. Halas, *New J. Phys.*, 2008, **10**, 105006–105006.
- 161 N. Calander, D. Jin and E. M. Goldys, *J. Phys. Chem. C*, 2012, **116**, 7546–7551.
- 162 Z. Zhang and Y. Zhao, *J. Phys.: Condens. Matter*, 2008, **20**, 345223–345223.
- 163 A. Pors, M. Willatzen, O. Albrektsen and S. I. Bozhevolnyi, *J. Opt. Soc. Am. B*, 2010, **27**, 1680–1687.

- 164 T. Zentgraf, T. P. Meyrath, A. Seidel, S. Kaiser, H. Giessen, C. Rockstuhl and F. Lederer, *Phys. Rev. B: Condens. Matter*, 2007, **76**, 033407.
- 165 L. Y. Wu, B. M. Ross and L. P. Lee, *Nano Lett.*, 2009, **9**, 1956–1961.
- 166 D. Rossouw and G. A. Botton, *Opt. Express*, 2012, **20**, 6968–6973.
- 167 F. von Cube, S. Irsen, J. Niegemann, C. Matyssek, W. Hergert, K. Busch and S. Linden, *Opt. Mater. Express*, 2011, **1**, 1009–1018.
- 168 C. M. Dutta, T. A. Ali, D. W. Brandl, T. H. Park and P. Nordlander, *J. Chem. Phys.*, 2008, **129**, 084706.
- 169 J. Ye, L. Lagae, G. Maes, G. Borghs and P. Van Dorpe, *Opt. Express*, 2009, **17**, 23765–23771.
- 170 J. Zhu and F. K. Li, *Eur. Phys. J. B*, 2011, **80**, 83–87.
- 171 E. S. Barnard, J. S. White, A. Chandran and M. L. Brongersma, *Opt. Express*, 2008, **16**, 16529–16537.
- 172 A. Aubry, D. Y. Lei, A. I. Fernández-Domínguez, Y. Sonnefraud, S. A. Maier and J. B. Pendry, *Nano Lett.*, 2010, **10**, 2574–2579.
- 173 N. Large, J. Aizpurua, V. K. Lin, S. L. Teo, R. Marty, S. Tripathy and A. Mlayah, *Opt. Express*, 2011, **19**, 5587–5595.
- 174 A. M. Kern and O. J. F. Martin, *Nano Lett.*, 2011, **11**, 482–487.
- 175 P. C. Lee and D. Meisel, *J. Phys. Chem.*, 1982, **86**, 3391–3395.
- 176 S. Kruszewski and M. Cyrankiewicz, *Acta Phys. Pol., A*, 2012, **121**, A68–A74.
- 177 K. Yoshida, T. Itoh, H. Tamaru, V. Biju, M. Ishikawa and Y. Ozaki, *Phys. Rev. B: Condens. Matter*, 2010, 81.
- 178 T. Itoh, H. Yoshikawa, K. Yoshida, V. Biju and M. Ishikawa, *J. Chem. Phys.*, 2009, **130**, 214706.
- 179 A. Walter, A. Marz, W. Schumacher, P. Rosch and J. Popp, *Lab Chip*, 2011, **11**, 1013–1021.
- 180 A. März, S. Trupp, P. Rösch, G. Mohr and J. Popp, *Anal. Bioanal. Chem.*, 2012, **402**, 2625–2631.
- 181 A. März, K. R. Ackermann, D. Malsch, T. Bocklitz, T. Henkel and J. Popp, *J. Biophotonics*, 2009, **2**, 232–242.
- 182 I. J. Hidi, A. Muhlíg, M. Jahn, F. Liebold, D. Cialla, K. Weber and J. Popp, *Anal. Methods*, 2014, **6**, 3943–3947.
- 183 I. J. Hidi, M. Jahn, K. Weber, D. Cialla-May and J. Popp, *Phys. Chem. Chem. Phys.*, 2015, **17**, 21236–21242.
- 184 B. Liu, W. Jiang, H. Wang, X. Yang, S. Zhang, Y. Yuan, T. Wu and Y. Du, *Microchim. Acta*, 2013, **180**, 997–1004.
- 185 R. Zhang, Z. Wang, C. Song, J. Yang, A. Sadaf and Y. Cui, *J. Fluoresc.*, 2013, **23**, 71–77.
- 186 G. Frens, *Nat. Phys. Sci.*, 1973, **241**, 20–22.
- 187 A. M. Giovannozzi, F. Rolle, M. Sega, M. C. Abete, D. Marchis and A. M. Rossi, *Food Chem.*, 2014, **159**, 250–256.
- 188 E. Kämmer, T. Dörfer, A. Csáki, W. Schumacher, P. A. Da Costa Filho, N. Tarcea, W. Fritzsche, P. Rösch, M. Schmitt and J. Popp, *J. Phys. Chem. C*, 2012, **116**, 6083–6091.
- 189 J. A. Creighton, C. G. Blatchford and M. G. Albrecht, *J. Chem. Soc., Faraday Trans. 2*, 1979, **75**, 790–798.
- 190 Y. Wang, Z. H. Li, H. Li, M. Vuki, D. K. Xu and H. Y. Chen, *Biosens. Bioelectron.*, 2012, **32**, 76–81.
- 191 M. Dendisová-Vyškovská, V. Prokopec, M. Člupek and P. Matějka, *J. Raman Spectrosc.*, 2012, **43**, 181–186.
- 192 R. Jin, Y. Cao, C. A. Mirkin, K. L. Kelly, G. C. Schatz and J. G. Zheng, *Science*, 2001, **294**, 1901–1903.
- 193 K. Munechika, Y. Chen, A. F. Tillack, A. P. Kulkarni, I. J.-L. Plante, A. M. Munro and D. S. Ginger, *Nano Lett.*, 2010, **10**, 2598–2603.
- 194 N. Leopold and B. Lendl, *J. Phys. Chem. B*, 2003, **107**, 5723–5727.
- 195 I. A. Larmour, K. Faulds and D. Graham, *J. Raman Spectrosc.*, 2012, **43**, 202–206.
- 196 N. E. Mircescu, M. Oltean, V. Chiş and N. Leopold, *Vib. Spectrosc.*, 2012, **62**, 165–171.
- 197 I. B. Cozar, L. Szabó, D. Mare, N. Leopold, L. David and V. Chiş, *J. Mol. Struct.*, 2011, **993**, 243–248.
- 198 A. Bebu, L. Szabó, N. Leopold, C. Berindean and L. David, *J. Mol. Struct.*, 2011, **993**, 52–56.
- 199 E. del Puerto, C. Domingo, J. V. Garcia Ramos and S. Sanchez-Cortes, *Langmuir*, 2014, **30**, 753–761.
- 200 N. Mircescu, H. Zhou, N. Leopold, V. Chiş, N. Ivleva, R. Niessner, A. Wieser and C. Haisch, *Anal. Bioanal. Chem.*, 2014, **406**, 3051–3058.
- 201 H. Zhou, D. Yang, N. P. Ivleva, N. E. Mircescu, R. Niessner and C. Haisch, *Anal. Chem.*, 2014, **86**, 1525–1533.
- 202 V. Shautsova, V. Zhuravkov, O. Korolik, A. Novikau, G. Shevchenko and P. Gaiduk, *Plasmonics*, 2014, **9**, 993–999.
- 203 M. M. Harper, J. A. Dougan, N. C. Shand, D. Graham and K. Faulds, *Analyst*, 2012, **137**, 2063–2068.
- 204 C. Morasso, D. Mehn, R. Vanna, M. Bedoni, E. Forvi, M. Colombo, D. Prospero and F. Gramatica, *Mater. Chem. Phys.*, 2014, **143**, 1215–1221.
- 205 G. Lu, H. Li, C. Liusman, Z. Yin, S. Wu and H. Zhang, *Chem. Sci.*, 2011, **2**, 1817–1821.
- 206 C. Hu, Y. Liu, J. Qin, G. Nie, B. Lei, Y. Xiao, M. Zheng and J. Rong, *ACS Appl. Mater. Interfaces*, 2013, **5**, 4760–4768.
- 207 R. Prucek, V. Ranc, O. Balzerová, A. Panáček, R. Zbořil and L. Kvítek, *Mater. Res. Bull.*, 2014, **50**, 63–67.
- 208 K. Herman, L. Szabó, L. Leopold, V. Chiş and N. Leopold, *Anal. Bioanal. Chem.*, 2011, **400**, 815–820.
- 209 Z. W. Liu, W. H. Hung, M. Aykol, D. Valley and S. B. Cronin, *Nanotechnology*, 2010, 21.
- 210 T. Shegai, B. Brian, V. D. Miljkovic and M. Kall, *ACS Nano*, 2011, **5**, 2036–2041.
- 211 N. Hajduková, M. Procházka, J. Štěpánek and M. Špírková, *Colloids Surf., A*, 2007, **301**, 264–270.
- 212 M. Potara, A.-M. Gabudean and S. Astilean, *J. Mater. Chem.*, 2011, **21**, 3625–3625.
- 213 K. L. Wustholz, A.-I. Henry, J. M. McMahon, R. G. Freeman, N. Valley, M. E. Piotti, M. J. Natan, G. C. Schatz and R. P. V. Duyne, *J. Am. Chem. Soc.*, 2010, **132**, 10903–10910.
- 214 D.-K. Lim, K.-S. Jeon, H. M. Kim, J.-M. Nam and Y. D. Suh, *Nat. Mater.*, 2010, **9**, 60–67.

- 215 Y. D. Jin and X. H. Gao, *Nat. Nanotechnol.*, 2009, **4**, 571–576.
- 216 K. C. Grabar, R. G. Freeman, M. B. Hommer and M. J. Natan, *Anal. Chem.*, 1995, **67**, 735–743.
- 217 S. P. Mulvaney, M. D. Musick, C. D. Keating and M. J. Natan, *Langmuir*, 2003, **19**, 4784–4790.
- 218 J. F. Li, X. D. Tian, S. B. Li, J. R. Anema, Z. L. Yang, Y. Ding, Y. F. Wu, Y. M. Zeng, Q. Z. Chen, B. Ren, Z. L. Wang and Z. Q. Tian, *Nat. Protoc.*, 2013, **8**, 52–65.
- 219 B. Küstner, M. Gellner, M. Schütz, F. Schöppler, A. Marx, P. Ströbel, P. Adam, C. Schmuck and S. Schlücker, *Angew. Chem., Int. Ed.*, 2009, **48**, 1950–1953.
- 220 T. P. Tyler, A.-I. Henry, R. P. Van Duyne and M. C. Hersam, *J. Phys. Chem. Lett.*, 2011, **2**, 218–222.
- 221 A. De Luca, M. Ferrie, S. Ravaine, M. La Deda, M. Infusino, A. R. Rashed, A. Veltri, A. Aradian, N. Scaramuzza and G. Strangi, *J. Mater. Chem.*, 2012, **22**, 8846.
- 222 L. Zhao, T. Ming, H. Chen, Y. Liang and J. Wang, *Nanoscale*, 2011, **3**, 3849–3849.
- 223 A. Gole, N. Agarwal, P. Nagaria, M. D. Wyatt and C. J. Murphy, *Chem. Commun.*, 2008, 6140–6140.
- 224 V. Uzayisenga, X. D. Lin, L. M. Li, J. R. Anema, Z. L. Yang, Y. F. Huang, H. X. Lin, S. B. Li, J. F. Li and Z. Q. Tian, *Langmuir*, 2012, **28**, 9140–9146.
- 225 H. Wang, Q. Jin, L. Yang and Y. Liu, *J. Nanopart. Res.*, 2013, **15**, 1803.
- 226 J. Ye, L. Lagae, G. Maes and P. Van Dorpe, *J. Mater. Chem.*, 2011, **21**, 14394–14394.
- 227 X. Q. Huang, S. H. Tang, B. J. Liu, B. Ren and N. F. Zheng, *Adv. Mater.*, 2011, **23**, 3420–3425.
- 228 Z. Ran, Y. Sun, B. Chang, Q. Ren and W. Yang, *J. Colloid Interface Sci.*, 2013, **410**, 94–101.
- 229 N. Yin, Y. Liu, L. Liu, J. Lei, T. Jiang, H. Wang, L. Zhu and X. Xu, *J. Alloys Compd.*, 2013, **581**, 6–10.
- 230 W. Deng, D. Jin, K. Drozdowicz-Tomsia, J. Yuan, J. Wu and E. M. Goldys, *Adv. Mater.*, 2011, **23**, 4649–4654.
- 231 Z. Wang, S. Zong, H. Chen, C. Wang, S. Xu and Y. Cui, *Adv. Healthcare Mater.*, 2014, **3**, 1889–1897.
- 232 S. J. Guo, J. Li, S. J. Dong and E. K. Wang, *J. Phys. Chem. C*, 2010, **114**, 15337–15342.
- 233 W. Deng, L. Sudheendra, J. Zhao, J. Fu, D. Jin, I. M. Kennedy and E. M. Goldys, *Nanotechnology*, 2011, **22**, 325604.
- 234 Y. Pu, R. Grange, C.-L. Hsieh and D. Psaltis, *Phys. Rev. Lett.*, 2010, **104**, 207402.
- 235 S. Zaiba, F. Lerouge, A. M. Gabudean, M. Focsan, J. Lerme, T. Gallavardin, O. Maury, C. Andraud, S. Parola and P. L. Baldeck, *Nano Lett.*, 2011, **11**, 2043–2047.
- 236 R. Liu, F. Qu, Y. Guo, N. Yao and R. D. Priestley, *Chem. Commun.*, 2013, **50**, 478–480.
- 237 X.-D. Lin, V. Uzayisenga, J.-F. Li, P.-P. Fang, D.-Y. Wu, B. Ren and Z.-Q. Tian, *J. Raman Spectrosc.*, 2012, **43**, 40–45.
- 238 X.-D. Lin, J.-F. Li, Y.-F. Huang, X.-D. Tian, V. Uzayisenga, S.-B. Li, B. Ren and Z.-Q. Tian, *J. Electroanal. Chem.*, 2013, **688**, 5–11.
- 239 L. Zhang, D. A. Blom and H. Wang, *Chem. Mater.*, 2011, **23**, 4587–4598.
- 240 M. Li, H. Yang, S. Li, K. Zhao, J. Li, D. Jiang, L. Sun and A. Deng, *J. Agric. Food Chem.*, 2014, **62**, 10896–10902.
- 241 Y. Zhou and P. Zhang, *Phys. Chem. Chem. Phys.*, 2014, **16**, 8791–8794.
- 242 I. Al-Ogaidi, H. Gou, A. K. A. Al-kazaz, Z. P. Aguilar, A. K. Melconian, P. Zheng and N. Wu, *Anal. Chim. Acta*, 2014, **811**, 76–80.
- 243 I. O. Osorio-Román, A. R. Guerrero, P. Albella and R. F. Aroca, *Anal. Chem.*, 2014, **86**, 10246–10251.
- 244 M. Procházka, P. Šimáková and N. Hajduková-Šmidová, *Colloids Surf., A*, 2012, **402**, 24–28.
- 245 R. A. Alvarez-Puebla, J. P. Bravo-Vasquez, P. Cheben, D.-X. Xu, P. Waldron and H. Fenniri, *J. Colloid Interface Sci.*, 2009, **333**, 237–241.
- 246 K. L. McGilvray, C. Fasciani, C. J. Bueno-Alejo, R. Schwartz-Narbonne and J. C. Scaiano, *Langmuir*, 2012, **28**, 16148–16155.
- 247 S. Barbosa, A. Agrawal, L. Rodriguez-Lorenzo, I. Pastoriza-Santos, R. A. Alvarez-Puebla, A. Kornowski, H. Weller and L. M. Liz-Marzan, *Langmuir*, 2010, **26**, 14943–14950.
- 248 M. A. Mahmoud, *Langmuir*, 2013, **29**, 6253–6261.
- 249 X. Le Guevel, F. Y. Wang, O. Stranik, R. Nooney, V. Gubala, C. McDonagh and B. D. MacCraith, *J. Phys. Chem. C*, 2009, **113**, 16380–16386.
- 250 J. Roh, J. Yi and Y. Kim, *Langmuir*, 2010, **26**, 11621–11623.
- 251 X. Li, F.-J. Kao, C.-C. Chuang and S. He, *Opt. Express*, 2010, **18**, 11335–11346.
- 252 X. Ye, L. Jin, H. Caglayan, J. Chen, G. Xing, C. Zheng, V. Doan-Nguyen, Y. Kang, N. Engheta, C. R. Kagan and C. B. Murray, *ACS Nano*, 2012, **6**, 2804–2817.
- 253 R. Kattumenu, C. H. Lee, L. Tian, M. E. McConney and S. Singamaneni, *J. Mater. Chem.*, 2011, **21**, 15218.
- 254 Y.-C. Yang, T.-K. Huang, Y.-L. Chen, J.-Y. Mevellec, S. Lefrant, C.-Y. Lee and H.-T. Chiu, *J. Phys. Chem. C*, 2011, **115**, 1932–1939.
- 255 S. Pedireddy, A. Li, M. Bosman, I. Y. Phang, S. Li and X. Y. Ling, *J. Phys. Chem. C*, 2013, **117**, 16640–16649.
- 256 N. Pazos-Pérez, S. Barbosa, L. Rodríguez-Lorenzo, P. Aldeanueva-Potel, J. Pérez-Juste, I. Pastoriza-Santos, R. A. Alvarez-Puebla and L. M. Liz-Marzán, *J. Phys. Chem. Lett.*, 2009, **1**, 24–27.
- 257 A. Tao, P. Sinsersuksakul and P. Yang, *Angew. Chem., Int. Ed.*, 2006, **45**, 4597–4601.
- 258 J. Chen, J. M. McLellan, A. Siekkinen, Y. Xiong, Z.-Y. Li and Y. Xia, *J. Am. Chem. Soc.*, 2006, **128**, 14776–14777.
- 259 J. C. Kotz, P. M. Treichel and G. C. Weaver, *Chemistry and Chemical Reactivity*, Cengage Learning, 2006.
- 260 V. Sebastian, S.-K. Lee and K. F. Jensen, *Nanoscale*, 2014, **6**, 13228–13235.
- 261 M. A. Mahmoud and M. A. El-Sayed, *J. Am. Chem. Soc.*, 2010, **132**, 12704–12710.
- 262 S. H. Han, J. Y. Cheon, S. H. Joo and J.-S. Lee, *Mater. Res. Bull.*, 2013, **48**, 2333–2339.

- 263 H. Lu, H. Zhang, X. Yu, S. Zeng, K.-T. Yong and H.-P. Ho, *Plasmonics*, 2011, **7**, 167–173.
- 264 M. A. Mahmoud, M. A. El-Sayed, J. Gao and U. Landman, *Nano Lett.*, 2013, **13**, 4739–4745.
- 265 Q. Zhang, Y. Yang, J. Li, R. Iurilli, S. Xie and D. Qin, *ACS Appl. Mater. Interfaces*, 2013, **5**, 6333–6345.
- 266 H. L. Chang, T. Limei, A. Abdennour, K. Ramesh and S. Srikanth, *Nanotechnology*, 2011, **22**, 275311.
- 267 L. Shao, K. C. Woo, H. Chen, Z. Jin, J. Wang and H.-Q. Lin, *ACS Nano*, 2010, **4**, 3053–3062.
- 268 J. Wang, X. Cao, L. Li, T. Li and R. Wang, *J. Phys. Chem. C*, 2013, **117**, 15817–15828.
- 269 M. P. Cecchini, V. A. Turek, J. Paget, A. A. Kornyshev and J. B. Edel, *Nat. Mater.*, 2013, **12**, 165–171.
- 270 Y. Kang, M. Si, Y. Zhu, L. Miao and G. Xu, *Spectrochim. Acta, Part A*, 2013, **108**, 177–180.
- 271 J. C. Fraire, L. A. Pérez and E. A. Coronado, *ACS Nano*, 2012, **6**, 3441–3452.
- 272 L. Motte, F. Billoudet and M. P. Pileni, *J. Phys. Chem.*, 1995, **99**, 16425–16429.
- 273 H. Chen, L. Shao, Q. Li and J. Wang, *Chem. Soc. Rev.*, 2013, **42**, 2679–2724.
- 274 R. W. Taylor, T.-C. Lee, O. A. Scherman, R. Esteban, J. Aizpurua, F. M. Huang, J. J. Baumberg and S. Mahajan, *ACS Nano*, 2011, **5**, 3878–3887.
- 275 L. Jiang, Y. Sun, C. Nowak, A. Kibrom, C. Zou, J. Ma, H. Fuchs, S. Li, L. Chi and X. Chen, *ACS Nano*, 2011, **5**, 8288–8294.
- 276 A. Lee, G. F. S. Andrade, A. Ahmed, M. L. Souza, N. Coombs, E. Tumarkin, K. Liu, R. Gordon, A. G. Brolo and E. Kumacheva, *J. Am. Chem. Soc.*, 2011, **133**, 7563–7570.
- 277 C. Lee, E. A. Josephs, J. Shao and T. Ye, *J. Phys. Chem. C*, 2012, **116**, 17625–17632.
- 278 H.-n. Xie, I. A. Larmour, V. Tileli, A. L. Koh, D. W. McComb, K. Faulds and D. Graham, *J. Phys. Chem. C*, 2011, **115**, 20515–20522.
- 279 P. Moutet, N. M. Sangeetha, L. Ressler, N. Vilar-Vidal, M. Comesana-Hermo, S. Ravaine, R. A. L. Vallee, A. M. Gabudean, S. Astilean and C. Farcau, *Nanoscale*, 2015, **7**, 2009–2022.
- 280 R. G. Freeman, K. C. Grabar, K. J. Allison, R. M. Bright, J. A. Davis, A. P. Guthrie, M. B. Hommer, M. A. Jackson, P. C. Smith, D. G. Walter and M. J. Natan, *Science*, 1995, **267**, 1629–1632.
- 281 M. Fan and A. G. Brolo, *Phys. Chem. Chem. Phys.*, 2009, **11**, 7381–7389.
- 282 R. Carles, C. Farcau, C. Bonafos, G. Benassayag, M. Bayle, P. Benzo, J. Groenen and A. Zwick, *ACS Nano*, 2011, **5**, 8774–8782.
- 283 Y. Xia, B. Gates, Y. Yin and Y. Lu, *Adv. Mater.*, 2000, **12**, 693–713.
- 284 L. A. Dick, A. D. McFarland, C. L. Haynes and R. P. Van Duyne, *J. Phys. Chem. B*, 2002, **106**, 853–860.
- 285 C. Farcau and S. Astilean, *J. Phys. Chem. C*, 2010, **114**, 11717–11722.
- 286 V. Peksa, M. Jahn, L. Štolcová, V. Schulz, J. Proška, M. Procházka, K. Weber, D. Cialla-May and J. Popp, *Anal. Chem.*, 2015, **87**, 2840–2844.
- 287 C. Steuwe, C. F. Kaminski, J. J. Baumberg and S. Mahajan, *Nano Lett.*, 2011, **11**, 5339–5343.
- 288 R. M. Cole, S. Mahajan, P. N. Bartlett and J. J. Baumberg, *Opt. Express*, 2009, **17**, 13298–13308.
- 289 S. H. Lee, K. C. Bantz, N. C. Lindquist, S. H. Oh and C. L. Haynes, *Langmuir*, 2009, **25**, 13685–13693.
- 290 H. Im, K. C. Bantz, S. H. Lee, T. W. Johnson, C. L. Haynes and S.-H. Oh, *Adv. Mater.*, 2013, **25**, 2678–2685.
- 291 W. Z. Shen, M. Z. Li, B. L. Wang, J. Liu, Z. Y. Li, L. Jiang and Y. L. Song, *J. Mater. Chem.*, 2012, **22**, 8127–8133.
- 292 C. Li, Z. Y. Tang and L. Jiang, *J. Mater. Chem.*, 2010, **20**, 9608–9612.
- 293 W. D. Li, F. Ding, J. Hu and S. Y. Chou, *Opt. Express*, 2011, **19**, 3925–3936.
- 294 R. Luchowski, N. Calander, T. Shtoyko, E. Apicella, J. Borejdo, Z. Gryczynski and I. Gryczynski, *J. Nanophotonics*, 2010, **4**, 043516.
- 295 H. Fredriksson, Y. Alaverdyan, A. Dmitriev, C. Langhammer, D. S. Sutherland, M. Zäch and B. Kasemo, *Adv. Mater.*, 2007, **19**, 4297–4302.
- 296 Y. S. Hu, J. Jeon, T. J. Seok, S. Lee, J. H. Hafner, R. A. Drezek and H. Choo, *ACS Nano*, 2010, **4**, 5721–5730.
- 297 C. H. Lee, M. E. Hankus, L. Tian, P. M. Pellegrino and S. Singamaneni, *Anal. Chem.*, 2011, **83**, 8953–8958.
- 298 F. C. Cabrera, P. H. B. Aoki, R. F. Aroca, C. J. L. Constantino, D. S. dos Santos and A. E. Job, *J. Raman Spectrosc.*, 2012, **43**, 474–477.
- 299 M. A. Mahmoud, A. J. Poncheri, R. L. Phillips and M. A. El-Sayed, *J. Am. Chem. Soc.*, 2010, **132**, 2633–2641.
- 300 K. K. Hering, R. Moller, W. Fritzsche and J. Popp, *ChemPhysChem*, 2008, **9**, 867–872.
- 301 K. K. Strelau, T. Schüler, R. Möller, W. Fritzsche and J. Popp, *ChemPhysChem*, 2010, **11**, 394–398.
- 302 S. Yüksel, M. Ziegler, S. Goerke, U. Hübner, K. Pollok, F. Langenhorst, K. Weber, D. Cialla-May and J. Popp, *J. Phys. Chem. C*, 2015, **119**, 13791–13798.
- 303 M. K. Gupta, S. Chang, S. Singamaneni, L. F. Drummy, R. Gunawidjaja, R. R. Naik and V. V. Tsukruk, *Small*, 2011, **7**, 1192–1198.
- 304 Y. Bao, L. Vigdeman, E. R. Zubarev and C. Y. Jiang, *Langmuir*, 2012, **28**, 923–930.
- 305 Z. Y. Bao, D. Y. Lei, J. Dai and Y. Wu, *Appl. Surf. Sci.*, 2013, **287**, 404–410.
- 306 J. Casas, M. Venkataramasubramani, Y. Wang and L. Tang, *Biosens. Bioelectron.*, 2013, **49**, 525–530.
- 307 Y.-J. Guo, G.-M. Sun, L. Zhang, Y.-J. Tang, J.-J. Luo and P.-H. Yang, *Sens. Actuators, B*, 2014, **191**, 741–749.
- 308 W. Tang, D. B. Chase and J. F. Rabolt, *Anal. Chem.*, 2013, **85**, 10702–10709.
- 309 D. Huang, J. Cui and X. Chen, *Colloids Surf., A*, 2014, **456**, 100–107.
- 310 Z. Yi, J. Luo, Y. Yi, X. Xu, P. Wu, X. Jiang, Y. Yi and Y. Tang, *RSC Adv.*, 2014, **4**, 23670–23678.

- 311 J. He, X. Huang, Y.-C. Li, Y. Liu, T. Babu, M. A. Aronova, S. Wang, Z. Lu, X. Chen and Z. Nie, *J. Am. Chem. Soc.*, 2013, **135**, 7974–7984.
- 312 E. V. Barmina, G. A. Shafeev, P. G. Kuzmin, A. A. Serkov, A. V. Simak and N. N. Melnik, *Appl. Phys. A*, 2014, **115**, 747–752.
- 313 V. Amendola, S. Scaramuzza, S. Agnoli, S. Polizzi and M. Meneghetti, *Nanoscale*, 2014, **6**, 1423–1433.
- 314 M. R. Jones, K. D. Osberg, R. J. Macfarlane, M. R. Langille and C. A. Mirkin, *Chem. Rev.*, 2011, **111**, 3736–3827.
- 315 J. C. Hulteen and R. P. Van Duyne, *J. Vac. Sci. Technol., A*, 1995, **13**, 1553–1558.
- 316 J. C. Hulteen, D. A. Treichel, M. T. Smith, M. L. Duval, T. R. Jensen and R. P. Van Duyne, *J. Phys. Chem. B*, 1999, **103**, 3854–3863.
- 317 T. R. Jensen, M. L. Duval, K. L. Kelly, A. A. Lazarides, G. C. Schatz and R. P. Van Duyne, *J. Phys. Chem. B*, 1999, **103**, 9846–9853.
- 318 M. Baia, L. Baia and S. Astilean, *Chem. Phys. Lett.*, 2005, **404**, 3–8.
- 319 L. Baia, M. Baia, J. Popp and S. Astilean, *J. Phys. Chem. B*, 2006, **110**, 23982–23986.
- 320 L. J. Sherry, R. Jin, C. A. Mirkin, G. C. Schatz and R. P. Van Duyne, *Nano Lett.*, 2006, **6**, 2060–2065.
- 321 A. J. Haes, S. Zou, J. Zhao, G. C. Schatz and R. P. Van Duyne, *J. Am. Chem. Soc.*, 2006, **128**, 10905–10914.
- 322 A. V. Whitney, J. W. Elam, S. Zou, A. V. Zinovev, P. C. Stair, G. C. Schatz and R. P. Van Duyne, *J. Phys. Chem. B*, 2005, **109**, 20522–20528.
- 323 G. Liu, W. Cai, L. Kong, G. Duan, Y. Li, J. Wang, G. Zuo and Z. Cheng, *J. Mater. Chem.*, 2012, **22**, 3177–3184.
- 324 G. Liu, W. Cai, L. Kong, G. Duan, Y. Li, J. Wang and Z. Cheng, *J. Hazard. Mater.*, 2013, **248–249**, 435–441.
- 325 Y. Fan, H. Cheng, C. Zhou, X. Xie, Y. Liu, L. Dai, J. Zhang and L. Qu, *Nanoscale*, 2012, **4**, 1776–1781.
- 326 Y. Li, Y. Hu, Y. Zhao, G. Shi, L. Deng, Y. Hou and L. Qu, *Adv. Mater.*, 2011, **23**, 776–780.
- 327 J. Yin, Y. Zang, C. Yue, Z. Wu, S. Wu, J. Li and Z. Wu, *J. Mater. Chem.*, 2012, **22**, 7902.
- 328 M. N. Liu, X. L. Li, S. K. Karuturi, A. I. Y. Tok and H. J. Fan, *Nanoscale*, 2012, **4**, 1522–1528.
- 329 S. Tian, Q. Zhou, Z. Gu, X. Gu and J. Zheng, *Analyst*, 2013, **138**, 2604–2612.
- 330 X. W. Lou, L. A. Archer and Z. Yang, *Adv. Mater.*, 2008, **20**, 3987–4019.
- 331 Y. Wang, T. Gao, K. Wang, X. Wu, X. Shi, Y. Liu, S. Lou and S. Zhou, *Nanoscale*, 2012, **4**, 7121–7126.
- 332 C. T. Kresge, M. E. Leonowicz, W. J. Roth, J. C. Vartuli and J. S. Beck, *Nature*, 1992, **359**, 710–712.
- 333 K. D. Jernshoj, S. Hassing, R. S. Hansen and P. Krohne-Nielsen, *J. Chem. Phys.*, 2011, **135**, 124514.
- 334 X. Lang, T. Qiu, W. Zhang, Y. Yin and P. K. Chu, *J. Phys. Chem. C*, 2011, **115**, 24328–24333.
- 335 S. Habouti, M. Mátéfi-Tempfli, C.-H. Solterbeck, M. Es-Souni, S. Mátéfi-Tempfli and M. Es-Souni, *J. Mater. Chem.*, 2011, **21**, 6269–6269.
- 336 H. Zhu, H. Chen, J. Wang and Q. Li, *Nanoscale*, 2013, **5**, 3742–3746.
- 337 X. Wang, S. Xu, H. Li, J. Tao, B. Zhao and W. Xu, *J. Raman Spectrosc.*, 2012, **43**, 459–463.
- 338 S. Yao, C. Zhou and D. Chen, *Chem. Commun.*, 2013, **49**, 6409–6411.
- 339 S. Y. Lee, S.-H. Kim, M. P. Kim, H. C. Jeon, H. Kang, H. J. Kim, B. J. Kim and S.-M. Yang, *Chem. Mater.*, 2013, **25**, 2421–2426.
- 340 J. Erlebacher and R. Seshadri, *MRS Bull.*, 2009, **34**, 561–568.
- 341 S. Sun and P. Wu, *ACS Appl. Mater. Interfaces*, 2013, **5**, 3481–3486.
- 342 W. Yuan, Z. Lu, H. Wang and C. M. Li, *Phys. Chem. Chem. Phys.*, 2013, **15**, 15499–15507.
- 343 J. Zhu, M. Q. Xue, D. Zhao, M. N. Zhang, L. Duan, Y. Qiu and T. B. Cao, *Angew. Chem., Int. Ed.*, 2011, **50**, 12478–12482.
- 344 P. Nagpal, N. C. Lindquist, S.-H. Oh and D. J. Norris, *Science*, 2009, **325**, 594–597.
- 345 M. Coluccio, F. Gentile, M. Francardi, G. Perozziello, N. Malara, P. Candeloro and E. Di Fabrizio, *Sensors*, 2014, **14**, 6056.
- 346 K. Ju-Hyun, K. Taejoon, Y. Seung Min, L. Sang Yup, K. Bongsoo and C. Yang-Kyu, *Nanotechnology*, 2009, **20**, 235302.
- 347 Z. Li, S.-W. Chung, J.-M. Nam, D. S. Ginger and C. A. Mirkin, *Angew. Chem., Int. Ed.*, 2003, **42**, 2306–2309.
- 348 Y. Fang, V. W. Chen, Y. Cai, J. D. Berrigan, S. R. Marder, J. W. Perry and K. H. Sandhage, *Adv. Funct. Mater.*, 2012, **22**, 2550–2559.
- 349 K. Dietrich, D. Lehr, C. Helgert, A. Tünnermann and E.-B. Kley, *Adv. Mater.*, 2012, **24**, OP321–OP325.
- 350 U. Huebner, K. Weber, D. Cialla, H. Schneidewind, M. Zeisberger, H. G. Meyer and J. Popp, *Microelectron. Eng.*, 2011, **88**, 1761–1763.
- 351 D. Cialla, K. Weber, R. Böhme, U. Hübner, H. Schneidewind, M. Zeisberger, R. Mattheis, R. Möller and J. Popp, *Beilstein J. Nanotechnol.*, 2011, **2**, 501–508.
- 352 P. Rai-Choudhury, *Handbook of Microlithography, Micromachining, and Microfabrication: Microlithography*, SPIE Optical Engineering Press, 1997.
- 353 A. E. Grigorescu and C. W. Hagen, *Nanotechnology*, 2009, **20**, 292001.
- 354 B. Bilenberg, M. Schøler, P. Shi, M. S. Schmidt, P. Bøggild, M. Fink, C. Schuster, F. Reuther, C. Gruetzner and A. Kristensen, *J. Vac. Sci. Technol., A*, 2006, **24**, 1776–1779.
- 355 M. Switkes and M. Rothschild, *J. Vac. Sci. Technol., A*, 2001, **19**, 2353–2356.
- 356 W. Chen and H. Ahmed, *J. Vac. Sci. Technol., A*, 1993, **11**, 2519–2523.
- 357 T. H. P. Chang, *J. Vac. Sci. Technol., A*, 1975, **12**, 1271–1275.
- 358 U. Huebner, E. Pshenay-Severin, R. Alae, C. Menzel, M. Ziegler, C. Rockstuhl, F. Lederer, T. Pertsch,

- H.-G. Meyer and J. Popp, *Microelectron. Eng.*, 2013, **111**, 110–113.
- 359 G. Wiederrecht, *Handbook of Nanofabrication*, Elsevier Science, 2010.
- 360 E. Sheremet, R. D. Rodriguez, D. R. T. Zahn, A. G. Milekhin, E. E. Rodyakina and A. V. Latyshev, *J. Vac. Sci. Technol., A*, 2014, **32**, 04E110.
- 361 Y. Hou, J. Xu, P. Wang and D. Yu, *Appl. Phys. Lett.*, 2010, **96**, 203107.
- 362 A. W. Clark, A. Glidle, D. R. S. Cumming and J. M. Cooper, *Appl. Phys. Lett.*, 2008, 93.
- 363 G. Das, F. Mecarini, F. De Angelis, M. Prasciolu, C. Liberale, M. Patrini and E. Di Fabrizio, *Microelectron. Eng.*, 2008, **85**, 1282–1285.
- 364 A. A. Tseng, C. Kuan, C. D. Chen and K. J. Ma, *IEEE Trans. Electron. Packag. Manuf.*, 2003, **26**, 141–149.
- 365 T. W. Johnson, Z. J. Lapin, R. Beams, N. C. Lindquist, S. G. Rodrigo, L. Novotny and S.-H. Oh, *ACS Nano*, 2012, **6**, 9168–9174.
- 366 V. G. Kravets, G. Zorinants, C. P. Burrows, F. Schedin, A. K. Geim, W. L. Barnes and A. N. Grigorenko, *Nano Lett.*, 2010, **10**, 874–879.
- 367 F. J. Bezares, J. D. Caldwell, O. Glembocki, R. W. Rendell, M. Feygelson, M. Ukaegbu, R. Kasica, L. Shirey, N. D. Bassim and C. Hosten, *Plasmonics*, 2012, **7**, 143–150.
- 368 H.-Y. Wu and B. T. Cunningham, *Appl. Phys. Lett.*, 2011, **98**, 153103.
- 369 J. D. Caldwell, O. Glembocki, F. J. Bezares, N. D. Bassim, R. W. Rendell, M. Feygelson, M. Ukaegbu, R. Kasica, L. Shirey and C. Hosten, *ACS Nano*, 2011, **5**, 4046–4055.
- 370 Q. Yu, S. Braswell, B. Christin, J. Xu, P. M. Wallace, H. Gong and D. Kaminsky, *Nanotechnology*, 2010, **21**, 355301.
- 371 P. Krohne-Nielsen, S. M. Novikov, J. Beermann, P. Morgen, S. I. Bozhevolnyi and O. Albrektsen, *J. Raman Spectrosc.*, 2012, **43**, 834–341.
- 372 P. Nielsen, P. Morgen, A. C. Simonsen and O. Albrektsen, *J. Phys. Chem. C*, 2011, **115**, 5552–5560.
- 373 J. H. Park, P. Nagpal, K. M. McPeak, N. C. Lindquist, S. H. Oh and D. J. Norris, *ACS Appl. Mater. Interfaces*, 2013, **5**, 9701–9708.
- 374 J. Jose, L. R. Jordan, T. W. Johnson, S. H. Lee, N. J. Wittenberg and S.-H. Oh, *Adv. Funct. Mater.*, 2013, **23**, 2812–2820.
- 375 N. C. Lindquist, T. W. Johnson, J. Jose, L. M. Otto and S. H. Oh, *Ann. Phys.*, 2012, **524**, 687–696.
- 376 X. Zhu, Y. Zhang, J. Zhang, J. Xu, Y. Ma, Z. Li and D. Yu, *Adv. Mater.*, 2010, **22**, 4345–4349.
- 377 R. E. Lee, *J. Vac. Sci. Technol.*, 1979, **16**, 164–170.
- 378 Q. Hao, D. Du, C. Wang, W. Li, H. Huang, J. Li, T. Qiu and P. K. Chu, *Sci. Rep.*, 2014, **4**, 6014.
- 379 F. De Angelis, M. Malerba, M. Patrini, E. Miele, G. Das, A. Toma, R. P. Zaccaria and E. Di Fabrizio, *Nano Lett.*, 2013, **13**, 3553–3558.
- 380 S. Kundan, L. Jiunn-Der and Y. Chih-Kai, *Appl. Phys. Exp.*, 2014, **7**, 092202.
- 381 Y. Y. Lin, J. D. Liao, Y. H. Ju, C. W. Chang and A. L. Shiau, *Nanotechnology*, 2011, **22**, 185308.
- 382 T. T. Gao, Z. W. Xu, F. Z. Fang, W. L. Gao, Q. Zhang and X. X. Xu, *Nanoscale Res. Lett.*, 2012, **7**, 399.
- 383 F. De Angelis, M. Patrini, G. Das, I. Maksymov, M. Galli, L. Businaro, L. C. Andreani and E. Di Fabrizio, *Nano Lett.*, 2008, **8**, 2321–2327.
- 384 H. Aouani, O. Mahboub, N. Bonod, E. Devaux, E. Popov, H. Rigneault, T. W. Ebbesen and J. Wenger, *Nano Lett.*, 2011, **11**, 637–644.
- 385 K. Wu, T. Rindzevicius, M. S. Schmidt, K. B. Mogensen, A. Hakonen and A. Boisen, *J. Phys. Chem. C*, 2015, **119**, 2053–2062.
- 386 R. Alvarez-Puebla, B. Cui, J.-P. Bravo-Vasquez, T. Veres and H. Fenniri, *J. Phys. Chem. C*, 2007, **111**, 6720–6723.
- 387 B. Radha, S. H. Lim, M. S. M. Saifullah and G. U. Kulkarni, *Sci. Rep.*, 2013, **3**, 1078.
- 388 Y. Zhong and M. M. F. Yuen, *2014 IEEE 64th Electronic Components and Technology Conference (ECTC)*, 2014, pp. 1822–1827, DOI: 10.1109/ECTC.2014.6897546.
- 389 M. Cottat, N. Lidgi-Guigui, I. Tijnelyte, G. Barbillon, F. Hamouda, P. Gogol, A. Aassime, J. M. Lourtioz, B. Bartenlian and M. de la Chapelle, *Nanoscale Res. Lett.*, 2014, **9**.
- 390 T. Ding, D. O. Sigle, L. O. Herrmann, D. Wolverson and J. J. Baumberg, *ACS Appl. Mater. Interfaces*, 2014, **6**, 17358–17363.
- 391 J. M. Yao, A. P. Le, S. K. Gray, J. S. Moore, J. A. Rogers and R. G. Nuzzo, *Adv. Mater.*, 2010, **22**, 1102–1110.
- 392 A. J. Baca, T. T. Truong, L. R. Cambrea, J. M. Montgomery, S. K. Gray, D. Abdula, T. R. Banks, J. M. Yao, R. G. Nuzzo and J. A. Rogers, *Appl. Phys. Lett.*, 2009, **94**, 243109.
- 393 S. Kumar, S. Cherukulappurath, T. W. Johnson and S.-H. Oh, *Chem. Mater.*, 2014, **26**, 6523–6530.
- 394 J. S. Wi, E. S. Barnard, R. J. Wilson, M. L. Zhang, M. Tang, M. L. Brongersma and S. X. Wang, *ACS Nano*, 2011, **5**, 6449–6457.
- 395 D. J. Lipomi, R. V. Martinez and G. M. Whitesides, *Angew. Chem., Int. Ed.*, 2011, **50**, 8566–8583.
- 396 Y.-K. Baek, S. M. Yoo, T. Kang, H.-J. Jeon, K. Kim, J.-S. Lee, S. Y. Lee, B. Kim and H.-T. Jung, *Adv. Funct. Mater.*, 2010, **20**, 4273–4278.
- 397 N. Vogel, J. Zieleniecki and I. Koper, *Nanoscale*, 2012, **4**, 3820–3832.
- 398 P. Krohne-Nielsen, S. M. Novikov, J. Beermann, P. Morgen, S. I. Bozhevolnyi and O. Albrektsen, *Opt. Express*, 2012, **20**, 534–546.

6.1.3 Observation of Giant Infrared Circular Dichroism in Plasmonic 2D-Metamaterial Arrays [P3]

Richard Knipper, Thomas G. Mayerhöfer, Vladimir Kopecky Jr., Uwe Huebner, and Jürgen Popp *Observation of Giant Infrared Circular Dichroism in Plasmonic 2D-Metamaterial Arrays*, ACS Photonics (2018), DOI:10.1021/-acsphotonics.7b01477

Reprinted with permission from ACS Photonics. Copyright (2018) American Chemical Society.

Observation of Giant Infrared Circular Dichroism in Plasmonic 2D-Metamaterial Arrays

Richard Knipper,^{†,§} Thomas G. Mayerhöfer,[†] Vladimír Kopecký, Jr.,[‡] Uwe Huebner,[†] and Jürgen Popp^{*,†,§}

[†]Leibniz Institute of Photonic Technology (IPHT), Albert-Einstein-Straße 9, Jena, D-07745, Germany

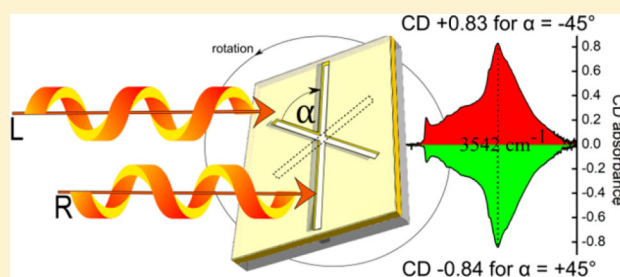
[‡]Institute of Physics, Faculty of Mathematics and Physics, Charles University, Ke Karlovu 5, Prague 2, CZ-12116, Czech Republic

[§]Institute of Physical Chemistry and Abbe Center of Photonics, Friedrich-Schiller-Universität Jena, Helmholtzweg 4, Jena, D-07743, Germany

Supporting Information

ABSTRACT: We report the observation of an enormous circular dichroism (CD) response in broadband surface-enhanced infrared absorption sensing arrays. In our experiment, a 2D-metamaterial chiral cross-slit array adjusted for application in conventional measurement setups was used. The inherent chirality of the design results in a very strong CD absorbance of 0.83 at around $2.86 \mu\text{m}$ (3500 cm^{-1}). This far surpasses our predictions based on the finite-difference time-domain simulations. This is probably the highest CD response ever reported for the mid-infrared region. Our observation was rigorously validated; thus most error sources were ruled out. Further, this Letter discusses our results in view of possible remaining artifacts that might have had an influence on our observations, as both chiral enantiomers and an achiral counterpart with similar structure were created and measured. A giant CD 2D-metamaterial might lead toward surface-enhanced vibrational circular dichroism spectroscopy, a field that is subject to lively discussions.

KEYWORDS: chiral plasmonics, infrared spectroscopy, metamaterials, surface enhancement, vibrational circular dichroism



Since its first description by Hartstein et al.,¹ plasmonic enhancement in the IR range has moved from being a mere theoretical consideration to a potential tool for practical applications.² In the last couple of years, plasmonic enhancement has promised to boost signal intensities far beyond the monolayer capacity already available by conventional methods such as attenuated total reflection³ and buried metal layer infrared (IR) reflection absorption spectroscopy,⁴ as well as the combination of both,⁵ interference-enhanced attenuated total reflection. Even though infrared absorption cross sections are typically much larger than those in Raman spectroscopy (RS), they are still 3 to 4 orders of magnitude lower than, for example, fluorescence,⁶ so a further boost of signal intensities by improving conventional methods cannot be expected.

Naturally, the weak $\propto E^2$ signal enhancement in surface-enhanced IR spectroscopy (as compared to $\propto E^4$ for surface-enhanced RS) reduces applicability in “real-life” spectroscopic tasks, also due to the problems of hot-spots.⁷ By employing slotted membranes, one can utilize extraordinary optical transmission (EOT)⁸ to counteract this problem. The corresponding idea of subwavelength hole arrays (SHAs) with slits dates back to 2014,⁹ making this a rather recent approach. One year later, Mayerhöfer et al.¹⁰ presented an SHA based on a combination of EOT and perfect absorption.

Deviating from a simple array of a single slit, even before the works of Huck et al.,¹¹ Cetin et al.⁹ published a study about H-shaped slits where the slit connecting the two parallel and vertically oriented slits was extended beyond the vertical slits. This system showed highly anisotropic plasmon resonances, one polarized along the horizontal slit and two in the vertical polarization direction, which allowed tuning the resonance frequencies of the three resonances independently. This design permits covering a broader range of the infrared spectrum. In addition, the plasmonic active layer is supported by a freestanding membrane, enabling measurements both in reflection as well as in transmission mode. While using a similar support structure, the slit structure employed in this work consists of two slits, one vertically oriented and the second 45° rotated clockwise or anticlockwise with the pivot at the center of both slits. When the slits are of different length, also two different plasmonic resonances occur; however, the resonances are not orthogonal to each other. More important, the unit cell structure, when embedded in an array, is chiral like early substrates shown by Decker et al.,¹² as compared to achiral substrates also demonstrated.^{13–17}

Received: December 4, 2017

Published: February 14, 2018

Generally, there is a dissent in the literature if a plasmonic active substrate needs to be chiral itself to enhance the relatively weak circular dichroism (CD) effects of chiral molecules that originate from absorptions in the UV spectral range, while they are usually probed by plasmons in the near-IR. This assumption is supported by experimental results provided in, for example, refs 18–20. The opposite position is equally represented in the literature,^{21–24} and theoretical considerations by Tang and Cohen,²⁵ later picked up by Schäferling et al.,²⁶ suggest that a substrate offering enhancement of CD should mainly feature conditions where **E** and **H** field orientation within the hot-spots of the structure is not orthogonal. In general, claims can be found that 2D structures are inherently incapable of boosting chiral response²⁷ and may even have detrimental effects.

Our measurements conducted to explore the chiral response of the explained structures have resulted in a giant CD response situated in the mid-IR spectral region, in the same spectral regions where the vibrations of organic molecules are located. The observed CD response was then carefully verified with artifact suppression techniques and nonchiral control substrates, e.g., substrates of the analogous structure supporting similar plasmonic excitations but without intrinsic chirality. To the best of our knowledge, the reported CD response is the highest ever measured of a 2D-metamaterial in the IR.

The authors of ref 10 are convinced that the giant CD response shown here, which is located in contrast to the aforementioned substrates in the same spectral range as the chiral molecular excitations, will be a valuable tool to explore the possibility of surface-enhanced vibrational circular dichroism (VCD). For this task, the effect at work needs to be fully understood, with this Letter presenting an experimental approach to the aforementioned topic providing experimental results in order to validate our findings.

MATERIALS AND METHODS

Numerical Modeling. Numerical modeling was carried out using the finite-difference time-domain (FDTD) method as implemented in the software “FDTD Solutions” by Lumerical. Selected simulations were cross-checked by modeling the structure again with the finite element method. Generally, we enforced stronger discretization within the parallel slit ($\Delta x = 5$ nm, $\Delta y = 10$ nm, $\Delta z = 5$ nm, where x is oriented parallel to the main-slit width, y to the length, and z to the depth). The residual structure was covered with only slightly coarser mesh to account for the presence of the second slit ($\Delta x = 10$ nm, $\Delta y = 10$ nm, $\Delta z = 5$ nm). The total modeling volume was 1000 nm (the period in x) by 1800 nm (the period in y) by 11 μm (z -direction; the direction of the incoming light). Periodic boundary conditions were applied at the x - and y -boundaries. The z -boundaries were surrounded by perfectly matched layers. CD spectra were generated using two linearly, perpendicular to each other polarized sources with a $\pm 90^\circ$ phase change.

Sample Fabrication. To fabricate the stacked metal–dielectric SHA, a standard silicon wafer (100 mm semistandard, 5 ppm Boron, 100-oriented) was coated using low-pressure chemical vapor deposition with 150 nm of low-stress (<50 MPa tensile stress), nonstoichiometric silicon nitride. Wafers were then covered with 50 nm of gold and a subsequent coating of SiO_2 fabricated using atomic layer deposition. This passivation layer was covered with 30 nm of NiCr, which was structured by electron-beam lithography (see Figure S1 for the full process flow). The X patterns of the SHA gratings were made by shaped electron-beam lithography. The electron-beam exposure of the

individual SHA gratings on the wafer was performed using the shaped electron-beam writer SB350 OS at an electron dose of $400 \mu\text{C}/\text{cm}^2$. The resist was developed for 60 s in AR600-546 (Allresist) and rinsed for 30 s in 2-propanol. Ar^+ -ion-beam etching opened the hard mask NiCr layer. The silicon wafer was structured backside using silicon wet-etching (KOH) to open up the membrane, which was then slitted via CHF_3 -RIE etching to structure the $\text{SiO}_2/\text{Au}/\text{SiN}$ sandwich. After removing the NiCr hard mask with wet etching, chips were separated to $1.5 \times 1.5 \text{ cm}^2$ by notching and breaking. The samples were cleaned in ethanol, blown dry, and then O_2 plasma-cleaned. Resulting slits are 1700 nm in length for the primary and 1000 nm for the secondary slit, both with 50 nm width.

Infrared Spectroscopy. The IR reflection spectra were recorded with a Vertex 80v FT-spectrometer (Bruker) with an attached HYPERION 2000 (Bruker) IR microscope equipped by a $15\times$ Cassegrain IR objective (0.4 NA). The angle of incidence was $<16.7^\circ$. Reflection measurements were referenced against an unstructured part of the substrate with a blank Au/ SiO_2 surface. The spectrometer was evacuated (3 mbar) with the microscope body, and the purge box was flushed continuously with N_2 . Transmission references were recorded with an aperture of the membrane size. Record mode was single-sided forward–backward sampling with Mertz and Blackman–Harris three-term chosen for phase correction and apodization, respectively. Sixty-four spectra were averaged with a resolution of 1 cm^{-1} . VCD measurements were recorded on ChiralIR-2X (BioTools), using two standard MIR sources, a KBr beamsplitter, a dual PEM setup (i.e., photoelastic modulator), and a MCT detector.²⁸ The samples, placed with their Au side toward the MIR sources, were continuously rotated using a SyncRoCell (BioTools). Fourteen blocks of 4000 scans were averaged with 4 cm^{-1} spectral resolution and a Blackman–Harris three-term apodization function. The photoelastic modulators were set at $\lambda/4$ for 2800 cm^{-1} . The spectrometer was purged with dry air during all experiments. The absorbance was given relative to the aperture of the membrane size.

RESULTS AND DISCUSSION

The fabricated SHAs, which are shown in Figure 1, have been optimized for broadband enhanced IR sensing and are based on design ideas reported before.¹⁰ As the array has been adapted for transmission measurements, the layer stack of $\text{SiO}_2/\text{Au}/\text{SiN}$ features extraordinary optical transmission without the perfect

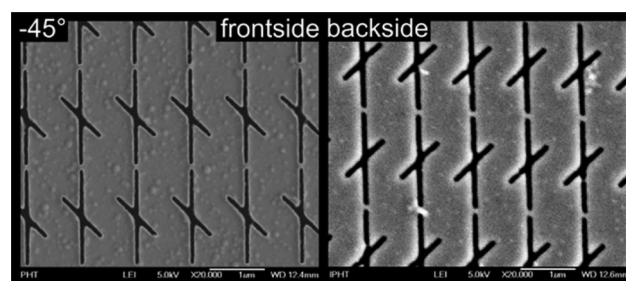


Figure 1. (Frontside) Top-side SEM image of -45° cross structure, recorded with a secondary electron detector, showing the material contrast of the opened-up Au layer passivated with SiO_2 . (Backside) Bottom view of the same chip, displaying an opened-up SiO_2 membrane. It becomes evident that the slits run through the whole length of the membrane and that they are fully opened throughout the whole membrane.

absorber layer present in the structure reported in ref 10. Due to its specific nature, the chiral array raised the question of its chiral plasmonic behavior, e.g., its CD. To approach this question, we employed VCD measurements conducted on a commercial setup specifically equipped to suppress artifacts. With the help of this, an outstanding circular dichroism with an absorbance rate of 0.83 and perfect 2D-mirror symmetry was observed. However, we had to rule out possible contributions of linear depolarization in the mid-IR region. Thus, to validate our findings, we fabricated the other enantiomer (+45° orientation) alongside a “negative” control (+90° orientation of the second slit). Taken as an array, both the +45° and −45° unit cell structures were chiral, while the 90° unit cell structure stays achiral. Due to this, it was expected and verified that a similar plasmonic behavior in IR linear polarized measurements was present, as can be seen in Figure 2.

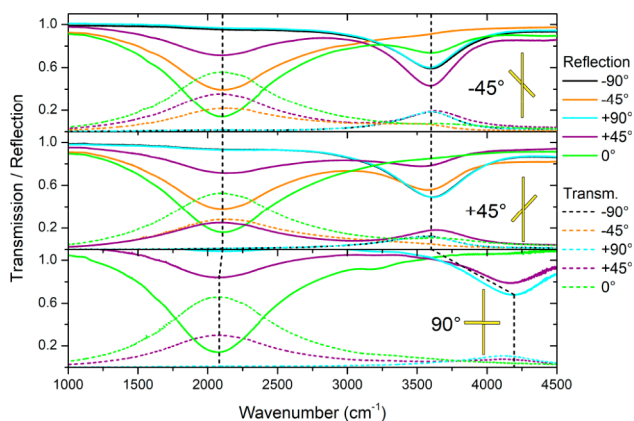


Figure 2. Measured FT-IR reflectance (solid curves)/transmittance (dashed curves) spectra: −45°, +45°, and 90° slit orientations are shown. Main resonance position for the ±45° cases is 2129 cm^{−1}. The same behavior is observed for the second resonance. For 90°, an isosbestic point is seen in reflection and transmission at 3603 and 3786 cm^{−1}, respectively. All spectra illustrations share the same legend depicting the excitation polarization.

The observation of an isosbestic point in both reflection (at 3603 cm^{−1}) and transmission (at 3786 cm^{−1}) spectra of the 90° array confirmed that no coupling between the two plasmonic resonances was present. Nevertheless, resonance positions were nearly identical in the 90° array and its chiral counterparts with the main resonances' position at 2129 cm^{−1} for the ±45° case and 2073 cm^{−1} for the 90° array, which was slightly red-shifted by 56 cm^{−1}. Mirror symmetry in the spectra for the ±45° array could be observed for changing excitation polarizations.

These results were used to rule out possible artifact sources. As can be seen in Figure 3, both enantiomers of the substrate show nearly perfect mirror symmetry. Measurements with several different enantiomeric arrays and different fabrication dates showed similar behavior. Furthermore, the achiral 90° array shows nearly no CD signal, with a CD absorbance below 0.03. This remaining circular dichroism is most likely caused by minute deviations in structure size caused by etching the slit structure and gives an idea of the fabrication influence. To experimentally rule out depolarization as a source of the giant CD response, sample rotation was employed. Furthermore, simulations show that depolarization through the monoclinic structure of the unit cell is not the cause of the gigantic experimental circular dichroism. The effect also remained stable

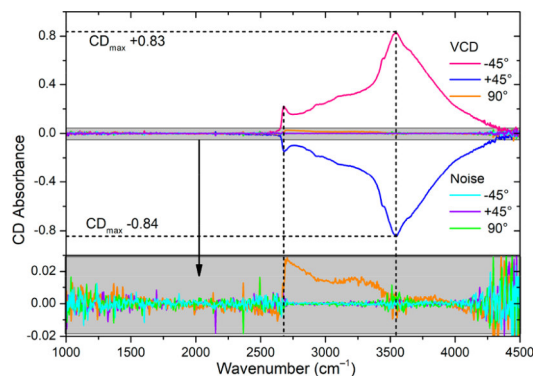


Figure 3. (Top) Measured CD absorbance of the +45°, −45°, and 90° arrays in a ChiralIR-2X spectrometer with dual PEMs set at 2800 cm^{−1}. Strong mirror symmetry of the CD response can be observed with a CD_{max} of +0.83 and −0.84, respectively, at exactly the same position. (Bottom) CD absorbance for the 90° array and noise spectra. The observed small CD response of the achiral substrate is most likely a linear depolarization effect with a magnitude of CD_{max} 0.028 at 2706 cm^{−1}.

throughout the whole measurement. Together with a dual PEM setup, this eliminates most known artifact sources. The CD signal also remained stable against sample inversion, with the correct change in sign. One artifact that remains despite all efforts is the peak at 2667 cm^{−1}. Up to now of unknown origin, it was present in all our measurements but absent in the noise spectra, confirming it is stable and reproducible. One explanation for this artifact might be a sharp change in signal intensity of the plasmonic resonances for the case of chiral polarized excitation. As further proof, we conducted simulations of chiral excitation behavior, as can be seen in Figure 4 and could thus confirm our

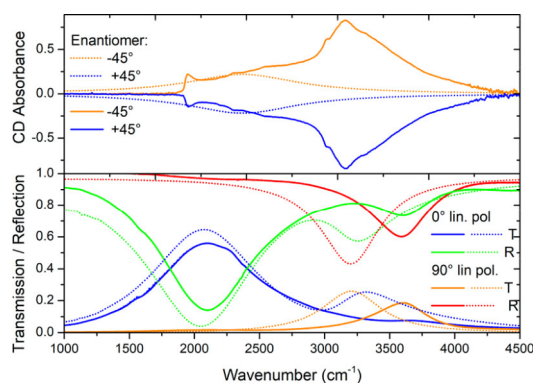


Figure 4. (Top) Simulation of chiral CD transmission absorbance behavior (dashed curves) and CD absorbance measurements (solid curves) of −45° and +45° enantiomers. (Bottom) Comparison of simulated (dashed curves) and measured (solid curves) −45° enantiomer in reflectance (R)/transmittance (T) for 0° and 90° linear-polarized light. While IR simulations are clearly predicting the real behavior, this is not the case for CD, showing the need for further investigation of the giant CD signal.

findings. The deviation between simulations and measurements might be due to varying excitation conditions or a limited quality of the material constants used. Simulations of IR behavior show correct predictions (deviations are due to minute changes in slit geometry and nitride composition, a result of fabrication). Still, taking the magnitude and overall signal shape of our findings, we are convinced that, indeed, a remarkable CD was observed.

Variation of the PEM's working point causes no significant change in spectra, the spectral window being around $\pm 800\text{ cm}^{-1}$ wide. To the best of our knowledge, all predictable artifact sources were addressed and eliminated, leaving us with a high plausibility that the CD signal we could observe is genuine.

These findings may open the way to answer questions about chiral plasmonic enhanced sensing, so-called SE-VCD, which has recently been a topic of high interest. The strength of the CD signal could make these substrates a valuable tool to determine a positive or detrimental effect of the substrate's intrinsic chirality when VCD spectra are recorded. Further, the polarization direction after transmission will be of interest for future investigations, possibly enabling the substrates to act as circular blocks of very high efficiency and low volume combined with a very high damage threshold as compared to polymers. Still, further experiments are needed to fully utilize this unique behavior in the mid-IR and exploit the characteristics of the substrate in order to shed light on questions regarding enhancing VCD measurements by plasmonic resonances.

■ ASSOCIATED CONTENT

Supporting Information

The Supporting Information is available free of charge on the ACS Publications website at DOI: 10.1021/acsphtonic.7b01477.

Figure of the fabrication scheme of the chiral SHA array (PDF)

■ AUTHOR INFORMATION

Corresponding Author

*E-mail: Juergen.Popp@ipht-jena.de.

ORCID

Richard Knipper: 0000-0002-5850-7272

Thomas G. Mayerhöfer: 0000-0001-9396-7365

Vladimír Kopecký Jr.: 0000-0002-7331-9018

Uwe Huebner: 0000-0002-4885-9477

Jürgen Popp: 0000-0003-4257-593X

Notes

The authors declare no competing financial interest.

■ ACKNOWLEDGMENTS

V.K. acknowledges financial support from the Czech Science Foundation (P205/12/G118). The project JBCI2.0 (03IPT513Y, InnoProfile-Transfer, Unternehmen Region), supported by the Federal Ministry of Education and Research (BMBF) Germany, is gratefully acknowledged.

■ REFERENCES

- (1) Hartstein, A.; Kirtley, J. R.; Tsang, J. C. Enhancement of the Infrared Absorption from Molecular Monolayers with Thin Metal Overlayers. *Phys. Rev. Lett.* **1980**, *45*, 201–204.
- (2) Ataka, K.; Heberle, J. Biochemical Applications of Surface-Enhanced Infrared Absorption Spectroscopy. *Anal. Bioanal. Chem.* **2007**, *388*, 47–54.
- (3) Fahrenfort, J. Attenuated Total Reflection: A New Principle for the Production of Useful Infrared Reflection Spectra of Organic Compounds. *Spectrochim. Acta* **1961**, *17*, 698–709.
- (4) Zhang, Y.; Sato, S.; Ohshima, H.; Hattori, T.; Urisu, T. Buried Metal Layer Enhanced Infrared Reflection Absorption Spectroscopy for Photoreactions Induced by Synchrotron Radiation on SiO₂ Surfaces. *Appl. Surf. Sci.* **1994**, *79*, 422–427.
- (5) Mayerhöfer, T. G.; Popp, J. Electric Field Standing Wave Effects in Internal Reflection and ATR Spectroscopy. *Spectrochim. Acta, Part A* **2018**, *191*, 165–171.
- (6) Albota, M. A.; Xu, C.; Webb, W. W. Two-Photon Fluorescence Excitation Cross Sections of Biomolecular Probes from 690 to 960 nm. *Appl. Opt.* **1998**, *37*, 7352–7356.
- (7) Mayerhöfer, T. G.; Popp, J. Periodic Array-Based Substrates for Surface-Enhanced Infrared Spectroscopy. *Nanophotonics* **2018**, *7*, 39–798.
- (8) Ebbesen, T. W.; Lezec, H. J.; Ghaemi, H. F.; Thio, T.; Wolff, P. A. Extraordinary Optical Transmission through Sub-Wavelength Hole Arrays. *Nature* **1998**, *391*, 667–669.
- (9) Cetin, A. E.; Turkmen, M.; Aksu, S.; Etezadi, D.; Altug, H. Multi-Resonant Compact Nanoaperture with Accessible Large Nearfields. *Appl. Phys. B: Lasers Opt.* **2015**, *118*, 29–38.
- (10) Mayerhöfer, T. G.; Knipper, R.; Hübner, U.; Cialla-May, D.; Weber, K.; Meyer, H.-G.; Popp, J. Ultra Sensing by Combining Extraordinary Optical Transmission with Perfect Absorption. *ACS Photonics* **2015**, *2*, 1567–1575.
- (11) Huck, C.; Vogt, J.; Sendner, M.; Hengstler, D.; Neubrech, F.; Pucci, A. Plasmonic Enhancement of Infrared Vibrational Signals: Nanoslits versus Nanorods. *ACS Photonics* **2015**, *2*, 1489–1497.
- (12) Decker, M.; Klein, M. W.; Wegener, M.; Linden, S. Circular dichroism of planar chiral magnetic metamaterials. *Opt. Lett.* **2007**, *32*, 856–858.
- (13) Cao, T.; Cryan, M. J. Enhancement of circular dichroism by a planar non-chiral magnetic metamaterial. *J. Opt.* **2012**, *14*, 085101.
- (14) Cao, T.; Wei, C.; Mao, L.; Li, Y. Extrinsic 2D chirality: giant circular dichroism from a metal-dielectric-metal square array. *Sci. Rep.* **2015**, *4*, 7442.
- (15) Cao, T.; Wei, C.; Zhang, L. Modeling of multi-band circular dichroism using metal/dielectric/metal achiral metamaterials. *Opt. Mater. Express* **2014**, *4*, 152610.1364/OME.4.001526.
- (16) Cao, T.; Wei, C. W.; Mao, L. B.; Wang, S. Tuning of giant 2D-chiroptical response using achiral metasurface integrated with graphene. *Opt. Express* **2015**, *23*, 18620–18629.
- (17) Maoz, B. M.; Moshe, A. B.; Vestler, D.; Bar-Elli, O.; Markovich, G. Chiroptical effects in planar achiral plasmonic oriented nanohole arrays. *Nano Lett.* **2012**, *12*, 2357–2361.
- (18) Jack, C.; Karimullah, A. S.; Tullius, R.; Khorashad, L. K.; Rodier, M.; Fitzpatrick, B.; Barron, L. D.; Gadegaard, N.; Laphorn, A. J.; Rotello, V. M.; Cooke, G.; Govorov, A. O.; Kadodwala, M. Partial Control of Chemical Processes on Nanostructures through Nano-Localized Water Heating. *Nat. Commun.* **2016**, *7*, 10946.
- (19) Zhao, Y.; Askarpour, A. N.; Sun, L.; Shi, J.; Li, X.; Alù, A. Chirality Detection of Enantiomers Using Twisted Optical Metamaterials. *Nat. Commun.* **2017**, *8*, 14180.
- (20) Khoo, E. H.; Leong, E. S. P.; Wu, S. J.; Phua, W. K.; Hor, Y. L.; Liu, Y. J. Effects of Asymmetric Nanostructures on the Extinction Difference Properties of Actin Biomolecules and Filaments. *Sci. Rep.* **2016**, *6*, 19658.
- (21) Abdulrahman, N. A.; Fan, Z.; Tonooka, T.; Kelly, S. M.; Gadegaard, N.; Hendry, E.; Govorov, A. O.; Kadodwala, M. Induced Chirality through Electromagnetic Coupling Between Chiral Molecular Layers and Plasmonic Nanostructures. *Nano Lett.* **2012**, *12*, 977–983.
- (22) Maoz, B. M.; Chaikin, Y.; Tesler, A. B.; Bar Elli, O.; Fan, Z.; Govorov, A. O.; Markovich, G. Amplification of Chiroptical Activity of Chiral Biomolecules by Surface Plasmons. *Nano Lett.* **2013**, *13*, 1203–1209.
- (23) Guerreiro, J. R. L.; Frederiksen, M.; Bochenkov, V. E.; De Freitas, V.; Ferreira Sales, M. G.; Sutherland, D. S. Multifunctional Biosensor Based on Localized Surface Plasmon Resonance for Monitoring Small Molecule–Protein Interaction. *ACS Nano* **2014**, *8*, 7958–7967.
- (24) Lin, D.; Huang, J. S. Slant-Gap Plasmonic Nanoantennas for Optical Chirality Engineering and Circular Dichroism Enhancement. *Opt. Express* **2014**, *22*, 7434–7445.
- (25) Tang, Y.; Cohen, A. E. Optical Chirality and Its Interaction with Matter. *Phys. Rev. Lett.* **2010**, *104*, 163901.

(26) Schäferling, M.; Yin, X. H.; Giessen, H. Formation of Chiral Fields in a Symmetric Environment. *Opt. Express* **2012**, *20*, 26326–26336.

(27) Schäferling, M.; Dregely, D.; Hentschel, M.; Giessen, H. Tailoring Enhanced Optical Chirality: Design Principles for Chiral Plasmonic Nanostructures. *Phys. Rev. X* **2012**, *2*, 031010.

(28) Nafie, L. A. *Vibrational Optical Activity: Principles and Applications*; Wiley: Chichester, 2011.

6.1.4 Slit-enhanced chiral- and broadband infrared ultra-sensing [P4]

Richard Knipper, Vladimir Kopecky Jr, Uwe Hübner, Jürgen Popp, Thomas G. Mayerhöfer, *Broadband Ultra Sensing in Chiral Metamaterials by Extraordinary Optical Transmission*, submitted to: ACS Photonics

Reproduced with permission from ACS Photonics, submitted for publication. Unpublished work copyright [2018] American Chemical Society.

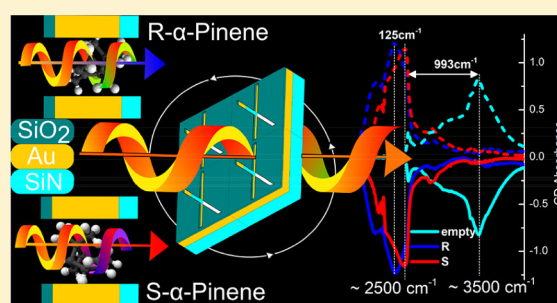
Slit-Enhanced Chiral- and Broadband Infrared Ultra-Sensing

Richard Knipper,[†] Vladimír Kopecký, Jr.,[‡] Uwe Huebner,[†] Jürgen Popp,^{†,§}
and Thomas G. Mayerhöfer^{*,†,§}[†]Leibniz Institute of Photonic Technology (IPHT), Albert-Einstein-Str. 9, Jena, D-07745, Germany[‡]Institute of Physics, Faculty of Mathematics and Physics, Charles University, Ke Karlovu 5, Prague 2, CZ-12116, Czech Republic[§]Institute of Physical Chemistry and Abbe Center of Photonics, Friedrich-Schiller-Universität Jena, Helmholtzweg 4, Jena, D-07743, Germany

Supporting Information

ABSTRACT: This work demonstrates a membrane-based chiral plasmonic metamaterial with two plasmonic absorption bands which can be used for broadband surface-enhanced infrared absorption (SEIRA) and vibrational circular dichroism (VCD) sensing in the spectral range $\sim 1000\text{--}4000\text{ cm}^{-1}$ (SEIRA) and $\sim 2000\text{--}4000\text{ cm}^{-1}$ (VCD). Based on finite-difference time-domain simulations, the chiral plasmonic response was optimized for enhancement at around 3200 cm^{-1} . Accordingly, the chiral cross-slit array was adjusted for application in conventional transmission measurement setups and covers an area of 1 mm^2 . Polyethylene was used as a model analyte to simulate the SEIRA broadband response and the results were compared with octadecanethiol measurements due to their spectral similarity. Signal enhancement was observed from 3000 cm^{-1} down to 1400 cm^{-1} by tuning the polarization of the incoming radiation. Due to the inherent chirality of the design, a strong VCD absorbance of 0.83 at $\sim 3500\text{ cm}^{-1}$ could be observed for the unloaded substrate. For substrates loaded with α -pinene, it was observed that this value even increased to more than unity and, in addition, direct enhancement of VCD could be achieved, although the VCD signal is not directly comparable with that of the neat substance. Since the substrate–analyte complex also shows a giant circular birefringence effect, most likely due to the formation of a chiral effective medium, it has great potential to be used as a sensor and may be applicable in a multitude of different scenarios in the analysis of biologic and pharmaceutical substances.

KEYWORDS: chiral plasmonics, infrared spectroscopy, metamaterials, surface enhancement, vibrational circular dichroism



Being first reported by Hartstein et al.,¹ plasmonic enhancement in the infrared (IR) range has moved to become a potential tool for practical applications² instead of being a mere theoretical consideration. In the last couple of years, plasmonic enhancement demonstrated the boost of signal intensities beyond the monolayer capacity already available by conventional methods. Methods like attenuated total reflection,³ buried metal layer IR reflection absorption spectroscopy,⁴ have thus far helped to enable monolayer sensitivity, despite IR absorption cross sections being typically 3 to 4 orders of magnitude lower than, for example, fluorescence.⁵ However, a further boost of signal intensities beyond this point by improving conventional methods is unlikely. On the other hand, plasmonic enhancement helped to enhance the small Raman cross sections up to single molecule sensitivity,⁶ so while absorption as a one-photon process does not profit in the same way as two-photon processes it can be assumed that sensitivity of infrared spectroscopy can be greatly amplified by plasmonic enhancement, with theoretical values approaching those of regular surface-enhanced Raman spectroscopy (SERS) substrates.⁷ As a drawback, this enhancement is only available in so-called hot spots with high electric field

intensities which are sparsely distributed, for example, in arrays of metallic nanoantennas,⁸ so that the overall signal intensities remain comparably weak.

Naturally, this reduces applicability in “real-life” spectroscopic tasks due to the weak αE^2 signal enhancement in surface-enhanced IR absorption (SEIRA). This could have rendered the approach mostly useless for tasks in life-science and where the analyte is not abundantly available. With a design optimized toward applicability, it is nevertheless possible to achieve “hot-spots” and sufficient overall signal intensity (yet still weak compared to αE^4 for SERS). By utilizing slotted membranes, one can combine extraordinary optical transmission (EOT)⁹ with a passivation layer to prevent the analyte from binding outside the slit itself, thus light and analyte are confined in the same area, for example, inside slits. The corresponding idea of plasmonic subwavelength hole arrays (SHA), consisting of holes in the form of squares, goes back as far as 2003.¹⁰

Received: April 12, 2018

Published: July 23, 2018

Huck et al.¹¹ compared the benefits of slits (as a subgroup of nanoholes) to those of linear nanoantennas in 2015. They found that slits are beneficial, as the electric field intensity decline within said slits is smaller than that of corresponding linear nanoantennae. In the same year, Mayerhöfer et al.¹² presented an SHA based on a combination of EOT and perfect absorption and Cheng, Yang, and Gao published a study about a dolmen-type slit structure.¹³

In another approach, even before the works of Huck et al.,¹¹ Cetin et al. demonstrated H-shaped slits,¹⁴ where the slit connecting the two parallel and vertically oriented slits was extended beyond the vertical slits. The H-slit design showed highly anisotropic plasmon resonances, with one polarized along the horizontal slit and another two being oriented in the vertical polarization direction. This allowed tuning the resonance frequencies of the two resonances independently and further allowed to cover a broader range of the infrared spectrum. Additionally, to enabling both measurements in reflection as well as in transmission mode, a freestanding membrane was used to support the plasmonic active layer. While using the same approach for the support layer, our slit structure consists of two slits, one vertically oriented and the second one at an angle of $\pm 45^\circ$, with both slits intercepting at the center. When the slits are of different length, also two plasmonic resonances occur, however, the resonances are not orthogonal to each other. When this unit cell is multiplied to form an array, the resulting array is chiral, like substrates shown prior by Decker et al.,¹⁴ and might be a promising candidate for plasmonic enhanced chiral sensing. This is not necessarily the case, as achiral 2D metamaterial arrays are also regularly employed in enhanced circular dichroism (CD) sensing.^{15,16}

This work is motivated by a dissent in the literature whether a plasmonic-active substrate needs to be chiral itself to enhance the relatively weak CD effects of chiral molecules caused by absorptions in the UV spectral range while they are usually probed by plasmons resonances situated in the NIR. This assumption is, for example, supported by experimental results provided in refs 17–24.

The contraposition is also well represented in the scientific community,^{25–29} and theoretical considerations by Tang and Cohen²⁵ were further refined by Schäferling et al.³⁰ in 2012 and suggest that a substrate offering enhancement of CD should mainly feature conditions where E and H field orientation within the hotspots of the structure is not orthogonal. Derived from these considerations, claims were made that 2D structures are inherently incapable to boost chiral response³¹ and may even have detrimental effects. The authors of ref 31 aim to find an answer as to whether the chiral substrate's plasmonic near-field inside the slit geometry indeed cancels out each other's signal contribution or if the chiral enhancement is possible. To also shed some light onto this problem, we decided to investigate chiral plasmonic enhancement in the IR spectral region with the advantage that the plasmonic absorption can be tuned to have the same resonance frequency as the vibrational absorptions of the analyte, thereby enhancing potential effects by several orders of magnitude.

With first experiments showing a giant CD effect of our substrates, as was reported in ref 32, it is evident that the body of knowledge regarding plasmonic chiral enhanced sensing is not complete as the observed giant CD effect is very large for our pseudo-2D chiral substrate. Continuing the work, we have further verified our findings and observed an even larger CD when a chiral molecule is present in the slits of the chiral

metamaterial. In addition to a very strong circular birefringence effect, an enhancement of CD is also evident, indicating the formation of an effective chiral metamaterial. Contradictory to prior examples,³³ we believe to have observed the formation of enantiomeric substrate–analyte complexes, whereas Hendry et al.¹⁸ observed the formations of diastereomeric complexes. However, in contrast to the effect Hendry et al.¹⁸ came across, the one observed in this paper is, as we will show in the following, several orders of magnitude larger since plasmon and molecular excitation are on resonance. This is, as far as we know, the first time that an on-resonance case could be experimentally studied.

MATERIALS AND METHODS

Numerical Modeling. Numerical modeling was carried out using the finite-difference time-domain (FDTD) method as implemented in the software “FDTD Solutions” by Lumerical. FDTD is based on the time-dependent Maxwell equations in their partial differential form. To solve these, both space and time are discretized. The differentials are then estimated using central-difference approximations. The resulting equations are solved iteratively until a steady-state behavior is reached. The convergence of the solutions to the exact solutions of the Maxwell equations depends on a suitable choice of the number of discretization steps and the simulation time. For our simulation, we validated convergence by letting selected simulations run with stronger discretization and longer simulation times. Selected simulations were cross-checked by modeling the structure again with the finite element method. Generally, we enforced stronger discretization within the parallel slit ($\Delta x = 5$ nm, $\Delta y = 10$ nm, $\Delta z = 5$ nm, where x is oriented parallel to the main-slit width, y to the length, and z to the depth). The residual structure was covered with only slightly different constants to account for the presence of the second slit ($\Delta x = 10$ nm, $\Delta y = 10$ nm, $\Delta z = 5$ nm). The total modeling volume was 1000 nm (the period in x -axis) by 1800 nm (in y) by 11 μm (in z -direction; the direction of the incoming light), see Figure 1. Periodic boundary conditions

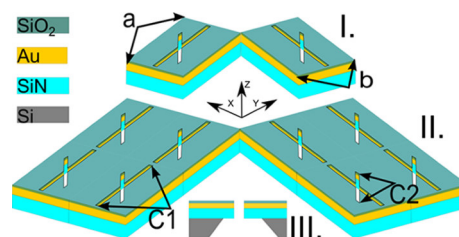


Figure 1. (I) Unit cell as simulated with periodic boundary conditions; (II) Optimized subwavelength hole array; $a = 1800$ nm, $b = 1000$ nm, primary slit length $C1 = 1700$ nm, secondary slit length $C2 = 1000$ nm, and the gap width is 50 nm; (III) Cross-section of the membrane structure.

were applied at the x - and y -boundaries. This assumption neglects the supporting grid, where periodic conditions are disturbed. The z -boundaries were surrounded by perfectly matched layers. For the gold layer, we used optical constants based on Johnson and Christy³⁴ in parametrized form, as suggested by Etchegoin et al.^{35,36} Since these allowed for an overall better prediction of the experimental data than recent results for dielectric functions measured directly in the MIR, SiO₂ layers were modeled with our own data³⁷ and a

conducted dispersion analysis. Polyethylene (PE)³⁸ was chosen as an organic analyte stand-in primarily because its optical constants in the IR are known and because the bands in the spectral region-of-interest resemble those of one of the model analytes, that is, octadecanethiol.

Fabrication of SHA. To fabricate the SHA, a standard silicon wafer (100 mm semistandard, 5 ppm bor, 100-oriented) was coated using low-pressure chemical vapor deposition with 150 nm of low stress (<50 MPa tensile stress), non-stoichiometric silicon-nitride. Wafers were then covered with a sandwich of 3 nm titanium as sticking-layer, 50 nm of gold, and again 2 nm of titanium to prepare an interface for a subsequent coating of silicon oxide (SiO₂) fabricated using atomic layer deposition (ALD). The plasma-enhanced ALD process was performed with an OpAL-reactor from Oxford Instruments (upgraded with an inductive-coupled plasma source). As precursors in the ALD processes, we used tris(dimethylamino)-silane for SiO₂ which was deposited with remote oxygen plasma at a plasma pressure of 22.3 Pa. The growth rate of SiO₂ was estimated to be $1.19 \pm 0.06 \text{ \AA}$ per cycle, with a target thickness of 10 nm and a resulting number of 90 cycles. This passivation layer was covered with 30 nm of sputter-deposited NiCr, which was structured by e-beam lithography and used as an etching mask. The X patterns of the SHA gratings were made by shaped electron beam lithography. The electron beam resist was AR6200.09 by Allresist GmbH Berlin. It was spun to a thickness of 155 nm and, additionally, covered with a 10 nm thick gold conduction-layer created by using thermal evaporation. The e-beam exposure of the individual SHA gratings on the wafer (each with a size of $1 \times 1 \text{ mm}$) was performed using the shaped e-beam writer SB350 OS (50 keV, Vistec Electron Beam GmbH) at an electron dose of $400 \mu\text{C}/\text{cm}^2$. Exposure time per grating was as low as 18 min. The resist was developed for 60 s in AR600–546 (Allresist) and rinsed for 30 s in isopropanol and Ar⁺-ion beam etching opened the hard mask NiCr layer. The silicon was structured using silicon wet-etching (KOH) to open up the membrane which then slit via RIE etching by CHF₃ to structure the SiO₂Au/SiN sandwich. After removing the NiCr hard mask with wet-etching, chips were separated to $1.5 \times 1.5 \text{ cm}$ by notching and breaking (to avoid any contamination by the protective resist layers that are needed for separating the chips on a wafer with a dicing saw), resulting in the structure seen in Figure 2.

Sample Preparation. As analytes, we used organic solvents, ethanol, isopropanol, and octadecanethiol (p.a., Sigma-Aldrich). Octadecanethiol was drop-casted as 1:1 diluted saturated solution in ethanol on the backside of the membrane ($2 \mu\text{L}$) and was transported into the slit area by capillary forces. Samples were allowed to dry naturally before storing them under vacuum conditions to remove any remaining traces of ethanol. When needed, samples were cleaned with ethanol, blow dried and then O₂ plasma-cleaned in a remote plasma vacuum chamber to remove organic contamination on the arrays. The cleaning time was 3 min at 500 W. As chiral analytes, $4 \mu\text{L}$ of R- and S- α -pinene (97% of enantiomeric excess, Aldrich) was drop-casted, and the substrates were rinsed with ethanol in between measurements. The racemic mixture was combined from the two enantiomers in a 1:1 ratio and $4 \mu\text{L}$ were used as well. All CD samples were incubated in the sequence of enantiomers: clean, S; cleaned with ethanol, R; cleaned with ethanol, R/S.

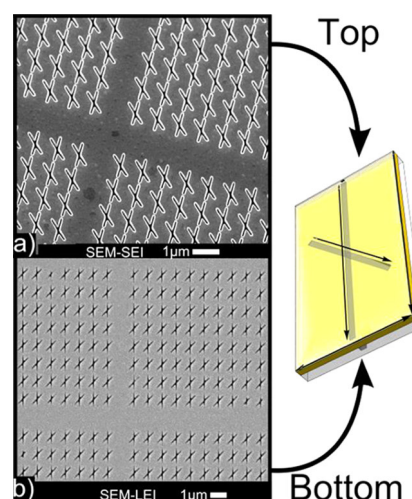


Figure 2. (a) Top-side SEM image of cross-structure, recorded with a secondary electron detector. The detector, showing the material contrast of opened-up Au-layer passivated with SiO₂. (b) Bottom view of the same chip, showing the opened-up SiN membrane. It becomes evident that the slit runs through the whole length of the membrane and slits are fully opened through the whole membrane.

Infrared Spectroscopy. The IR reflection spectra were recorded with a Bruker Vertex 80v FT-spectrometer with an attached IR Microscope (HYPERION 2000) and a $15\times$ Cassegrain IR objective with 0.4 NA. The angle of incidence was $<23.6^\circ$. A KRS-5 linear polarizer with a spectral window from 7500 to 370 cm^{-1} was used and an LN-MCT detector from Bruker (MCT-D316). Reflection measurements were referenced against Au mirrors or blank sample surfaces. The spectrometer compartment was evacuated below 3 mbar with the microscope body and purge box being flushed continuously with N₂. Transmission references were recorded with an aperture the exact size of the membrane (i.e., a chip where the membrane had been removed). Record mode was single-sided forward–backward sampling with the Mertz and Blackman-Harris three-term chosen for phase correction and apodization, respectively. As a default, 64 spectra were averaged; the octadecanethiol measurements consisted of 256 scans. The experiments were conducted with a resolution of 1 cm^{-1} .

Vibrational Circular Dichroism. VCD measurements were recorded on ChiralIR-2X (BioTools), using two standard MIR sources, a KBr beamsplitter, Dual PEM setup, and an MCT detector.³⁹ A total of 4000 scans in one block (taking ca. 75 min) were collected with 4 cm^{-1} spectral resolution (at least 14 scan blocs were collected to check the signal stability and final spectrum proceeded as an average of these blocks) and a Blackman-Harris three-term apodization function. The photoelastic modulators (PEM) and subsequent corrections were set for $\lambda/4$ at 2800 cm^{-1} . The absorbance is given relatively to the aperture of the membrane size. The spectrometer was purged by dry air during all experiments. The continual rotation of the samples (one turn per ca. 10 s) was performed using SyncRoCell (BioTools). The samples (mounted onto a holder consisting of two aluminum plates with Teflon spacers) were placed with their Au-side toward the MIR sources (i.e., directly opposite the MCT detector).

RESULTS AND DISCUSSION

Resulting Design of the SHA. To enable transmission measurements, in particular for VCD measurement setups, the metamaterial perfect absorber (MPA) part featured in our prior work¹² (i.e., a nontransparent reflective layer) had to be removed since it limited the measurement conditions to only work in reflection geometry. A silicon nitride (SiN) membrane was chosen as the supporting structure. The slits cut through the whole of the plasmonic active Au and SiN-layer, effectively connecting the top and the bottom side. Following the example of our prior work,¹² we chose a thin gold layer to limit columnar growth within that layer while maintaining a low transmission rate of 1×10^{-3} for wavenumbers longer than 4425 cm^{-1} . This way, the resonance wavelength of the substrate will be tunable throughout most of the IR spectral range. One advantage of this structure is, that capillary forces transport analyte with solvent placed on the SiN side of the membrane through the slits, ensuring full coverage of the array's active area, avoiding incubation problems based on surface tension on the gold side. (For a detailed view, see Figure 1 and subsection "Fabrication of SHA" in the Materials and Methods section.) The cross-like structure that can be seen in Figure 2 represents one unit cell, which was repeated over a 1 mm^2 area, with every 11th slit left out to improve mechanical stability. Thus, immersion in organic and inorganic solvents does not show any detrimental effects, and the array can be blow-dried with N_2 . To ensure that the only binding sites are inside the slits, all exposed gold on the surface of the chip is covered by either SiO_2 or SiN, respectively. The overall area of $1 \times 1 \text{ mm}$ contained 860×800 slits, that is, a total of 688 000 single cross-structures. Due to the supporting grid of SiN ribbons, ruptured membranes as a result of nitride flaws or mechanical stress were observed to be confined to only one field of 10×10 crosses in most cases.

The simulations (without PE) show the two resonances we expected, the narrow secondary mode around 3200 cm^{-1} and the broader primary resonance around 2050 cm^{-1} . Reflection and transmission values and resulting absorption values are shown in Figure 3 along with simulations of PE filled slits (right column). Judging from Figure 3, the primary plasmonic resonance at $\sim 2050 \text{ cm}^{-1}$ shows a theoretical minimum reflectance of around 4% for light polarized perpendicular to the axis of the long slit, while the secondary resonance at $\sim 3200 \text{ cm}^{-1}$ shows around 15% in the absence of an analyte (note that the theoretical minimum would actually be reached at a polarization direction of 45° , since the simulations have been carried out for the -45° slit). The corresponding maximum transmittance values for these polarization directions are 65% for the $\sim 2050 \text{ cm}^{-1}$ resonance and 35% for the secondary resonance at about $\sim 3200 \text{ cm}^{-1}$. The shift observable for both resonances (when filling the gaps with PE) is a result of the higher dielectric function of PE, effectively detuning the plasmonic resonances. For PE-filled slits, a shift toward higher wavelength is confirmed in the simulations with a shift from 2058 to 1733 cm^{-1} for the primary resonance and from 3195 to 2681 cm^{-1} for the secondary resonance (see dashed lines in Figure 3). In comparison to the spectra of the bare fabricated samples (see Figure 4), only a slight mismatch in resonance position can be seen for the primary 2050 cm^{-1} resonance while a larger shift can be observed for the secondary 3200 cm^{-1} resonance, which is situated at 3401 cm^{-1} having a blue shift of around 150

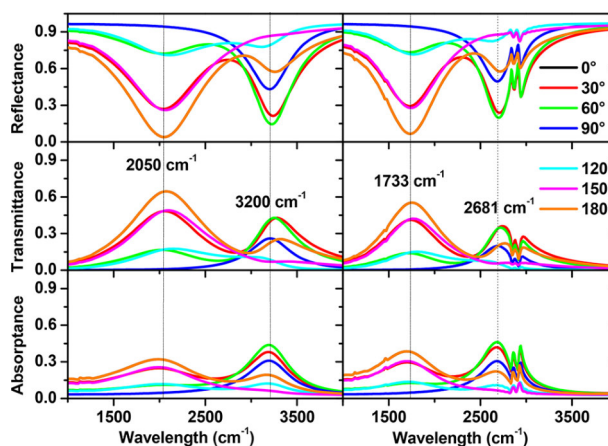


Figure 3. Calculated reflection–transmission–absorption values (with 0° to 180° polarized light) for membrane-based subwavelength hole arrays for empty gap regions (left) and polyethylene-filled gaps (right); dashed lines indicate marked plasmonic peak positions. A shift in primary peak position from 2050 to 1733 cm^{-1} for polyethylene-filled gaps is observable, as well as from 3200 to 2681 cm^{-1} for the secondary resonance. (See Figure S3 in Supporting Information for a detailed depiction of the array's relative orientation.)

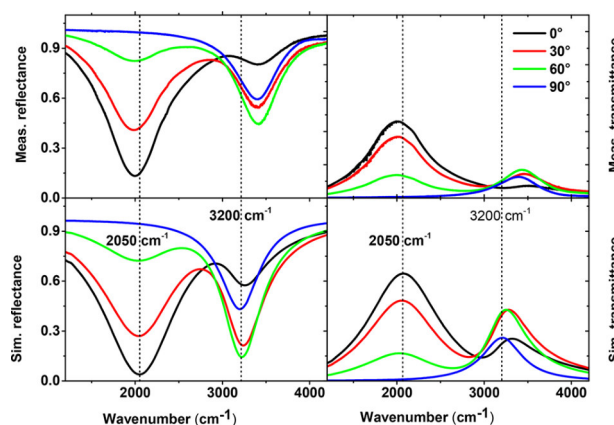


Figure 4. Measured (top) and simulated (bottom) reflection (left) and transmission (right) values for membrane-based subwavelength hole arrays for empty gap regions with 0° to 90° polarized light.

cm^{-1} . The same behavior can be found in transmission measurements. For the measured reflectance and transmittance values, reflectance has been reduced to 13.3% and 44%, respectively, indicating deviations for the secondary gap. For transmission, 46% and 13% are transmitted, well below the theoretical numbers. This may be due to an inhomogeneous gap profile (rather unlikely) or incompletely opened gaps which may not be detectable by SEM imaging seen in Figure 2, since deviation from the calculated values is higher than in the case of reflection. Control over the gap geometry thus seems to be crucial for transmission conditions.

Infrared Measurements. For analyte experiments, octadecanethiol measurements demonstrate the broadband enhancement of the SHA with both the expected symmetric CH_2 stretching vibration at $\sim 2849 \text{ cm}^{-1}$ (asymmetric at $\sim 2924 \text{ cm}^{-1}$) and asymmetric CH_3 stretching vibrations at $\sim 2959 \text{ cm}^{-1}$ and also the CH_2 scissoring vibration $\sim 1466 \text{ cm}^{-1}$, as seen in Figure 5. By selecting a specific plasmonic

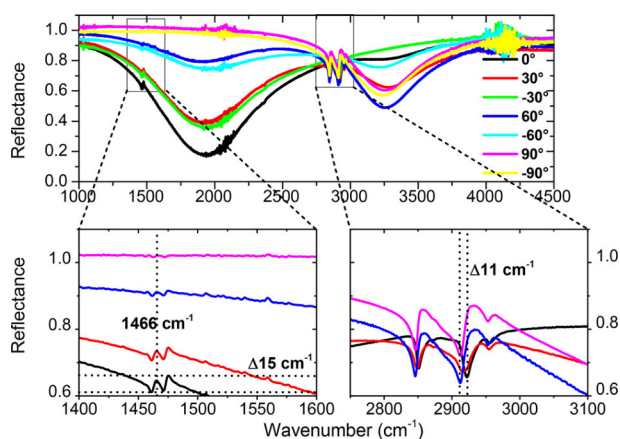


Figure 5. Measurement of the octadecanethiol-filled gap array with from $+90^\circ$ to -90° oriented polarized light (0° being orthogonal to the primary, nonangled slit with -90° being clockwise rotation). The increased enhancement of the vibrational CH_2 and CH_3 bands becomes apparent. (Lower left) CH_2 scissoring vibrational signal at 1466 cm^{-1} increasing with the excitation of the affiliated plasmon band (90° to 0° , resulting in a reflectance reduction of 4.1% (tuned from 0.5% reduction to 4.6% reduction)); note the inverse form of the vibrational signal due to coupling with the plasmonic resonance. (Lower right) CH_2 and CH_3 symmetric and asymmetric vibrational signals. Note the shift in band position of around 11 cm^{-1} , depending on band position (0° to 60° yields maximum shift).

resonance, this vibration can be turned on and off, respectively, see Figure 5 (bottom left). Despite the passivation layer present, small quantities of octadecanethiol may remain on the surface but do not contribute to the spectral information. This is due to the surface selection rules for metallic surfaces which still apply with only 10 nm of the passivation layer. Since only very minor bands can be observed for the nonresonant case of polarization, this guarantees that the reported increase in the signal intensity is indeed due to plasmonic coupling. Because of the inherent weakness of the scissoring vibration, being still detectable, is a hint to the enhancement present. A detailed examination of the CH_2 and CH_3 resonances at $\sim 2900\text{ cm}^{-1}$ showed a shift in band position of around 11 cm^{-1} . Caused by Fano-like coupling of the analyte and plasmonic resonance, this shift is in accordance with Maxwell's law and further supports a plasmonic enhancement mechanism (since analyte on the surface cannot couple to a localized plasmonic resonance inside the gap region). The signal intensity is nonzero for every polarization-direction since the bands are situated between two plasmon bands, one of which is always excited. For this case, the signal increases from 8.6% to 16% reflectance for the CH_2 band. With plasmonic enhancement present over a range of more than 1500 cm^{-1} , it is possible to excite not only singular vibrational bands (like the demonstrated CH_2 and CH_3 stretching vibrations at $\sim 2900\text{ cm}^{-1}$) but also scissoring vibrations, supporting our claim of true broadband enhancement.

Vibration Circular Dichroism of α -Pinene. For chiral measurements, the substrates were rotated continuously during long-time measurements to avoid possible linear dispersion artifacts (one of the main sources of incorrect CD signals). Further, since no cuvette walls were present, no standing-wave effect had to be considered.⁴⁰ Measurements performed on unloaded substrates with $+45^\circ$ and -45° of the shorter slit resulted in a nearly perfect mirror symmetry in their CD

spectra (see Figure 6 and 7), much as expected from the simulations. A very small background variation can be noticed

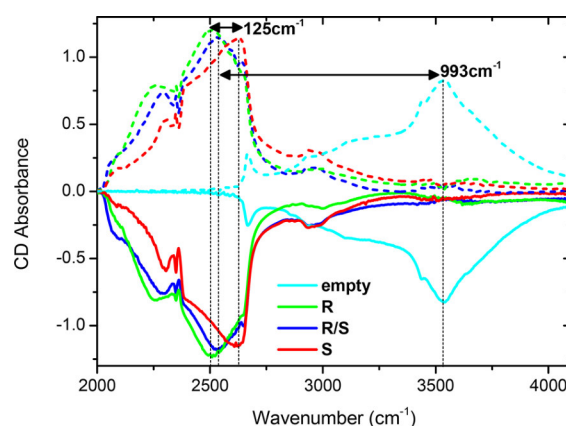


Figure 6. Comparison of front-side illuminated (solid lines) and back-side illuminated (dashed lines) orientation (i.e., change in chirality) measurements of *R*-, *S*-, and racemic α -pinene (*R/S*) VCD on a $+45^\circ$ oriented array. The spectrum is showing a major impact of plasmonic shift changes along with broadening of analyte bands presenting a distorted resulting spectrum. Unexpectedly, a very strong difference in the shift is observable, depending on the analytes' chirality. Counterintuitively, it is independent on the second slit orientation, supporting the assumption of an effective medium. "Dashed empty" line is depicted as a guide to the eye.

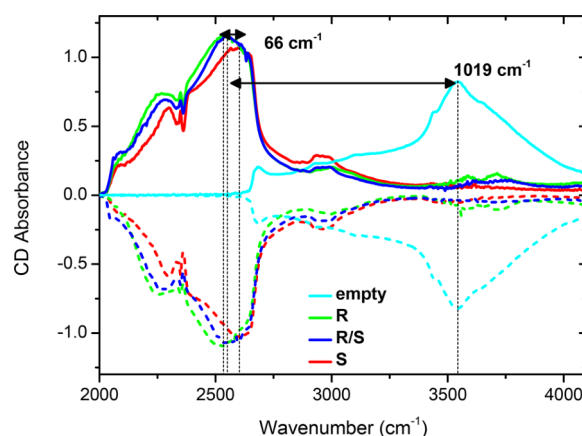


Figure 7. Comparison of normal front-side illuminated (solid lines) and inverted back-side illuminated (dashed lines) orientation (i.e., change in chirality) measurements of *R*-, *S*- and racemic α -pinene (*R/S*) VCD on a -45° oriented array demonstrating the strong compliance of both -45° and $+45^\circ$ arrays with nearly identical shifts and band positions. Despite the marginally smaller distance between *R*- and *S*- α -pinene, the behavior is similar to Figure 6. "Dashed empty" line is depicted as a guide to the eye.

together with the CO_2 band being present in all spectra which stems from the ambient air despite of the dry purge. The presence of CO_2 in CD spectra might be surprising. However, simulation with PE showed that the vibrational signals of nonchiral molecules occur in VCD spectra since circularly polarized light leads to strong differences in the field enhancements of the $+45^\circ$ and -45° substrates (see Figure S1 in Supporting Information). The CD response of the substrates is maximal with an absorbance of 0.83 at $\sim 3500\text{ cm}^{-1}$. For simulations, we calculated the absorbance, while the

ChiralIR-2X setup measures transmission, but its software does not allow retrieving transmittance spectra. Instead, the software calculates absorbance according to the equation $A = -\lg(T)$. This is the usual practice in molecular infrared spectroscopy, even though absorbance as a quantity is to be avoided to ensure compliance with Maxwell's equations,⁴¹ in particular, since the substrates are highly reflective. Regarding the steeper descent in CD signal intensity of the real samples at lower wavenumbers, reasons can most likely be found in the photoelastic modulators characteristics, something that could not be addressed with the current setup. With the PEMs having a narrow bandwidth, the system has a spectral window of $2800 \pm 800 \text{ cm}^{-1}$.

Before investigating the spectra of the substrate and chiral molecules, it might be instructive to shortly summarize what could be expected based on the existing theories. According to the theory of superchiral fields,^{23,25} our substrates should not show any chiral response, as the chiral enhancements should cancel each other as corresponding calculations showed. Furthermore, it seems to be a disadvantage to using substrates that are chiral itself, as the strong signals from the substrates should veil the signals of the chiral molecules.²⁹ Nevertheless, Hendry et al.¹⁷ presented a clear spectral signature in case of the presence of chiral macromolecules close to their chiral plasmonic structures. This signature consisted in a red-shift of the CD peaks using one enantiomeric form of their chiral substrate and a blue-shift in case of the other. This could be interpreted by the assumption of the formation of a diastereomeric complex between the chiral macromolecule and chiral plasmonic structure, according to which the complexes should no longer show enantiomeric CD responses. In the case of our substrates, it seems that the $+45^\circ$ and -45° substrates even after loading with the α -pinene molecules behave like enantiomers irrespective if we apply a pure enantiomer or the racemic mixture.

When applying the racemic mixture of both α -pinene enantiomers to the $+45^\circ$ chip (see Figure 6), a very strong shift of about 990 cm^{-1} of the position of the plasmon band is observable. This shift lies in between the shift that is observed when the pure *S*- or the pure *R*-form of α -pinene is observed. The overall difference in the shift of the plasmonic band between the enantiomeric form is 125 cm^{-1} , with the racemic mix being situated between both forms, but not in the center as would be expected, since the difference in the shift is accompanied by changes in the shape of the plasmon band. The difference in the shift is in our opinion a strong indicator of a circular birefringence effect, since the shift itself is, as is well-known, a function of the index of refraction of the analyte. The shifts are observable for both, the $+45^\circ$ (see Figure 6) and -45° arrays (see Figure 7) and are present independently of the arrays illumination direction. Note that the dashed curves in Figures 6 and 7 belong to spectra recorded with back-side illumination of the substrates, effectively changing its chirality resulting in a sign change; the back-side illumination can only lead to approximate mirror images concerning the spectra as the top and the bottom layer are different. The corresponding deviations are, however, small. Both shift strengths are between about 990 and 1020 cm^{-1} nearly identical. Also, the band positions are of remarkable similarity and the enantiomer-dependent shift is present in both data sets. The present smaller asymmetries are nothing out of the order if compared to those of chiral measurements in the literature and may, at least, partly be caused by fabrication imperfections. Overall, as

already stated above, no diastereomeric asymmetries occur. To further support our findings, an achiral control array with a 90° angle was fabricated and measured. Here, no giant CD signal was observed, although a minute CD signal of around ± 0.04 of unknown origin is observable (see Figure S2 in Supporting Information). The band shape is independent of the used analyte and already present on the empty array, leading us to the conclusion that an artifact caused by the plasmonic resonance itself is present. The width of 896 cm^{-1} rules out a molecular contribution to the signal. Nevertheless, neither the primary nor the secondary plasmonic resonance is observable for the presence of α -pinene. This is another strong indicator of true VCD observation on the chiral arrays.

The fact that the $+45^\circ$ and -45° substrates filled with the same enantiomeric form of α -pinene (e.g., $+45^\circ + S$ - α -pinene and $-45^\circ + S$ - α -pinene) still show enantiomeric and not diastereomeric behavior in contrast to the results of refs 17 and 24 (actually, while the simulations in ref 24 predict diastereomeric behavior, the experimental findings are much closer to an enantiomeric than a diastereomeric relationship in this case, cf., Figure 3d with Figure 3g) is unexpected and leads us to the conclusion that the small chiral molecules together with the chiral substrates form a chiral effective medium. We think that the larger shift in the plasmon band for *R*- α -pinene relative to *S*- α -pinene could be caused by a difference in the chiral birefringence of the substrate–analyte complex, which is related by the Kramers–Kronig relations to the difference in the chiral dichroism in the region between 2900 – 3000 cm^{-1} , where the analyte's C–H group vibrations are located. The related bands indeed show corresponding characteristic shape and intensity changes. Unfortunately, these spectral regions do not directly correspond with the infrared circular dichroism spectra of the neat enantiomers. This could, however, also not be expected since in this spectral region also the nonchiral infrared bands are differently excited by the different enantiomeric forms of the substrate if circularly polarized light is employed (cf., Figure S1). Therefore, as already stated above, the presence of signals for the racemic mix of α -pinene is not surprising and our assumption was that these are the pure vibrational infrared signals that we see. However, a comparison with these bands in the IR spectra (e.g., ref 42) shows that already the peak heights are somewhat altered. Nevertheless, based on the assumption that the racemic mixture shows pure vibrational bands, we tried to extract the VCD signals by fitting a baseline and then subtracting the signal of the racemic mixture from that of the pure enantiomeric forms (see Figure 8). At least for the $+45^\circ$ substrate, the resulting spectra again show that the complex formed between substrate and analyte again behaves as a chiral effective medium with two enantiomeric forms. In the case of -45° substrate, this conclusion is less well supported, since the signal for the racemic mixture and *S*- α -pinene seemed to be nearly the same, in particular, if the substrate is inverted. Nevertheless, the shift and shape change of the plasmonic band allows still to easily differentiate between the pure molecular enantiomers and their racemic mixture. Overall, while there is still need for clarification with regard to the microscopic mechanisms that underlie the macroscopic effective chiral medium that is established by substrate and molecule, our substrate allows to easily distinguish between the enantiomers and the racemic mixture with signals strong enough that allow potentially to replace the comparable complicated measuring

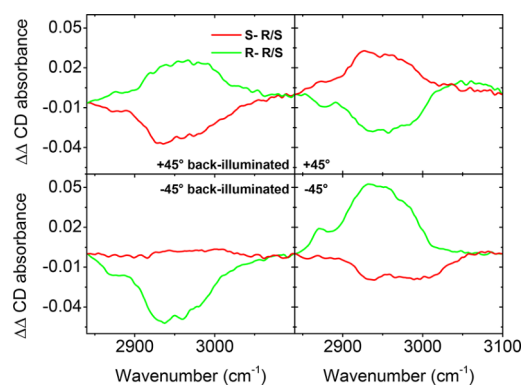


Figure 8. Comparison of $+45^\circ$ and -45° oriented slits modified with *R*- and *S*- α -pinene. The presented spectra are *R*- and *S*- α -pinene spectra from which the racemic spectrum has been subtracted after background correction. Both normal and back-illuminated orientation showing that the *R*- α -pinene absorbance is reduced and *S*- α -pinene absorbance is enhanced (a) and (b). For the -45° orientation, the behavior is inverse, but less dominant, with (c) showing only very little enhancement and (d) being marginally stronger.

scheme using PEMs with the much simpler one used in the UV/vis spectral region.

CONCLUSIONS

In general, we succeeded in our aim to fabricate a membrane-based SHA with a broadband plasmonic enhancement based loosely on our prior SHA-MPA design. For surface-enhanced infrared spectroscopy, the broadband SHA performed as expected and showed signal enhancements over a wide spectral range, with the potential to be applied in a multitude of measurement scenarios. The reflection–transmission capabilities together with the tunability of the plasmonic resonances are in the expected range and strength, as determined by spectral simulations.

The SHA further is, by design, not only a promising candidate for SEIRA with tunable plasmonic enhancement, but also for chiral plasmonic sensing. This is beneficial for real-life applications of the SHA in analytics, especially in VCD measurements where small sample volumes are predominant. The presence of capillary forces intrinsic in our design is another aspect which should be further addressed in terms of sample preparation and maybe size exclusion of larger particles. The chiral response of our chiral SHA increases from 0.83 in the empty form to around 1.2 for an analyte modified surface. This giant CD response, together with an enantiomer-dependent shift of the plasmon band, probably caused by an effective medium circular birefringence effect, is unexpectedly strong and does, to the best of our knowledge, not comply with the established theory. This shift is also a strong indicator for a plasmonic enhancement of the circular dichroism of the analyte, although the formation of the analyte–substrate complex strongly distorts the VCD bands of the analyte. With regard to routine controls after the preparation of an enantiomer, the shown concept could be employed to check the enantiomeric excess by our approach as it has the potential to work without the need for the use of PEMs, although it yet has to be checked how precisely the enantiomeric excess can be quantified. Our findings are a strong indicator that surface-enhanced VCD is indeed possible, but at the same time demonstrates the problems connected to the very strong

plasmon resonance being present at the same wavenumbers as the analyte. Still, this first indication of surface-enhanced VCD might also provide valuable insights into, so far unknown and yet to understand, interdependencies when combining chiral metamaterials with chiral molecules.

ASSOCIATED CONTENT

Supporting Information

The Supporting Information is available free of charge on the ACS Publications website at DOI: 10.1021/acsp Photonics.8b00476.

Simulated circular dichroism absorbance for the $+45^\circ$ and the -45° substrate, without PE and with PE in the slits depicted in Figure S1. A negative control experiment featuring a 90° oriented second slit (e.g., an achiral array) incubated with *S*-, *R*-, and *S/R*- α -pinene is shown in Figure S2. The relative orientation of the linearly polarized light with respect to the array orientation is described in Figure S3 (PDF).

AUTHOR INFORMATION

Corresponding Author

*E-mail: thomas.mayerhoefer@ipht-jena.de.

ORCID

Thomas G. Mayerhöfer: 0000-0001-9396-7365

Notes

The authors declare no competing financial interest.

ACKNOWLEDGMENTS

V.K. acknowledges financial support from the Czech Science Foundation (P205/12/G118). The project “JBC12.0” (03IPT513Y – InnoProfile-Transfer, Unternehmen Region), supported by the Federal Ministry of Education and Research (BMBF), Germany, is gratefully acknowledged. The authors thank D. Franke, B. Steinbach, M. Ziegler, and S. Goerke (IPHT) for their valuable help with the fabrication of the plasmonic substrates, K. Dietrich (Friedrich-Schiller-Universität Jena) for fruitful discussions regarding chirality and metamaterials, and Tomáš Pazderka (Charles University and BioTools) for discussions regarding the BioTools VCD setup.

REFERENCES

- Hartstein, A.; Kirtley, J. R.; Tsang, J. C. Enhancement of the Infrared Absorption from Molecular Monolayers with Thin Metal Overlayers. *Phys. Rev. Lett.* **1980**, *45* (3), 201–204.
- Ataka, K.; Heberle, J. Biochemical applications of surface-enhanced infrared absorption spectroscopy. *Anal. Bioanal. Chem.* **2007**, *388* (1), 47–54.
- Fahrenfort, J. Attenuated total reflection: A new principle for the production of useful infra-red reflection spectra of organic compounds. *Spectrochim. Acta* **1961**, *17* (7), 698–709.
- Zhang, Y.; Sato, S.; Ohshima, H.; Hattori, T.; Urisu, T. Buried metal layer enhanced infrared reflection absorption spectroscopy for photoreactions induced by synchrotron radiation on SiO₂ surfaces. *Appl. Surf. Sci.* **1994**, *79* (Supplement C), 422–427.
- Albota, M. A.; Xu, C.; Webb, W. W. Two-photon fluorescence excitation cross sections of biomolecular probes from 690 to 960 nm. *Appl. Opt.* **1998**, *37* (31), 7352–7356.
- Jiang; Bosnick, K.; Maillard, M.; Brus, L. Single Molecule Raman Spectroscopy at the Junctions of Large Ag Nanocrystals. *J. Phys. Chem. B* **2003**, *107* (37), 9964–9972.
- Dong, L.; Yang, X.; Zhang, C.; Cerjan, B.; Zhou, L.; Tseng, M. L.; Zhang, Y.; Alabastri, A.; Nordlander, P.; Halas, N. J. Nanogapped

Au Antennas for Ultrasensitive Surface-Enhanced Infrared Absorption Spectroscopy. *Nano Lett.* **2017**, *17* (9), 5768–5774.

(8) Mayerhöfer, T. G.; Popp, J. Periodic array-based substrates for surface-enhanced infrared spectroscopy. *Nanophotonics* **2018**, *7* (1), 39–79.

(9) Ebbesen, T. W.; Lezec, H. J.; Ghaemi, H. F.; Thio, T.; Wolff, P. A. Extraordinary optical transmission through sub-wavelength hole arrays. *Nature* **1998**, *391* (6668), 667–669.

(10) Williams, S. M.; Stafford, A. D.; Rodriguez, K. R.; Rogers, T. M.; Coe, J. V. Accessing surface plasmons with Ni microarrays for enhanced IR absorption by monolayers. *J. Phys. Chem. B* **2003**, *107* (43), 11871–11879.

(11) Huck, C.; Vogt, J.; Sendner, M.; Hengstler, D.; Neubrech, F.; Pucci, A. Plasmonic Enhancement of Infrared Vibrational Signals: Nanoslits versus Nanorods. *ACS Photonics* **2015**, *2* (10), 1489–1497.

(12) Mayerhöfer, T. G.; Knipper, R.; Hübner, U.; Cialla-May, D.; Weber, K.; Meyer, H.-G.; Popp, J. Ultra Sensing by Combining Extraordinary Optical Transmission with Perfect Absorption. *ACS Photonics* **2015**, *2* (11), 1567–1575.

(13) Cheng, F.; Yang, X.; Gao, J. Ultrasensitive detection and characterization of molecules with infrared plasmonic metamaterials. *Sci. Rep.* **2015**, *5*, 14327.

(14) Decker, M.; Klein, M. W.; Wegener, M.; Linden, S. Circular dichroism of planar chiral magnetic metamaterials. *Opt. Lett.* **2007**, *32* (7), 856–858.

(15) Cao, T.; Cryan, M. J. Enhancement of circular dichroism by a planar non-chiral magnetic metamaterial. *J. Opt.* **2012**, *14* (8), 085101.

(16) Cao, T.; Wei, C.; Mao, L.; Li, Y. Extrinsic 2D chirality: giant circular conversion dichroism from a metal-dielectric-metal square array. *Sci. Rep.* **2015**, *4*, 7442.

(17) Hendry, E.; Carpy, T.; Johnston, J.; Popland, M.; Mikhaylovskiy, R. V.; Laphorn, A. J.; Kelly, S. M.; Barron, L. D.; Gadegaard, N.; Kadodwala, M. Ultrasensitive detection and characterization of biomolecules using superchiral fields. *Nat. Nanotechnol.* **2010**, *5* (11), 783–787.

(18) Ma, W.; Kuang, H.; Xu, L.; Ding, L.; Xu, C.; Wang, L.; Kotov, N. A. Attomolar DNA detection with chiral nanorod assemblies. *Nat. Commun.* **2013**, *4*, 2689.

(19) Karimullah, A. S.; Jack, C.; Tullius, R.; Rotello, V. M.; Cooke, G.; Gadegaard, N.; Barron, L. D.; Kadodwala, M. Disposable Plasmonics: Plastic Templated Plasmonic Metamaterials with Tunable Chirality. *Adv. Mater.* **2015**, *27* (37), 5610–5616.

(20) Tullius, R.; Karimullah, A. S.; Rodier, M.; Fitzpatrick, B.; Gadegaard, N.; Barron, L. D.; Rotello, V. M.; Cooke, G.; Laphorn, A.; Kadodwala, M. "Superchiral" Spectroscopy: Detection of Protein Higher Order Hierarchical Structure with Chiral Plasmonic Nanostructures. *J. Am. Chem. Soc.* **2015**, *137* (26), 8380–8383.

(21) Jack, C.; Karimullah, A. S.; Tullius, R.; Khorashad, L. K.; Rodier, M.; Fitzpatrick, B.; Barron, L. D.; Gadegaard, N.; Laphorn, A. J.; Rotello, V. M.; Cooke, G.; Govorov, A. O.; Kadodwala, M. Spatial control of chemical processes on nanostructures through nano-localized water heating. *Nat. Commun.* **2016**, *7*, 10946.

(22) Khoo, E. H.; Leong, E. S.; Wu, S. J.; Phua, W. K.; Hor, Y. L.; Liu, Y. J. Effects of asymmetric nanostructures on the extinction difference properties of actin biomolecules and filaments. *Sci. Rep.* **2016**, *6*, 19658.

(23) Schäferling, M.; Engheta, N.; Giessen, H.; Weiss, T. Reducing the Complexity: Enantioselective Chiral Near-Fields by Diagonal Slit and Mirror Configuration. *ACS Photonics* **2016**, *3*, 1076.

(24) Zhao, Y.; Askarpour, A. N.; Sun, L.; Shi, J.; Li, X.; Alù, A. Chirality detection of enantiomers using twisted optical metamaterials. *Nat. Commun.* **2017**, *8*, 14180.

(25) Tang, Y.; Cohen, A. E. Optical chirality and its interaction with matter. *Phys. Rev. Lett.* **2010**, *104* (16), 163901.

(26) Abdulrahman, N. A.; Fan, Z.; Tonooka, T.; Kelly, S. M.; Gadegaard, N.; Hendry, E.; Govorov, A. O.; Kadodwala, M. Induced chirality through electromagnetic coupling between chiral molecular

layers and plasmonic nanostructures. *Nano Lett.* **2012**, *12* (2), 977–983.

(27) Maoz, B. M.; Chaikin, Y.; Tesler, A. B.; Bar Elli, O.; Fan, Z.; Govorov, A. O.; Markovich, G. Amplification of chiroptical activity of chiral biomolecules by surface plasmons. *Nano Lett.* **2013**, *13* (3), 1203–1209.

(28) Guerreiro, J. R. L.; Frederiksen, M.; Bochenkov, V. E.; De Freitas, V.; Ferreira Sales, M. G.; Sutherland, D. S. Multifunctional Biosensor Based on Localized Surface Plasmon Resonance for Monitoring Small Molecule–Protein Interaction. *ACS Nano* **2014**, *8* (8), 7958–7967.

(29) Lin, D.; Huang, J. S. Slant-gap plasmonic nanoantennas for optical chirality engineering and circular dichroism enhancement. *Opt. Express* **2014**, *22* (7), 7434–7445.

(30) Schäferling, M.; Yin, X. H.; Giessen, H. Formation of chiral fields in a symmetric environment. *Opt. Express* **2012**, *20* (24), 26326–26336.

(31) Schäferling, M.; Dregely, D.; Hentschel, M.; Giessen, H. Tailoring Enhanced Optical Chirality: Design Principles for Chiral Plasmonic Nanostructures. *Phys. Rev. X* **2012**, *2* (3), 031010.

(32) Knipper, R.; Mayerhöfer, T. G.; Kopecký, V.; Huebner, U.; Popp, J. Observation of Giant Infrared Circular Dichroism in Plasmonic 2D-Metamaterial Arrays. *ACS Photonics* **2018**, *5* (4), 1176–1180.

(33) Hendry, E.; Mikhaylovskiy, R. V.; Barron, L. D.; Kadodwala, M.; Davis, T. J. Chiral electromagnetic fields generated by arrays of nanoslits. *Nano Lett.* **2012**, *12* (7), 3640–4.

(34) Johnson, P. B.; Christy, R. W. Optical Constants of the Noble Metals. *Phys. Rev. B* **1972**, *6* (12), 4370–4379.

(35) Etchegoin, P. G.; Le Ru, E. C.; Meyer, M. An analytic model for the optical properties of gold. *J. Chem. Phys.* **2006**, *125* (16), 164705.

(36) Etchegoin, P. G.; Le Ru, E. C.; Meyer, M. Erratum: "An analytic model for the optical properties of gold" [*J. Chem. Phys.* **125**, 164705 (2006)]. *J. Chem. Phys.* **2007**, *127* (18), 189901.

(37) Mayerhöfer, T. G.; Shen, Z.; Leonova, E.; Eden, M.; Kriltz, A.; Popp, J. Consolidated silica glass from nanoparticles. *J. Solid State Chem.* **2008**, *181* (9), 2442–2447.

(38) Zolotarev, V. M.; Volchek, B. Z.; Vlasova, E. N. Optical constants of industrial polymers in the IR region. *Opt. Spectrosc.* **2006**, *101* (5), 716–723.

(39) Nafie, L. A. *Vibrational Optical Activity: Principles and Applications*, 1st ed.; Wiley, 2011.

(40) Mayerhöfer, T. G.; Mutschke, H.; Popp, J. The Electric Field Standing Wave Effect in Infrared Transmission Spectroscopy. *ChemPhysChem* **2017**, *18* (20), 2916–2923.

(41) Mayerhöfer, T. G.; Mutschke, H.; Popp, J. Employing Theories Far beyond Their Limits—The Case of the (Boguer-) Beer–Lambert Law. *ChemPhysChem* **2016**, *17* (13), 1948–1955.

(42) Ureña, F. P.; Moreno, J. R. A.; González, J. J. L. Rotational strength sign and normal modes description: A theoretical and experimental comparative study in bicyclic terpenes. *Chirality* **2010**, *22* (1E), E123–E129.

Supporting Information

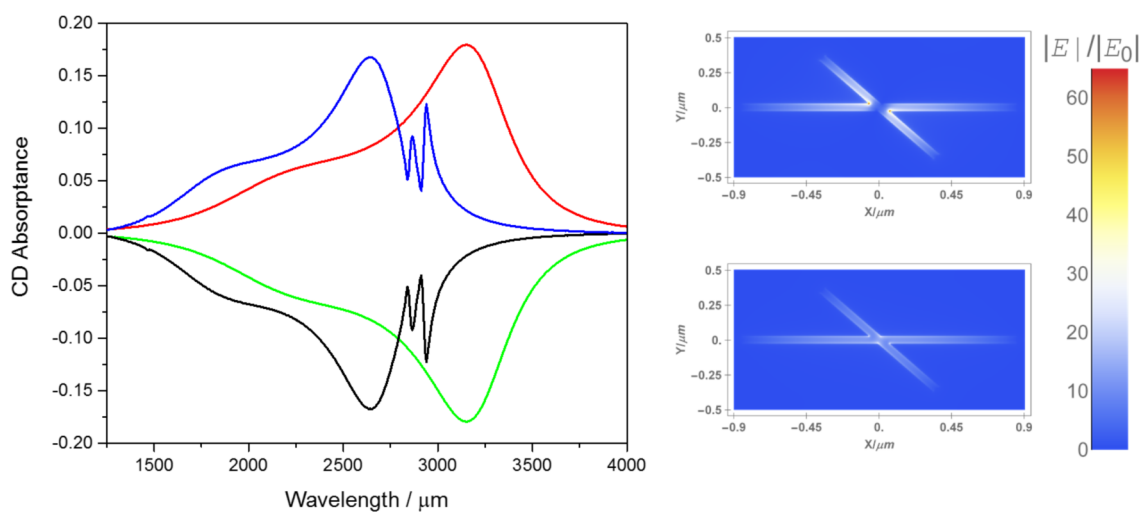


Figure S1. Left part: Simulated circular dichroism absorbance for the $+45^\circ$ (blue and red) and the -45° substrate (black and green), without polyethylene (red and green) and with polyethylene in the slits (blue and black). Accordingly, also non-chiral materials lead to bands in the spectra that are associated with vibrational transitions. Microscopically, this can be understood by the simulation of the electric field strengths shown in the right part for one of the $+45^\circ$ unit cell: For left-handed circularly-polarized light, the field enhancement is clearly stronger, which leads to a stronger vibrational signature of the non-chiral analyte.

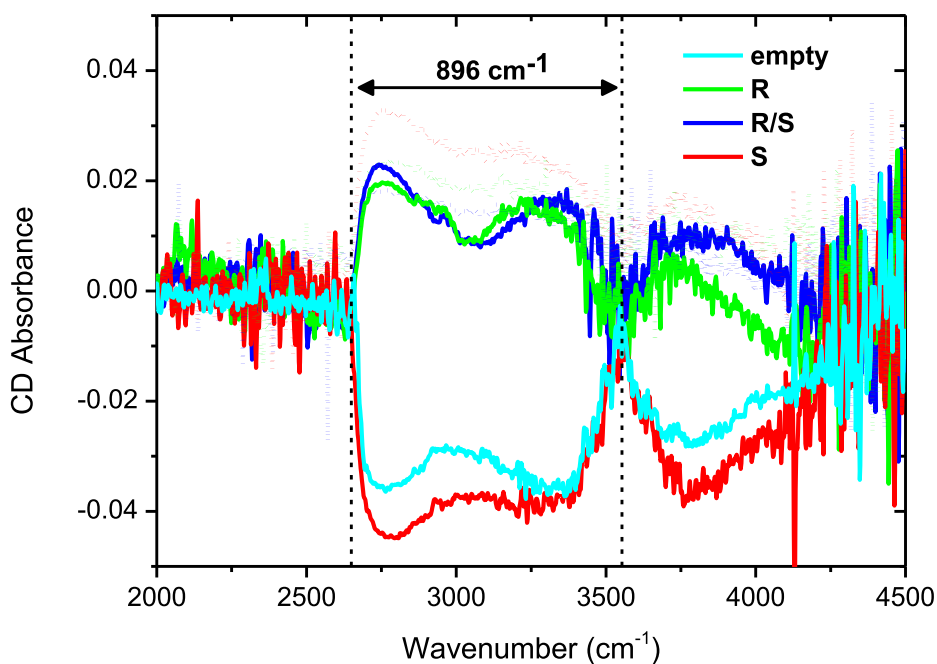


Figure S2. A control experiment with 90° angle between both slits resulting in no VCD enhancement and only minute overall CD signal in normal orientation (solid lines) and inverted orientation (dashed lines). The bandform is unchanged even at the empty array, leading to the conclusion that the minute CD signal results from a plasmonic effect being present in the CD spectra as an artifact. Due to the width 896 cm^{-1} , molecular absorptions can be excluded.

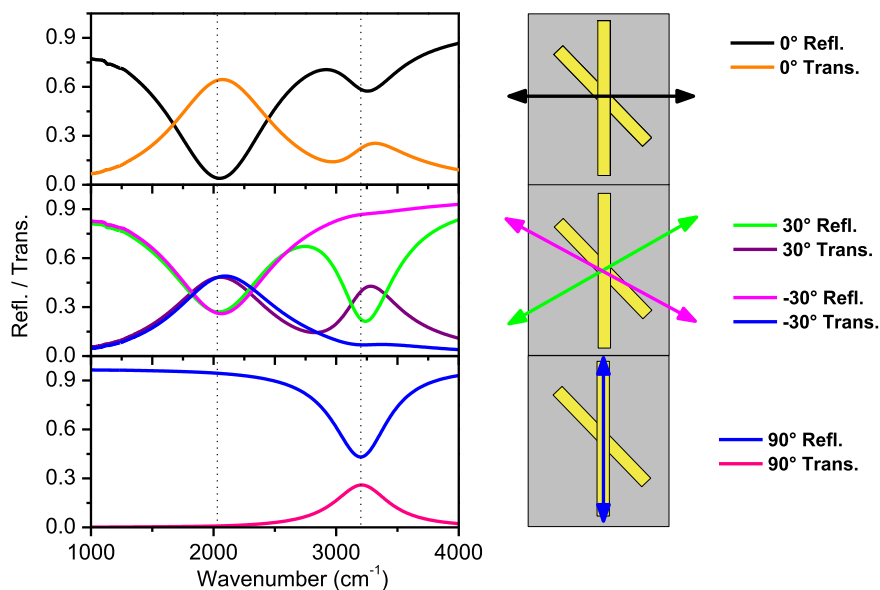


Figure S3. The relative orientation of the linearly polarized light is changed with respect to the array orientation. As can be seen, both 30° and $-30^\circ (=150^\circ)$ polarized light similarly excites the primary resonance at $\sim 2050\text{ cm}^{-1}$ but -30° oriented light nearly does not excite the secondary resonance at around 3200 cm^{-1} , since the polarization direction is almost parallel to the secondary slit orientation.

6.2 weitere Publikationen

6.2.1 THz Absorption in Fabric and Its Impact on Body Scanning for Security Application [P5]

R. Knipper, A. Brahm, E. Heinz, T. May, G. Notni, H.-G. Meyer, A. Tünnermann, J. Popp: *THz Absorption in Fabric and Its Impact on Body Scanning for Security Application*, IEEE Trans. Terahertz Sci. Technol. (2015), 5 (6), 999-1004 ©[2015] IEEE. Reprinted, with permission, from R. Knipper, A. Brahm, E. Heinz, T. May, G. Notni, H.-G. Meyer, A. Tünnermann, J. Popp: *THz Absorption in Fabric and Its Impact on Body Scanning for Security Application*, IEEE Trans. Terahertz Sci. Technol. (2015)

THz Absorption in Fabric and Its Impact on Body Scanning for Security Application

Richard Knipper, Anika Brahm, Erik Heinz, Torsten May, Gunther Notni, Hans-Georg Meyer, Andreas Tünnermann, and Jürgen Popp

Abstract—In recent years, body scanner technologies based on millimeter-wave and terahertz technologies have been shown to improve security in areas sensitive to terrorist attacks by detecting hazardous objects hidden underneath the clothing of people. Inevitably, useful devices have to provide an adequate compromise between spatial resolution limited due to diffraction and penetration through clothing. Within this context, the spectral absorption of a wide range of fabric, interference caused by the texture, and the effect of moisture within the fabric have to be considered. We have studied these effects by time-domain and Fourier transformation spectroscopy. The experimental findings are verified using a passive THz security camera operating in two frequency bands at 0.85 and 0.35 THz. The latter band was proven to be of superior use for security checks as it provides useful results even in cases of wet clothes.

Index Terms—Imaging and spectroscopy, material properties, imaging arrays.

I. INTRODUCTION

FOR a long time, the application of THz sensing was limited due to the lack of both strong sources and sensitive detectors. The spectral band from 0.1–10 THz was mostly unused, even though several features of THz radiation such as the beneficial penetration characteristics promised valuable results. This has changed due to the increasing availability of powerful radiation sources and sensitive detectors [1]. From

Manuscript received December 10, 2014; revised March 04, 2015, July 23, 2015; accepted July 30, 2015. Date of publication November 23, 2015. This work was supported in part by the Free State of Thuringia by project MUSTER under Grant 2010 FE 9020 and by the German Ministry of Research and Education by project THz Videocam TWO under Grant 13N12023. (Corresponding author: Torsten May.)

R. Knipper and J. Popp are with the Leibniz-Institut für Photonische Technologien (IPHT), 07745 Jena, Deutschland, and also with the Institut für Physikalische Chemie und Abbe Center of Photonics, Friedrich-Schiller-Universität Jena, 07743 Jena, Germany.

A. Brahm and A. Tünnermann are with the Fraunhofer Institute for Applied Optics and Precision Engineering (IOF), 07745 Jena, Germany, and also with the Institute of Applied Physics, Abbe Center of Photonics, Friedrich-Schiller-Universität Jena, 07743 Jena, Germany.

E. Heinz is with Supracon AG, 07751 Jena, Germany.

T. May and H.-G. Meyer are with Leibniz-Institut für Photonische Technologien (IPHT) (e-mail: Torsten.May@ipht-jena.de).

G. Notni is with the Fraunhofer Institute for Applied Optics and Precision Engineering (IOF), 07745 Jena, Germany, and also with the Department of Mechanical Engineering Quality Assurance and Industrial Image Processing, Technical University Ilmenau, 98693 Ilmenau, Germany.

Color versions of one or more of the figures in this paper are available online at <http://ieeexplore.ieee.org>.

Digital Object Identifier 10.1109/TTHZ.2015.2474115

this, several measurement concepts such as THz time-domain spectroscopy (THz-TDS, first shown in [2]) or THz imaging (see [3] for an overview) have emerged, benefiting application in, for example, nondestructive evaluation (NDE) [4] or quality control in the food industry [5]. Comprehensive studies of TDS measurements of fabric were done in [6]–[8] and [9], the latter two focusing on optical effects like scattering and diffraction. In particular, the application of THz imaging in the field of security screening of persons has attracted interest. Since most fabric is easily penetrated, whereas metals and ceramics are not, the idea of detecting hazardous objects hidden underneath clothing evolved. Today, millimeter-wave (mm-wave) scanners are already based on this concept. These devices operate at frequencies between 24 and 94 GHz [10], [11] and are already in use at several airports worldwide. However, because the rather large wavelength diminishes the achievable spatial resolution, this technology requires small working distances, making it inevitable for the person to be scanned to enter dedicated cabins or portals. One way to resolve this constraint is a shift to higher frequencies which makes reasonable spatial resolution possible for stand-off distances of a few meters. However, providing sufficient transmitter power becomes challenging at submillimeter wavelength. Presently several groups are investigating active [12] and passive [13], [14] systems, respectively. Because of the limited transmitter power and the strongly decreasing reflectance of human skin [15], passive systems are likely to achieve a better performance in stand-off scenarios. They have an additional benefit in public perception as no active radiation sources are used, thus avoiding any residual health concerns.

When developing such a camera system, it is essential to choose a frequency band with an optimal combination of spatial resolution and fabric absorption properties. Thus far, the frequency bands around 0.35 and 0.85 THz have been considered to best match both requirements. The band at 0.85 THz is achieving higher spatial resolution at the cost of lower fabric transparency [16]. In this paper, both frequency bands are analyzed thoroughly in terms of fabric properties and their impact on the performance of a practical security device. Therefore, measurements by THz-TDS and THz Fourier transform infrared spectroscopy (FTIR) are deployed to fully characterize the spectral properties of fabric samples. The significance of these results for passive imaging has been evaluated utilizing a practical security camera in view of assessing detrimental effects in a real life scenario.

II. EXPERIMENTAL TECHNIQUES

A. Sample Preparation

Relevant fabric samples were provided by the Textile Research Institute Thuringia-Vogtland (TITV), Greiz, Germany. The samples were measured without further drying under ambient condition (20%–50% relative humidity). For the transmission measurement of wet fabric, samples were moistened with high-purity water by dropping a grid of water droplets using a 10- μ l pipette (Eppendorf). Subsequently, the textiles were stored under sealed condition in a microfluidic chamber to keep the water content constant.

B. Spectroscopic Setups

Spectra of fabric were measured in a THz-TDS [17] system, which is based on a femtosecond Ti:Sapphire laser with a wavelength of 800 nm. The laser generates pulses with a width of 100 fs, 80-MHz repetition rate, and pulse energies of approximately 12.3 nJ. The semiconductor surface emitter is made of p-doped indium arsenide (InAs) arranged at an angle of 45 degrees. The THz pulses are guided via 90 degrees off-axis parabolic mirrors which generate a THz focus in the beam path and image the radiation onto a photoconductive antenna [17] which is made of low-temperature-grown gallium arsenid (lt-GaAs). A lock-in amplifier (LIA) is used to detect the modulated, induced photocurrents at the THz detector antenna.

In order to avoid additional water vapor absorption during the THz-TDS measurements, the complete beam path of the THz pulses was purged with nitrogen.

To verify the TDS results, a Bruker Vertex 80v FTIR spectrometer was used. The standard setup was modified with a fluid measurement cell. The cell windows were changed to Teflon with a thickness of 1 mm. This ensures a stable atmosphere without drying over the course of one measurement in an otherwise evacuated beam path, this being an issue also for samples at normal ambient moisture as opposed to TDS where the nitrogen atmosphere is drying samples much slower. The spectral resolution is theoretically as low as 0.07 cm^{-1} . A 1- cm^{-1} resolution was chosen because no narrow bands were to be expected (Fig. 1). A cryo-cooled semiconducting bolometer coupled to the spectrometer was used for the detection. To minimize the influence of water absorption, the measurements were conducted at pressure of around 3 mbar. A set of beamsplitters was used, ranging from 6 μm mylar (multilayer) to 125 μm mylar. The spectrometer was further modified with gold mirrors for maximal signal amplitude.

C. Imaging Setup

An application-oriented imaging setup was utilized in order to determine the significance of the spectroscopic data. A passive THz camera [18] was employed featuring a detector array of 20 superconducting bolometers. An optical scan yields a 100 \times 100 pixel video with a maximum frame rate of 10 Hz. The camera operates in a frequency band centered at 0.35 THz with an optical bandwidth of about 80 GHz. By exchanging the detector array and a set of optical filters, the operation frequency can be switched to 0.85 THz with almost the same bandwidth. Both bands correspond to atmospheric windows,

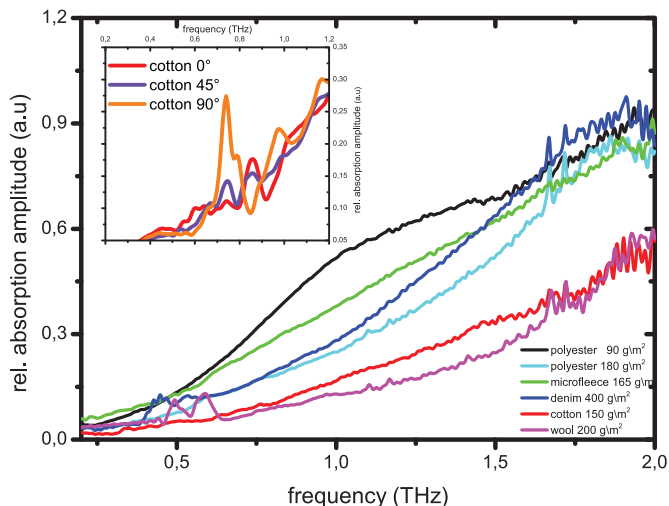


Fig. 1. Relative absorption of different fabric material, measured in a THz-TDS setup in nitrogen atmosphere. Inset: polarization dependence in single fabric layer.

ensuring a negligible attenuation due to air absorption for stand-off distances of several meters.

In order to quantify the effect of certain kinds of fabric on the contrast of typical images, an absorber test pattern was used. A metal slit mask in front of a black body source (Eccorsorb AN from Emerson & Cuming) was used to create a test pattern which was then covered with the fabric under investigation. Thicker fabric was simulated by stacking thin layers of fabric to the desired thickness. Images of the absorber setup were taken from a distance of 7 m. A modulation transfer function (relative contrast) was used to describe the measured contrast values. The relative contrast of the resulting images was then calculated as the ratio of the intensity differences of the pattern with and without fabric coverage within one single image. Thus, this value represents the absorption of the fabric only and eliminates the influence of the diffraction-related contrast deterioration (MTF).

III. RESULTS

A. Spectroscopic Analysis of Fabric

First, the TDS setup was used in order to determine the absorption strength of fabric in the range from 0.1 to 2.5 THz. THz pulses were measured after passing through a single layer of fabric. The time window was 70 ps, an optical delay of 0.5 (ps)/(s) and a LIA averaging time of 300 ms were chosen as best suited. Five different positions per sample were averaged. Sample spectra were calculated by the subtraction of reference spectra which had been determined without a sample in the THz beam path. Frequencies less than 0.1 THz and greater than 1.8 THz are negligible because of the low dynamic range of the system in this frequency range [19].

The results of these TDS measurements are shown in Fig. 1. Each fabric is transparent in a frequency range from 0.1 to 1.8 THz, exhibiting the same general trend of increasing absorption with higher frequencies as observed by other authors [7], [16]. Deviations in the fine structure of the spectra might be caused by optical effects such as interference and polarization

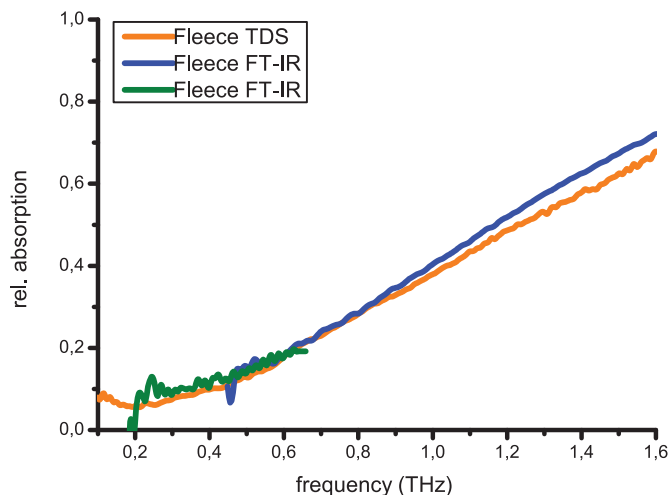


Fig. 2. Comparative measurement of a microfleece sample in both FT-IR and TDS setup. Split FT-IR spectrum due to the required change of beam splitter.

TABLE I
RELATIVE ABSORPTION OF FABRIC AT 0.35 AND 0.85 THZ

Fabric	abs. at 0.35 THz	abs. at 0.85 THz
Polyester 90 g/m ²	1,6%	8,9%
Polyester 180 g/m ²	4,4%	10,2%
Microfleece 165 g/m ²	3,5%	19,2%
Denim 410 g/m ²	7,6%	28,9%
Cotton 150 g/m ²	3,7%	17,9%
Wool 200 g/m ²	5,5%	35,8%

dependence as indicated in the work of Naftaly *et al.* For security application, frequencies below approximately 1 THz seem to be useful. However, because of the unavoidable influence of the atmosphere, the operation of the camera used for the subsequent experiments was restricted to atmospheric windows at 0.35 THz and 0.85 THz. In Table I, the values of the respective relative absorptions as measured by TDS are shown for these frequencies. Comparability between measurements conducted by TDS and FT-IR was ensured by side-by-side measurements of the same sample. At the example of microfleece, Fig. 2 shows a good agreement of both measurements, whereas the deviation at higher frequencies might be caused by the decreasing SNR of the TDS setup.

B. Fabric Analysis With the THz Camera

The relative contrast was shown to be linear with the thickness of the sample. As can be seen in Fig. 3, the 0.85-THz band exhibits a generally lower relative contrast value compared with the 0.35-THz band. This is due to the stronger absorption by fabric in this range (compare Figs. 1 and 2). As an example, four layers of cotton (600 (g/m²), representing, for example, a seam), decreased the relative contrast to 71% at 0.35 THz, whereas for 0.85 THz it is already as low as 17%. It became apparent that the relative decrease of the relative contrast between the 0.35 THz and 0.85 THz band is quite different for various fabric. The increase factor ranges from being as low as a factor of 2.3 for polyester to a factor of 6.5 for wool (Table I). On average, the absorption of single-layer fabric for typical clothes is of the order of 5% at 0.35 THz and 30% at 0.85 THz. As expected,

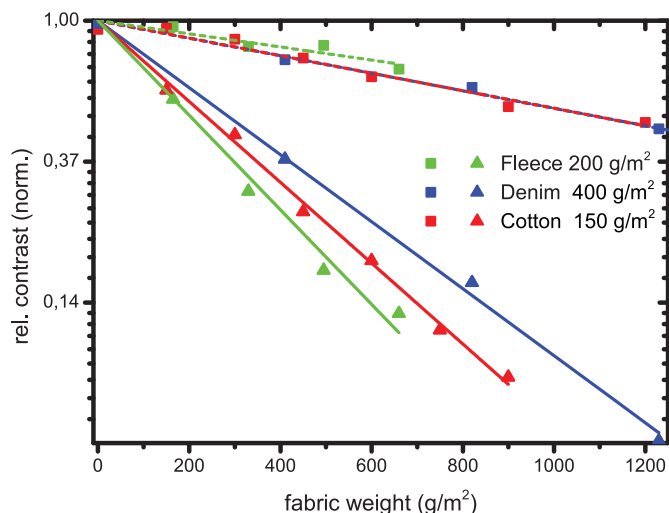


Fig. 3. Relative contrast for multiple layers of dry fabric at 0.35 THz (square) and 0.85 THz (pyramid) normalized against undisturbed beampath.

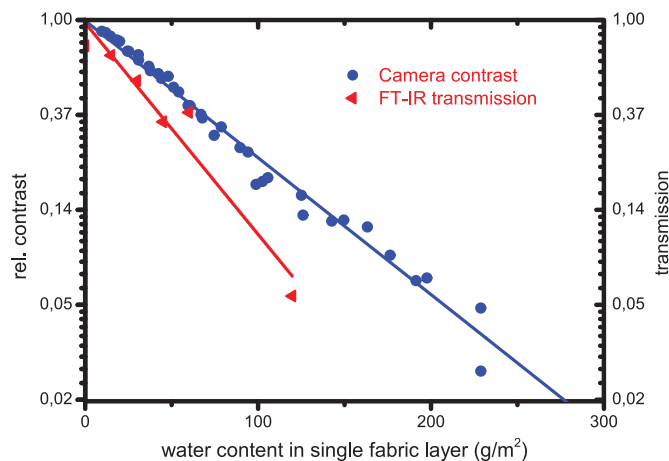


Fig. 4. Average transmission of all fabric samples at 0.35 THz (pyramid symbols) relative contrast ratio of a single fleece layer (circles, measured and weighed while drying).

our data show a direct correlation between the relative contrast of the camera and the spectral characteristics (see Fig. 5).

C. Influence of Water in Fabric

Any security scanner operating in the microwave/THz spectral range is strongly influenced by moisture. TDS measurements clearly show that for wet samples, transmission is severely attenuated. Moreover, the influence becomes notably stronger for higher frequencies, as depicted in the cotton example. Here, the absorption rate is increased by about 44% at 0.35 THz and about 61% at 0.85 THz in comparison to the dry sample. Follow-up FTIR measurements supported these findings as shown in Fig. 4. By comparing the relative camera contrast (Fig. 5) with the average transmission for 0.35 THz (Fig. 4), it becomes evident that predictions on camera performance by means of FT-IR are feasible also for wet clothing.

Nonetheless, measurements with the passive camera showed that reasonable security imaging remains possible for wet fabric. The amount of water in the fabric samples was varied by slowly drying them from the point of saturation. Images during the

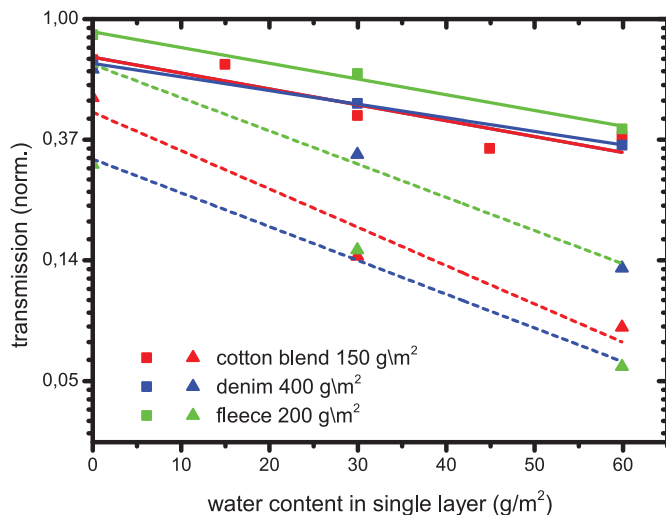


Fig. 5. Transmission through wet fabric samples, normalized against empty fluid cell at 0.35 THz (solid line) and 0.85 THz (dashed line) with eyeguide.

course of the drying process have been taken whilst recording the sample weight. The results are shown in Fig. 5. Partially wet samples, e.g., representing cases of slightly sweat imbued clothes, are fairly transparent. Surprisingly, even nearly saturated fabric samples can still be penetrated at 0.35 THz, whilst at 0.85 THz the influence of water renders security imaging impossible.

D. Influence of Textural Effects

Most fabric is woven with warp and weft yarns into weave patterns like plain or twill weave. In consequence, they can act as diffraction gratings in the THz range since the dimensions of the yarns and stitches are of the order of the corresponding wavelengths. Thus, optical effects like polarization dependent spectra can influence THz measurements. An example is shown in the inset of Fig. 1, where a woven piece of cotton ($1.5 \text{ (g)/(cm}^2\text{)}$) was measured for different rotation angles. For each angle, 20-THz pulses were measured at different positions of the sample. The cotton sample exhibits an absorption peak around 0.76 THz ($\approx 395 \mu\text{m}$) at 0 degrees orientation, which almost vanishes at 90-degree orientation. This effect is discussed in more detail by [7]. Although the current detector concept of the passive THz camera is independent of polarization, future implementations might favor polarization-dependent detectors. It has to be taken into account that typical weave dimensions would place the resulting polarization artifact closer to the 0.85-THz band than to the 0.35-THz band.

IV. CONCLUSION

We have studied the absorption properties of several fabrics for typical human clothing in the THz spectral range with three independent measurement techniques: THz-TDS, THz-FTIR and passive THz imaging. With respect to the intended application of security checks of people, our data demonstrate that the 0.35 THz band is of superior use in comparison to the 0.85-THz band. The lower frequency allows for a reasonable penetration of fabric in dry and wet conditions; even if several layers of fabric are on top of each other (e.g., in seams, see

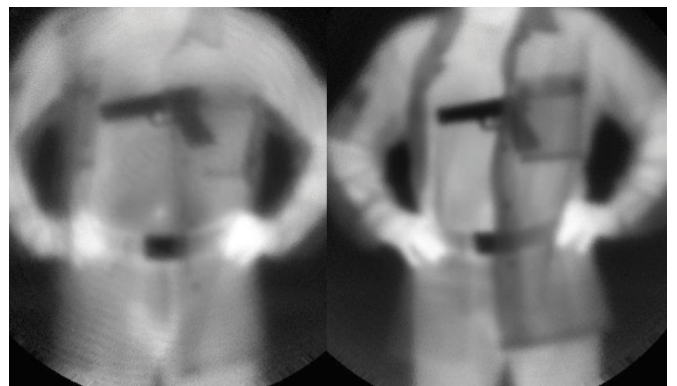


Fig. 6. Left: 0.35-THz image showing low resolution but less obstruction by fabric. Right: 0.85-THz image by THz camera showing good resolution (limited by the used THz optics) but strong influence by fabric cover (pistol grip, belt buckle).

Fig. 6). Regardless of the better diffraction-limited spatial resolution, the 0.85 THz band appears to be the less desirable option. Here, a generally higher absorption and polarization effects in the case of some widespread fabric can cause a severe degradation of the detection capability. Our study further shows that TDS and FTIR are equally suited to determine the spectral characteristics of fabric. This is of importance in two areas. First, a prediction of the camera performance in relevant spectral ranges becomes possible, thus benefiting the design of future camera generations. Second, the exact knowledge of fabric properties allows for the calculation of their expected shadowing effect on the objects to be detected for a given camera configuration. Taking into account typical designs for clothing, such prior knowledge would enable detection algorithms to eliminate the influence of absorption by the clothes which would otherwise be detected as artifacts. In the near future, a numerical model of relevant clothes based on data taken from this study can be integrated as a subroutine into object recognition software.

ACKNOWLEDGMENT

The authors would like to thank V. Reichmann, TITV Greiz, for the professional sample preparation, and for valuable technical discussions.

REFERENCES

- [1] E. Bründermann, H.-W. Hübers, and M. F. Kimmitt, *Terahertz Techniques*. New York, NY, USA: Springer, 2012.
- [2] M. van Exter, C. Fattinger, and D. Grischkowsky, "Terahertz time-domain spectroscopy of water vapor," *Opt. Lett.*, vol. 14, no. 20, pp. 1128–1130, 1989.
- [3] P. Jepsen, D. Cooke, and M. Koch, "Terahertz spectroscopy and imaging modern techniques and applications," *Laser & Photon. Rev.*, vol. 5, no. 1, pp. 124–166, 2011.
- [4] A. S. Skryl, J. B. Jackson, M. I. Bakunov, M. Menu, and G. A. Mourou, "Terahertz time-domain imaging of hidden defects in wooden artworks: Application to a russian icon painting," *Appl. Opt.*, vol. 53, no. 6, pp. 1033–1038, 2014.
- [5] C. Jansen, B. Scherger, C. Jördens, I. A. I. Al-Naib, and M. Koch, "Terahertz imaging spectroscopy for quality inspection in the food industry," *Food Eng. Ingredients*, pp. 11–14, 2010.
- [6] C. Gerth, A. Brahm, V. Reichmann, and G. Nothi, "Investigation of spectral properties of textile," in *Proc. 37th Int. Conf. Infrared, Millimeter, and Terahertz Waves*, 2012, vol. 1, pp. 23–28.
- [7] M. Naftaly, J. F. Molloy, G. V. Lanskie, K. A. Kokh, and Y. M. Andreev, "Terahertz time-domain spectroscopy for textile identification," *Appl. Opt.*, vol. 52, no. 19, pp. 4433–4437, 2013.

- [8] E. Heralut, M. Hofman, F. Garet, and J. L. Coutaz, "Observation of terahertz beam diffraction by fabrics," *Opt. Lett.*, no. 38, pp. 2708–2710, 2013.
- [9] I. N. Fokina, K. I. Zaytsev, V. E. Karasik, and K. P. Tsapenko, "Scattering of terahertz radiation in thin layers of dielectric materials," in *Proc. SPIE*, 2013, no. 8846, Art. ID 88460A.
- [10] , D. Saeedkia, Ed., *Handbook of Terahertz Technology for Imaging, Sensing and Communications*. Amsterdam, The Netherlands: Elsevier, 2013.
- [11] , J. Popp, V. V. Tuchin, A. Chiou, and S. H. Heinemann, Eds., *Handbook of Biophotonics: 3*. New York, NY, USA: Taylor and Francis, 2014.
- [12] D. Sheen, T. Hall, R. Severtsen, D. McMakin, B. Hatchell, and P. Valdez, "Active wideband 350 GHz imaging system for concealed-weapon detection," in *Proc. SPIE*, 2009, vol. 7309, Art. ID 73090I.
- [13] T. May, V. Zakosarenko, E. Kreysa, W. Esch, S. Anders, E. Heinz, and H.-G. Meyer, "Design, realization and characteristics of a transition edge bolometer for sub-millimeter wave astronomy," *Rev. Sci. Instrum.*, vol. 83, no. 11, 2012, Art. ID 114502.
- [14] A. Luukanen, L. Grnberg, P. Helistö, J. S. Penttilä, H. Seppä, H. Sipola, C. R. Dietlein, and E. N. Grossman, "Passive euro-american terahertz camera (peat-cam): Passive indoor THz imaging at video rates for security applications," in *Proc. SPIE*, 2007, vol. 6548, Art. ID 654808.
- [15] R. Appleby and H. Wallace, "Standoff detection of weapons and contraband in the 100 GHz to 1 THz region," *IEEE Trans. Antennas Propag.*, vol. 55, no. 11, pp. 2944–2956, Nov. 2007.
- [16] J. E. Bjarnason, T. L. J. Chan, A. W. M. Lee, M. A. Celis, and E. R. Brown, "Millimeter-wave, terahertz, and mid-infrared transmission through common clothing," *Appl. Phys. Lett.*, vol. 85, pp. 519–521, 2004.
- [17] A. Brahm, A. Wilms, M. Tymoshchuk, C. Grossmann, G. Notni, and A. Tünnermann, "Optical effects at projection measurements for terahertz tomography," *Opt. Laser Technol.*, vol. 62, pp. 49–57, 2014.
- [18] E. Heinz *et al.*, "Passive submillimeter-wave stand-off video camera for security application," *J. Infrared, Millimeter and THz Waves*, vol. 31, no. 11, pp. 1355–1369, 2010.
- [19] P. U. Jepsen and B. M. Fischer, "Dynamic range in terahertz time-domain transmission and reflection spectroscopy," *Opt. Lett.*, vol. 30, no. 1, pp. 29–31, 2005.



Richard Knipper received the Diploma in physics from the Friedrich Schiller Universität Jena, Jena, Germany, in 2012. He is currently working toward the Ph.D. degree at the Institut für Physikalische Chemie and the Leibniz Institute of Photonic Technology, Jena, Germany.

His research interests are plasmonic metamaterials and their fabrication, THz and FT-IR spectroscopy and superconductivity.



Anika Brahm received the B.Eng. and M.Eng. degree in laser and optotechnologies from the University of Applied Sciences, Jena, Germany, in 2006 and 2009, respectively. She is currently working toward the Ph.D. degree at the Faculty of Physics and Astronomy, Institute of Applied Physics, Friedrich Schiller University Jena, Germany.

In 2009, she joined the Fraunhofer Institute for Applied Optics and Precision Engineering, Jena, Germany, where she is currently a Research Associate. Her research interests include THz optics,

spectroscopy, imaging, and computed tomography.



Erik Heinz received the Diploma degree in physics and Ph.D. degree from the Friedrich Schiller University Jena, Germany, in 1988 and 1993, respectively.

From 1988 to 1995, he was a Research Associate with the Institute of Solid State Physics, Friedrich Schiller University, Jena, Germany. In 1996, he co-founded an Internet service provider startup company where he was a Network Designer and Consultant until 2008. From 2008 to 2013, he was a Research Associate with the Leibniz Institute of Photonic Technology, Jena, Germany. In 2013, he joined the company Supracon. His research interests include low-temperature radiation detectors, multiplexed readout, and low-temperature electronics.



Torsten May received the Diploma degree in physics from the Friedrich Schiller University, Jena, Germany, in 1997.

Since then, he has been a Research Associate with the Leibniz Institute of Photonic Technology, Department of Quantum Detection, Jena, Germany. Since 2007, he has been the head of the Quantum Radiometry research group. His research interest is focused on the development of detectors based on superconducting technology, in particular for sensing electromagnetic radiation.



Gunther Notni received the Diploma and Ph.D. degree in physics from the Friedrich Schiller University, Jena, Germany, in 1988 and 1992, respectively.

From 1992 to 2014, he was a Staff Member with the Fraunhofer Institution for Applied Optics and Precision Engineering, Jena, Germany, where he been head of the Optical Systems Department since 1994. Since October 2014, he has been a Professor with the Technical University Ilmenau, Ilmenau, Germany, and headed the Group for Quality Assurance and Industrial Image Processing. His

research interests include optical 3-D shape measurement, methods of surface characterization, interferometry, speckle interferometry, THz imaging, and the application of phase conjugation in optical metrology using photorefractive crystals.



Hans-Georg Meyer received the Ph.D. degree from the Friedrich Schiller University Jena, Germany, in 1981, and habilitated there in 1991.

Since 1974, he has been working on the subject of weak superconductivity, in particular on the development of ultra-sensitive magnetometers. Since 1993, he has been head of the Department of Quantum Detection, Leibniz Institute of Photonic Technology, Jena, Germany. Since 2009, he has also been a Professor of applied physics and solid-state physics at the Friedrich Schiller University Jena, Germany.

His research interests include the development of superconducting electronics and systems and their application in sophisticated measuring techniques.



Andreas Tünnermann was born in Ahnsen, Germany, on June 10, 1963. He received the Diploma and Ph.D. degrees in physics from the University of Hannover, Hannover, Germany, in 1988 and 1992, respectively, and the Habilitation in 1997.

He was head of the Department of Development at the Laser Zentrum Hannover from 1992 to 1997. In early 1998, he joined the Friedrich Schiller University, Jena, Germany, as a Professor and Director of the Institute of Applied Physics. In 2003, he was appointed as the Director of the Fraunhofer Institute

for Applied Optics and Precision Engineering IOF, Jena. He is author of more than 400 papers in renowned international journals. He is a sought-after expert in optics and photonics industry. He is founder and member of the board of directors of the industry-driven cluster OptoNet Jena, which is one of the most dynamic regional optics clusters in Europe. His main research interests include scientific and technical aspects associated with the tailoring of light.

Prof. Tünnermann is a Fellow of SPIE. He was the recipient of the Gottfried-Wilhelm-Leibniz-Award in 2005.



Jürgen Popp received the Ph.D. degree in chemistry from the University of Wuerzburg, Wuerzburg, Germany.

After completing his doctoral work, he joined Yale University for postdoctoral work. He subsequently returned to the University of Wuerzburg, where he finished his habilitation in 2002. Since 2002, he has held a chair for Physical Chemistry at the Friedrich-Schiller University, Jena, Germany. Furthermore, he has been the Scientific Director of the Leibniz Institute of Photonic Technology, Jena, since 2006. His research interests are mainly concerned with biophotonics, in particular, the development and application of innovative Raman techniques for biomedical diagnostics as well as environmental and food analysis is at the heart of his interests. He has published more than 450 journal papers.

Dr. Popp is a Fellow of SAS and SPIE. In 2012, he received an honorary doctor's degree from Babes-Bolyai University Cluj-Napoca, Romania, and the Robert-Kellner Lecture Award in 2013.

6.2.2 A low power 10 V programmable array based on Nb x Si_{1-x} Josephson junctions for metrology applications

Knipper, Richard; Anders, Solveig; Schubert, Marco; Peiselt, Katja; Scheller, Thomas; Franke, Dirk; Dellith, Jan; Meyer, Hans-Georg, *A low power 10 V programmable array based on Nb x Si_{1-x} Josephson junctions for metrology applications*, Superconductor Science and Technology (2016) 095015-1

6.2.3 A dry-cooled AC quantum voltmeter

Schubert, Marco; Starkloff, Michael; Peiselt, Katja; Anders, Solveig; **Knipper, Richard**; Lee, Jinni; Behr, Ralf; Palafox, Luis; Böck, Andreas Charles; Schaidhammer, Ludwig; Fleischmann, Philip M.; Meyer, Hans-Georg, *A dry-cooled AC quantum voltmeter*, Superconductor Science and Technology (2016) 105014-1

6.3 weitere Veröffentlichungen

6.3.1 Hochsensitive infrarotspektroskopische Analytik mittels plasmonischer Feldverstärkung

Thomas Mayerhöfer, Uwe Hübner, **Richard Knipper**, Jürgen Popp, *Hochsensitive infrarotspektroskopische Analytik mittels plasmonischer Feldverstärkung*, Aktuelle Wochenschau der Gesellschaft Deutscher Chemiker (GDCh), 2015

6.4 non-peer-review - Publikationen, Tagungsbände

6.4.1 Wafer- and membrane-based plasmonic sensor surfaces for ultra-sensitive molecular spectroscopy

Uwe Huebner , Thomas G. Mayerhoefer , **Richard Knipper** , Sophie Patze , Dana Cialla-May , Karina Weber , Juergen Popp - *Wafer- and membrane-based plasmonic sensor surfaces for ultrasensitive molecular spectroscopy*, Micro-Nano-Integration; 6. GMM-Workshop, Duisburg, Germany, 2016, pp. 1-6. ISBN: 978-3-8007-4278-3

6.4.2 Plasmonische Strukturen für die Bioanalytik

Richard Knipper, Uwe Hübner, Thomas Mayerhöfer, Torsten May, Dana Cialla, Karina Weber, Jürgen Popp, *Plasmonische Strukturen für die Bioanalytik*, Tagungsband 7. Doktorandenseminar 2013, ISBN:978-3-9815360-9-6

6.5 Autorenbeiträge

Ultra Sensing by Combining Extraordinary Optical Transmission with Perfect Absorption – ACS Photonics (2015), 2 (11), pp 1567–1575

Thomas G. Mayerhöfer	Konzeptentwicklung, Durchführung der Simulationen und Interpretation der Daten, Erstellung des Manuskripts
Richard Knipper	Planung der Messungen, Durchführung der experimentellen Arbeiten und Interpretation der Daten, Technologische Entwicklung, Erstellung des Manuskripts
Uwe Hüber	Technologische Entwicklung, Diskussion der Konzepte und der Ergebnisse
Dana Cialla-May	Diskussion der Konzepte und der Ergebnisse
Karina Weber	Diskussion der Konzepte und der Ergebnisse
Hans-Georg Meyer	Diskussion der Konzepte und der Ergebnisse
Jürgen Popp	Projektleitung, Diskussion der Konzepte und der Ergebnisse, Korrekturlesen des Manuskripts

6 Publikationen und Konferenzbeiträge

Plasmonic nanostructures for surface enhanced spectroscopic methods – Analyst 141, pp 756 (2016)

Martin Jahn	Konzeptentwicklung, Verfassung und Zusammenführen von Reviewkapiteln
Sophie Patze	Konzeptentwicklung, Verfassung und Zusammenführen von Reviewkapiteln
Izabella Jolan Hidi	Verfassung und Zusammenführen von Reviewkapiteln
Richard Knipper	Verfassung der Kapitel Theorie FT-IR und oberflächenverstärkender Substrate
Andreea Radu	Verfassung von Reviewkapiteln
Anna Mühlig	Verfassung von Reviewkapiteln
Sezin Yuksel	Verfassung von Reviewkapiteln
Karina Weber	Diskussion der Konzepte und der Ergebnisse, Korrekturlesen des Manuskripts
Thomas G. Mayerhöfer	Diskussion der Konzepte und der Ergebnisse, Korrekturlesen des Manuskripts
Dana Cialla-May	Diskussion der Konzepte und der Ergebnisse, Korrekturlesen des Manuskripts
Jürgen Popp	Projektleitung, Diskussion der Konzepte und der Ergebnisse, Korrekturlesen des Manuskripts

Observation of Giant Infrared Circular Dichroism in Plasmonic 2D-Metamaterial Arrays – ACS photonics 2018, pp. tba

Richard Knipper	Konzeptentwicklung, Durchführung der experimentellen Arbeiten sowie der Datenanalyse und -interpretation, Durchführung der chiralen Messungen (teilweise), Erstellung des Manuskripts
Vladimir Kopecky Jr	Durchführung der chiralen Messungen, Diskussion der Konzepte und der Ergebnisse
Uwe Hübner	Diskussion der Konzepte und der Ergebnisse, Korrekturlesen des Manuskripts
Jürgen Popp	Projektleitung, Diskussion der Konzepte und der Ergebnisse, Korrekturlesen des Manuskripts
Thomas G. Mayerhöfer	Konzeptentwicklung, Durchführung der Simulationen, Diskussion der Konzepte und der Ergebnisse, Korrekturlesen des Manuskripts

Slit-enhanced chiral- and broadband infrared ultra-sensing – submitted to: ACS Photonics (2018)

Richard Knipper	Konzeptentwicklung, Durchführung der experimentellen Arbeiten sowie der Datenanalyse und -interpretation, Erstellung des Manuskripts
Thomas G. Mayerhöfer	Konzeptentwicklung, Durchführung der Simulationen, Diskussion der Konzepte und der Ergebnisse, Korrekturlesen des Manuskripts
Vladimir Kopecky Jr	Durchführung der chiralen Messungen, Diskussion der Konzepte und der Ergebnisse
Uwe Hübner	Diskussion der Konzepte und der Ergebnisse, Korrekturlesen des Manuskripts
Jürgen Popp	Projektleitung, Diskussion der Konzepte und der Ergebnisse, Korrekturlesen des Manuskripts

6.5.1 Erklärung zu den Eigenanteilen des Promovenden**Erklärung zu den Eigenanteilen des Promovenden sowie der weiteren Doktoranden/Doktorandinnen als Koautoren an den Publikationen und Zweitpublikationsrechten bei einer kumulativen Dissertation**

Ultra Sensing by Combining Extraordinary Optical Transmission with Perfect Absorption - Mayerhöfer, Thomas G.; Knipper, Richard; Hübner, Uwe; Cialla-May, Dana; Weber, Karina; Meyer, Hans-Georg; Popp, Jürgen , ACS Photonics (2015), 2 (11), pp 1567–1575

Beteiligt an:	
	R. Knipper
Konzeption des Forschungsansatzes	X
Planung der Untersuchungen	X
Datenerhebung	X
Datenanalyse und -interpretation	X
Schreiben des Manuskripts	X
Vorschlag Anrechnung Publikationsäquivalente	1,0

Plasmonic nanostructures for surface enhanced spectroscopic methods – Jahn, Martin; Patze, Sophie; Hidi, Izabella Jolan; Knipper, Richard; Radu, Andreea; Mühlig, Anna; Yüksel, Sezin; Peksa, Vlastimil; Weber, Karina; Mayerhöfer, Thomas G.; Cialla-May, Dana; Popp, Jürgen Plasmonic nanostructures for surface enhanced spectroscopic methods, Analyst (2016), 141, pp 756

Beteiligt an:		
	R. Knipper	V. Peksa
Konzeption des Forschungsansatzes	X	
Planung der Untersuchungen	X	
Datenerhebung	X	
Datenanalyse und -interpretation	X	X
Schreiben des Manuskripts	X	
Vorschlag Anrechnung Publikationsäquivalente	0,5	0,25

Observation of Giant Infrared Circular Dichroism in Plasmonic 2D-Metamaterial Arrays – Richard Knipper, Thomas G. Mayerhöfer, Vladimir Kopecky Jr., Uwe Huebner, and Jürgen Popp, Observation of Giant Infrared Circular Dichroism in Plasmonic 2D-Metamaterial Arrays, ACS Photonics (2018)

Beteiligt an:	
	R. Knipper
Konzeption des Forschungsansatzes	X
Planung der Untersuchungen	X
Datenerhebung	X
Datenanalyse und -interpretation	X
Schreiben des Manuskripts	X
Vorschlag Anrechnung Publikationsäquivalente	1,0

Slit-enhanced chiral- and broadband infrared ultra-sensing – Richard Knipper, Vladimir Kopecky Jr, Uwe Hübner, Jürgen Popp, Thomas G. Mayerhöfer, Broadband Ultra Sensing in Chiral Metamaterials by Extraordinary Optical Transmission, submitted to: ACS Photonics

Beteiligt an:	
	R. Knipper
Konzeption des Forschungsansatzes	X
Planung der Untersuchungen	X
Datenerhebung	X
Datenanalyse und -interpretation	X
Schreiben des Manuskripts	X
Vorschlag Anrechnung Publikationsäquivalente	1,0

6.5 Autorenbeiträge

Für alle in dieser kumulativen Dissertation verwendeten Manuskripte liegen die notwendigen Genehmigungen der Verlage („Reprint Permissions“) für die Zeitpublikation vor. Die Co-Autoren der in dieser kumulativen Dissertation verwendeten Manuskripte sind sowohl über die Nutzung, als auch über die oben angegebenen Eigenanteile der weiteren Doktoranden/Doktorandinnen als Koautoren an den Publikationen und Zweitpublikationsrechten bei einer kumulativen Dissertation informiert und stimmen dem zu.

Name des Promovenden	Datum	Ort	Unterschrift
----------------------	-------	-----	--------------

Ich bin mit der Abfassung der Dissertation als publikationsbasiert, d.h. kumulativ, einverstanden und bestätige die vorstehenden Angaben. Eine entsprechend begründete Befürwortung mit Angabe des wissenschaftlichen Anteils des Doktoranden/der Doktorandin an den verwendeten Publikationen werde ich parallel an den Rat der Fakultät der Chemisch-Geowissenschaftlichen Fakultät richten.

Name Erstbetreuer(in)	Datum	Ort	Unterschrift
-----------------------	-------	-----	--------------

6.6 Konferenzbeiträge (Poster)

Richard Knipper, Uwe Hübner, Thomas Mayerhöfer, Torsten May, Dana Cialla, Karina Weber, Jürgen Popp, *Plasmonische Strukturen für die Bioanalytik*, 7. Doktorandenseminar 2013, 24.-26.02.2013, Berlin, Deutschland IBAN 978-3-9815360-9-6

Richard Knipper, Uwe Hübner, Thomas Mayerhöfer, Torsten May, Hans-Georg Meyer, Dana Cialla, Karina Weber, Jürgen Popp, *A Total Absorber for THz-Spectroscopy* IRMMW THz, 01.-06.09.2013, Mainz, Deutschland

Richard Knipper, Uwe Hübner, Thomas Mayerhöfer, Torsten May, Hans-Georg Meyer, Dana Cialla, Karina Weber, Jürgen Popp, *A Total Absorber for THz-Spectroscopy in Life sciences* MNE 16-19.09.2013, London, England

Richard Knipperra, Uwe Hübner, Thomas Mayerhöfer, Torsten May, Hans-Georg Meyer, Karina Weber, Dana Cialla-Maya, Jürgen Popp, *A tuneable THz total absorber for life science applications*, SES2014, 07.-10.08.2014, Chemnitz, Deutschland

Richard Knipper, Thomas Mayerhöfer, Uwe Hübner, Karina Weber, Dana Cialla-May, Jürgen Popp, *Fabrication and characterization of a SEIRA total absorber* META2015, 04.-07.08.2015, New York, Vereinigte Staaten von Amerika

6.6.1 weitere Poster und Publikationen

Richard Knipper, Solveig Anders, Katja Peiselt, Dirk Franke, Michael Starkloff, Marco Schubert, Jürgen Popp, Hans-Georg Meyer, *Nb/Si_x- Herstellungstechnologie für 10 V programmierbare Josephson-Spannungsnormalschaltungen*, Kryo 2015, 27.-29. September 2015, Braunschweig, Deutschland

6.7 Lebenslauf

Persönliche Daten:

Geburtsdatum 07.06.1984
 Geburtsort Barßel
 Familienstand ledig

Bildungsweg

2005–2011 **Studium der Physik (Diplom)** an der Friedrich-Schiller-Universität Jena
 2011–2012 **Diplomarbeit** am Leibniz-Institut für Photonische Technologien
 2012–heute **Doktorand** der Chemisch-Geowissenschaftlichen Fakultät - Institut für Physikalische Chemie und am Leibniz Institut für Photonische Technologie e.V

Beruflicher Werdegang

2016–2016 Projektleiter Energie bei der AViSpek-tro UG
 2016–heute Technologie im Bereich Sensorentwicklung am Leibniz Institut für Photonische Technologie e.V

(Unterschrift)

(Datum)

Appendix

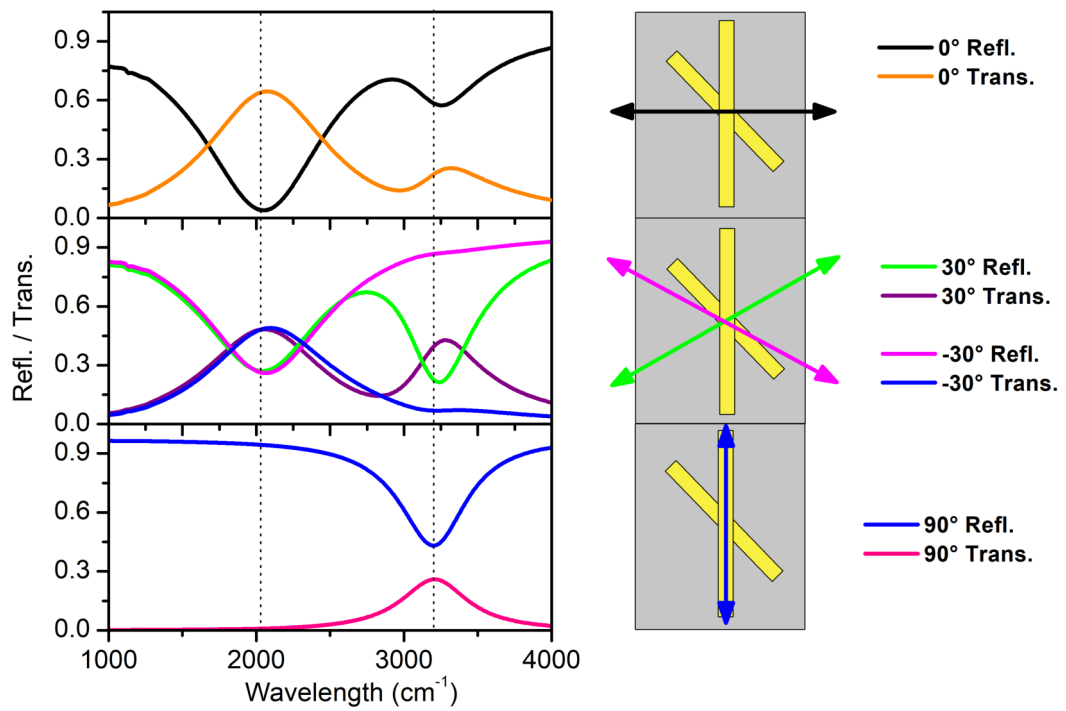


Abbildung .1: [Appendix 1] Relative Orientierung des linear polarisierten Anregungslicht zur Ausrichtung des Schlitzarray. Wie ersichtlich regt sowohl + wie auch -30° orientiertes Licht die primäre Resonanz bei 2050 cm⁻¹ an, jedoch ist die Anregung der sekundären Resonanz bei 3200 cm⁻¹ ungleich, da die Polarisationssebene für -30° fast parallel zum sekundären Schlitz orientiert ist. Aus [6.1.4, supplement]